TU Delft

Delft University of Technology

Document Version
Final published version

Licence
CC BY

Citation (APA)
Spinosa, A. (2026). *Data-driven tools for assessing ecosystem health*. [Dissertation (TU Delft), Delft University of Technology]. https://doi.org/10.4233/uuid:0550fde3-0826-42eb-957f-c1eec4fcf466

Important note
To cite this publication, please use the final published version (if applicable).
Please check the document version above.

Copyright
In case the licence states “Dutch Copyright Act (Article 25fa)”, this publication was made available Green Open Access via the TU Delft Institutional Repository pursuant to Dutch Copyright Act (Article 25fa, the Taverne amendment). This provision does not affect copyright ownership.
Unless copyright is transferred by contract or statute, it remains with the copyright holder.

Sharing and reuse
Other than for strictly personal use, it is not permitted to download, forward or distribute the text or part of it, without the consent of the author(s) and/or copyright holder(s), unless the work is under an open content license such as Creative Commons.

Takedown policy
Please contact us and provide details if you believe this document breaches copyrights.
We will remove access to the work immediately and investigate your claim.

This work is downloaded from Delft University of Technology.

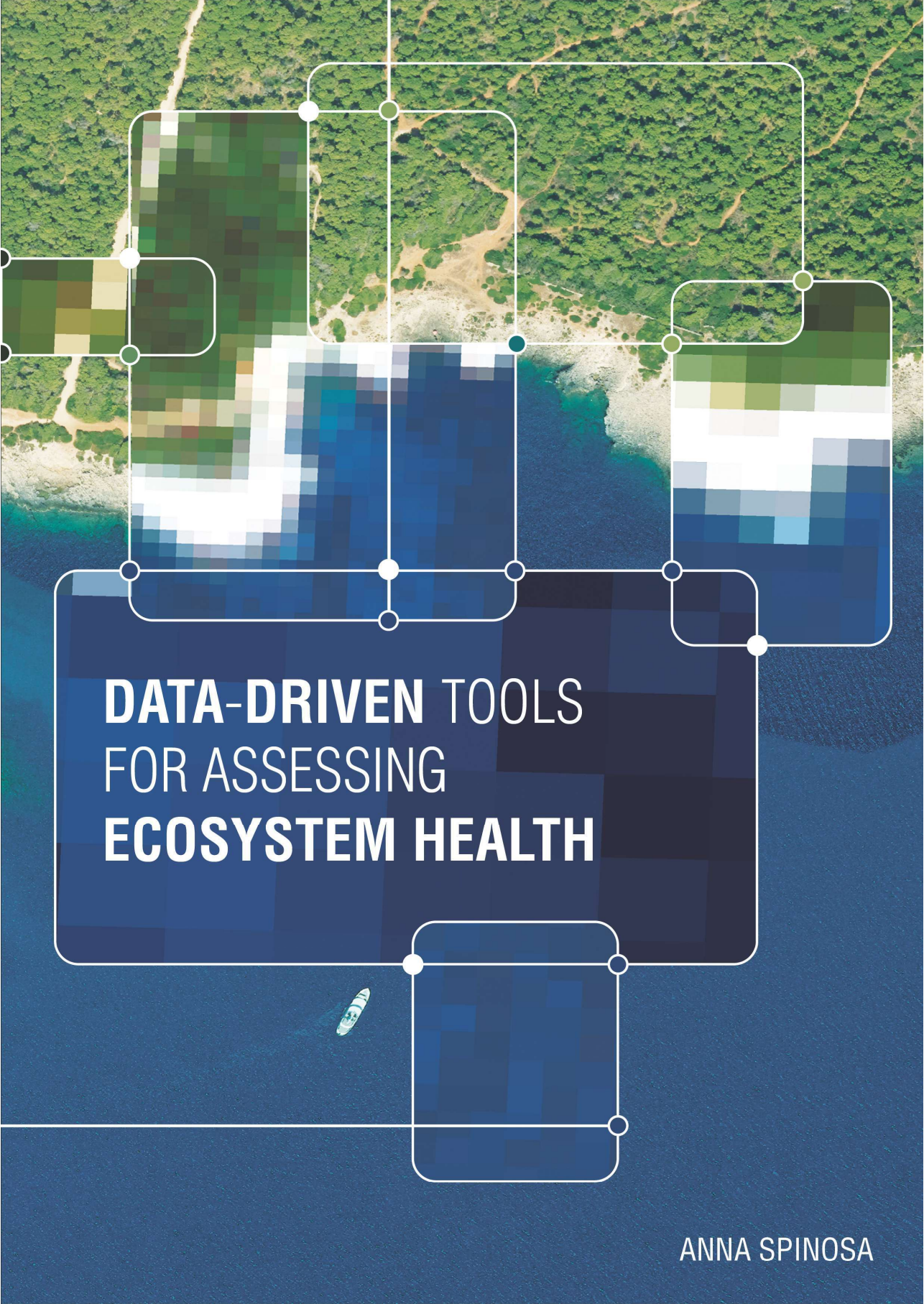

DATA-DRIVEN TOOLS FOR ASSESSING **ECOSYSTEM HEALTH**

ANNA SPINOSA

Data-driven tools for assessing ecosystem health

Data-driven tools for assessing ecosystem health

Dissertation

for the purpose of obtaining the degree of doctor
at Delft University of Technology
by the authority of the Rector Magnificus, prof. dr. ir. H. Bijl,
chair of the Board for Doctorates
to be defended publicly on Friday 26 June 2026 at 12:30 o'clock

by

Anna SPINOSA

This dissertation has been approved by the promotors.

Composition of the doctoral committee:

Rector Magnificus,	chairperson
Prof. dr. ir. A.W. Heemink,	Delft University of Technology, *promotor*
Prof. dr. ir. H.X. Lin,	Delft University of Technology, *promotor*
Dr. ir. G.Y.H. El Serafy,	Delft University of Technology, *copromotor*
Independent members:	
Prof. dr. ir. M. Verlaan,	Delft University of Technology
Prof. dr. E. Tarantino,	Politecnico di Bari, Italy
Dr. A. Provenzale,	Italian National Research Council, University of Turin
Dr. J. Masó Pau,	Centre for Ecological Research and Forestry Application, Spain
Reserved member:	
Prof. dr. H.M. Schuttelaars	Delft University of Technology

Keywords:	Remote sensing, ecosystems, ecosystem functions, gross primary productivity, LSTM, XGBoost, machine learning.
Printed by:	Gilderprint
Cover:	A multi-resolution view of the Apulian coastline. Graphic design: Roberto Cupertino and Marianna Turturo, from an idea of Anna Spinosa and Andrea Cupertino.

Copyright © 2026 by A. Spinosa

ISBN 978-94-6518-357-2

An electronic copy of this dissertation is available at
https://repository.tudelft.nl/.

Data supporting this dissertation is openly available at 4TU.ResearchData at
https://doi.org/10.4121/58b8d247-aa43-45f7-aa06-f0fa4942bae7.

Contents

Summary

This thesis investigates how in situ and satellite remote sensing data, combined via statistical and data-driven approaches, can be used to monitor coastal and terrestrial ecosystems in a scalable, cost-efficient, and scientifically robust way. The main objective of this work was to develop tools supporting the assessment and understanding of ecosystem health by exploiting the growing availability of Earth observation data. This thesis work revolves around two main facets: (i) the development of cost-efficient spatially scalable tools and (ii) the investigation of data integration of different data sources.

The research builds on satellite remote sensing data from the Copernicus mission (Sentinel-1 and Sentinel-2 data), complemented by in situ measurements from other open source repositories (such as Integrated Carbon Observation Systems (ICOS) and the European Fluxes Database Cluster) and additional remotely sensed data. All the models and algorithms used or developed during the research are published and available as open source.

The thesis starts by demonstrating the potential of satellite data as a complementary alternative to traditional in situ measurements. This was done by constructing a modeling framework for the retrieval of the shoreline position from Sentinel-1 data. The model is based on the Otsu method, a global thresholding method optimal for the recognition of the water/land interface. The resulting shorelines were validated against video monitoring systems-derived shorelines, showing sub-pixel accuracy. The results highlighted that satellite data may represent a cost-effective and low-maintenance complementary alternative to in situ measurements, especially in areas lacking dense ground-based instrumentation.

The remaining part of the thesis focuses on developing tools for the monitoring of terrestrial ecosystems by estimating gross primary productivity (GPP), the amount of carbon dioxide fixed by the ecosystem through photosynthesis, and a key indicator of ecosystem functioning and carbon cycling. First, an empirical model integrating in situ measurements of environmental variables and Sentinel-2 derived vegetation indices was developed for a coastal wetland ecosystem. The model outperformed the state-of-the-art global products. Additionally, a framework to upscale gross primary productivity estimates beyond the climatological footprint was developed and successfully applied.

Building on these findings, we proposed a cross-site approach for the estimation of gross primary productivity across different ecosystem types. To this end, we integrated ICOS and Sentinel-2 data using three modeling approaches: Seasonal AutoRegressive Integrated Moving Average with eXogenous regressors (SARIMAX), Extreme Gradient Boosting (XGBOOST), and Long Short-Term Memory (LSTM). A range of validation metrics was used to evaluate the performance of the different models, and the results highlighted both the potential and the challenges of building cross-site models capable of generalizing the prediction of gross primary productivity in unseen ecosystems. Com-

bining all the results, this thesis investigates and highlights the value of integrated satellite remote sensing with ground-based measurements to monitor environmental processes at multiple scales. These findings offer valuable insights and illustrate how Earth observation can support operational environmental monitoring and policy-relevant applications.

List of Abbreviations

Abbreviation	Meaning
ACF	Autocorrelation Function
ADF	Augmented Dickey-Fuller
AI	Artificial Intelligence
AIA	Artificial Intelligence Act
AIC	Akaike Information Criterion
ANN	Artificial Neural Network
AR	Autoregressive
ARIMA	Autoregressive Integrated Moving Average
AT	Air Temperature
AVIRIS	Airborne Visible/Infrared Imaging Spectrometer
BIC	Bayesian Information Criterion
BPLUT	Biome Parameter Look-up Table
CBD	Convention on Biological Diversity
CHIRPS	Climate Hazards Group InfraRed Precipitation with Station data
CLR	Red Edge Index
CMSAF	Climate Monitoring Satellite Application Facility
CO_2	Carbon Dioxide
DIAS	Data and Information Access Services
DL	Deep Learning
DNP	Doñana National Park
EBV	Essential Biodiversity Variable
EC	Eddy Covariance
EDT	Edge Detection Technique
EO	Earth Observation
ERS	European Remote Sensing
ESA	European Space Agency
E-SE	East-South-east
EU	European Union
EUMETSAT	European Organisation for the Exploitation of Meteorological Satellites
EV	Environmental Variable
EVI	Enhanced Vegetation Index
EVI2	Two-band Enhanced Vegetation Index
FAO	Food and Agriculture Organization
fAPAR	Fraction of Absorbed Photosynthetically Active Radiation

FFP	Flux Footprint Prediction
FR	Full Resolution
GEE	Google Earth Engine
GES	Good Environmental Status
GLIMR	Geosynchronous Littoral Imaging and Monitoring Radiometer
GMES	Global Monitoring for Environment and Security
GNDVI	Green Normalized Difference Vegetation Index
GPP	Gross Primary Productivity
GRD	Ground Range Detected
HR	High Resolution
HV	Horizontal-Vertical
ICTS-RBD	Infraestructura Tecnológica Singular Reserva Biológica de Doñana
IPBES	Intergovernmental Science-Policy Platform on Biodiversity and Ecosystem Services
IW	Interferometric Wide
L1D	Level-1 Data
LAI	Leaf Area Index
LIDAR	Light Detection and Ranging
LSTM	Long Short-Term Memory
LSWI	Land Surface Water Index
MA	Moving Average
MAE	Mean Absolute Error
ML	Machine Learning
MNDVI	Modified Normalized Difference Vegetation Index
MNDWI	Modified Normalized Difference Water Index
MODIS	Moderate Resolution Imaging Spectroradiometer
MR	Medium Resolution
MSE	Mean Squared Error
MSFD	Marine Strategy Framework Directive
MSI	Multispectral Instrument
MSS	Multispectral Scanner
NASA	National Aeronautics and Space Administration
NDII	Normalized Difference Infrared Index
NDVI	Normalized Difference Vegetation Index
NEE	Net Ecosystem Exchange
NIRV	Near-Infrared Reflectance of Vegetation
NN	Neural Network
N-NW	Nord-Nord-west
NPP	Net Primary Productivity
OLCI	Ocean and Land Colour Instrument
OLI	Operational Land Imager
OLS	Ordinary Least Squares
OpenCv	Python Open Source Computer Vision
PACE	Plankton, Aerosol, Cloud, Ocean Ecosystem

PACF	Partial Autocorrelation Function
PP	Primary Productivity
RADAR	Radio Detection and Ranging
RELU	Rectified Linear Unit
RMSE	Root Mean Squared Error
RS	Remote Sensing
S2	Sentinel-2
SAR	Synthetic-Aperture Radar
SARAH	Surface Solar Radiation Data Set - Heliosat
SARIMAX	Seasonal ARIMA with Exogenous Regressors
SCL	Scene Classification Layer
SDG	Sustainable Development Goal
SDS	Satellite Derived Shoreline
SLC	Single Look Complex
SRS	Satellite Remote Sensing
SW_IN	Incoming Shortwave Radiation
UAV	Unmanned Aerial Vehicle
UN	United Nations
UNFCC	United Nations Framework Convention on Climate Change
VDS	Video Derived Shoreline
VH	Vertical-Horizontal
VI	Vegetation Index
VPD	Vapor Pressure Deficit
VV	Vertical-Vertical
WWF	World Wide Fund for Nature
XGBOOST	Extreme Gradient Boosting

1

Introduction

1.1. Biodiversity loss and ecosystem threats

1

Biodiversity is the heartbeat of our living planet. It provides crucial support (materials and spiritual inspiration) for ensuring prosperity, well-being and development of the human population. Yet, human-induced habitat and species loss have been threatening life on Earth, making global biodiversity loss one of the most pressing environmental issues of our time. Biodiversity, or biological diversity, is *"the variability among living organisms from all sources including, inter alia, terrestrial, marine and other aquatic ecosystems and the ecological complexes of which they are part; this includes diversity within species, between species and of ecosystems"* [1].

The loss of diversity and variety of life on Earth is called "biodiversity loss". The World Wide Fund for Nature (WWF) reports an average decline of 73% of the monitored wildlife populations over the past 50 years (1970-2020), with freshwater populations showing the largest decline (85%), followed by terrestrial (69%) and marine populations (56%) [2]. The Intergovernmental Science-Policy Platform on Biodiversity and Ecosystem Services (IPBES) estimates that around one million out of eight million animal and plant species are threatened with extinction [3].

Given the alarming rate of biodiversity loss, the monitoring of biodiversity is crucial to understand and counteract biodiversity changes. However, such a complex concept as biodiversity – which includes all types and combinations of natural variation at every level of biological organization – cannot be represented or quantified by a single index. Biodiversity is, in fact, the result of many contributing factors operating at different spatial and temporal scales [4]. Biodiversity can be explored at three major levels: (i) genetic diversity: the variety of genes within species, populations or ecosystems; (ii) species diversity: the variety of species measured in terms of number of species (species richness) and their relative abundance; and (iii) ecosystem diversity: the variety of habitats, biotic communities and ecological processes in the biosphere. This work focuses on ecosystem diversity. Ecosystem diversity refers to the variety of ecosystems in a landscape, such as grasslands, rivers, and forests. It includes both the structural and functional complexity of these systems, which support many ecological processes. Ecosystem structural diversity is described as the three dimensional volumetric capacity, the physical arrangement, and the identity and traits of biotic components within ecosystems. In contrast, ecosystem functional diversity focuses on the variation of ecological processes, like nutrient cycling and decomposition. Ecosystem functions describe the dynamic processes occurring within a population, ecosystem, or region of interest.

Crucial for the life on Earth, which otherwise would not exist, are the interactions between abiotic and biotic components. These continuous, direct and indirect interactions and dependencies characterize and define what we call ecosystems [5]. As an example, photosynthesis would not happen without the interaction of light and water (abiotic components) with vegetation (biotic component) capable of transforming radiant energy into organic matter. This interlink between components, however, also means that a change in one component will affect all other ecosystem components that will have to adapt to the changes, move to another ecosystem or perish.

Healthy ecosystems are the primary source of vital resources for human health and quality of life [6]. Healthy ecosystems provide countless goods, also known as ecosystem services, such as fresh water, food, energy, clean air, building materials, clothes, and

medicines, among others. For instance, the Food and Agriculture Organization (FAO) of the United Nations estimated that forests play a crucial role in regulating fresh water supplies, with forested watersheds providing an estimated 75% of the worlds accessible freshwater, on which more than half the Earth's population relies for domestic, agricultural, industrial, and environmental purposes [7]. Similarly, wetlands play an important role in purifying water by filtering pollutants in their sediments, soil and vegetation, reducing mosquito breeding sites for the immediate benefit of the population, sequestrating atmospheric carbon dioxide (CO_2), reducing the impacts of natural hazards, controlling erosion and protecting human settlements against floods, landslides, and drought events [8].

Regardless of their importance for biodiversity and human beings, the extent and status of healthy ecosystems have declined drastically in recent decades [3, 9]. Over the last century, anthropogenic pressures have led to widespread habitat degradation and declining environmental quality [10–12]. Biodiversity is increasingly and continuously threatened by exponential population growth, rising poverty, land-use change and fragmentation, harmful non-native species, monocultured-based agriculture, deforestation, and other stressors [3, 10, 13, 14]. Despite efforts, such as the establishment and enlargement of Protected Areas (PAs) to limit human presence and resource exploitation in ecologically and culturally important areas, species loss and ecosystem degradation continue, undermining ecosystems capacity to sustain essential services that support human well-being [8].

Effective conservation and ecosystem monitoring practices are therefore essential for early detection of changing patterns in ecosystem health to prevent biodiversity loss. Yet monitoring biodiversity and ecosystem changes, especially in marine and coastal habitats, remains challenging. Sustainable management requires identifying reliable indicators to assess ecosystem resilience and regime shifts triggered by long-term stressors like climate change or sudden events such as pollution, fires, etc. A globally harmonized observation system for consistently tracking biodiversity change is still lacking, underscoring the urgent need for integrated, spatially scalable, cost-effective and efficient approaches to ecosystem monitoring and assessment [15–18].

1.2. Environmental directives and policy implications

This section aims at contextualizing the research in the socio-political landscape, therefore it provides a short overview of the international agreements that have expressed the importance of biodiversity monitoring.

Inspired by the world community's growing commitment to sustainable development, in 1992 the United Nations (UN) Conference on Environment and Development, also known as the Earth Summit, brought the importance of biodiversity to the global stage. On 5 June 1992, the UN Convention on Biological Diversity (CBD) was opened for signature and finally established in 1994. The CBD marked the beginning of global efforts towards the development of environmental economic accounts. Since then, the need of biodiversity data and global monitoring has been expressed by international treaties, including the Aichi Biodiversity Targets for 2020 in the CBD [19, 20], the UN Sustainable Development Goals (SDGs) [21], the RAMSAR Convention [8], and the European

Union (EU) Biodiversity Strategy 2020 (BD; COM/2011/0244) [22]. Those international environmental agreements have all increased emphasis on the importance of halting biodiversity loss.

In Europe, a growing push towards the use of ecosystem accounting in policy development and economic analysis is coming, among others, from the EU Marine Strategy Framework Directive (MSFD; 2008/56/EC) [23], the EU biodiversity strategy for 2030 [24], the EU Birds and Habitat Directives [25, 26], the EU Pollinators Initiative [27], and the European Green Deal [28]. The MSFD, for example, envisions the Good Environmental Status (GES) of all European Seas and mandates Member States to maintain their maritime ecosystems. To *"enable the sustainable use of marine goods and services* (paragraph 8 of the MSFD preamble), Member States shall adopt an *"ecosystem-based management approach"*, ensuring that the human interactions within those services are also analysed [23]. Similarly, the EU biodiversity strategy for 2030, aiming at building a society resilient to future threats as food insecurity, spread of diseases and climate change impact, sets an ambitious agenda to bend the trend in biodiversity loss enhancing ecosystem restoration [24]. To this end, the Commission introduced the EU Nature Restoration Law [29], which sets a comprehensive goal to support the long-term recovery of natural areas across both EU's land and sea, with binding targets aimed at restoring specific habitats and species.

The conservation of ecosystems and biodiversity is also envisioned by the SDGs and the Paris Neutral Agreement on Climate Change and Land Degradation [21]. The 17 SDGs are designed to be integrated and indivisible, in an attempt to address interconnected issues such as poverty, hunger, inequality, climate change, environmental degradation, access to clean water and sanitation, education, gender equality, and more. They encompass the three dimensions of sustainable development: social, economic, and environmental, and are intended to be achieved by the year 2030.

Several SDGs directly address the conservation and sustainable management of ecosystems. Those include:

- SDG 6: Clean Water and Sanitation envisioning the protection and restoration of water-related ecosystems, including mountains, forests, wetlands, rivers, aquifers and lakes;
- SDG 14: Life Below Water committed to the achievement of ecosystem integrity, with properly functioning biogeochemical and physical processes, required to conserve and sustainably use the oceans, seas and marine resources for sustainable development;
- SDG 15: Life on Land devoted to *"protect, restore and promote sustainable use of terrestrial ecosystems, sustainably manage forests, combat desertification, and halt and reverse land degradation and halt biodiversity loss"*.

Similarly, SDG 13: Climate Action also emphasizes the crucial role of ecosystems in climate regulation and adaptation, since ecosystems can help sequester carbon dioxide, mitigate climate change impacts, and enhance resilience to climate-related disasters. The adoption of the SDGs and of a stand-alone SDG 14 on oceans and seas represents an unprecedented opportunity to enhance marine governance and management globally.

This thesis work directly addressed the aforementioned SDGs and can be linked to others (e.g. SDG 13), particularly when considering upscaling of the methodologies for integrated solutions and adaptation, and different applications (e.g, identification of rivers during flood events or lakes). Links between GES and sustainable use of ecosystems goods and services are anticipated, still there is no operational assessment of ecosystem services and functions [16, 30].

In light of the growing awareness for a comprehensive approach to address climate change and biodiversity restoration challenges, new monitoring methods and technologies shall be explored. The EU Nature Restauration Law [29] and the EU Forest Strategy [31] reports that *"Member State monitoring systems shall [...] maximise the access and use of data and services from remote sensing technologies, Earth observation (Copernicus services), in situ sensors and devices, or citizen science data, leveraging the opportunities offered by artificial intelligence, advanced data analysis and processing"*. Policies emphasize the need for newly developed monitoring approaches that are cost-efficient and effective, ensuring the monitoring is done at high spatial and temporal resolution and data and reports are regularly updated. Priority lies in providing information and products relevant to key EU policy areas, including effects of climate change, biodiversity, health, damages, invasive alien species, forest management, and the use of biomass for different socio-economic purposes. This research aims to support these goals by developing new monitoring tools that can provide a valuable alternative to field studies or complement the latest, thereby optimizing the cost of in situ campaigns while ensuring broader spatial coverage.

1.3. Monitoring methods

The implementation and monitoring of environmental directives rely upon accurate mapping and monitoring changes in a broad range of physical, chemical, and biological components. Such information is required to assess and track the health of marine species and ecosystems, identify and reduce pressures, establish evidence-based measures, and evaluate the effectiveness of implemented management actions.
Traditionally, monitoring programs have relied on regular sampling and dedicated campaigns. Those methods are however expensive, labor intensive, and often have low horizontal and temporal resolution. Nowadays, continuous time series can be recorded using automated in situ sensors that provide data for longer periods of time and with high vertical resolution. Additionally, the advent of Earth Observation (EO) technologies, particularly Satellite Remote Sensing (SRS), has increased the global coverage of measurements. Among the key benefits of SRS are the users' cost-effectiveness of monitoring efforts, timely and systematic data delivery, and accessibility to remote places [32–34].

Satellite remote sensing can help track progress towards the UN CBD targets on ecosystems services, allowing the assessment of ecosystem benefits at a global scale. SRS is key to generating actionable knowledge in real-time for improved decision-making [33, 35]. It can capture coastal zones and biodiversity changes at relatively high spatial and temporal resolutions, both at global and regional scales [35–37]. Further, SRS-based proxies can be used to meet the reporting obligations in the Essential Biodiversity Variables (EBVs) framework [38], clarify the biodiversity-ecosystem functioning-ecosystem

services paradigm [39], and assist national authorities in monitoring programs for the achievement, among others, of the SDGs [40–42]. However, satellite observations alone are not always able to provide all the information needed by users at sea or policymakers. In the rapid development of marine aquaculture activities, for example, it is necessary to assess the water quality and the environmental conditions in marine aquaculture areas, and among others the concentration of constituents of water as dissolved oxygen concentration or pH. Remote sensing is, however, not capable of measuring and estimating such constituents since those do not interact with light and thus do not change the energy spectrum of reflected solar radiation from waterbodies. Still, non-linear relations among remotely sensing retrieved variables and non-optical variables can be found using machine learning techniques. Moreover, the revisit time of low-orbiting satellites or the cloud coverage can preclude the monitoring of specific phenomena. The use of multi-sensor imagery, data fusion, and data integration can help overcome these limitations.

The quantification of processes and ecosystem response to anthropogenic and natural conditions can also be simulated via models. Models can be divided into two main categories: (i) physically-based models, and (ii) data-driven models. The former resolves a set of equations and provides precise parametrisations of ecosystems and their complex interactions. These models rely on an accurate description of the key ecological and environmental processes, which can be coupled with biological and hydrological models, and can be further improved through the assimilation of in situ and remotely sensed data [43–45]. However, modelling complex ecological and biogeochemical processes often requires a large amount of input data often only available at coarse resolution, a big challenge for calibration and validation purposes. Moreover, the timely provision of model results also remains a challenge.

Recent advances in Artificial Intelligence (AI) have enhanced the modelling of biogeochemical processes, and have been extensively replacing physically-based models when a large observation dataset is available [46]. The European Artificial Intelligence Act (AIA) defines an Artificial Intelligence system as *"software that is developed with one or more of the techniques and approaches [...]"* that *"can, for a given set of human-defined objectives, generate outputs such as content, predictions, recommendations, or decisions influencing the environments they interact with"* [47]. The AIA's identified techniques include:

(i) Machine Learning (ML) approaches: including supervised, unsupervised and reinforcement learning;

(ii) Logic- and knowledge-based approaches: including knowledge-based representation, inference and expert systems;

(iii) Statistical approaches: including Bayesian estimation, search and optimization methods.

Chapter 2 provides an overview of some of these approaches, with particular emphasis on the machine learning methods and statistical techniques applied in this thesis, with the former being more extensively explored compared to the limited use of statistical methods. All those data-driven methods rely on the correlation between the provided data and the targeted specific indicator. Since *data-driven*, those models need to

be trained with a representative set of data with appropriate statistical properties that capture different hydrodynamics and biogeochemical settings to capture a large range of responses. Specific attention should also be paid to bias mitigation, ensuring trustworthy AI. Data-driven approaches can incorporate and analyse large volumes of data, and allow for the integration of data from various sources, including satellite imagery, sensor data, and historical records, to capture non-linear patterns. This comprehensive integration can support a deeper understanding of the system being modeled and may lead to more accurate predictions and insights. Taking advantage of the freely available satellite data, in situ measurements gathered by global monitoring programs, and machine learning, the products developed within this work demonstrate the capabilities of satellite data to contribute to the monitoring of ecosystems health.

1.4. Thesis objective and outline

This thesis work addresses the need for a) robust integration of in situ measurements and remote sensing data to improve the accuracy and reliability of ecosystem monitoring, and b) spatially scalable tools that could be of direct use to different targeted users. While both the in situ and remotely sensed data can be used to create long-term and consistent time series data, a standardized protocol for upscaling and assessing these time series to different spatial scales is still lacking. Upscaling using high-resolution remote sensing data remains a challenge in environmental monitoring. Local measurements (e.g., from field sensors, flux towers, or manual sampling) are often highly accurate and available at high frequency and vertical resolution but are spatially limited. Conversely, satellite data provide relevant information at sufficient spatial resolution and high spatial coverage but may not capture fine-scale variability or local dynamics in the vertical dimension [33]. This issue is a core aspect of this thesis, and it is addressed throughout Chapters 3 – 5.

When effectively integrated, these sources can complement each other resulting in a more robust and versatile tool. Data integration is defined as the process of combining and harmonizing heterogeneous data from multiple sources, providing the user with a unified and consistent view of these data [48, 49]. Multi-sensors and multi-platform integration can contribute not only to the development of upscaled products but also lead to temporal gaps filling. Common approaches to integrating in situ measurements with satellite observations include, but are not limited to, empirical and semi-empirical models, physically based models, and data assimilation techniques. Chapter 4 addresses this challenge by exploring empirical models to combine in situ measurements with satellite observations, demonstrating their potential and limitations for scaling local data to a broader area.

While these traditional methods have been proven effective in many applications, they also face limitations, particularly in their ability to generalize across spatial and temporal scales and to adapt to complex, non-linear environmental dynamics. Artificial intelligence models offer a promising alternative to overcome those limitations and produce reliable and reproducible results over time and space. Building on the findings of Chapter 4, Chapter 5 explores the use of AI-based methods and discusses their potential for supporting effective environmental modeling and policymaking, addressing the need

for autonomous, spatially scalable, cost-effective, and non-invasive methods [50].

The conceptual flow of this thesis and the connections between the chapters are depicted in Figure 1.1. It consists of four main parts. Chapter 2 is dedicated to an in-depth description of the methods used in this thesis. The different technologies (i.e., active and passive remote sensing) and the algorithms employed in the following chapters (Chapters 3 – 5) are presented with the primary aim of providing a theoretical foundation to guide the reader throughout the thesis.

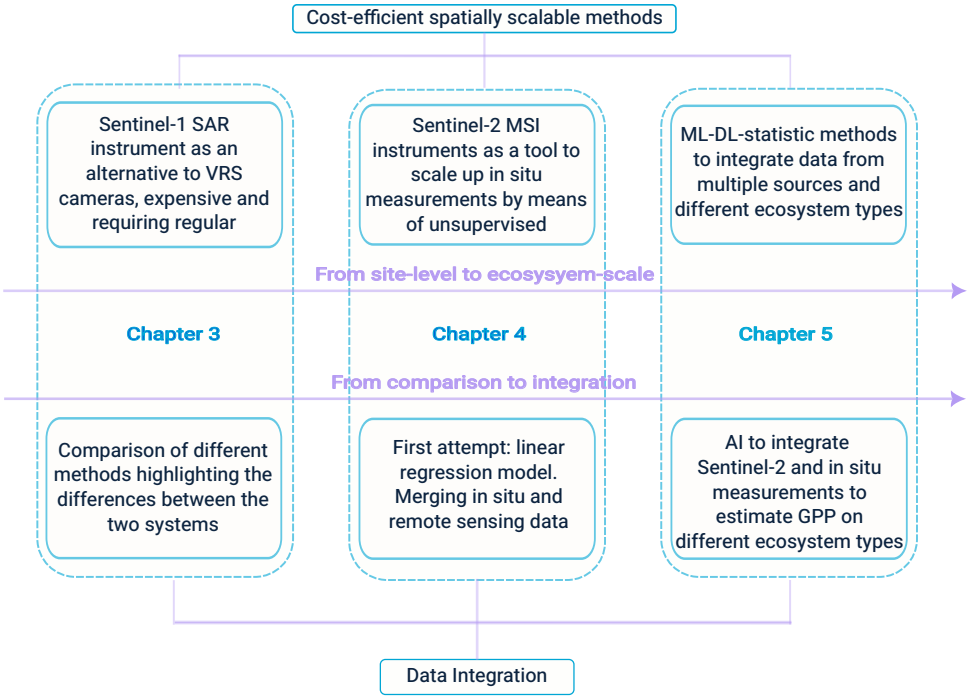

Figure 1.1.: Thesis structure and connection.

Chapters 3 – 5 emphasize data integration and the development of spatially scalable methods. In particular, Chapter 3 introduces an approach to retrieving shoreline position. It investigates the accuracy and limitations of satellite data in retrieving the shoreline position, widely used as an indicator to quantify erosion and accretion processes in coastal areas and assess their vulnerabilities. Changes in land-use, climate, population growth, etc., have altered the distribution of the coastline, causing significant changes to the structure and values of coastal ecosystems services. Knowledge of coastal erosion and accretion is therefore important to better quantify the changes in ecosystem services and implement actions to better protect marine ecosystems. The main objective of this chapter is therefore to evaluate the reliability of Sentinel-1 Synthetic Aper-

ture Radar (SAR)-based automated shoreline detection by comparing its delineation of shoreline positions against those derived from traditional video monitoring systems. The approach aims to test whether SAR images can provide a spatially scalable and cost-effective alternative to video monitoring systems. The chapter further investigates the challenges in transferring local calibrated information to a larger monitoring scale.

Chapter 4 introduces an empirical model to integrating in situ and satellite measurements, and upscaling local observations to a broader area. In particular, Chapter 4 investigates the use of Copernicus Sentinel-2 to upscale in situ measurement of net ecosystem exchange (NEE) at the ecosystem scale. Gross Primary Production (GPP), a key indicator of ecosystem health and performance, is modeled as a function of environmental variables derived from in situ flux tower measurements and vegetation indices derived from Sentinel-2 data. The model automatically performs an interdependency analysis and selects the model leading to the highest accuracy and statistical significance. The methodology is tested on a wetland ecosystem, increasingly recognized as a primary source of vital resources for human welfare and survival, playing a crucial role in regulating the impacts of natural hazards and protecting human settlements against floods, landslides, and drought events. The resulting products are compared with state-of-the-art data.

Chapter 5 builds upon the outcomes of the previous chapter and investigates to what extent a data-driven model can appropriately be used to estimate GPP across different ecosystem types. To this end, data are collected from different ecosystem types (grassland, deciduous broadleaf forest, evergreen needleleaf forest, and cropland), and three models – SARIMAX, XGBoost, and LSTM – are implemented and compared. Site-specific models are developed to capture the individual site characteristics; additionally unified models are developed for generalizing predictions across different ecosystems. The models are tested on unseen sites to better assess their reliability in generalizing the predictions beyond the training sites.

Finally, Chapter 6 summarizes the research findings of all chapters, and overarching conclusions and recommendations of this thesis work are drawn. Limitations are highlighted, and outlook for future improvements are formulated.

2

Theoretical background

Remote sensing and data-driven methods are revolutionizing the way we approach and analyze various subjects in the context of biodiversity monitoring. This chapter introduces the methods used in this thesis. By providing a comprehensive overview, we aim to establish a solid foundation for the subsequent chapters and facilitate a deeper understanding of the topic's significance and implications.

This chapter intends to provide a theoretical background to guide the reader through this thesis work. The different technologies (i.e., active and passive remote sensing) and the algorithms employed in the following chapters (Chapters 3 – 5) are presented.

2.1. Remote Sensing

The modern era of Earth remote sensing can be traced back to 1972, with the launch of Landsat Multispectral Scanner System (MSS) by the National Aeronautics and Space Administration (NASA). Since then, technological advancements, both in spatial and temporal resolution, have been achieved. Remote Sensing (RS) was initially defined as "the acquisition of physical data of an object without touch or contact" [51]. It can therefore be seen as an attempt to measure and derive information about Earths land and water surface using images acquired from an overhead perspective. In other words, at a distance rather than in situ. Remote sensing systems offer a repetitive and consistent view of the Earth that allows monitoring of both short- and long-term environmental changes, as well as the impact of human activities. Applications of the RS technology are various and include meteorology, environmental assessment, agriculture, mapping, surveillance, etc. Based on the employed instruments, remote sensing can be classified into two broad categories: active and passive.

2.1.1. Active Remote Sensing

Active remote sensing carries an artificial source of radiation as a probe that makes active sensors capable of emitting their own source of radiation. The sensor records the radiation reflected or backscattered from the terrain. Active sensors work in the microwave portion of the electromagnetic spectrum, capable of passing through gases and clouds. This enables the acquisition of images regardless of any light availability and weather conditions, a great advantage when compared to passive sensors. Active remote sensing technologies include Radio Detection and Ranging (RADAR), such as Synthetic Aperture Radar (SAR), Light Detection and Ranging (LiDAR), and altimeters (e.g., radar altimetry). Active remote sensing has been proven effective, among others, in the estimation of soil moisture content over different vegetation conditions, leaf area index (LAI), canopy height, permafrost dynamics, snowpack structure and snowmelt, lake ecology and river discharge, making its use an additional tool to complement passive remote sensing [35].

2.1.2. Passive Remote Sensing

Passive remote sensors measure the radiation naturally reflected or emitted from Earths surfaces, atmosphere and clouds. These systems measure reflected sunlight (in the visible and near-infrared spectrum) or emitted thermal radiation (in the thermal infrared spectrum). As such, data acquisition is limited to daytime and clear-sky conditions. Passive remote sensing technologies include the Multispectral Imager (MSI) on board of Sentinel-2, the Ocean and Land Colour Instrument (OLCI) of Sentinel-3, the Operational Land Imager (OLI-2) of Landsat-9, and hyperspectral instruments as the Airborne Visible/Infrared Imaging Spectrometer (AVIRIS). Passive remote sensing has been extensively employed for inland and near-shore water quality and ecosystems assessment. For

instance, it has been used for the monitoring of turbidity levels, algal pigment concentration, chlorophyll-a concentration, sea surface temperature, bathymetry, but also land cover classification, vegetation monitoring, and ecological indicators [52, 53].

In this thesis, both technologies are used. Active remote sensing is used in Chapter 3 for the retrieval of the coastline position, while passive remote sensing is used to estimate gross primary productivity (Chapters 4 – 5).

2.2. Segmentation

Segmentation techniques play a crucial role in extracting meaningful information from remotely-sensed imagery, regardless of the sensing modality. Segmentation is defined as the process of grouping objects (or pixels) in meaningful and non-overlapping regions of interest. Image segmentation is a common technology widely used in different fields, including medical imaging, autonomous vehicles, and robotics, beyond satellite imagery analysis. Image segmentation techniques vary widely, and several classifications of the methods have been proposed. Yu et al. [54] for instance, suggested that algorithms can be grouped into three main categories based on their working methods: a) classic segmentation methods, traditional methods that extract structural or boundary information; b) collaborative segmentation methods, also referred to as semi-supervised methods, which identify objects across multiple images; and c) semantic segmentation methods, which rely on machine learning and deep neural networks to automatically learn and classify high-level semantic features. In their review on image segmentation techniques for remote sensing, Dey et al. [55] identified three main segmentation approaches: a) image driven approaches, which rely solely on image features to identify objects; b) model driven approaches, methods that assume objects within an image follow a specific pattern; and c) homogeneity-based approaches, which use measures based on spectral, spatial, texture and temporal properties of the image. A more simplistic classification has been proposed by Kaur D. and Kaur Y. [56]. The authors suggested that all the segmentation techniques can be classified into two broad categories: a) discontinuity detection-based approaches, when segmentation is performed by identifying regions that exhibit discontinuities; and b) similarity detection-based approaches, when segmentation is performed by grouping pixels with similar attributes. Yet, it is important to note that these categories are not mutually exclusive, and most segmentation methods integrate elements from multiple approaches at different stages of the process.

Choosing an appropriate segmentation technique largely depends on the nature of the data and the specific application. Ciecholewski [57] presented an overview of the state-of-the-art segmentation techniques used for the extraction of the shoreline from SAR images. According to the author, who proposed an additional classification of the segmentation techniques, the most used methods for shoreline retrieval are active contour, machine learning and thresholding methods (Figure 2.1). An active contour model, also called snakes, is an energy-minimizing spline guided by external constraint forces, able to accurately localize edges in the image. Active contour models can be edge-based or region-based models. Edge-based models use intensity- or gradient-derived external forces to find edges. Edge-based methods include the geometric active contour model and the gradient vector flow [58]. Those models can be robust to weak edges; however,

their performances are strongly influenced by contour initialization. Re-initialization may be required before obtaining a stable contour, which increases the computational time. On the other hand, region-based models, in which the contour evolves based on constraints derived from foreground and background regions, can more easily fit irregular edges, even though they require higher computational costs than edge-based models [59]. Machine learning methods for segmentation can be divided into supervised and unsupervised models. Supervised models are trained using already labelled data often obtained by experts segmentation. The model learns to classify each pixel (or region) into predefined categories, knowing both the number of classes present in the image and their statistical characteristics. Among the most used supervised models for segmentation are Convolutional Neural Network (CNN) and U-NET models [60, 61]. Those models have the advantage of learning complex patterns, being fully aware of which classes are present in each segmentation node. This can therefore lead to an accurate and rigorous segmentation, yet the algorithms require a highly accurate training dataset, and well preprocessed input. Moreover, the preparation of the data, including data collection, preprocessing and labelling, as well as the model training itself, can be computationlly expensive. Unsupervised machine learning methods do not require a training dataset as they are capable of learning patterns from the statistical distribution of specific imaging features as intensity or gradients, although their computational cost may still be considerable for large or high-dimensional datasets. Among the most used unsupervised segmentation methods are k-means clustering (section 2.3) and k-median algorithm. These methods are easy to compute but often require manual post-processing, as they tend to over-segment images and are sensitive to noise and high variance regions [57].

In thresholding-based segmentation methods, binary or multi-class images are obtained by partitioning the image histogram into two classes (bi-level thresholding) or multiple classes (multi-level thresholding). Thresholding methods can be based on global or local thresholds. Global thresholding methods, such as the Otsu method [62], are computationally efficient and easy to implement. These methods, however, can lead to poor results when the objects are not uniformly illuminated, often resulting in broken or non-continuous edges. Local thresholding methods can be more suitable for non-uniformly illuminated images and can better preserve small feature details that global thresholding methods might miss, particularly in regions with varying intensity or gradients [54]. Local thresholding methods are however computationally slower and can introduce artefacts or lead to over-segmentation. Moreover, some of the methods need parametrization, which can be difficult for non-experts [57].

After reviewing all potential methods for image segmentation, the Otsu's method has been selected as the most suitable approach for the detection of the shoreline position. The method, which allows for fully automated shoreline detection in a short amount of time, has been selected for its simplicity among all other algorithms, as it does not require image partitioning or a training dataset. The Otsu's method is an unsupervised and nonparametric method based on the zeroth and first moments of the grayscale histograms.

The binarization automatically calculates the optimal threshold at level k value by using discriminant criterion measures. Pixels are divided into two classes C_0 and C_1 with levels [1, 2, , k] and [k+1, k+2, , L] respectively, where L is the grayscale level.

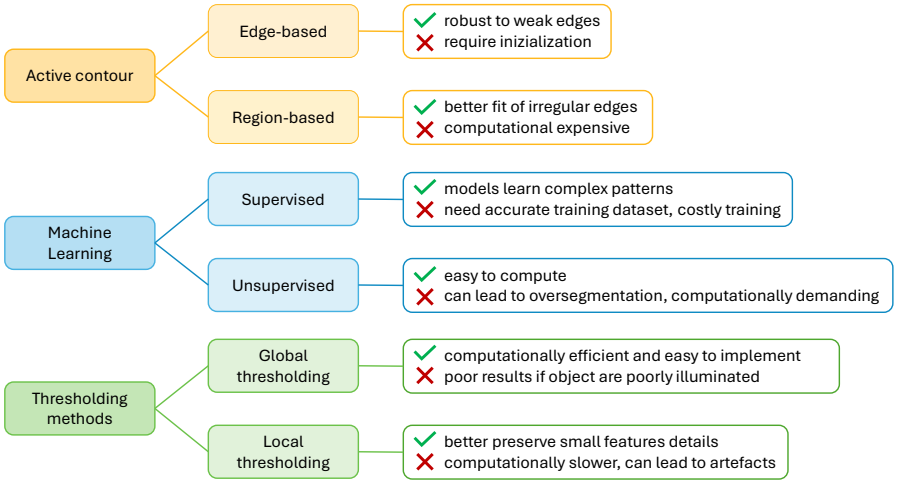

Figure 2.1.: Schematization of the most used segmentation techniques for the extraction of shoreline from SAR images. Based on the classification proposed by Ciecholewski [57].

The probability of occurrence ω (equation 2.3), class means levels μ (equation 2.4) and class variance σ (equation 2.5) are calculated from the histogram of the pixel values distribution for the two classes. Then, to evaluate the threshold goodness, the class separability is evaluated using specific discriminant criteria. The adopted criterion η (equation 2.1) is defined as the product between the probability of occurrence and the first and second order cumulative moments of the histogram. The total mean intensity (μ_t) and variance (σ_T) are computed over all pixel values. The aim is to find the threshold that minimizes η, or equivalently, the weighted within class variance given by σ_B (equation 2.2):

$$\eta = \frac{\sigma_B^2}{\sigma_T^2}, \tag{2.1}$$

where:

$$\sigma_B^2 = \omega_0(\mu_0 - \mu_t)^2 = \omega_1(\mu_1 - \mu_t)^2 = \omega_o\omega_1(\mu_1 - \mu_0)^2, \tag{2.2}$$

$$\omega_0 = Pr(C_0) = \sum_{i=1}^{k} p_i, \qquad \omega_1 = Pr(C_1) = \sum_{i=k+1}^{L} p_i = 1 - \omega_0, \tag{2.3}$$

$$\mu_0 = \sum_{i=1}^{k} \frac{i\,p_i}{\omega_0}, \qquad \mu_1 = \sum_{i=k+1}^{L} \frac{i\,p_i}{\omega_1}, \qquad \mu_T = \mu(L) = \sum_{i=1}^{L} p_i = \omega_0\mu_0 + \omega_1\mu_1, \tag{2.4}$$

$$\sigma_0^2 = \sum_{i=1}^{k} (1-\mu_0)^2 \frac{p_i}{\omega_0}, \qquad \sigma_1^2 = \sum_{i=k+1}^{L} (1-\mu_1)^2 \frac{p_i}{\omega_1} \qquad \sigma_T^2 = \sum_{i=1}^{L} (i-\mu_t)^2 p_i, \tag{2.5}$$

2.2.1. Preprocessing techniques

Despite their differences, all segmentation algorithms share a common need for effective image preprocessing and noise reduction. Reducing noise before processing the images is essential to ensure that segmentation produces reliable results. One of the most common noises affecting all SAR images is the speckle noise, also known as salt-pepper noise. Speckle is due to the interference of electromagnetic waves backscattered by many scatters. Although these signals remain coherent in frequency, phase incoherence can lead to constructive or destructive interference, producing random fluctuations in pixel intensity. This results in a granular pattern, known as speckle. This granular pattern reduces image interpretability by making single-pixel intensities unreliable indicators of target reflectivity [63].

The most common and efficient approach to reduce speckle is image averaging [64]. Standard filtering approaches include the linear, Huang [65], Kuan [66], Frost [67], and Gamma [68] filters. Those filters generally perform well on most SAR images, even though spatial resolution is often lost. Due to its low computational cost, simplicity, and good performance in preserving edges, the median filter is popular and widely used. Median filtering replaces the intensity of each image pixel $y(m,n)$ with the median of the intensities in a defined neighborhood w around the pixel location (m,n) defined as follows:

$$y[m,n] = median\{x[i,j],(i,j) \in w\} \tag{2.6}$$

The neighborhood is defined by the user. The median filter has the advantage of preserving image brightness and edge locations while requiring low computational effort [64].

Another common preprocessing step often applied to the images is contrast enhancement. Contrast enhancement techniques aim at increasing the difference in intensity values between pixels so that they can be better identified and classified. Contrast enhancement techniques include gray-level transformations and histogram-based techniques.

2.3. Artificial Intelligence

In recent years, terms such as *artificial intelligence*, *machine learning*, and *data-driven* have permeated the scientific literature (and public media), attracting growing attention across a wide range of fields. Powered by increased computational power and data availability, along with the development of new advanced algorithms, such as boosting, bagging and random forest, over the past two decades, machine learning has experienced a bloom. Machine learning has, among others, enhanced time series analysis across multiple fields, facilitated water management, improved speech recognition and object detection, and accelerated medical science discoveries [69, 70].

Artificial intelligence (AI) is the scientific field focused on developing computer system capabilities to perform processes and tasks commonly performed by humans and associated with human intelligence. Although often used interchangeably, Machine Learning (ML) is a subdomain of AI, capable of deriving information from data and to *learn* from it. From Mitchell [71]: "A computer program is said to learn from experience E with

respect to some class of tasks T and performance measure P, if its performance at tasks in T, as measured by P, improves with experience E". Within ML is the subfield of Deep Learning (DL). DL methods use Artificial Neural Network (ANN) characterized by multiple successive layers – hence the term "deep". These networks are composed of simple but non-linear modules that can learn hierarchical representations of the data they are trained on, transforming raw input data into meaningful representations of the data [72].

Within ML, it is possible to distinguish among three main learning techniques: supervised learning, unsupervised learning, and reinforcement learning. Additional strategies (i.e., semi-supervised learning, zero-shot learning) are often hybrid versions of the previous ones. In the following paragraphs, more details will be provided on the different techniques, even though only the models used in this thesis work will be described in detail.

SUPERVISED ML

To execute a ML task, two sets of data along with an assessment method are required. In supervised machine learning, both input and output data are provided to the model. By looking at the input data (feature data) and its corresponding output (target), the ML model will discover rules for executing a given data processing task. The model applies various transformations to the input data so that it can resample the target data. These transformations are iteratively evaluated and refined based on their success to make a good approximation of the target data. In this context, the automatic search process for data transformation producing meaningful representations of the data, guided by a feedback signal, is what we call "learning" [73]. This type of learning is called "supervised" since the ML model has a priori knowledge of what it tries to predict. In supervised learning, when provided with a feature matrix X and a response vector y, the problem is classified as a *classification* task if y is discrete, and as a *regression* task if y is continuous. Examples of supervised tasks in the context of ecosystem modelling are species recognition from video and audio analysis, species distribution modelling, and predictive modelling. The main scope of a predictive ML model is to make accurate predictions on new data, those unseen by the model. While a model may perform well on training data, it can exhibit poor performance on new inputs. This is known as overfitting. The balance between model complexity and prediction accuracy is captured by the bias-variance tradeoff [74]. ML algorithms typically involve adjusting model parameters to fit training data while controlling complexity to ensure good generalization.

Artificial Neural Network

As the name suggests, an Artificial Neural Network (ANN) is a computational model inspired by the structure and function of the human brain, designed to loosely replicate the behaviour of biological neural networks. An ANN is composed of interconnected units called *neurons*, which are organized into distinct layers:

- input layer: where the explanatory variables are introduced,
- output layer: where the response variables are generated,

- hidden layer(s): one or more intermediate layers that enable the network to model complex, non-linear relationships.

Neurons in successive layers are interconnected by weights and biases. In general, an ANN (Figure 2.2) consists of the following items:

- k explanatory variables $X = \{X_1(t), \dots, X_k(t)\}_{t \in T}$ and a response variable $\{Y(t)\}_{t \in T}$,
- H hidden layers with $\ell_1, \dots, \ell_H$ neurons respectively,
- $H+1$ weight matrices $W^1, \dots, W^H, W^{\text{out}}$, which connect the layers. Specifically, for each layer i, the matrix $W^i \in \mathbb{R}^{\ell_{i-1} \times \ell_i}$ contains the weights between the neurons in layers $i-1$ and i,
- $H+1$ bias vectors $b^1, \dots, b^H, b^{\text{out}}$, where each $b_i \in \mathbb{R}^{\ell_i}$ assigns a bias to each neuron in layer i.

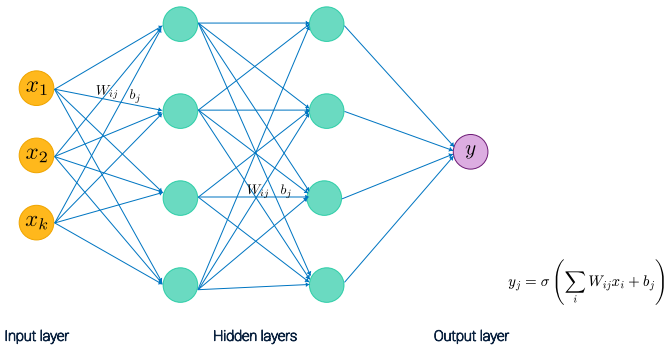

Figure 2.2.: Structure of an ANN, showing the input, hidden and output layers.

The value of a neuron is computed by applying a non-linear function to the weighted sum of its inputs, plus a bias term. For a single neuron j, the output y_j can be expressed as:

$$y_j = \sigma\left(\sum_i W_{ij} x_i + b_j\right), \tag{2.7}$$

where σ is the activation function, w_{ij} are the weights, i represents the neurons in the previous layer, x_i are the inputs from the previous layer, and b_j is the bias associated with neuron j. Common choises for the activation function σ include:

1. the sigmoid function:

$$\sigma(x) = \frac{1}{1+e^{-x}} \tag{2.8}$$

in which $x \in (-\infty, +\infty)$, $\sigma \in (0,1)$,

2. the hyperbolic tangent ($tanh$) function:

$$\sigma(x) = \tanh(x) = \frac{e^x - e^{-x}}{e^x + e^{-x}} \tag{2.9}$$

with output ranging between -1 and $+1$, and

3. the Rectified Linear Units (ReLU) function, defined as:

$$\sigma(x) = max(0, x) = \begin{cases} x & \text{if } x \geq 0, \\ 0 & \text{otherwise.} \end{cases} \tag{2.10}$$

Advantages of the sigmoid function include its simple derivative and the fact that it is differentiable at all points due to its continuity. However, it only achieves zero gradient in the limit ($\lim_{x \to +\infty} g'(x) = 0$ and $\lim_{x \to -\infty} g'(x) = 0$). This causes soft saturation, reducing learning efficiency due to the vanishing gradient problem during training [75]. Similarly, the hyperbolic tangent function also suffers from the vanishing gradient problem, and its derivative is more complex to compute than that of the sigmoid function. However, since tanh is zero-centered, it often leads to faster convergence during training, making it preferable to the sigmoid function. ReLU function has been more recently introduced to better mimic the biological neural network behaviour and is now the most popular activation function used in deep neural networks. Advantages of the ReLU function include computation efficiency (no need for computing the exponential function), faster convergence, and non-saturation [75]. Despite its effectiveness, however, the ReLU activation function can suffer from the "dying ReLU" problem, occurring when neurons become inactive and stop learning because their inputs are consistently negative, and their weights are not updated during training because the gradient flowing through them is also zero.

A neural network learns by optimizing (minimizing) a certain cost function, which measures the discrepancy between the predicted and the target values. Commonly used cost functions for regression include squared error loss, mean absolute error, and Huber loss. During training, the weight matrices and the bias vectors are typically initialized randomly, and the estimated value is assessed against the responsible variable. Learning in Neural Network (NN) consists of updating the weights and biases by *backpropagating* the error and minimizing the chosen cost function through the computation of its gradients with respect to the weights and biases. The iterative process of feedforwarding and backpropagating is repeated many times until the loss function converges to a (local) minimum, resulting in the desired trained neural network.

Recurrent Neural Network and Long Short Term Memory

Recurrent Neural Network (RNN) is a class of ANN designed to process sequential data, such as time series data or speech recognition. RNNs extend traditional feedforward NN by incorporating a feedback loop, which makes it possible for the network to retain information from the hidden state, thus from a previous state, and use it to make predictions (Figure 2.3). This architecture enables the network to capture temporal dependencies and patterns within sequences by learning from past inputs and incorporating that

knowledge in the current predictions. At each time step t, the RNN takes an input vector $x_t \in \mathbb{R}^d$ and updates its hidden state $h_t \in \mathbb{R}^m$ using the following recurrence relation:

$$h_t = \phi(W_{xh}x_t + W_{hh}h_{t-1} + b_h), \tag{2.11}$$

where:

2

- $W_{xh} \in \mathbb{R}^{m\times d}$ is the weight matrix mapping the input to the hidden state,
- $W_{hh} \in \mathbb{R}^{m\times m}$ is the recurrent weight matrix applied to the previous hidden state,
- $b_h \in \mathbb{R}^m$ is the bias vector for the hidden layer,
- $\phi(\cdot)$ is a non-linear activation function, typically tanh or ReLU.

The hidden state h_t carries information from previous time steps, enabling the RNN to model temporal dependencies in the input sequence $\{x_1, x_2, \ldots, x_t\}$. The output at each time step is computed as:

$$y_t = W_{hy}h_t + b_y, \tag{2.12}$$

where:

- $W_{hy} \in \mathbb{R}^{o\times m}$ maps the hidden state to the output space,
- $b_y \in \mathbb{R}^o$ is the output bias,
- $y_t \in \mathbb{R}^o$ is the output vector at time step t.

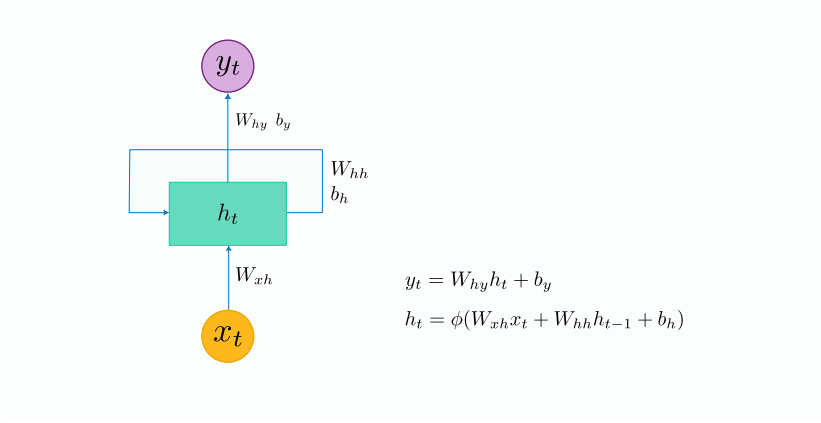

Figure 2.3.: Structure of an RNN, showing the temporal dependency in the input sequence.

Training an RNN involves minimizing a loss function L over the entire sequence $\{x_1, \ldots, x_t\}$. To compute the gradient of L with respect to the parameters (e.g., W_{hh}),

the backpropagation through time (BPTT) is used to reduce the discrepancy between the predicted output and the actual target. One of the most widely used loss functions for regression is the Mean Squared Error (MSE). During training, weights and biases are updated using the gradient descent or another optimization algorithm, based on the gradients of the loss function with respect to each parameter (the weight matrices W_{xh}, W_{hh} and W_{hy} and the biases b_h and b_y, where W_{hy} are the output weights).

If we consider the gradient of the loss with respect to the recurrent weight matrix W_{hh}, the total loss L is given by:

$$\frac{\partial L}{\partial W_{hh}} = \sum_{t=1}^{T} \frac{\partial \mathscr{L}_t}{\partial W_{hh}} = \sum_{t=1}^{T} \frac{\partial \mathscr{L}_t}{\partial h_t} \cdot \frac{\partial h_t}{\partial W_{hh}}, \tag{2.13}$$

where $\mathscr{L}_t$ is the loss at time t. Since W_{hh} is a matrix, the gradient $\frac{\partial L}{\partial W_{hh}}$ is also a matrix of the same dimensions as W_{hh} where each element represents the partial derivative of L with respect to the corresponding element of W_{hh}. Since the hidden state h_t depends on all previous states, the term $\frac{\partial h_t}{\partial W_{hh}}$ can be expanded using the chain rule:

$$\frac{\partial h_t}{\partial W_{hh}} = \sum_{k=1}^{t} \left(\prod_{j=k+1}^{t} \frac{\partial h_j}{\partial h_{j-1}} \right) \cdot \frac{\partial h_k}{\partial W_{hh}}. \tag{2.14}$$

The recursive partial derivative (i.e., $\frac{\partial h_j}{\partial h_{j-1}}$) is a Jacobian matrix:

$$\frac{\partial h_j}{\partial h_{j-1}} = W_{hh}^{\top} \cdot \operatorname{diag}\left(\phi'(a_{j-1})\right), \tag{2.15}$$

where a_{j-1} is the pre-activation input to ϕ at time $j-1$.

The recursive product of these Jacobians over time steps can cause gradients to grow or decay exponentially. If the largest singular value of W_{hh} is greater than 1, the repeated product of Jacobians leads to exploding gradients. If it is less than 1, gradients shrink and vanish. In both cases, learning is disrupted, either by divergence or by the inability to capture long-term dependencies.

To overcome these issues, in 1997, Hochreiter and Schmidhuber [76] introduced the Long Short Term Memory (LSTM) network, a type of RNN capable of learning long-term dependencies. The LSTM architecture also has a chain-like structure, but it consists of self-connected memory cells and three multiplicative units. An LSTM block commonly incorporates a *memory cell*, a *forget gate*, an *input gate*, and an *output gate*, alongside the *hidden state* (Figure 2.4).

The cell state C_t (illustrated by the blue line in Figure 2.4) represents the "long-term" memory of the network. It tracks the information (memory) retained over time by the network and interacts with the gates through element-wise multiplication and addition. The cell state is not directly modified by any weights or biases, allowing information to propagate through long sequences without causing gradients to vanish or explode.

The hidden state h_t (represented by the orange line in Figure 2.4) represents the "short-term" memory. It is directly influenced by weights, which can modify the network's short-term memory at each time step. The cell state and hidden state interact via gates that determine which information should be added, updated, or removed from

the cell state. These gates use sigmoid and hyperbolic tangent activation functions to regulate the flow of information.

The forget gate determines how much of the previous cell state C_{t-1} should be retained. The gate combines the input x_t at time t, the hidden state from the previous time step h_{t-1} and a bias term b_f via a sigmoid function. The compact equation of the forget gate is:

$$f_t = \sigma\left(W_f x_t + U_f h_{t-1} + b_f\right) \tag{2.16}$$

where W_f and U_f are the trainable weights. The sigmoid function is used to produce values between 0 and 1. Thus, a forget gate output of zero means that the component of the cell state will be discarded. Next, the input gate identifies which part of the new information will be added to the cell state. The input gate i_t includes a sigmoid function to filter the values and determine the proportion of the new information to be written, and a tanh function used to generate the candidate cell state $\tilde{C}_t$:

$$i_t = \sigma\left(W_i x_t + U_i h_{t-1} + b_i\right) \tag{2.17}$$

$$\tilde{C}_t = \tanh\left(W_c x_t + U_c h_{t-1} + b_c\right) \tag{2.18}$$

The cell state C_t is then updated by combining the old memory (C_{t-1}), modulated by the forget gate, with the new candidate memory $\tilde{C}_t$, modulated by the input gate:

$$C_t = f_t \odot C_{t-1} + i_t \odot \tilde{C}_t, \tag{2.19}$$

where $\odot$ denotes the Hadamard product (element-wise multiplication). Finally, the output gate determines the final output of the LSTM unit at step t. The gate combines the cell state value (C_t) filtered via tanh function and the last sigmoid function in the block used to determine what part of the memory is used to generate the output. The compact equations of the output gate o_t and of the final output h_t are:

$$o_t = \sigma\left(W_o x_t + U_o h_{t-1} + b_o\right), \tag{2.20}$$

$$h_t = o_t \odot \tanh(C_t). \tag{2.21}$$

The hidden state h_t serves as both the short-term memory and the output of the LSTM block at time step t.

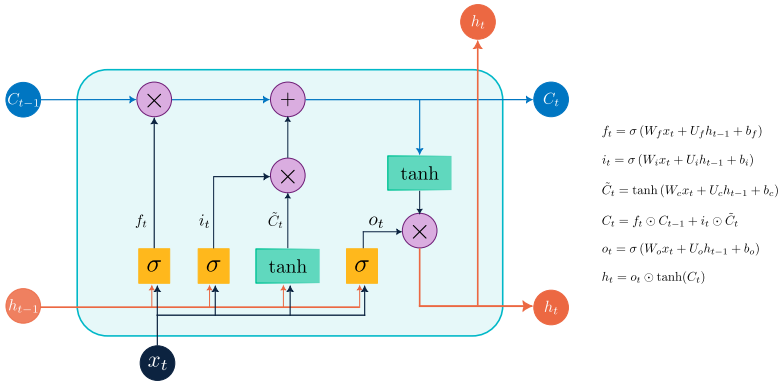

Figure 2.4.: Structure of an LSTM block, showing cell state, hidden state, and gating mechanisms.

Similar to RNN, LSTM networks are trained using BPTT. During training, the network computes gradients of the loss with respect to all parameters by unrolling the sequence over time and applying the chain rule. During training, LSTM networks aim to minimize a defined loss function over multiple epochs. An epoch refers to one complete pass through the entire training dataset, during which the model updates its internal parameters to reduce prediction error. Monitoring the training and validation loss across epochs is important to assess whether the model is learning effectively. For example, if the training loss decreases while the validation loss starts to rise, overfitting may be happening. To improve the performance and stability during training, hyperparameters such as the learning rate, batch size, and number of epochs are also tuned. Additionally, techniques like early stopping and dropout are often used to prevent overfitting and enhance generalization. The gates architecture allows the LSTMs to mitigate the vanishing gradient problem, enabling effective learning over long sequences, making it one of the most widely used networks for time series.

Ensemble learning and Extreme Gradient Boosting

Another subset of ML, frequently used for regression tasks, is ensemble learning. Ensemble learning methods create and combine a large number of simple decision trees, the combination of which reduces overall variance and bias, mitigates the limitations of individual models, and produces a more accurate and stable output. Typically, an ensemble learning model comprises a method to split the dataset into subsets, a predictive model and a combination mechanism. For the first component, the dataset is either split randomly (bagging) by generating samples from the training observations and fitting the same model to each different sample – also known as homogeneous parallel ensembles – or following an iterative process (boosting) by sequentially training new trees that correct the errors made by the previous ones – also known as sequential ensemble learning.

Fundamental in ensemble learning are the predictive models used, with decision trees being a common choice. A decision tree is a predictive model that splits data into

branches based on certain criteria. A tree structure consists of a root node, internal nodes, and terminal nodes. The root node is the initial point from which the splitting process is initiated. Internal nodes are either decision nodes, when they are split into further sub-nodes, or terminal nodes, when they are not split further. Terminal nodes are also known as leaves. Data is split based on whether a particular feature is less or greater than a defined threshold. The partitioning continues recursively until stopping criteria (e.g., maximum depth – the maximum number of splits allowed in a decision tree, or minimum child weight – the minimum amount of data required in a leaf node after split) are met.

A single tree is usually limited by high variance or bias; therefore, ensemble models using decision trees as weak learners have been proposed. Those include, among others, Random Forest [77], a method that creates a big number of simple independent decision trees implemented to random subsets of the feature space and then averages their predictions, and Gradient Boosting, a method that reduces the bias by sequentially adding trees to an ensemble learning, to correct the error of the previous trees.

The Extreme Gradient Boosting (XGBoost) builds upon the original gradient boosting by introducing a regularization term, which helps smooth the final learnt weights and avoid overfitting, enhancing the model performance and allowing the model to make better predictions on unseen data [78]. The construction of an XGBoost model follows the one of a gradient boosting, with a simple model. Given a dataset with n samples and K trees, the model of an ensemble tree learning is:

$$\hat{y}_i^{(t)} = \phi(x_i) = \sum_{k=1}^{K} f_k(x_i), \quad f_k \in F \tag{2.22}$$

where F is the space of regression trees. We can define the objective function as:

$$\mathscr{L} = \sum_{i=1}^{n} \ell(y_i, \hat{y}_i) + \sum_{k=1}^{K} \Omega(f_k) \tag{2.23}$$

where ℓ is the function measuring the difference between the prediction ($\hat{y}$) and the target value (y), while $\Omega(f) = \gamma T + \frac{1}{2}\lambda \| w \|^2$ is the regularization term that penalizes the model complexity, where T is the number of leaves in the tree and w the leaf weights. γ and λ represent the parameters that penalize the number of leaves and the leaf weights, respectively. A higher value of γ means the model penalizes trees with more leaves, while λ encourages leaves with smaller weights. The objective is to learn and optimize the structure of the tree and the parameters in the leaves. The tree ensemble model is trained in an additive manner. At each iteration t, the model $\hat{y}^{(t)}$ is updated by adding a new function that minimizes the residuals:

$$\hat{y}_i^{(t)} = \hat{y}_i^{(t-1)} + f_t(x_i), \tag{2.24}$$

thus at the t-th interation, the objective function will be:

$$\mathscr{L}^{(t)} = \sum_{i=1}^{n} \ell(y_i, \hat{y}_i^{(t-1)} + f_t(x_i)) + \Omega(f_t). \tag{2.25}$$

To efficiently optimize the loss function, XGBoost uses a second-order Taylor expansion of the loss function around the previous prediction $\hat{y}_i^{(t-1)}$:

$$\mathscr{L}^{(l)} \approx \sum_{i=1}^{n} \left[\ell(y_i, \hat{y}_i^{(l-1)}) + g_i f_t(x_i) + \frac{1}{2} h_i f_t^2(x_i) \right] + \Omega(f_t) \tag{2.26}$$

where g_i and h_i are respectively the first and second order gradient of the loss function:

$$g_i = \frac{\partial \ell(y_i, \hat{y}_i^{(t-1)})}{\partial \hat{y}^{t-1}}, \tag{2.27}$$

$$h_i = \frac{\partial^2 \ell(y_i, \hat{y}_i^{(t-1)})}{\partial \hat{y}^{(t-1)^2}}. \tag{2.28}$$

In this expansion, the term $\ell(y_i, \hat{y}_i^{(t-1)})$ represents the current loss (from the previous iteration) and is therefore constant with respect to $f_t(x_i)$. It does not influence the optimization process of $f_t(x_i)$ and therefore can be omitted from the final objective function:

$$\mathscr{L}^{(l)} \approx \sum_{i=1}^{n} \left[g_i f_t(x_i) + \frac{1}{2} h_i f_t^2(x_i) \right] + \Omega(f_t) \tag{2.29}$$

Assuming that the tree f_t assigns a constant score w_j to each data point in leaf j, so that $f_t(x_i) = w_{q(x_i)}$, where $q(x_i)$ maps sample i to its leaf index j, and defining I_j as the set of data points i such that the function $q(x_i)$ maps the input x_i to leaf j ($I_j = \{i : q(x_i) = j\}$), the objective becomes:

$$\mathscr{L}^{(t)} = \sum_{j=1}^{T} \left[\sum_{i \in I_j} \left(g_i w_j + \frac{1}{2} h_i w_j^2 \right) \right] + \gamma T + \frac{1}{2} \lambda \sum_{j=1}^{T} w_j^2, \tag{2.30}$$

grouping:

$$\mathscr{L}^{(t)} = \sum_{j=1}^{T} \left[G_j w_j + \frac{1}{2} (H_j + \lambda) w_j^2 \right] + \gamma T, \tag{2.31}$$

where $G_j = \sum_{i \in I_j} g_i$ and $H_j = \sum_{i \in I_j} h_i$. For a fixed structure $q(x)$, the optimal weight of each leaf (w_j^*) and resulting objective values are:

$$\begin{aligned} w_j^* &= -\frac{G_j}{H_j + \lambda}, \\ \mathscr{L}^{(t)}(q) &= -\frac{1}{2} \sum_{j=1}^{T} \frac{G_j^2}{H_j + \lambda} + \gamma T. \end{aligned} \tag{2.32}$$

The latest can be used as a measure of the tree quality. Still, there are infinite possible tree structures, thus, to learn the tree, XGBoost uses a greedy algorithm that starts from a single leaf (tree with depth = 0) and adds branches iteratively. To evaluate the goodness of the split, the gain is computed as:

$$Gain = \frac{G_j^2}{H_l + \lambda} + \frac{G_r^2}{H_r + \lambda} - \frac{G_l + {G_r}^2}{H_l + H_r + \lambda} - \gamma \tag{2.33}$$

where l and r represent the instance of the left and right nodes after split and γ represents the complexity cost introduced by a new leaf. The gain is used to quantify the average enhancement in the loss function when a feature is used to split nodes. If the gain is negative, the tree growth is interrupted, and the branch is pruned.

UNSUPERVISED LEARNING

2

Unsupervised learning refers to tasks where labelled data are not provided to the model that optimizes some general loss function without explicit supervision. Unsupervised methods can be broadly divided into agglomerative hierarchical approaches and techniques that require the number of clusters to be specified in advance, such as k-means. The primary goal of unsupervised learning is to discern key features in the dataset; for instance, by reducing data dimensionality, identifying clusters of similar instances, or detecting anomalies. Examples of unsupervised tasks in the context of ecosystem modelling include species delimitation using genetic data, habitat mapping, single-tree detection, and leafwood separation.

k-means

The k-means clustering is one of the oldest and most widely used clustering methods to partition a dataset into distinct non-overlapping clusters. It dates back to the 50s, when it was first proposed by Lloyd as a technique for pulse-code modulation and later used by MacQueen. Its popularity can be attributed to simplicity and easy to implement algorithm, and to its versatility.

Given a set of observations $X = \{x_1, x_2, \ldots, x_n\} \subset \mathbb{R}^d$, k-means aims at partitioning the n observations into $k (\leq n)$ clusters C so as to minimize the objective function:

$$\min_{\{C_1,\ldots,C_k\}} \sum_{i=1}^{k} \sum_{x \in C_i} \|x - \mu_i\|^2 \tag{2.34}$$

where:

μ_i is the centroid (mean) of points in cluster i, i.e., $\mu_i = \frac{1}{|C_i|} \sum_{x \in C_i} x$

$|C_i|$ is the size of the cluster i,

$\|\cdot\|$ denotes the Euclidean norm.

To minimize the potential function, a two-steps iterative approach is adopted. At first, k centroids $\mu_1, \ldots, \mu_k$ are randomly initialize. Then the algorithm proceeds by alternating the following two steps:

- assignment step: each data point x_j is assigned to the nearest cluster centroid c_i Assign each data point x_j to the nearest cluster centroid:

$$C_i = \{x_j : \|x_j - \mu_i\|^2 \leq \|x_j - \mu_l\|^2 \text{ for all } l = 1, 2, \ldots, k\} \tag{2.35}$$

  where C_i is the set of points assigned to cluster i.

- update step: the cluster centroids are recalculated as the mean of all points assigned to each cluster:

$$\mu_i = \frac{1}{|C_i|} \sum_{x_j \in C_i} x_j \tag{2.36}$$

Those two steps are repeated until convergence, or in other words, until the clusters no longer change. The convergence is guaranteed in a finite number of iterations because after each iteration, the objective function monotonically decreases. However, the k-means may converge to a local minimum and it is therefore not guaranteed to find the global optimum. The algorithm is also sensitive to the initial selection of the centroids, which can lead to empty clusters, slower convergence rates, and a higher risk of convergence in local minima [79]. A comprehensive study by Celebi et al. [80] compares several initialization methods and emphasizes their computational efficiency. Among the recent advancements is the use of k-means++ initialization that outperforms the k-means in terms of accuracy and speed. Proposed by Arthur and Vassilvitskii [81], the k-means++ first randomly selects the first centroid (c_1) from the dataset. Then, the i-th ($i \in 2, 3, \ldots, k$) centroid is chosen taking a point $x \in X$ with probability

$$P(x) = \frac{D(x)^2}{\sum_{x \in X} D(x)^2}$$

where $D(x)$ represent the shortest Euclidean distance from a point $x \in X$ to the closest already selected centroid. This last step is repeated until all k centers are taken altogether, then the standard k-means algorithm steps are applied.

REINFORCEMENT LEARNING

In reinforcement learning, a computer learns and adapts based on experience. Unlike supervised learning, reinforcement learning does not require labelled input-output pairs; instead, a learning agent interacts with its environment to achieve a goal. The agent explores a variety of actions and learning is guided by delayed reward signals that progressively favour those actions that appear to be "the best". Reinforcement learning is mainly used in the fields of robotics and autonomous vehicles and has enabled major advances in game playing applications like Checkers and Go [82, 83]. Despite having emerged as a state-of-the-art methodology in several disciplines, the adoption of reinforcement learning in environmental engineering remains very limited. Although reinforcement learning offers the ability to adapt control strategies to dynamic system conditions, its practical deployment in real-world environmental contexts is constrained by the immaturity of current methods as well as legislative and organizational barriers. For these reasons, reinforcement learning approaches have not been investigated within this thesis, and no further details will be provided.

SARIMAX

While machine learning techniques like artificial neural networks and ensemble trees have shown great performances in capturing complex, nonlinear patterns in data, traditional statistical models remain valuable tools, especially for time series analysis. Among

these, the Auto Regressive Integrated Moving Average (ARIMA) model, popularized by Box and Jenkins [84], has been extensively used to predict trends based on historical data. The SARIMAX model is an extension of the ARIMA, that incorporates seasonality (S-component) and exogenous variables (X-component) that can influence time series prediction. SARIMAX is therefore particularly useful when the time series is influenced by seasonality and external variables. SARIMAX has been shown to improve forecasts in the fields of hydrology, ecology and healthcare.

The ARIMA is itself an extension of the ARMA model, which consists of AutoRegressive (AR) component – that captures the autocorrelation in the data by including lagged values as a predictor – and Moving Average (MA) component – that captures the influence of unexpected fluctuation in the dataset by incorporating previous error terms. ARIMA integrates the Integrated (I) component, which accounts for non-stationarity in the time series. The ARIMA model, usually denoted as $ARIMA(p,q,d)$ where p,q,d are non-negative integers representing the order of the AR, MA and the degree of differencing of the I component, respectively, is defined as:

$$(1-B)^d x_t = c + \sum_{i=1}^{p} \phi_i x_{t-i} + \sum_{j=1}^{q} \theta_j \epsilon_{t-j} + \epsilon_t \tag{2.37}$$

where x_t represents the time series value at time t, B is the backshift operator, ϕ and θ are the coefficients representing the influence of the past values and errors respectively, and ϵ_t is the white noise term. p,q, and d can also be seen as the number of lagged observations used to predict the current value, the number of past errors included in the model to predict the current value, and the number of times the time series is differenced to make it stationary (i.e., constant mean and variance over time). For example, in this configuration $ARIMA(p,d,q) = (2,1,3)$, the autoregressive term ($p = 2$) indicates that the current observation x_t depends on the two most recent past observations x_{t-1} and x_{t-2}; the differencing order ($d = 1$) means the time series is differenced once to remove non-stationarity; whereas the moving average component ($q = 3$) means the model incorporates the last three forecasting errors ϵ_{t-1}, ϵ_{t-2} and ϵ_{t-3}.

The seasonal component used to remove the seasonality is given by:

$$(1-B^s)X_t = X_t - X_{t-s} \tag{2.38}$$

where s is the seasonal period; whereas the term $\beta^T Z_t$ represents the linear combination of the m exogenous variables Z_t and their coefficients β quantifying the impact of each external variable in Z_t on the time series. Incorporating both terms, the SARIMAX $(p,d,q) \times (P,D,Q)$ model is therefore given by:

$$(1-B)^d(1-B^s)^D x_t = c + \sum_{i=1}^{p} \phi_i x_{t-i} + \sum_{j=1}^{q} \theta_j \epsilon_{t-j} + \sum_{k=1}^{P} \Phi_k x_{t-ks} + \sum_{l=1}^{Q} \Theta_l \epsilon_{t-ls} + \beta^T Z_t + \epsilon_t \tag{2.39}$$

where D is the degree of seasonal differencing, s is the seasonal period, ϕ_i are the non-seasonal autoregressive coefficients, θ_j are non-seasonal moving average coefficients, Φ_k are the seasonal autoregressive coefficients, Θ_l are the seasonal moving average coefficients.

To fit a SARIMAX model to the data, the SARIMAX parameters (i.e., p, q, d, P, Q, s) need to be specified and then optimized. Tools like the Augmented Dickey-Fuller (ADF) test, the autocorrelation function (ACF) plot and the partial autocorrelation function (PACF) plot, or grid search, can help identify the best model's parameters. Using autocorrelation, the ACF plot is useful for visualizing how well the present values relate to their past values, without removing the effect of intermediate values. This is particularly useful for the identification of the MA component's order. The PACF plot instead describes the correlation between a time series values and its lagged values, after removing the effects of intermediate lag, and it is therefore used to identify the AR component order. Grid search optimization iterates over the parameter grid. The model is fit and evaluated at each iteration using criteria like the root mean squared error or the Akaike information criterion (AIC) and the Bayesian information criterion (BIC).

3

Remote sensing-based automatic detection of shoreline position: a case study in Apulia region

Remote sensing and satellite imagery have become commonplace in efforts to monitor and model various biological and physical characteristics of the Earth. The land/water interface is a continually evolving landscape of high scientific and societal interest, making the mapping and monitoring thereof particularly important. This paper aims at describing a new automated method of shoreline position detection through the utilization of Synthetic Aperture Radar (SAR) images derived from European Space Agency satellites, specifically the operational Sentinel Series. The resultant delineated shorelines are validated against those derived from video monitoring systems and in situ monitoring; a mean distance of 1 and a maximum of 3.5 pixels is found.

This chapter has been published in Journal of Marine Science and Engineering Volume 9, Number 6, Page 575, May 2021, https://doi.org/10.3390/jmse9060575.

3.1. Introduction

Coastal areas represent complex and highly dynamic environmental systems continuously facing changes due to natural as well as anthropogenic factors. The monitoring of their evolution is crucial for the safeguarding thereof. Wind, waves, coastal storms, and sea level rise represent some of the natural coastal threats that have been shaping the coastal zones and the consequences of which have been exacerbated in the last century [85, 86]. Sea hazards and extreme storm surges are increasingly threatening coastal areas causing, among others, flooding, coastal erosion, and damages to ecosystems and infrastructures [87]. Urban pressure, shifting land use and variations in dunes and sea bed stability [88–90] have and are also contributing to a further exacerbation of these hazards. Many coasts throughout Europe, and specifically in the Mediterranean [91], are expected to experience increased flooding in response to current coastal and dune management strategies.

In this context, effective management is of paramount importance to address the effects of the high concentration of human population and activities along the coasts. The assessments of coastal vulnerability and hazards can provide decision- and policymakers with diagnostic management tools to support sustainable development of coastal zones and face the negative effects of both human activities and extreme events [92, 93]. Environmentally friendly interventions and nature-based solutions may help in this direction promoting the restoration of the environment and the ecosystem [94, 95].

Information on long-term shoreline variability and periodic surveys of emerged and submerged beaches [96] help to quantify erosion or accretion processes. Among the several physical indicators used to assess beach erosion/accretion is the delineation of shoreline trends [97, 98]. An idealized definition of shoreline is the physical interface between land and water [99], identified by means of [100]: (i) visually discerning coastal features; (ii) the evaluation of the intersection between beach profile and the local tidal datum; (iii) specific image-processing techniques.

For a specific study area, the employed shoreline indicator is often related to the availability of data. Common data sources used to monitor coastlines are historical land-based photographs, coastal maps and charts, aerial photographs [101], beach surveys [102], LiDAR [103], remote sensing techniques [104–111], video imaging systems [112–115], and GPS [116–118].

Traditionally, the coastline has been detected by manual visual comparison and interpretation of different sources and images derived from all manner of Earth Observation (EO). However, by using subjective visually discernible features, shoreline position may be strongly influenced by the operator since the boundary between water and land can be difficult to identify due to operational constraints and can vary depending on tidal cycle information. Moreover, such manual delineation is time consuming, resulting in a high degree of inefficiency.

To overcome such limits, several techniques have been proposed to semi-automatically and automatically extract coastline from images acquired by both remote sensing [106, 119] and video monitoring systems [112, 120]. Remote sensing systems provide a repetitive and consistent view of the Earth, useful for monitoring short- and long-term changes of coastal zones and specifically shoreline position on a global scale with minimal individual user infrastructure requirements. Video monitoring systems

generally consist of more than one camera to cover multiple view angles on the area of interest and typically provide data at very high spatial and temporal resolution. Usually, the spatial scales of such systems vary from decimeters to kilometers based on the distance of the target from the camera. Images are acquired at a specified time sampling period varying from minutes to hours and are generally automatically collected and processed with low operating costs. A further benefit of such systems is their indifference to most atmospheric obstructions, mainly weather features and events such as clouds, allowing continuous data collection. Camera systems also offer a higher degree of customization per local monitoring objective, since different types of images can be collected to obtain information. For example, an averaged image is useful for the submerged and bar topography [121], while other sophisticated operational video-analysis techniques enable the quantification of detailed coastal features such as shoreline evolution and wave run-up [122, 123]. Moreover, the evaluation of waves, flow, and rip-currents empowers the management of dynamic navigational channels [124–126], whereas visitor density detection allows the monitoring of defining stressing factors for zones having an important ecological role [127, 128]. Hyper-specific features or data requirements from satellite are not as easily customized, though a wide portfolio of private purchasable data series complements the readily and publicly available data.

Satellites are more sensitive to weather conditions than video systems (particularly for passive and optical data acquisition, whilst radar and active sensors are limited to a lesser degree) and provide imagery on a lower temporal frequency than video camera systems. However, when considering large temporal time frames, the persistence of satellite imagery provides a powerful resource; whereas video monitoring campaigns last years, satellite imagery spans decades and continues to grow.

Remote sensing instruments fall into two categories: passive and active. Passive sensors measure various radiation naturally reflected or emitted from Earths surfaces, atmosphere and clouds. Passive sensors are primarily employed in the monitoring of morphological changes of the nearshore zone and for the monitoring of water quality. ESA, NASA and other national and international agencies operate an array of satellite missions providing large amounts of data on key physical and environmental indicators, including total suspended matter concentration, algal pigment concentration, chlorophyll-a [129, 130], and sea surface temperature. Furthermore, post-processing techniques can derive currents [131], alongshore and offshore significant waves and tides. New ocean colour sensors, such as the Plankton, Aerosol, Cloud, ocean Ecosystem (PACE) sensor, will enable the tracking of new ecological indicators and thus contribute to water quality monitoring.

Active remote sensing, which generates its own signals and records the amount of energy backscattered from the terrain, is capable of passing through gases and clouds, collecting clear data regardless of any light availability and weather conditions, a great advantage when compared to passive sensors. The most common methods to detect the shoreline from active sensors are based on segmentation and edge detection.

Segmentation is a process of grouping objects (or pixels) having similar characteristics later assigned to a specific class. Several methods have been developed for image segmentation, mainly belonging to supervised or unsupervised methods. Supervised segmentation uses a priori training dataset (or input classes) selected based on the ex-

perts knowledge, while unsupervised segmentation is trained during the segmentation process allowing for a fully automatic recognition of the classes. Post-segmentation processes might be required to merge regions that may derive from an over-segmentation [132]. To overcome these limits, Dellepiane et al.[119] proposed the adaptation of fuzzy sets in defining the shoreline contour. Coherence information extracted by the European Remote sensing Satellite (ERS)-1 and ERS-2 with a spatial resolution $20x20$ m is used as input for the segmentation process. An accuracy of about 3.5 pixels mean offset resulted by a comparison with the shoreline position detected from aerial images.

Edge detection is a process of finding boundaries between different regions and it is generally simpler than segmentation. When pursuing edge detection, locally adaptive thresholding algorithms can be employed. Thresholds are analytically determined by fitting a bimodal Gaussian curve and the accuracy of the results depends upon their reliability and correctness [132]. Previous studies [133–135] used an edge-detection method to determine the boundary area between land and water. Niederman et al. [135] apply an edge detection method [136, 137] on ERS satellites images. At first, all edges above a certain threshold are recognized, then a local edge selection is performed to refine the determined land/water boundary. Compared with the shoreline extracted by visual decision, the authors found a mean offset of 2.5 pixels. In general, edge detection methods are simpler than segmentation; however, edges may be discontinuous, leading to an erroneous definition of the shoreline [133, 134], a drawback that may require additional post-processing.

The present work shows a new automatic method based on edge detection aiming at retrieving shoreline position from Synthetic Aperture Radar (SAR) images. To extract the contour on land/water boundary, the method relies on a global threshold value derived by means of the Otsu method [62]. This is a key component of the method since it determines its simplicity in comparison to locally adaptive thresholding algorithms, since it does not require the partitioning of the whole image into subimages or statistic examination of the intensity values of the local neighborhood of each pixel [138]. The method allows for a fully automatic detection of the coastlines in a short amount of time. Sentinel-1 SAR images with a spatial resolution of 20 m are used as input.

Understanding and quantifying the positional accuracy of the satellite-derived shoreline positions is essential. For this reason, the method is tested along an Apulian beach in Southern Italy, Torre Canne (Brindisi), facing the Mediterranean Sea, where spatial and temporal variations of shoreline derived from a video system are available. The accuracy of the method in detecting the shoreline position (Satellite Derived Shoreline, SDS) is quantified with respect to shoreline data collected by a video system. The comparison is quantified and reported in terms of average offset and root mean square difference.

The following subsection 3.2.1 describes the morphological characteristics of the study area. The data employed in this study and the methodology steps are described in Section 3.2. Results, actual validation and main findings are discussed in Section 3.3 while a summary of the main outcomes with a recommendation for further study is addressed in Section 3.4.

3.2. Materials and Methods

To support decision-makers and policy with a management tool for coastal zones defense, this study proposes a new methodology for shoreline detection using Copernicus Sentinel-1 data. This section describes the study area, the datasets used to develop and validate the method, as well as the methodological steps employed in this research.

3.2.1. Study Area

The algorithm is tested along Torre Canne beach (Figure 3.1), in the south of Italy. Located in Apulia region and facing the Adriatic Sea, Torre Canne beaches are characterized by medium grain size. The emerged shore width may vary from a minimum of about 20 m to a maximum of about 50 m with a gentle foreshore and a steep berm, periodically covered by organic deposits of *Posidonia oceanica*. During the last decades, despite the mean wave climate being moderate (mostly propagating from N-NW and E-SE with an annual significant wave height comprised between 0.5 and 1.4 m and peak period ranging between 3 to 7 s), the study area has suffered remarkable erosive processes. Human activities and overexploitation of the coastal area, mainly due to touristic activities, combined with the increase in extreme storm occurrences, have been negatively affecting the sedimentary balance of the area. The long-term erosive trend has imposed an extensive monitoring programme of the area, including topographic and bathymetric surveys. In December 2015, a new video coastal monitoring system was deployed and integrated into the Apulian Region Monitoring Network, managed by the local Basin Authority to study both morphodynamic and hydrodynamic processes [112]. Further detail of the system is reported in Section 3.2.2.

Figure 3.1.: Torre Canne location along Apulia region coasts in the southern of Italy.

3.2.2. Materials

COPERNICUS Sentinel-1 satellite data

Sentinel-1 is the first satellite mission developed by the European Space Agency (ESA) for the Copernicus Programme, the European Unions Earth observation programme, previously known as GMES (Global Monitoring for Environment and Security). This program aims to serve as Europes eyes on the Earth and to provide high-quality and high-resolution EO data to public and private industries to aid in the monitoring and strategic planning of activities. Sentinel-1 carries a C-band Synthetic Aperture Radar (SAR) instrument capable of collecting data regardless of weather conditions or light availability. These data are freely available and downloadable via the Copernicus Data Space Ecosystem web portal (https://www.sentinel-hub.com/explore/copernicus-data-space-ecosystem/, accessed in May 2026) or via the European Data and Information Access Services (DIAS) platforms that allow users to discover, manipulate, process, and download Copernicus data and information.

In the present work, Sentinel-1 products acquired on Interferometric Wide (IW) swath mode are selected to test the developed methodology. The IW mode combines a large swath width (250 km) with high geometric resolution (5 × 20 m on the ground) and is implemented as Terrain Observation with Progressive Scans SAR (TOP-SAR) mode [139]. Depending on electromagnetic wave transmission and reception directions, data are available in single or dual polarization. Partial dual polarization vertical+horizontal (VH) is tested here. Dual polarization HV and VH have proved to be adequate for the mapping of flood water [140] and to be less sensitive to wind-induced surface roughness that can influence the backscattering coefficient, especially for VV polarization [141, 142]. Moreover, VH polarization generally yields the highest contrast between land and open water and thus is suitable for the purpose of this study.

IW products are acquired at Level-0, the raw data, and processed to Level-1 and Level-2 products through filtering techniques and processing algorithms to obtain higher level information. Level-1 Data (L1D) preprocesses include radiometric normalization, terrain correction and geolocation. L1D products are available at single look complex (SLC) or ground range detected (GRD). SLC products are provided in slant-range geometry, where coordinates are defined as the line-of-sight from the radar to each reflecting object, and with variable pixel resolution. GRD products are SLC projected using an Earth ellipsoid model. The resulting pixels have approximately square resolutions and square pixel spacing. Depending on the level of the applied multi-look, GRD files are available in Full (FR), High (HR) and Medium (MR) Resolutions. Sentinel-1 GRD HR products acquired in IW mode are suitable to test the proposed algorithm for shoreline detection, due to the easy and low-cost data accessibility and usability. Products have a pixel size equal to 10 × 10 m and a spatial resolution of 20 × 22 m, resulting from the aggregation of pixels in the post-processing phase. An example of the downloaded images is shown in Figure 3.2.

Validation Data

In order to obtain accuracy and precision metrics, optical images acquired by a video monitoring system installed in 2015 at Torre Canne, Italy (Apulia, South Italy) [112, 120,

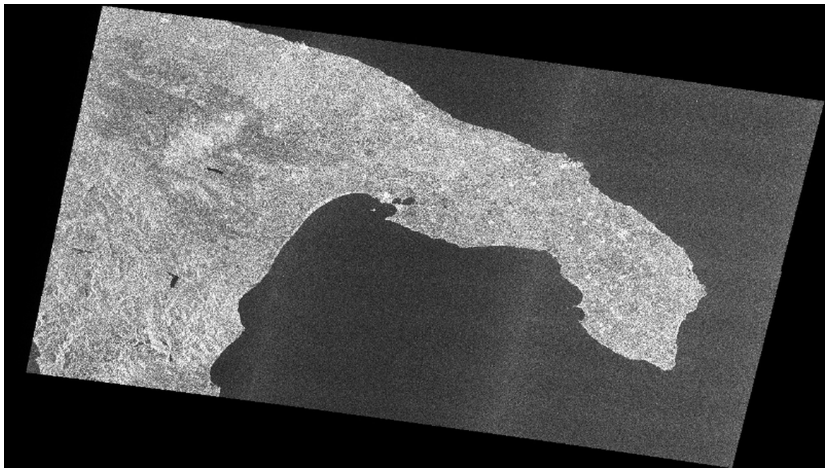

Figure 3.2.: High resolution images Level-1 Ground Range Detected product acquired in interferometric wide swath mode by Sentinel-1 platform on 7 June 2017.

143] are used to compare satellite versus in situ monitoring strategies. Video-derived images spatial resolution varies from decimetres to around 13 m, based on the distance of the near-alongshore footprint from the camera (Figure 3.3).

The camera system is configured to acquire images with a sampling interval of 30 minutes. The acquisition cycle is of 10 minutes with a frequency of 1Hz, thus resulting in 600 images. Those images are automatically processed to extract the shoreline position. The averaged shoreline is then returned every 30 minutes as a collection of points geolocated into a specific UTM projection identified with the code EPSG:6708. Those points can be transformed into a continuous element defining the shoreline. Results have been validated in a previous work [112] by a comparison with the shoreline manually recognized by an operator. A mean difference of 1.17 pixels was found.

The time of acquisition of both satellite and video system is a key element when comparing the two methods, since shoreline detection from image processing is highly influenced by both tide and wave run-up levels. Those can indeed influence the water content and thus the saturation degree of the emerged beach and, consequently, the colours and the reflection properties of the sand, based on which the land/water interface is distinguished. Video-derived shorelines are already processed by considering the effect of the tide but not satellite images. For this reason, to ensure a reliable validation of the algorithm developed within this research, only the images acquired with a maximum lapse of time of 20 minutes are compared (e.g., on 29 September, image acquired at 16:48 by Sentinel-1 is compared with the image acquired at 16:30 by the video system), namely the shoreline position variations are assumed to be negligible within the time laps of 20 minutes.

Figure 3.3.: Example of the image acquired by IP camera placed on-site along Torre Canne beaches.

3.2.3. Methods

The algorithm is based on edge detection techniques, mainly consisting of finding the boundary which separates two different regions. Figure 3.4 below reports the block diagram of the method. It consists of four main processes: despeckling, binarization, morphological operations and edge detection. Those processes aim to (i) reduce the speckle effects (despeckling); (ii) recognize water/land boundary by intensity values (binarization, morphological operations); and (iii) automatically extract the shoreline (edge detection). The procedural architecture for automatic shoreline edge extraction from preprocessed Level-1 GRD satellite images obtained from Copernicus Services is built on Python Open Source Computer Vision (OpenCV) library [144] and Scikit-image processing toolbox [145] for SciPy.

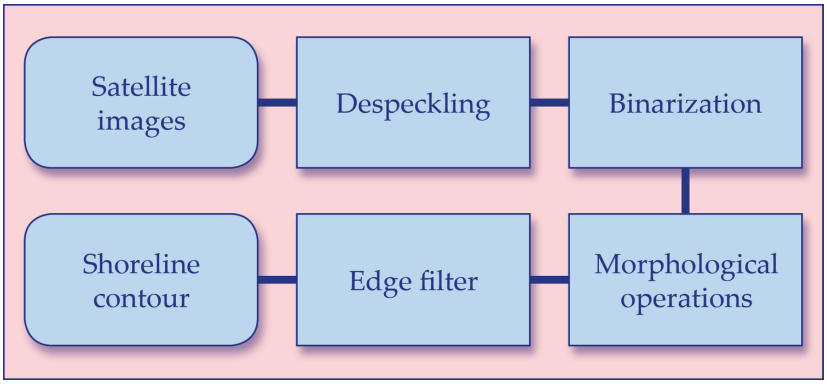

Figure 3.4.: Block diagram of the processes composing the algorithm.

Despeckling

Due to the constructive/destructive interferences of backscattered electromagnetic waves, a speckling appears as a salt-pepper noise in the image. The first operation aims at reducing speckle effects on SAR images to obtain an image characterized by lower noises, making the output easier to be processed in subsequent functions. Without this step, such disturbances preclude the further recognition of the water/land boundary by intensity values.

The reduction of speckle noise can be obtained by applying a multi-look integration or a post-image formation method [146]. Multi-look processing technique averages, pixel by pixel, several independent or dependent images, corresponding here to different looks of the same image [147]. Each look is obtained by dividing the signal bandwidth into parts and processing each part as a single look image of the same scene [148]. Post-image formation methods are based on the application of standard filters, such as Huang [65], Kuan [66], Frost [67] and Gamma Filter [68]. Usually, those filters perform well on most SAR images even though spatial resolution is often lost [146]. Due to its low computational cost, simplicity, and good performance in preserving edges [149], a median-filtering approach is used in the present work on Sentinel-1 images. Median filtering replaces the intensity of each image pixel $y(m,n)$ with the median of the intensities in a defined neighborhood w around the pixel location (m,n) as defined in the following equation:

$$y[m,n] = median\{x[i,j],(i,j) \in w\} \tag{3.1}$$

The neighborhood is defined by the user. The median filtering approach is implemented by means of a structuring element, also called kernel, with a size of 5×5.

Binarization

Pixels classification is then applied to the denoised image via the Otsu's method [62] to allow the creation of a binary image. The Otsu's method is one of the best-known thresholding methods and has been proven to obtain satisfactory results when applied to satellite images for the land/water classification [150–152]. As discussed in Chapter 2 and here reported for completeness, the Otsu's method is an unsupervised and non-parametric method based on the zeroth and first moments of the grayscale histograms.

The binarization automatically calculates the optimal threshold at level k value by using discriminant criterion measures. Pixels are divided into two classes C_0 and C_1 with levels [1, 2, , k] and [k+1, k+2, , L] respectively, where L is the grayscale level.

The probability of occurrence ω (3.4), class means levels μ (3.5) and class variance σ (3.6) are calculated from the histogram of the pixels values distribution for the two classes. Then, to evaluate the threshold goodness, the class separability is evaluated using specific discriminant criteria. The adopted criterium η (3.2) is defined as the product between the probability of occurrence and the first and second order cumulative moments of the histogram. The total mean intensity (μ_t) and variance (σ_T) are computed over all pixel values. The aim is to find the threshold that minimizes η (3.2), or equivalent, the weighted within class variance given by σ_B (3.3):

$$\eta = \frac{\sigma_B^2}{\sigma_T^2}, \tag{3.2}$$

where:

$$\sigma_B^2 = \omega_0(\mu_0 - \mu_t)^2 = \omega_1(\mu_1 - \mu_t)^2 = \omega_o\omega_1(\mu_1 - \mu_0)^2, \tag{3.3}$$

$$\omega_0 = Pr(C_0) = \sum_{i=1}^{k} p_i, \qquad \omega_1 = Pr(C_1) = \sum_{i=k+1}^{L} p_i = 1 - \omega_0, \tag{3.4}$$

$$\mu_0 = \sum_{i=1}^{k} \frac{i\,p_i}{\omega_0}, \qquad \mu_1 = \sum_{i=k+1}^{L} \frac{i\,p_i}{\omega_1}, \qquad \mu_T = \mu(L) = \sum_{i=1}^{L} p_i = \omega_0\mu_0 + \omega_1\mu_1, \tag{3.5}$$

$$\sigma_0^2 = \sum_{i=1}^{k} (1-\mu_0)^2 \frac{p_i}{\omega_0}, \qquad \sigma_1^2 = \sum_{i=k+1}^{L} (1-\mu_1)^2 \frac{p_i}{\omega_1} \qquad \sigma_T^2 = \sum_{i=1}^{L} (i-\mu_t)^2 p_i, \tag{3.6}$$

The Otsus method can be easily implemented on the denoised images by means of a Python OpenCv function. In the present work, the binary image is obtained by setting the values of the minimum and maximum pixels based on the gray levels and assigning, respectively, to classes C_0 and C_1. The described classification relies on the found global threshold value, which may therefore strongly influence the position of the satellite-derived shoreline. Threshold values estimated using a global thresholding method can be, indeed, arbitrary values in the middle of two peaks. Kittler and Illingworth [153] identified a good performance of the Otsus method when the pixel distribution histogram is bimodal with a sharp valley. In this study, we assess the impact of the size of the despeckling kernel on the pixel distribution by analyzing the pixel distribution of the despeckled image.

Morphological operation

Two morphological operations are then applied to the binary image to distinguish meaningful shape information (water/land) from irrelevant elements present in the satellite image, such as ships or small isolated areas. Morphological operations are widely used in image processing since they clarify the image by eliminating irrelevancies and by preserving objects shape.

Mathematical morphologies are based on set theory [154, 155]. Operations such as union, intersection, translation, and subtraction can be performed on each image. Dilation and erosion processes are two of the basic morphological operations. Dilation combines two vectors using addition, whereas erosion uses subtraction [155]. Applying iterative dilation and erosion, it is possible to remove details smaller than the kernel size without causing geometric distortion of the objects [156]. The composition of dilation and erosion results in opening and closing processes. Opening smooths contours by removing sharp peaks and small areas, whereas the closing operation helps in filling holes and fusing narrow breaks [157]. If A is the binary image and B is the structuring element (both set in Euclidean N-space), the opening of A by B is defined as follows:

$$O(A,B) = E(D(A,B),-B) = (A \ominus (-B)) \oplus B \tag{3.7}$$

whereas the closing of A by B is defined as follows:

$$C(A,B) = E(D(A,B),-B) = (A \oplus (-B)) \ominus B \tag{3.8}$$

where Dilation (D) and Erosion (E) are defined respectively as:

$$D(A,B) = A \oplus (-B) \tag{3.9}$$

$$E(A,B) = A \ominus (-B) \tag{3.10}$$

The defined morphological operations are employed in the method here proposed by means of a structuring element with a size 7×7 . The binary image obtained from the Otsu's method is used as input for the opening operation. The resulting image is then used as input for the closing operation.

Canny Edge detector

The recognition of the objects and their boundaries is obtained through Edge Detection Techniques (EDTs). EDTs convolve the image with an operator sensitive to discontinuities in grayscale level from one pixel to another.

Operators mainly belong to a gradient-based or Laplacian-based algorithm. Gradient methods look for the maximum and minimum of the first derivative of the image. Laplacian-based method search, instead, for the zero crossing of the second derivative of the image. Based on its geometry, each operator recognizes edges along a fixed direction (vertical, horizontal, diagonal). Local operators can be used to estimate vertical and horizontal edges. Among the local operators, the most used are the Sobel's and Prewitt's ones consisting of two 3×3 convolution kernels. However, the latter, as well as the Laplacian operators, are sensitive to image noises [158]. To overcome these limits, Marr-Hildreth [159] proposed an algorithm based on the convolution of the image with the Laplacian of the Gaussian function, able to smooth the image and, consequently, reduce the noises influence on the edges extraction.

The Canny edge detector algorithm [160] also allows for the reduction of noises, localization of edges and suppressing of false edges. The Canny edge detector includes three steps: smoothing, differentiation and labelling, and shows good performance when compared to other filters [161]. The Canny method recognizes edges by convolving the image with an operator that is the first derivative of a two-dimensional Gaussian. Edges are determined by an optimization process and marked at the maxima in gradient magnitude of a Gaussian-smoothed image [160].

In the present work, in the beginning, the Sobel operator with a default size of 3×3 is used to find gradient values in both x and y direction (3.11). If A is the binary image set in Euclidean N-space, the gradients in each direction are defined by the convolution of A and Sobel operators ($\boldsymbol{S_x}$, $\boldsymbol{S_y}$). The edge gradient magnitude ($\mathbf{G}$) and direction ($\boldsymbol{\theta}$) are then found as in (3.12, 3.13):

$$S_x = \begin{bmatrix} -1 & 0 & +1 \\ -2 & 0 & +2 \\ -1 & 0 & +1 \end{bmatrix} S_y = \begin{bmatrix} +1 & +2 & +1 \\ 0 & 0 & 0 \\ -1 & -2 & -1 \end{bmatrix} \tag{3.11}$$

$$G = \sqrt{G_x^2 + G_y^2} \tag{3.12}$$

$$\theta = \arctan\left(\frac{G_y}{G_x}\right) \tag{3.13}$$

where:

$$G_x = A * S_x = A * \begin{bmatrix} -1 & 0 & +1 \\ -2 & 0 & +2 \\ -1 & 0 & +1 \end{bmatrix} G_y = A * S_y = A * \begin{bmatrix} +1 & +2 & +1 \\ 0 & 0 & 0 \\ -1 & -2 & -1 \end{bmatrix} \tag{3.14}$$

Then, by using a minimum and a maximum threshold value, here set respectively as 100 and 200, pixels are treated as edges if their intensity gradient is higher than the maximum threshold and discarded if lower.

3.3. Results

3.3.1. Sentinel-1 retrieved shoreline

Figure 3.5 shows the outcomes of each of the aforementioned methodology steps. Figure 3.5a shows an example of the input images used for testing the proposed methodology. At first, the salt-pepper noise effect visible in the image is reduced by a median-filtering approach executed with a kernel of 5×5 size, thus allowing for a better recognition of the water/land boundary (Figure 3.5b). The image binarization, namely the classification of the pixels for water and land, is automatically executed on the denoised image by means of the Otsu's method which allows for the calculation of the optimal threshold value for water/land recognition. The output is a binary image (Figure 3.5c) where 0 is assigned to the pixels below the threshold, namely water, whereas 1 is assigned to those pixels in exceedance, corresponding to land.

It is observed that the application of both opening (Figure 3.5d) and closing (Figure 3.5e) operations contributes to reducing uncertainties and improving the edges detection. The effects of such operations are clearly shown in Figure 3.5e with the reduction of the number of black dots visible in the mainland when compared to Figure 3.5c.

Figure 3.5f shows that by applying the Canny edge filter, edges in the binary image are successfully recognized. The pixels ranging between the two thresholds are considered edges only if connected to pixels above the maximum threshold. Figure 3.5f also shows that the Canny method ensures the filtering of other small pixels noises, under the assumption that edges are long lines.

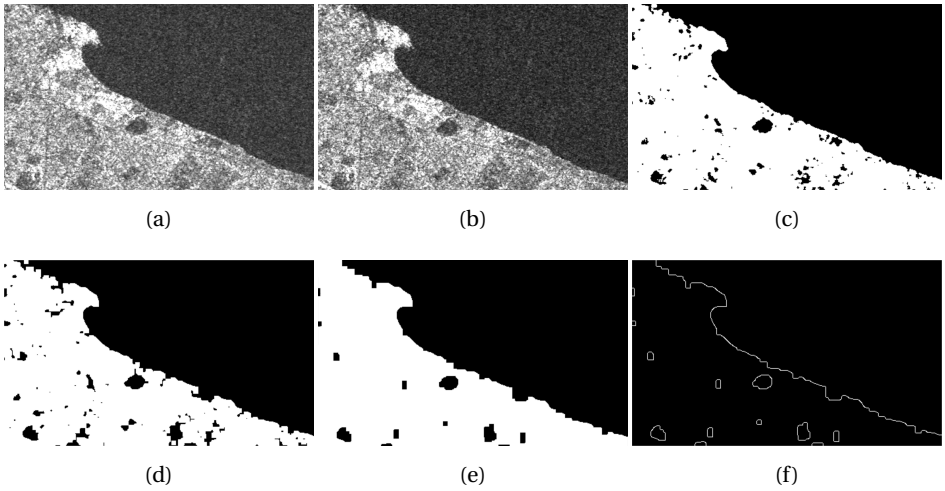

Figure 3.5.: Example of automatic shoreline extraction by Sentinel-1 Synthetic Aperture Radar image. (a): original S1 image; (b): denoised image; (c) binary image; (d): image resulting from the opening process, by applying the Canny edge filter; (e) image resulting from the closing process; (f): shoreline extraction.

3.3.2. Shoreline position validated against video monitoring system-derived shoreline

Satellite Derived Shorelines (SDSs) are extracted here for the year 2017, and the comparison with Video Derived Shorelines (VDSs) is performed on a total of 11 satellite images. For each point composing the VDS, the distance with respect to the SDS is automatically calculated to evaluate the accuracy of the proposed model in extracting the shoreline position and the influence of the employed filters on the model performance. Figure 3.6 shows an example of the SDS (red line) and VDS (blue line) acquired on 15 January 2017 at Torre Canne overlapped on the Sentinel-1 image. The average offset is about 10 m, whereas the Root Mean Square Difference (RMSD) is equal to 12.48 m. Both metrics indicate a sub-pixel accuracy. The measured pixel spacing of the processed images is, indeed, 12.75 m. The maximum distance is equal to 44.74 m, which corresponds to an accuracy of 3.51 pixels (Table 3.1).

3.3.3. The effect of the despeckling kernel size on the shoreline position

In order to study the effect of different despeckling kernel sizes on the final threshold based on which the shoreline position is defined, different kernel sizes have been applied to the same images and the variation of the threshold has been evaluated.

Figure 3.7 shows an example of the variation of the pixels distribution histogram obtained by increasing the kernel size from 5×5 to 25×25. It can be observed that the distribution is characterized by a bimodal distribution, which varies with the kernel size. In

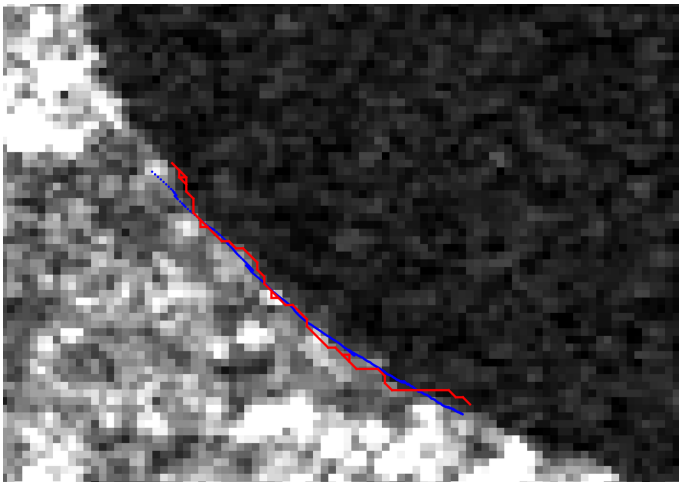

Figure 3.6.: Example of the shoreline extracted along Torre Canne beaches and overlapped on the corresponding Sentinel-1 image. Shoreline extracted by the video monitoring system is shown with a blue line, whereas the satellite-derived shoreline is represented by a red line.

Table 3.1.: Results of the validation measures estimated for each image.

Date	Time Sentinel-1	Time Webcam	Minimum distance [m]	Maximum distance [m]	RMSE [m]
19-02-2017	04:55	05:00	0.001	23.381	8.373
27-03-2017	04:55	05:00	0.026	36.172	9.601
15-05-2017	16:40	17:00	2.401	31.482	15.329
26-05-2017	04:55	05:00	0.005	35.565	13.065
27-05-2017	16:40	16:30	0.008	31.010	11.285
07-06-2017	04:55	05:00	0.012	18.638	6.132
08-06-2017	16:40	17:00	0.002	27.671	10.061
06-10-2017	16:40	17:00	11.108	44.737	23.206
18-10-2017	16:40	17:00	0.002	33.328	12.615
30-10-2017	16:40	17:00	0.706	37.797	14.049
16-12-2017	04:55	05:00	0.045	32.315	13.454
		average			12.479

fact, by replacing the pixel with the median of it and its adjacent neighboring values, the despeckling filters influence the histogram distribution and, thus, the threshold. Particularly, it can be seen that, by increasing the kernel size, two different peacks and a sharp valley are better recognized. The calculated threshold value for each kernel size varies in a range of 10 pixels. In the meantime, as shown in Figure 3.8, it is observed that the spatial resolution decreases as the despeckling kernel size increases. Smaller kernels preserve better spatial resolution, even if the roughness of the extracted shoreline in-

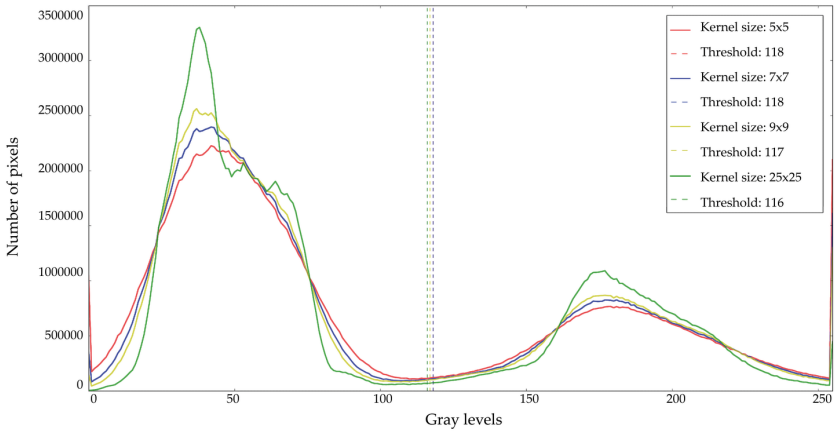

Figure 3.7.: Pixel values distribution of the image denoised by means of kernel with different sizes.

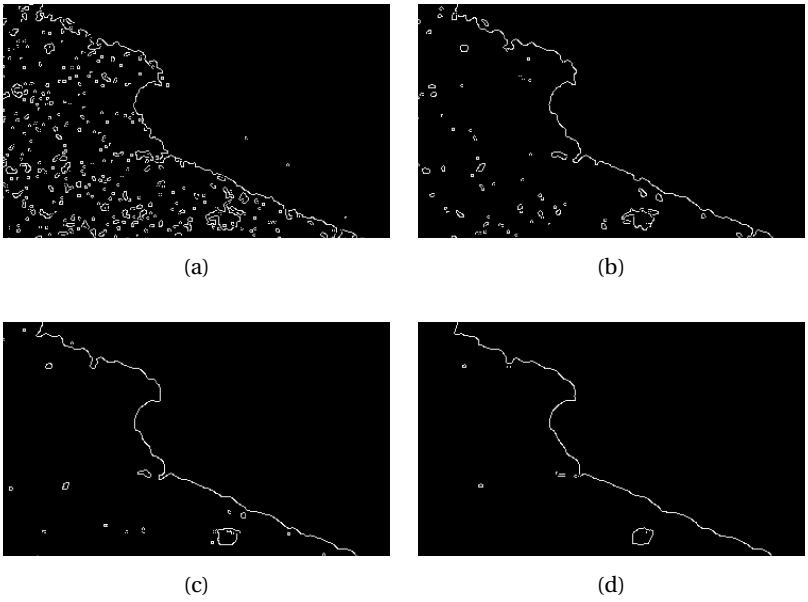

Figure 3.8.: Example of the influence of the despeckling kernel size in the final retrieval of the edges. Results obtained by using a median-filtering approach by varying the kernel size in order to reduce speckle noise. (a): kernel size 3×3; (b) kernel size 5×5; (c): kernel size 7×7; (d) kernel size 9×9.

creases, and several edges far from the shoreline are detected close to the coasts. On the contrary, the use of bigger kernel sizes results in a smooth and discontinuous line. For this reason and considering that the final shoreline position does not change by varying the threshold on such a range of 10 pixels, the 5×5 structural element was chosen as the optimal kernel to reduce the speckle effects.

3.3.4. Versatility of the presented methodology

The validated method is applied on other test sites to investigate its versatility.

Torre Lapillo

Torre Lapillo, hamlet of Porto Cesareo (Lecce), located in the Apulian region facing the Ionian Sea (see Figure 3.9) is selected for its interesting morphology. It is constituted by the typical sub-environment of low-lying coasts and narrow sandy beaches, with emerged beach widths ranging from less than 10 m to about 50 m.

Figure 3.9.: Torre Lapillo location along Apulia region coasts in the southern of Italy.

As shown in Figure 3.10a, the morphology of Torre Lapillo results in a limiting factor for the method. Within the study area, a basin, called “Bacino dell’Uomo Morto”, is situated just behind the dunes. The basin has a maximum width of about 190 m. The beach width, being comparable to the pixel spacing and coupled with the proximity of the basin to the sea, leads to some difficulties in detecting the shoreline position. However, the use of VV polarization on acquired images enables overcoming such a problem (Figure 3.10b).

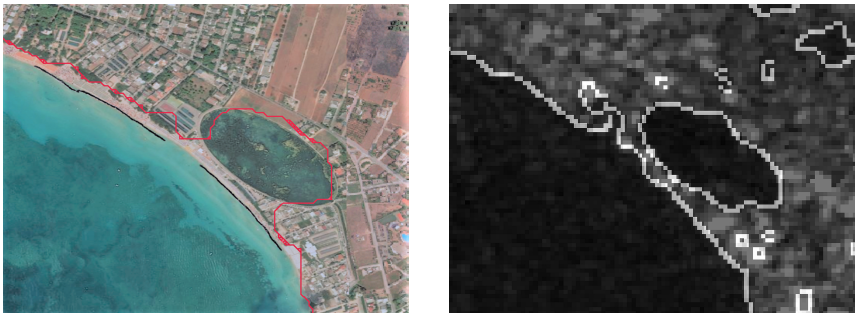

(a) (b)

Figure 3.10.: Comparison between the Torre Lapillo shoreline extracted by using (a) VH polarized image and VV images; (b): VV polarized image.

Aerial images: Giovinazzo

The algorithm is also applied to optical aerial images to test its versatility on different images. Ortho-images are photogrammetric images obtained from cameras fixed on airplanes. Several images are captured through photogrammetric flights. The resultant image is then retrieved by overlapping pictures in the order of 60% forward and 20-40% in lateral direction. Freely ortho-images with a spatial resolution of 0.5×0.5 m and 0.2×0.2 m available as Web Map Services (WMS) for the Apulian region (http://www.sit.puglia.it/portal/portale_cartografie_tecniche_tematiche/WMS, accessed in May 2026) are eligible for our purpose.

The method shows good performance when applied to aerial images. Figures 3.11 and 3.12a show the shoreline extracted along Giovinazzo (northern Apulia) beaches, where breakwaters, rocky, and sand beaches come in succession. Nevertheless, beach slopes, shadows, and wave foam may constitute limiting factors for using this method on images acquired by using optical sensors, as shown in Figure 3.12b.

3.4. Discussion

In this study, the feasibility of an automated method for shoreline position delineation is demonstrated. The dataset used is freely available and easily accessible, making the methodology reproducible in any geographical area; the methodology yields satisfactory results when applied to Sentinel-1 data. The number of processing steps applied to the images is relatively small, making the method straightforward and allowing for a fully automated procedure capable of long-term shoreline evolution assessment. Sentinel-1 satellite-derived shorelines have been extracted for the year 2017. The retrieved shorelines have been validated against video monitoring system-derived shorelines at Torre Canne beaches, and deterministic verification measures such as RMSE have been computed. Results are very promising with the average RMSE of 12.48 meters reported, indicating a sub-pixel accuracy. The minimum distance suggests a good overlap between video monitoring and satellite-based shorelines, except for the 6^{th} of October, during which the maximum distance between the two shorelines also occurs. This suggests a

Figure 3.11.: Example of the shoreline extracted along Apulian beaches overlapped on ortho-images. The yellow box delimits the breakwater zones, the blue box marks the rocky beaches, and the black box delimits sandy beaches limits.

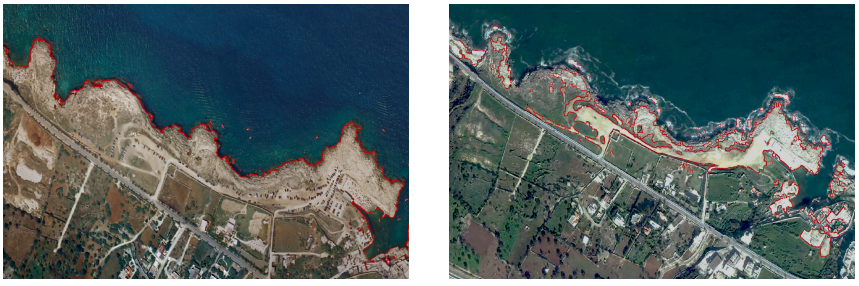

(a) (b)

Figure 3.12.: Comparison between shoreline detected during calm and rough sea. Example of the influence of wave foam on the shoreline detection. (a): Rocky beaches shoreline extraction along the Apulian region during calm sea; (b): Rocky beaches shoreline extraction along the Apulian region during rough sea.

lower geolocation accuracy, and thus the importance of accurate georeferenced and orthorectified products for the model.

Tests have been executed in order to evaluate the influence of the kernel size on pixel distribution, and thus on the optimum threshold for water/land classification. Significant improvement of the shoreline position has not been observed; on the contrary a degradation in the spatial resolution has been observed, suggesting a size of 5×5 as optimum for the kernel.

The study also attempted to explore the versatility of the proposed methodology. To this end, Torre Lapillo, situated along the Apulian coast, has been selected for its pecu-

liar morphology as constituted by narrow sandy beaches with emerged beach width typically ranging from less than 10 to about 50 meters, comparable to the pixel size, and the presence of a basin behind the dunes. As shown in Figure 3.10a, the morphology of the area may represent a limiting factor of the methodology. However, imagery collected using a different polarization combination can help overcome this issue (see Figure 3.10b), allowing a more accurate water/land classification [162].

Depending on the transmitted and received polarizations, the radiation interacts with and is back-scattered differently by the surface. Therefore, different polarizations cause variations in radar response, providing different and complementary information about the targets in the area. This suggests that the combination of different polarization channels can be a potential candidate for further investigation.

A first attempt to employ the methodology on optical images has also been successfully performed. Ortho-images with a spatial resolution of 20 cm have been employed for this purpose. Preliminary results are promising but also show that parameters such as wave foam, shadows, and shallow beaches can influence the retrieved edges and thus the shoreline position. Additional filters may help overcome this issue and need to be further explored.

Areas of methodological improvements include utilizing segmentation algorithms such as locally adaptive thresholding algorithms which can enhance the land/water boundary recognition and thus reduce discontinuity of coastal edges that may occur in low contrast areas of the image [132]. The proposed method of shoreline detection might face difficulties within intertidal areas, where porous medium is characterized by a higher saturation degree which induces some uncertainties in the detection of the shoreline. Indeed, the higher the moisture content is, the higher the probability that its reflectance behavior is assimilated to that of water. In fact, at saturation, the optical path length in water is at its maximum and certain wavelengths may be completely absorbed [163]. For these areas, a multilevel Otsu thresholding algorithm can be used and three classes may be defined as suggested by [164]. It is therefore recommended to further explore the method's performance in different types of coastal landform and different hydrodynamic conditions, and to analyze its dependence on the tide and wave run-up and on the different grain sizes of sandy beaches.

Small changes in the coastal areas over short periods may be difficult to detect due to the coarse spatial resolution often obtained via satellite imagery. To enhance the spatial resolution of the employed satellite images, image fusion techniques may be explored. Shoreline mapping can indeed be performed by using a single satellite sensor, as done in this study, or by the combination of multiple images derived from different sensors. Image fusion allows for the combination of different images to enhance the classification accuracy [165–167] and has been applied to shoreline mapping studies and to identify dynamic shoreline trends [168, 169].

Additional significant improvements of the spatial and temporal resolution of the satellite imagery are also promised by emerging micro- and nanosatellite constellations (PACE, Geosynchronous Littoral Imaging and Monitoring Radiometer (GLIMR)) and commercial satellites (e.g. Radarsat, WorldView, Pleiades). Those promise to compensate for the limit imposed by the currently implemented satellite's temporal and spatial resolution, providing data at a daily temporal resolution and at a higher spatial res-

olution. The capability of those satellites to retrieve the shoreline position has already been proven [170–172].

3.5. Conclusions

This paper presents a new methodology for shoreline detection, based on edge detection techniques of preprocessed SAR images, freely available from ESA and the Copernicus program. The developed procedure of land/water boundary recognition is carried out with a script, which allows the generation of both shorelines and error statistics given the availability of in situ data. When compared to the outcomes from in situ and monitoring programs, the obtained shorelines provide reliable results given the spatial resolution of the satellite data. Moreover, in the case of calm sea and high contrast in the imagery, the method shows good performance in detecting the shoreline from aerial images.

Long-term variability of shoreline trends is widely used in risk management and planning activities on coastal areas and represents one of the most used indicators when accounting for assessing defense strategies for preventing beach erosion or flooding. In such a context, the availability of data with high temporal and spatial resolution is crucial. Shoreline detection from satellite images could represent a valid alternative to the traditional field survey. The detection method proposed in the present work has the advantage of using freely-available SAR images which are processed automatically to retrieve shoreline position. If applied continuously, it could allow for effective and timely monitoring of long-term changes in coastal areas, supporting decision-makers and administrations to manage defense interventions against beach erosion and flooding. The free and ready availability of Sentinel-1 images, the functionality of the algorithm, its operationalization, and its computational efficiency may indeed represent an efficient instrument to store and process a large number of images and data useful for monitoring coastal zones and detecting erosion, assisting in the reporting efforts of EU member countries, and potentially for identifying flooding events.

4

Assessing the use of Sentinel-2 data for spatio-temporal upscaling of flux tower gross primary productivity measurements

The conservation, restoration and sustainable use of the wetlands is the target of several international agreements, among which are the Sustainable Development Goals (SDGs). Earth Observation (EO) technologies can assist national authorities in monitoring wetland conditions and ecosystem functioning. In this study, we assess the capabilities of Sentinel-2 instrument to model Gross Primary Productivity (GPP) as a proxy for ecosystem health monitoring. To estimate the spatial and temporal variation of GPP, we develop an empirical model correlating in situ measurements of GPP, eight Sentinel-2 derived vegetation indexes (VIs), and different environmental drivers of GPP. The model automatically performs an interdependency analysis and selects the formulation with the highest accuracy and statistical significance. Additionally, the model is upscaled across larger areas and monthly maps of GPP are produced. The methodology is applied to a marsh ecosystem in Doñana National Park, Spain. In this application, a combination of the red-edge chlorophyll index (CL_r) and rainfall data results in the highest correlation with in situ measurements of GPP. The resulting model achieves a coefficient of determination (R^2) of 0.93, Mean Absolute Error (MAE) of 0.52 $gCm^{-2}d^{-1}$, Root Mean Squared Error (RMSE) equal to 0.63 $gCm^{-2}d^{-1}$, and significance level $p < 0.05$. The model outputs are compared with the MODIS GPP global product (MOD17) for reference; an enhancement of the estimation of GPP is found.

This chapter has been published in Remote Sensing Volume 15, Number 3, Page 562, January 2023, https://doi.org/10.3390/rs15030562.

4.1. Introduction

Healthy ecosystems are a primary source of vital resources for human welfare and survival while regulating the impacts of natural hazards and protecting human settlements against floods, landslides, and drought events, thus playing a key role in mitigating climate change effects [173]. Conserving biodiversity and preventing biodiversity shifts is therefore of significant importance and a main target of multiple international conventions. The Sustainable Development Goals (SDGs) [21] and the Paris Agreement by the United Nations Framework Convention on Climate Change (UNFCCC) [174] promote the conservation of ecosystems and their associated biodiversity. The conservation, restoration, and sustainable use of ecosystems is specifically mentioned in SDG 6.6 and SDG 15.1. The first, SDG 6.6, aims to protect and restore water-related ecosystems, including mountains, forests, wetlands, rivers, aquifers and lakes, while SDG 15.1 aims at ensuring the conservation, restoration and sustainable use of terrestrial and inland freshwater ecosystems and their services, in particular forests, wetlands, mountains and drylands, in line with obligations under international agreements. Other agreements and commitments include the Aichi Biodiversity Targets by Parties of the United Nations (UN) and the Convention on Biological Diversity (CBD) [19, 38].

Providing information on the health of ecosystems through monitoring activities is essential for applying suitable conservation and restoration practices. In recent years, Earth Observation (EO) technologies, particularly Satellite Remote Sensing (SRS), have been used to assist national authorities in monitoring programs for the achievement of the SDGs [41]. The main advantages of SRS include the provision of data in a systematic and timely way, the cost-effectiveness of monitoring activities, and the accessibility to remote areas [34, 175, 176]. SRS can capture biodiversity changes both at global and regional scales [33, 177], thus the joint use of SRS data with in situ data and images obtained from other technologies (Light Detection and Ranging (LiDAR), Unmanned Aerial Vehicle (UAV), etc.) is a key factor to generate actionable knowledge in real-time for improved decision-making [33].

To generate actionable knowledge, SRS data needs to be translated into information and specific metrics, maps, or consumable information products that can then be used to inform decision makers. Structural and functional indicators are both required to evaluate the ecosystems heath. Structural indicators reflect the extension and composition of the ecosystems; functional indicators are useful to understand whether the areas are fulfilling their ecosystem role [178]. Structural indicators are often used in monitoring programs, whereas ecosystem functions are rarely measured [179–182], although they are sensitive indicators of ecosystems health [183] and losses of biodiversity [184]. Ecosystem functions are the aggregation of multiple processes that overall define the ecosystems capacity to bring benefits to a range of species [176, 185]. Among these components is Primary Productivity (PP). PP can be categorized into Gross Primary Production (GPP), the total amount of carbon or energy captured by plants and Net Primary Production (NPP), the carbon allocated to plant tissue after accounting for the costs of autotrophic respiration. PP is a process that underpins most of the ecosystem functions essential for the understanding of the global carbon cycle [35]. Due to its relevance in the characterization of biodiversity change, PP is considered an Essential Biodiversity Variable (EBV). EBVs are defined as the derived measurements to study and manage biodi-

versity change, and their estimation is a step forward for integral monitoring programs and holistic health assessments in ecosystems [37, 38].

PP has been widely related to the Vegetation Indexes (VIs), used as a proxy for vegetation productivity and to create long-term and consistent data series. Since their first use in the early 1970s, VIs have evolved rapidly together with the increased number of spectral bands of the sensors and the new demand for measuring specific ecological indicators [34]. Particularly, the Normalized Difference Vegetation Index (NDVI) and the Enhanced Vegetation Index (EVI) have been widely used for the monitoring of primary productivity. Empirical models linking the NDVI and EVI with GPP or NPP in situ observations have shown accurate NDVI-GPP correlation in low biomass vegetation areas [176, 186] and good performance of the EVI in high biomass vegetated areas such as dense grass or forest ecosystems [187, 188]. Additional VIs have also been investigated, as the two-band Enhanced Vegetation Index (EVI2) used by Cai et al. to assess the relationship between the EVI2, meteorological variables, and GPP within the Nordic region [189]. A recently suggested vegetation index, the Near-Infrared Reflectance of terrestrial vegetation (NIRv) [190] has also shown high correlation with GPP across different ecosystems [191, 192] and temporal scale [193, 194]. Recent outcomes in research suggest that given that GPP is not only connected to the greenest of vegetation, but also to other processes such as temperature or water content of leaves, different VIs sensitive to these factors need to be evaluated in carbon fluxes studies [195]. Moreover, since specific VIs are more sensitive to particular ecosystems, a broader analysis for the selection of a specific VI depending on the study region is required for a better model formulation [196–198].

Currently, remote sensing-based global products of PP are provided by the National Aeronautics and Space Administration (NASA) through the Moderate Resolution Imaging Spectroradiometer (MODIS) sensor. This product, known as MOD17 product, provides estimates of GPP on an 8-days basis, aggregated to annual products to compute NPP, with a spatial resolution of 250 m, 500 m and 1km. MOD17, designed to provide an accurate regular measure of terrestrial vegetation growth, has been available since the mid-2000s [199–202]. Although MOD17 product is widely utilized, its use and applicability in conservation and management practice are limited by the trade-off between its temporal resolution, spatial resolution, and spatial extent [199, 203, 204]. MOD17 coarse spatial resolution (1km) does not provide sufficient relevant information to monitor processes at a fine-local scale and represents a critical factor for carbon flux estimation, especially in heterogeneous landscapes [205, 206]. Additionally, MOD17 GPP products are estimated by means of biome-specific parameters, parametrized and applied to biomes at a global scale [199]. While this simplification is suitable for global estimations of GPP, the coarse inputs and the use of global Biome Parameter Look-up Table (BPLUT) parameters reduce the capacity of MOD17 to describe ecologically significant variation at finer scales [199, 201, 207, 208].

Different authors have identified the Copernicus Sentinel-2 multispectral instrument (MSI) as a potential sensor capable to improve the estimation of PP at a local scale, given its higher spatial resolution (10 m, 20 m, and 60 m). Pettorelli et al. [35] listed several potential applications of Sentinel-2 sensors, including the generation of indicators of vegetation phenology, fire damage extent, defoliator control, habitat extent, habitat quality,

production of biomass, etc. According to Cai et al. [189], Sentinel-2 data can better capture the spatial variation in heterogeneous landscapes in comparison to MOD17 products and enable the estimation of GPP at finer scales. Lin et al. [197] have shown that the narrow red bands from Sentinel-2 sensors enhance the GPP estimations, increasing the accuracy of the empirical relationship between remote sensing-based VIs and GPP which is influenced by the spectral resolution of the satellite products.

To provide information on ecosystems and biodiversity status, this study builds on the methodology proposed by Cai et al. [189] and further investigates the use of Sentinel-2 MSI in modelling GPP. The methodology of Cai et al. is extended to evaluate not only several EVs but also multiple VIs, therefore assessing the sensitivity of specific bands to the climate conditions and vegetation characteristics of the studied area. Eight Sentinel-2 derived VIs are integrated with in situ measurements of different EVs; their relation with ground-based GPP is investigated to select a model with the highest accuracy. A robust empirical approach employed by Cai et al. that follows previous researches [209, 210] is adopted. Additionally, a methodology is implemented to upscale the model across larger areas. This upscaling methodology relies on an unsupervised classification algorithm used to identify regions with similar reflectance properties to those within the eddy covariance (EC) area. Those regions are assumed to have vegetation with similar biophysical properties and photosynthesis activity. The study methodology is demonstrated at the case study in a marshland ecosystem located in Doñana National Park, Spain. High resolution maps of GPP at local scale are provided to support conservation and restoration practices, policy, and decision making. The integration of multiple remotely sensed indices and additional environmental variables (EVs) allows our workflow to be flexible, facilitating its uptake to different ecosystems.

4.2. Materials and Methods

4.2.1. Study Area

The workflow is implemented in a wetland ecosystem located in Doñana National Park, situated in southwest Spain (Figure 4.1). The Doñana National Park (DNP), with an extension of 537 km^2, is a UNESCO Biosphere Reserve and a Natural Heritage and a Ramsar site [8]. It shelters the largest wetland in Western Europe, composed of a complex environment of marshlands and dune ponds (270 km^2) enclosed by Mediterranean scrubland, pine forests, a dune ecosystem, and cultivated areas [211]. This study focuses on the areas dominated by salt marsh bulrush (*Bolboschoenus maritimus*).

The wetlands of the Doñana National Park are essential for the conservation of biodiversity and the provision of ecosystem services [211–213]. Regardless of their importance, the area has experienced numberless threats associated with ecological disasters, both due to anthropogenic pressure [214, 215] and exceptional weather conditions [216], diversion of water and overexploitation of groundwater for agricultural purposes, and land-use changes [211, 217, 218]. These activities have affected both the water quantity and quality available to the marsh and dune pond ecosystems [219, 220]. Previous research predicted exacerbation of the problems due to climate change in the absence of better management of the water resources in the catchment and the aquifer [219]. The need for monitoring activities in the region is, therefore, crucial.

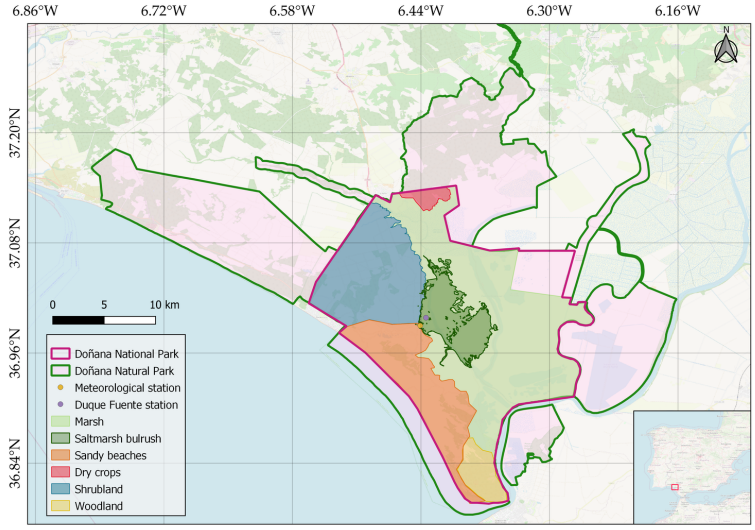

Figure 4.1.: Protected boundaries of Doñana Natural Park and Doñana National Park in southwestern Spain, together with the distribution of its major habitats.

4.2.2. Materials

Doñanas Singular Scientific-Technical Infrastructure (ICTS-RBD) provided data access and support to carry out the case study at the Doñana Protected Areas. The in situ monitoring infrastructure operated by the ICTS-RBD consists of an eddy covariance tower, the "Duque Fuente flux tower" and a meteorological station, named the "Palacio Doñana station". The location of both the station and the tower is displayed in Figure 4.1.

The eddy covariance data set consisted of 30-minutes measurements of Net Ecosystem Exchange (NEE) and ancillary meteorological data collected between 1 October 2020 and 8 June 2021. The meteorological data set from "Palacio Donana station" consisted of daily estimations of multiple environmental variables of the region, including daily cumulative precipitation and average temperature collected between 1976 and 2021. Table 4.1 and Table 4.2 display the data and metadata available in the ICTS-RBD monitoring system respectively.

To differentiate the night periods for the NEE data processing, the Global Radiation data set (SW_IN) was retrieved from the Surface Solar Radiation Data Set - Heliosat (SARAH) data records provided by the European Organisation for the Exploitation of Meteorological Satellites (EUMETSAT) Climate Monitoring Satellite Application Facility (CM SAF). The SW_IN records were available for the years 2005 to 2016; therefore, we assumed that the global radiation data for 2020 and 2021 were equal to the daily average value of solar radiation for the years 2005 to 2016. Night periods were identified by using a threshold of $20 W m^{-2}$.

Additionally, meteorological precipitation data were retrieved from a global data set to assess the capacity of these products to compute the study workflow and supply sites

Table 4.1.: Data collected from the ICTS-RBD monitoring system.

Data	Time range	Description	Variable	Unit
Eddy covariance data	01/10/2020 - 08/06/2021	Preprocessed eddy covariance measurements. Corrected 30-minute estimations of gas analyzer and anemometer data.	CO_2 flux	$\mu mol\, m^{-2}\, s^{-1}$
			Quality flag CO_2 flux	-
			Air temperature	K
			Relative humidity	%
			Vapour pressure deficit	Pa
			Friction velocity	ms^{-1}
			Monin-Obukhov length	m
			Wind speed	ms^{-1}
			Maximum wind speed	ms^{-1}
			Wind direction	°
			Variance of wind component along the v anemometer axis	ms^{-1}
Meteorological data	01/09/1976 - 31/10/2021	Daily estimations of meteorological data from analogic instruments.	Rainfall	mm
			Maximum temperature	°C
			Minimum temperature	°C
			Mean temperature	°C
			Thermal oscillation	°C

Table 4.2.: Metadata of the ICTS-RBD monitoring system.

Station	Variable	Value
Duque Fuente flux tower	Location	36.9985N, -6.4345E
	Canopy height	0.7 m
	Displacement height	0.2 m
	Roughness length	-
	Anemometer sensor height	3.95 m
	Gas analyser sensor height	4.03 m
	Tower fetch	375 m
	Anemometer sensor type	Gill HS-50
	Gas analyser sensortype	LI-700 Enclosed CO_2/H_2O analyser
Palacio Doñana meteorological station	Location	$36.9905N, -6.4426E$
	Sensor type	Manual analogic instruments

lacking daily measurements of meteorological variables. Daily measurements of precipitation were collected from the Climate Hazards Group InfraRed Precipitation with Station data (CHIRPS) database (https://www.chc.ucsb.edu/data/chirps, accessed in May 2026) at the Duque Fuente tower location. ICTS-RBD also provided the vegetation map of the wetlands of Doñana. The latest was used to qualitatively assess the results of our unsupervised classification, used to upscale the outputs of the model beyond the climatological footprint. The 2009 vegetation map was previously computed

using supervised classification approaches by the ICTS-RBD.

Remote Sensing Imagery

For this study, Level-2A Sentinel-2 (S2) products were used. Images were accessed through the Google Earth Engine (GEE) data catalogue "COPERNICUS/S2_SR" by means of the python client *"ee"* package (https://gee-python-api.readthedocs.io/en/latest/ee.html, accessed in May 2026). All images available in the region of interest were collected; these correspond to the tiles T29SQA and T29SQB Figure 4.2. Images with high cloud coverage were removed. The cloud coverage threshold was set at 30%. Specific treatment was applied afterward to remove remaining pixels with high cloud coverage and not belonging to vegetation (e.g., water bodies, snow, temporal floods, or other temporal phenomena). The cloud mask was applied to the images using the Scene Classification Map (SCL) and the supplementary band QA60. The SCL allows tracing or marking defective pixels, whereas the QA60 band helps distinguish between opaque and cirrus clouds (https://sentiwiki.copernicus.eu/web/s2-processing, accessed in May 2026).

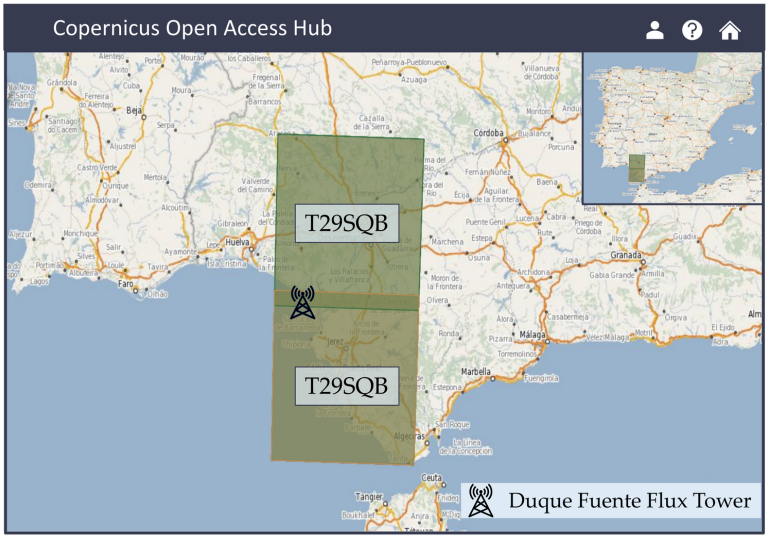

Figure 4.2.: Tiles of Sentinel-2 products over the study area of Doñana National Park. Image retrieved from the Copernicus Open Access Hub.

To remove flooded pixels, at first, we applied the water mask of the SCL on the images, however, the mask also covered and removed flooded regions with standing vegetation or biomass contributing to the GPP of the ecosystems. Previous research estimating PP through correlation with satellite-derived VI suggested removing the influence of water pixels at Doñana National Park by selecting a threshold corresponding to the baseline of the phenological curve [221]. Kordelas et al. [222] suggested the use of the Modified Normalized Difference Vegetation Index (MNDVI) to identify vegetation in the flooded

area of Doñana National Park, preferred over the Normalized Difference Vegetation Index (NDVI) which created false positives in areas where vegetation was not expected. For this reason, we decided to filter the water pixels by defining a threshold of the MNDVI. A baseline of MNDVI = 0.1, corresponding to the minimum reflectance observed in the vegetation throughout the year was found. A threshold of 0.05 was then selected to identify and remove water pixels (MNDVI<0.05) not contributing to the GPP of the ecosystem. Table 4.3 displays the number of images for each tile for different cloud coverage thresholds and months during the period of analysis. All available images from the 1 October 2020 to 8 June 2021 with cloud coverage lower than 30% were used for the computation of the workflow.

Table 4.3.: Available Sentinel-2 images from October 2020 to June 2021 for different cloud coverage.

Month	< 100%		<50%		<30%	
	T29SQA	T29SQB	T29SQA	T29SQB	T29SQA	T29SQB
10-2020	6	6	6	5	5	3
11-2020	6	6	5	4	4	5
12-2020	6	6	4	5	4	4
01-2021	7	7	4	4	3	3
02-2021	5	5	1	1	1	1
03-2021	6	6	4	6	4	6
04-2021	6	6	2	1	2	0
05-2021	8	8	7	7	5	5
06-2021	6	6	5	4	3	3
Total	56	56	38	37	31	30

Together with the Sentinel-2 images, MOD17 products were also retrieved from the GEE catalog for the same period (1 October 2020 to 8 June 2021). This data set was used to compare the Sentinel-2-based GPP results with the MOD17 products and analyze their performance in comparison with in situ measurements.

4.2.3. Methods

The research workflow is schematized in Figure 4.3. It consists of eight main processes: (1) derivation of in situ GPP daily measurements from NEE measurements; (2) estimation of the climatological footprint; (3) computation of the VIs time series within the climatological footprint; (4) computation of time series of all the environmental/meteorological variables; (5) interdependency analysis between in situ GPP and the VIs-EVs and model formulation; (6) calibration and validation of the model; (7) unsupervised classification of the area to select an upscaling region; (8) computation of GPP maps. The details of each process are provided in the sections below.

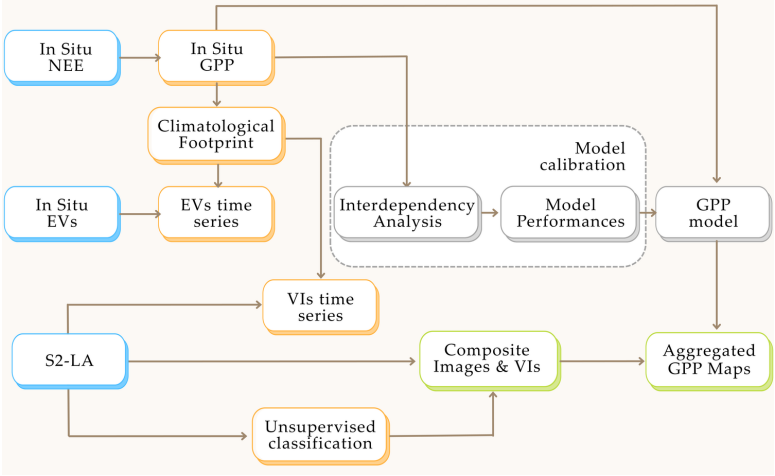

Figure 4.3.: Schematization of methodology with details of data requirements (blue), data preprocessing (yellow), modeling processing (gray), and post-process and workflow outputs (green).

In Situ Time Series of GPP

In situ measurements of NEE were used to derive the time series of GPP. NEE is measured at the Duque Fuente flux tower (Figure 4.1) by means of the Eddy Covariance (EC) technique, a method to ascertain the exchange rate of carbon dioxide in ecosystems [223]. We processed the 30-minute NEE records following the standardized processing methodology proposed by Papale et al. [223] and using the ancillary meteorological data of the EC system. The methodology included four steps aiming at correcting the data and estimating the GPP: (1) outlier detection, (2) velocity friction filtering, (3) carbon fluxes partitioning to derive GPP, and (4) gap filling using ancillary environmental data. The estimates were finally aggregated to derive daily values of GPP (in $gCm^{-2}d^{-1}$) used in the model calibration and validation. For a detailed description of the steps, refer to the paper by Papale et al. [223]. The aforementioned process was implemented through the "hesseflux" Python package [224] adapted to process the European Fluxes Database Cluster (EFDC) format files (`http://www.europe-fluxdata.eu`, accessed in May 2026). Full documentation of the hesseflux package is available at `https://mcuntz.github.io/hesseflux/` (accessed in May 2026). In the context of the study case, we adopted a velocity friction filtering threshold of 0.14, as previously done for salt marshes [225], since the threshold could not be automatically computed because of the lack of full-year measurements.

Climatological Foortprint

To better interpret flux tower measurements, flux footprint models have been used to estimate the size and position of the surface area contributing to the measured flux [226]. The knowledge of this area, also known as flux footprint, is of extreme importance in

upscaling the model from a single site flux measurement to an ecosystem or regional scale. Wind and turbulence conditions, atmospheric conditions and surface characteristics contribute to the flux measured at a specific point in time. To estimate the flux footprint, we used the Flux Footprint Prediction (FFP) model of Kljun et al. [226] available in Python code (https://geography.swansea.ac.uk/nkljun/ffp/www/, accessed in May 2026). We derived two aggregated footprints, also known as footprint climatology, three months of half-hourly input data for 2020 (October to December 2020), and six months of half-hourly input data for 2021 (January to July 2021). Most of the input variables required for the FFP model were collected as part of the EC system at the Duque Fuente flux tower. The variables included mean wind speed, measurement height above displacement height, equal to the anemometer sensor height minus the displacement height (3.75 m), the Obukhov length, the standard deviation of lateral velocity fluctuations, and the friction velocity. The boundary layer height was estimated with the expressions described by Kljun et al. [226] for atmospheric near-neutral and stable conditions and here reported for completeness:

$$h = \frac{L}{3.8}\left[-1+\left(1+2.28\frac{u_*}{fL}\right)^{0.5}\right] \tag{4.1}$$

where L is the Obukhov length, u_* is the friction velocity and f is the Coriolis parameter calculated using the sites latitude. The boundary layer is set to be at 1500 m at convective conditions defined as records in the eddy covariance data set when Obukhov length < 10 m [227]. The FFP model was computed to derive 20%, 40%, 60%, and 80% isolines. The 100% was not calculated with the FFP model but set as the fetch of the Duque Fuente tower according to the 1:100 displacement height-fetch ratio [228]. The derived footprints can be seen in Figure 4.4. The climatological footprints did not differ significantly in shape and size, having a surface of 5.72 and 5.30 ha within the 80% contour lines for 2020 and 2021, respectively.

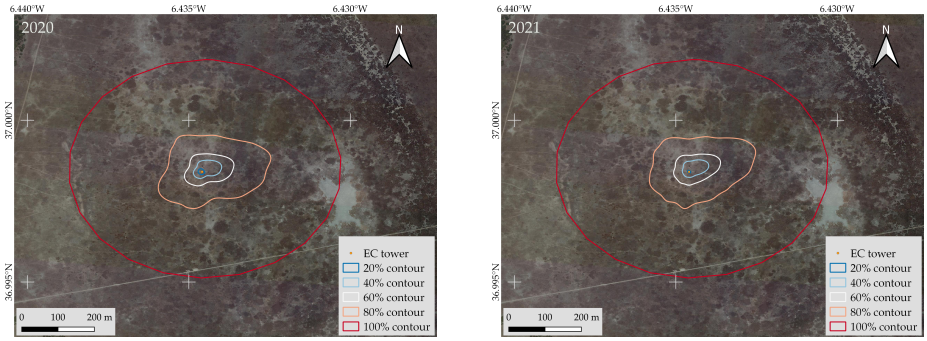

Figure 4.4.: Climatological footprint of 2020 (left image) and 2021 (right image).

Time Series of Vegetation Index

The filtered and masked Sentinel-2 images were post-processed to calculate multiple VIs. Table A.1 lists the VIs employed in this research together with their equations. In

total, eight VIs were computed per image and selected based on a literature review of GPP modeling for different ecosystem types. Those VIs can be divided into two major classes: (i) greenness-sensitive VIs (Normalized Difference Vegetation Index (NDVI), Enhanced Vegetation Index (EVI), Two-bands Enhanced Vegetation Index (EVI-2), Red-edge Index (CL_r), Modified Normalized Difference Vegetation Index (MNDVI)), and (ii) water-sensitive VIs (the Modified Normalized Difference Water Index (MNDWI), Land Surface Water Index (LSWI), and Normalized Difference Infrared Index (NDII)). At first, we calculated the VI for each region within the climatological footprint, then we averaged them by a scaling factor. Finally, the total VI was computed as the sum of the VIs as:

$$VI = \sum_{j=1}^{k} \left[w_j \times \sum_{i=1}^{n} VI_i \right] \tag{4.2}$$

where i is the number of pixels, j is the number of regions, and wj is the weight of the j region calculated as:

$$w_j = \frac{OCL_j - ICL_j}{n_i} \tag{4.3}$$

being OCL_j and ICL_j the outside and inner contour lines of the region j, respectively. With our approach, the weight is a constant value per region. This is a simplification of Cai et al.s approach [189] that reduces the computational time of the calculation of the VIs. For our study, we computed five regions within the climatological footprint, each of them accounting for 20% of the NEE measured at the Duque Fuente flux tower. Finally, we used the Akima [229] fitting algorithms to obtain a continuous time series. Fitting algorithms were not implemented as we addressed the noise in the time series through the filtering and masking processes of the satellite images. Figure 4.5 summarizes the processing chain applied to the Sentinel-2 images to obtain the VIs time series (preprocessing steps have been described in Section 4.2.2.

Environmental Variables

PP is driven by several environmental drivers [200], therefore our model formulation integrates different EVs. In this research, we integrated the Air Temperature (AT), the Vapour Pressure Deficit (VPD) both retrieved from the EC tower and the temperature data provided by the meteorological station of the Doñana National Park (Table 4.4). Those EVs were smoothed with a 7-day moving average window to reduce the noise in the time series.

Additionally, we integrated precipitation data from in situ measurements and from the CHIRPS data set as a proxy for the ecosystem water availability. Water stress has been indeed identified as one of the main limiting environmental conditions of PP [175, 230]. Particularly for the studied areas, the water availability is mainly regulated by rainfall events [221, 231, 232]. Precipitation, however, was not expected to have an immediate impact on the PP but rather the water accumulated in the system. Therefore, to account for the long-term soil moisture repletion process, we shifted the rainfall time series in

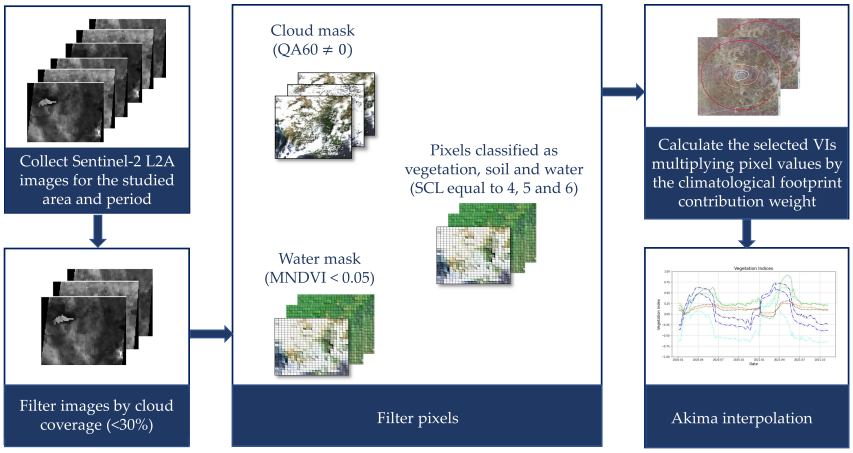

Figure 4.5.: Schematization of the processing chain applied to the Sentinel-2 images to obtain the VIs time series. At first, S2 L2A images (with orthorectification and atmospheric correction) are collected and filtered by cloud coverage (<30%). Then, pixels are filtered using (i) the supplementary band QA60 to mask the clouds; (ii) the SCL band to select pixels classified as vegetation, soil and water, and (iii) a water mask to remove flooded pixels without standing vegetation (MNDVI < 0.05). Finally, the VI is calculated for each pixel within the climatological footprint, multiplied by its contribution weight and summed to obtain the final VI, a single value of VI per image per day. The Akima fitting algorithm is then applied to fill in the gaps and obtain a continuous time series.

time, delaying the precipitation. Different time lags were considered. Moreover, the rainfall data were smoothed with a multiple moving average window to reduce the noise in the time series. Table 4.4 displays the environmental variables used in the study.

Interdependence Analysis and Model Calibration

An analysis of interdependence was performed to assess the correlation between the calculated in situ GPP and the set of all the possible combinations of VI × EV. The squared Pearson correlation coefficient (r^2) was used to identify the product (VI × EV) with the highest correlation selected for the final model formulation. The latest followed the linear formulation suggested by Schubert et al. [209] and used by Cai et al. [189] reported in the following equation:

$$GPP = m \times (VI \times EV) + b \tag{4.4}$$

where m and b are slope and intercept parameters of the linear regression model, respectively. The Ordinary Least Squares (OLS) method was used to compute the parameters of the regression model. The OLS method is a statistical analysis aiming at deriv-

Table 4.4.: Available Sentinel-2 images from October 2020 to June 2021 for different cloud coverage. *f stands for measurements collected at the flux tower. **N represents 0, 7, 15, 30, 60, 90, 120, 150 or 180-days delays in precipitation data.

Variable	Units	Description
AT_MAX	°C	Maximum temperature
AT_MIN	°C	Minimum temperature
AT_MEAN	°C	Daily mean of temperature
AT_OSC	°C	Daily thermal oscillation
AT_MEAN_f*	°C	Daily mean of temperature (flux tower)
VPD_MEAN_f	Pa	Daily mean of vapour pressure deficit (flux tower)
RAIN	mm	Daily rainfall
RAIN_7	mm	7-day rainfall average
RAIN_15	mm	15-day rainfall average
RAIN_30	mm	30-day rainfall average
RAIN_60	mm	60-day rainfall average
RAIN_90	mm	90-day rainfall average
RAIN_7_N**	mm	7-day rainfall average with N-day lag
RAIN_15_N	mm	15-day rainfall average with N-day lag
RAIN_30_N	mm	30-day rainfall average with N-day lag
RAIN_60_N	mm	60-day rainfall average with N-day lag
RAIN_90_N	mm	90-day rainfall average with N-day lag
RAIN_C	mm	Daily CHIRPS rainfall
RAIN_C_7_N	mm	7-day CHIRPS rainfall rolling average with N-day lag
RAIN_C_15_N	mm	15-day CHIRPS rainfall rolling average with N-day lag
RAIN_C_30_N	mm	30-day CHIRPS rainfall rolling average with N-day lag
RAIN_C_60_N	mm	60-day CHIRPS rainfall rolling average with N-day lag
RAIN_C_90_N	mm	90-day CHIRPS rainfall rolling average with N-day lag

ing the m and b parameters of a linear model by minimizing the sum of squared errors, where the errors are the differences between the observed and predicted dependent variables. The m and b linear regression parameters were calculated using the OSL method with the following expressions:

$$m = \frac{n\sum xy - \sum x \sum y}{n\sum x^2 - \left(\sum x\right)^2} \tag{4.5}$$

$$b = \frac{n\sum x^2 \sum y - \sum x \sum xy}{n\sum x^2 - \left(\sum x\right)^2} \tag{4.6}$$

where y is the independent variable (GPP), x is the dependent variable (VI × EV), and n is the number of data pairs. The estimation of the parameters was performed with a data set consisting of 80% of the original samples of in situ GPP. The statistical significance of

the linear parameters and the overall model was evaluated with a confidence level of 95% (p-value < 0.05). In the case that statistical significance was achieved, the model was accepted and used in the validation process.

Model Validation

The model was validated with an independent data set corresponding to 20% of the data. The validation data set was used to generate GPP predictions ($GPP_{predicted}$). The predictions were compared with the flux-derived GPP ($GPP_{observation}$). The performances of the model were estimated in terms of Mean Absolute Error (MAE, equation 4.7), Root Mean Squared Error (RMSE, equation 4.8), and relative standard error of the estimates (S_{est}, equation 4.9). The coefficient of determination (R^2) between predicted and measured GPP was also calculated to evaluate to which extent the model explains the variance of the GPP.

$$MAE = \frac{|GPP_{predicted} - GPP_{observation}|}{n} \tag{4.7}$$

$$RMSE = \sqrt{\frac{\sum \left(GPP_{predicted} - GPP_{observation}\right)^2}{n}} \tag{4.8}$$

$$S_{est} = \sqrt{\frac{\frac{\sum \left(GPP_{predicted} - GPP_{observation}\right)^2}{n-2}}{\frac{\sum GPP_{observation}}{n}}} \tag{4.9}$$

where $GPP_{observation}$ is the in situ GPP retrieved from the eddy covariance measurements, $GPP_{predicted}$ is the GPP derived with the empirical formulation, and n is the number of observations in the validation data set.

Vegetation Classification Maps

In order to observe the spatial pattern of GPP, the model was upscaled to the surrounding areas of the eddy covariance tower. An unsupervised classification algorithm was used to identify regions with the same land cover (reflectance properties) as those identified within the flux footprint. The identified regions were assumed to have homogeneous vegetation with similar biophysical properties, photosynthesis activity and GPP seasonality to those within the footprint. The unsupervised classification was performed on a composite image created by using all the Sentinel-2 images available for the study period, preprocessed as described in Section 4.2.2. The k-means clustering algorithm developed by Arthur and Vassilvitskii [81] was used to perform the unsupervised classification and implemented through the Clusterer.wekaKMeans method of the “ee” package in python. The algorithm minimizes the average squared distance between the points in the same cluster. The use of this robust unsupervised clustering method helps overcome the need for expert human knowledge required for supervised classification and has already been used in similar studies [233–235]. Our area of study was classified into seven classes using 5000 training pixels with a scale of 10 m retrieved from the study area.

GPP Maps with Composite Images

Once the vegetation classification map was obtained, the model was applied to the regions having the same land cover as the area within the climatological footprint. By doing so, we produced GPP maps for each Sentinel-2 available image. Then, we aggregated the obtained maps to produce an estimate of the monthly/annual GPP. The latest is indeed a highly important product relevant for further analysis of the ecosystems status. Annual maps of GPP are useful for trend analysis, the identification of the degradation of the ecosystem functions, and for computing annual NPP if knowledge of the autotrophic respiration processes of the ecosystem is known [199, 200]. To create an operational monitoring tool easy to implement by stakeholders and policymakers that bypasses the limitations of cloudy satellite data, we propose a simplified model for the calculation of GPP for a specified time window. Aggregated products of GPP are computed as:

$$GPP = \sum_{i=1}^{n} GPP_i = \sum_{i=1}^{n} \left(m \times \left(VI_i \times EV_i\right) + b\right) \tag{4.10}$$

where n is the number of days within the time window, and m and b are the model parameters, and therefore, constant. Assuming that the VI is constant within the selected time window ($VI_i = VI$), equation 4.10 can be written as:

$$GPP = m \times VI_i \sum_{i=1}^{n} \left(EV_i\right) + b \times n \tag{4.11}$$

The model formulation (equation 4.11) is susceptible to high deviation if the assumption cannot be guaranteed. In this research, we propose to work with a 30-day time window; however, we also applied a 15-day time window to compare the benefits of increasing the frequency of the map generation. The GPP products are finally aggregated to derive a GPP map for the full period of analysis.

4.3. Results

4.3.1. Interdependency Analysis and Model Calibration

The interdependency analysis between the in situ GPP and VIs showed that greenness-sensitive VIs derived the highest coefficients of determination. The CL_r resulted in the highest correlation with GPP, with a coefficient of determination $R^2 = 0.90$ and statistical significance $p < 0.05$. The NDVI showed the lowest correlation among the greenness-related VIs with $R^2 = 0.57$. Water-sensitive vegetation indices did not show a high correlation with the GPP measurements. Among those, the NDII had the highest R^2 of 0.39 and a significance level of $p < 0.05$. Table 4.5 summarizes the results of the interdependency analysis, obtained using only SRS VIs.

By including the EV in the model formulation, we observed an increase in the correlation with in situ GPP. In total 784 models (VI × EV) were analyzed and the coefficient of determination was acquired for all the models. In general, the VIs showed a higher correlation when combined with rainfall-related variables in contrast with temperature or vapor pressure deficit data. The first fifty VIs and environmental variables combinations with higher correlation are displayed in Table A.2. The product between the CL_r

Table 4.5.: Coefficient of determination between different VIs and in situ GPP.

Vegetation Index	R^2
CL_r	0.904
MNDVI	0.899
EVI2	0.853
EVI	0.853
NDVI	0.576
NDII	0.358
LSWI	0.329
MNDWI	0.189

4

and the rainfall data calculated with a rolling average of 90 days and delay of five months ($RAIN_{90\_150}$) yielded the strongest correlation with an R^2 of 0.93. We, therefore, selected the CL_r and the $RAIN_{90\_150}$ for the model formulation, which resulted in:

$$GPP = m\big(CL_r \times RAIN_{90\_150}\big) + b \tag{4.12}$$

where m and b represent the slope and intercept parameters of the linear model, estimated by means of the OLS method. The summary of the calibration process, including the parameter values and their corresponding significance levels, is displayed in Table 4.6.

Table 4.6.: Summary of model fit using the linear least-squared method from Statsmodels python tool. The table shows the coefficients of the linear model and their statistical significance.

	Coef.	Std Err	t	P > |t|	0.025	0.975
Intercept	0.331	0.061	5.420	0	0.210	0.451
CL_r × $RAIN\_90\_150$	3.374	0.065	52.017	0	3.246	3.502

From the calibration process, an offset parameter b = 0.3308 and a scale parameter m = 3.3743 were derived. The final linear model for GPP prediction was, therefore, formulated as follows:

$$GPP_{model} = 3.3746\big(CL_r \times RAIN_{90\_150}\big) + 0.3308 \tag{4.13}$$

The scatter plot between the observed GPP values and the estimated ones is shown in Figure 4.6 together with the 95% confidence interval. It can be seen that the model performances were accurate, with most of the points within the prediction interval.

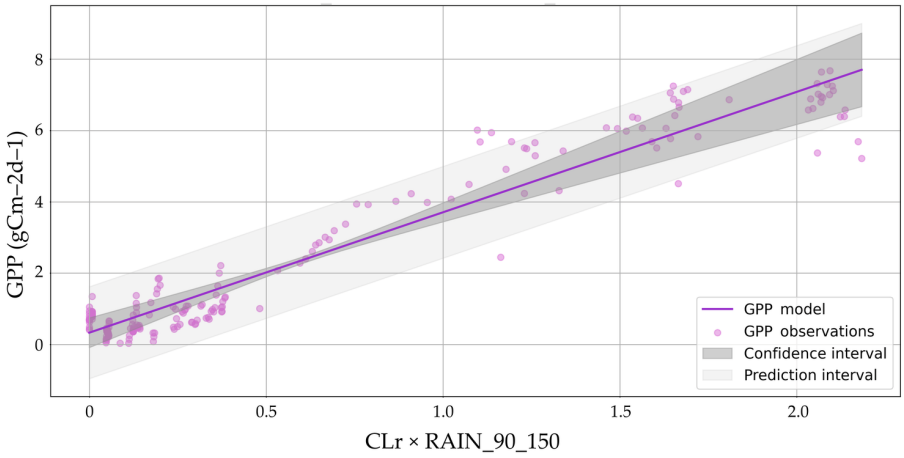

Figure 4.6.: Scatter plot and corresponding regression line and 95% confidence interval for the relationship between the GPP calculated as the product between the Red-edge index (CL_r) and the rainfall data calculated with a rolling average of 90 days and delay of five months ($RAIN_{90\_150}$) and the ground measurements of GPP.

4.3.2. Model Validation

The calibrated model was used to predict GPP ($GPP_{predicted}$). The results were compared with an independent validation data set corresponding to 20% of the original GPP sample ($GPP_{observed}$). The model resulted in an MAE of 0.52 $gCm^{-2}d^{-1}$, RMSE of 0.63 $gCm^{-2}d^{-1}$ and S_{est} equal to 0.27. The latest indicated that the model predictions had a standard deviation of 27% with respect to the GPP observations. The scatterplot of observed versus estimated values of GPP for the validation phase (Figure 4.7) shows that the slope of the predicted-observed relationship did not differ significantly from 1 (0.97), indicating that the model predictions neither under- nor overestimated the observed values of GPP.

Comparison with MOD17 Products

To evaluate our model performance in comparison with existing satellite-based products, we produced time series of MOD17. At first, we compared in situ GPP and the MOD17 1 km 8-day GPP products. From the scatter plot in Figure 4.8, we can observe that the slope of the predicted-observed relationship of the MOD17 product is higher than 1 (1.62), indicating that the MODIS model is underestimating the ground GPP.

Then, we compared both our model and the MOD17-based time series with in situ measurements of GPP. Both the MOD17 and our GPP products showed a general agreement with the observed data, especially during the fall and winter months when low primary productivity was observed (October 2020 to February 2020). For the months with a peak of GPP (April 2021 to June 2021), our simulated GPP performed better than the

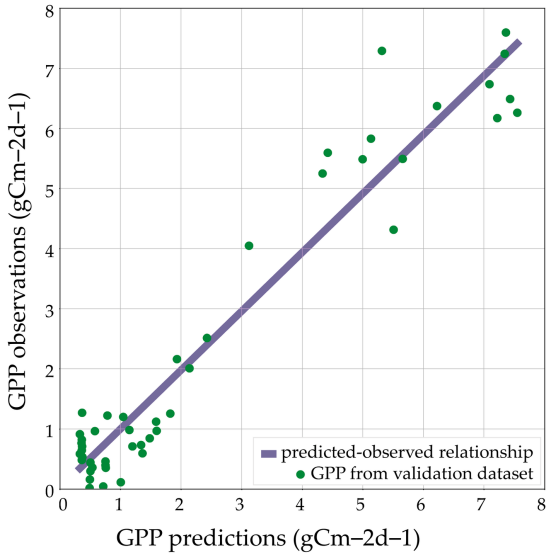

Figure 4.7.: Scatter plot with fitted regression line showing the correlation between the predicted GPP values (x-axis) obtained by our model and the observed GPP values (y-axis).

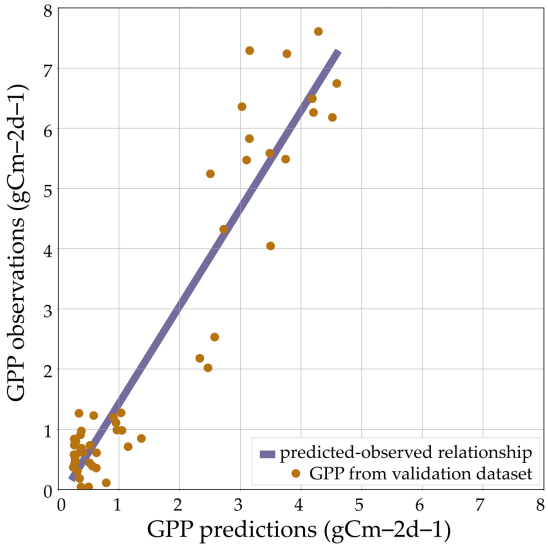

Figure 4.8.: Scatter plot with fitted regression line showing the correlation between the predicted GPP MOD17 predictions (x-axis) and the observed GPP values (y-axis).

MOD17 product, which was underestimating the observed GPP measurements (Figure 4.9).

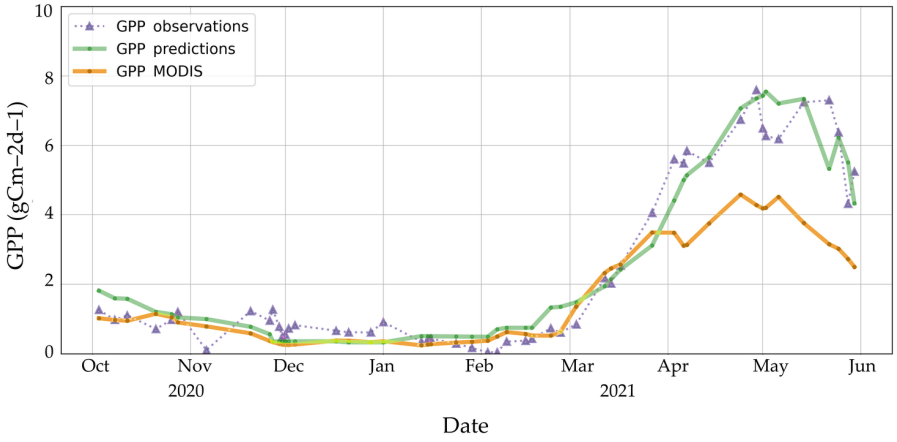

Figure 4.9.: Time series of our model GPP predictions, MOD17 GPP prediction and in situ measurements of GPP.

A comparison of the two models in terms of MAE, RMSE, and S_{est} is presented in Table 4.7. While having a high correlation with flux-derived GPP, the MOD17 products presented higher prediction standard errors due to the high underestimation of the GPP during the peak biomass, suggesting that the calibration of the MOD17 products should be performed together with the investigation of the sampling procedure that can ensure that collected ground measurements are adequately representative and sufficient to validate the target low resolution EO product.

Table 4.7.: Summary of our model and MOD17 GPP product errors.

	MAE [$gCm^{-2}d^{-1}$]	RMSE [$gCm^{-2}d^{-1}$]	S_{est}
Our model	0.52	0.63	0.27
MOD17	0.94	1.44	0.62

Vegetation Maps

The unsupervised classification of the wetlands of Doñana National Park derived seven classes displayed in Figure 4.10. Classes can be grouped into (i) vegetated areas (green areas); (ii) sand depression areas (yellow and orange areas) and (iii) flooded areas (blue areas). Visual comparison of the outcomes with different land cover classification maps of the region [211, 221, 236, 237] showed good performances of the unsupervised classification algorithm. The flux tower is located within the green zone (dense biomass area) and measures carbon fluxes from the densely vegetated areas on the west side of the wetlands (Figure 4.10).

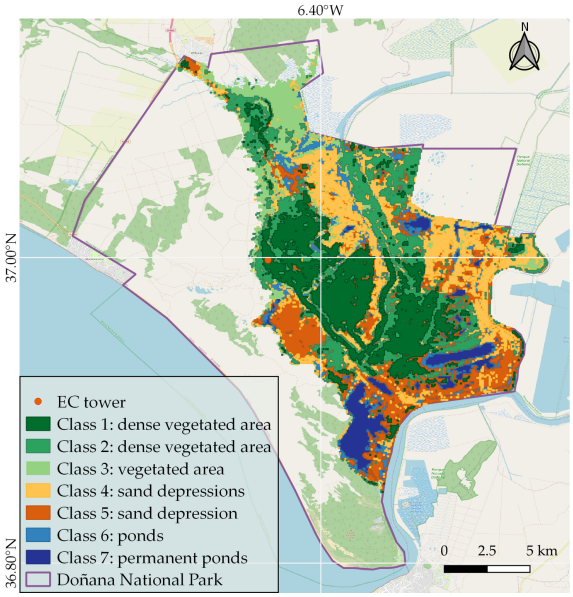

Figure 4.10.: Vegetation classification maps showing the seven classed identified by k-means algorithm implemented in Google Earth Engine API and ee python package using a Sentinel-2 Level 2A mean composite image from 1 October 2020 to 31 May 2021. Class 1 and 2 correspond to the dense vegetated area, mainly dominated by the *Cyperus rotundus*, and the *Cyperus rotundus* and *Sarcocornietea fruticosae* plants, respectively. Class 3 is a vegetated area mainly dominated by the *Cyperus rotundus*. Class 4 and 5 are sand depression areas mainly characterized by salt marshes and shrubs and salt marshes, respectively. Class 6 and 7 correspond to ponds, temporarily and permanently flooded areas, respectively.

By a visual comparison with the vegetation classification map of 2009 provided by ICTS-RBD (Figure 4.11), we could see that those green areas corresponded to the regions dominated by *Bolboschoenus maritimus* vegetation, commonly named salt marsh bulrush. The vegetated-marsh area of the Doñana National Park was also identified in 2017 by Lumberries et al. [221] (highlighted with the red line in Figure 4.11). Being one of the most recent classifications we could find in literature, we decided to adapt our model to the same region identified by Lumbierres et al. [221]. This area dominates the region surrounding the eddy covariance tower and has similar biomass production.

GPP Maps with Composite Images

The following figures display the monthly maps of GPP derived with composite images per month (Figure 4.12). The model well represented the interannual variability and trend of GPP over the study area. GPP is low during the start of the fall and winter months (October – January). At the end of the wet season, when the water availability in the

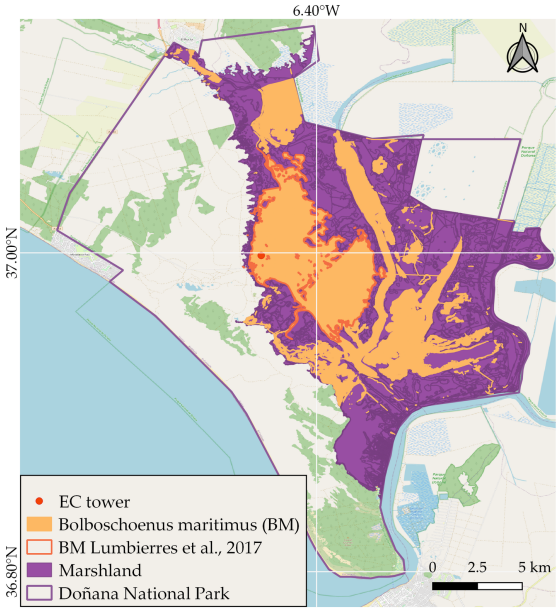

Figure 4.11.: Vegetation classification over the Doñana park for 2009 (shapefiles provided by ICTS-RBD). The *Bolboschoenus maritimus* vegetation identified in 2009 is displayed in orange. The "BM Lumbierres et al., 2017" red limited area represents the *Bolboschoenus maritimus* dominated area identified by Lumbierres et al. [221] and used in their research on biomass production. The red limited area has been adopted in our study for the estimation of GPP in the marsh area surrounding the EC tower.

ecosystem is at its maximum [221], the GPP content increases and reaches its maximum during the springtime (April – May). More spatial and temporal details of the variation of GPP can be seen in Figure A.1, where a comparison between the Sentinel-2 and MOD17-derived products obtained using a monthly composite image is presented.

The model accuracy in the selected area could not be directly assessed given the lack of in situ measurements outside the climatological footprint. Attempting to quantify the goodness of the model, we compared the predicted GPP within the footprint with the monthly carbon flux measured at the Duque Fuente flux tower (Table 4.8).

From Table 4.8, we observed that the model generally overestimates the ground measurements of GPP which varies within a range of $\pm 13 \mathrm{gCm}^{-2}\mathrm{d}^{-1}$ in comparison to the in situ measurements. A MAE equal to 9.97 $\mathrm{gCm}^{-2}\mathrm{d}^{-1}$, RMSE equal to 14.64 $\mathrm{gCm}^{-2}\mathrm{d}^{-1}$, and a S_{est} of 0.24 are found.

To improve the estimations of the GPP, we decided to reduce the time window and produce 15-day maps. Reducing the time window indeed allows for a better discretization in time and particularly accounts for the high variation of the CL_r index during the spring. Equation 4.11 assumes that the VI is constant during the months and, with high

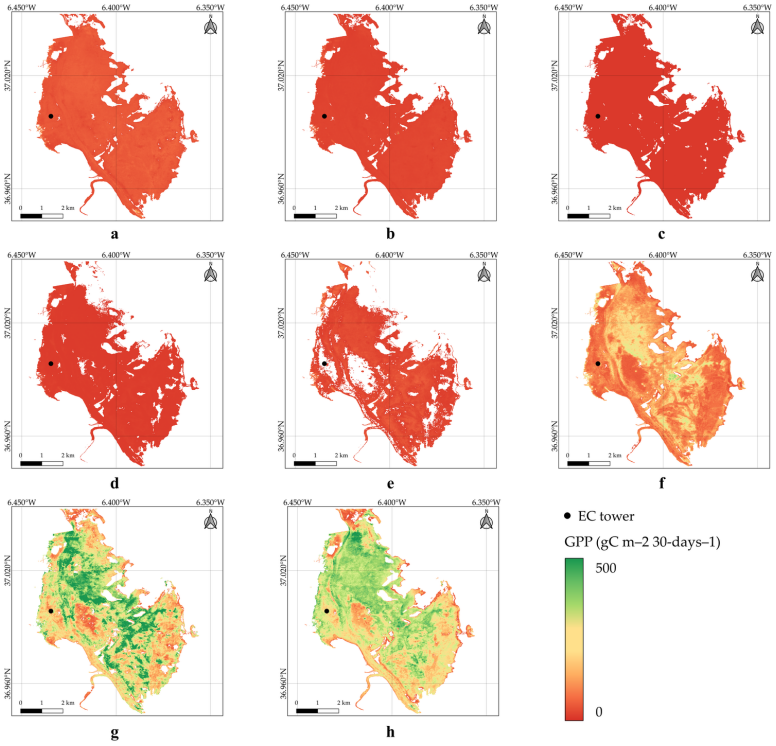

Figure 4.12.: Monthly GPP maps obtained using a single composite image per month. The maps show the spatial and temporal pattern of GPP ($gCm^{-2}d^{-1}$): (a) October 2020, (b) November 2020, (c) December 2020, (d) January 2021, (e) February 2021, (f) March 2021, (g) April 2021, (h) May 2021.

Table 4.8.: Monthly carbon fluxes retrieved from the Duque Fuente flux tower and predicted for the climatological footprint using a single monthly composite image. GPP in $gCm^{-2}d^{-1}$.

Month	GPP Flux Tower	GPP Composite Image
October	32.40	45.92
November	22.61	24.70
December	23.18	10.84
January	12.27	14.99
February	10.74	19.52
March	75.96	80.18
April	186.89	187.32
May	197.25	232.93

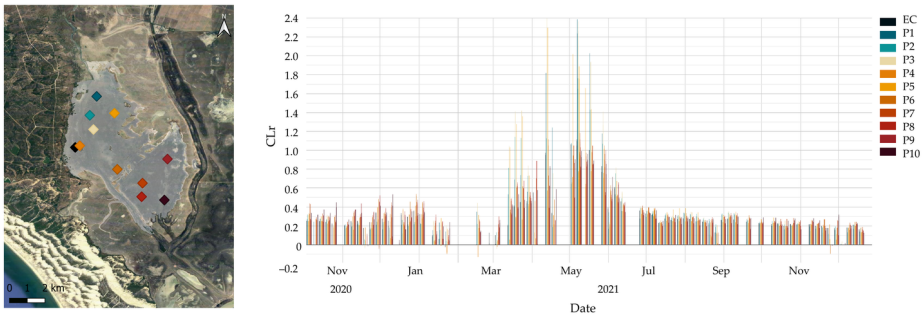

Figure 4.13.: Time series of the CL_r index for different pixels in the upscaling area (pointers) and for the eddy covariance footprint (black dot).

Table 4.9.: Monthly carbon fluxes retrieved from the Duque Fuente flux tower and predicted for the climatological footprint using a single 15-day composite image.

Month	GPP Flux Tower	GPP Composite Image
October 115	15.45	25.70
October 1631	16.96	20.54
November 115	8.96	13.88
November 1630	13.66	10.63
December 115	12.15	5.38
December 1631	11.04	5.41
January 115	6.92	7.23
January 1631	5.36	7.11
February 115	3.29	-
February 1628	7.46	-
March 115	22.01	25.86
March 1631	53.95	51.18
April 115	85.87	90.26
April 1630	101.02	-
May 115	97.93	132.93
May 1631	99.32	115.24

variation of CL_r, the GPP can be under- or overestimated. The time series of CL_r for different pixels within the studied area is shown in Figure 4.13. GPP maps were, therefore, retrieved for the entire period using a 15-days composite image. The resulting maps are displayed in the figures below (Figure 4.14 and Figure 4.15).

The production of maps using 15-day composite images was affected by the high cloud coverage over the study area. This phenomenon can be clearly observed in the maps produced for the second half of February and April 2021. This hampered the estimation of GPP for the considered time range. The 15-day composite image, however, also allowed

for better identification of the flooded period. This was the case for the month of January 2021. Comparing the first and second half of the month, we can observe that some pixels were left out in the second half of the month. Those corresponded to a phase of high flood and thus pixels were masked and GPP set to zero in the flooded regions. Table 4.9 shows the comparison between the 15-day GPP predictions and the ground measurements of GPP. We observed that the model performances slightly improved compared to the monthly prediction, confirming that a smaller time window could improve the estimation of GPP.

Finally, a GPP map was produced for the entire period of study (Figure 4.16). An average GPP of 770.20 $gCm^{-2}8months^{-1}$ was found. This value is comparable with reported GPP values [221].

When compared to in situ measurements at the Duque Fuente station, a MAE equal to 9.68 $gCm^{-2}month^{-1}$, an RMSE equal to 13.81 $gCm^{-2}month^{-1}$, and a S_{est} of 0.23 were derived.

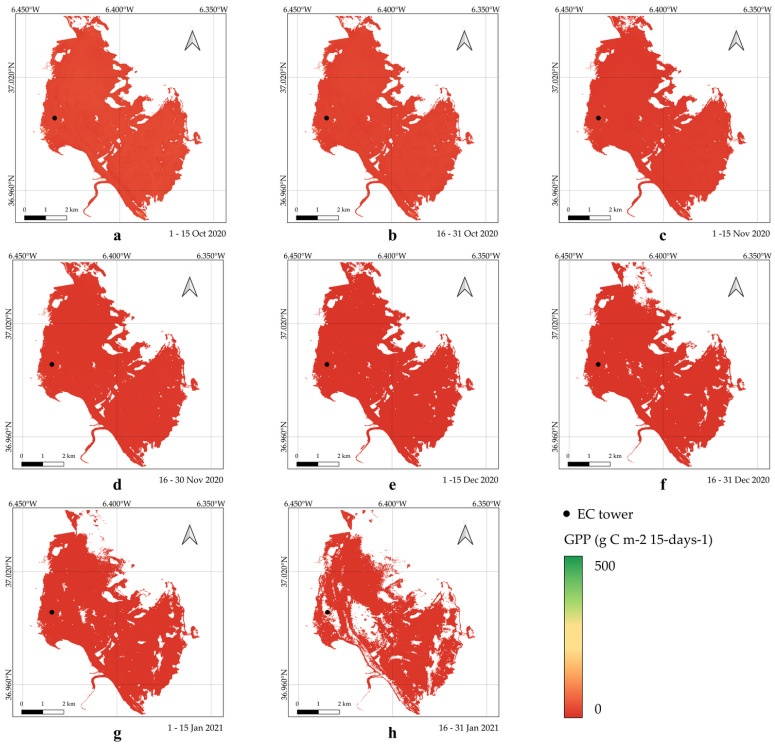

Figure 4.14.: 15-days GPP maps. The maps show the spatial and temporal pattern of GPP ($gCm^{-2}d^{-1}$). (a) 115 October 2020, (b) 1631 October 2020, (c) 115 November 2020, (d) 1630 November 2020, (e) 115 December 2020, (f) 1631 December 2020, (g) 115 January 2021, (h) 1631 January 2021.

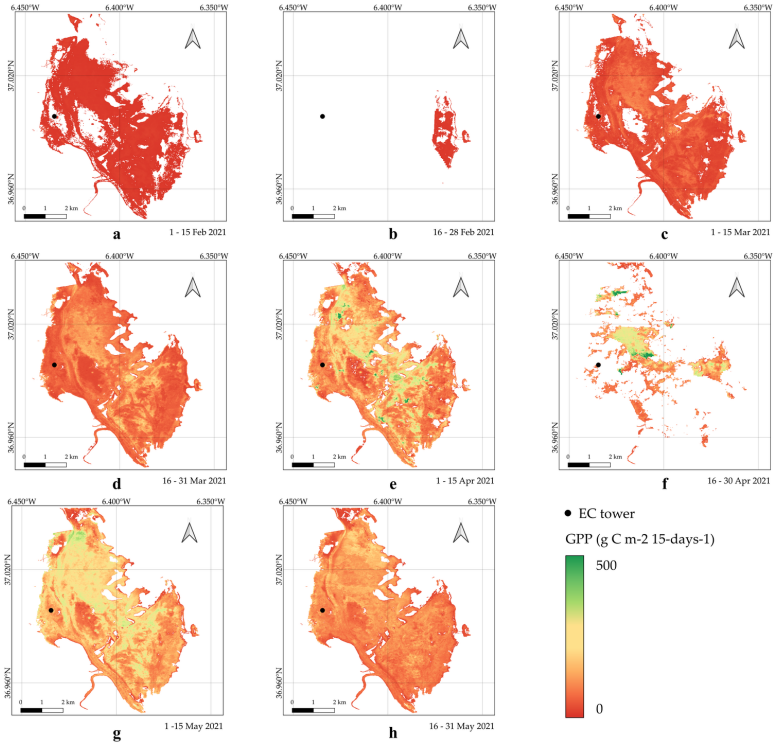

Figure 4.15.: 15-days GPP maps. The maps show the spatial and temporal pattern of GPP ($gCm^{-2}d^{-1}$). (a) 115 February 2021, (b) 1628 February 2021, (c) 115 March 2021, (d) 1631 March 2021, (e) 115 April 2021, (f) 1630 April 2021, (g) 115 May 2021, (h) 1631 May 2021.

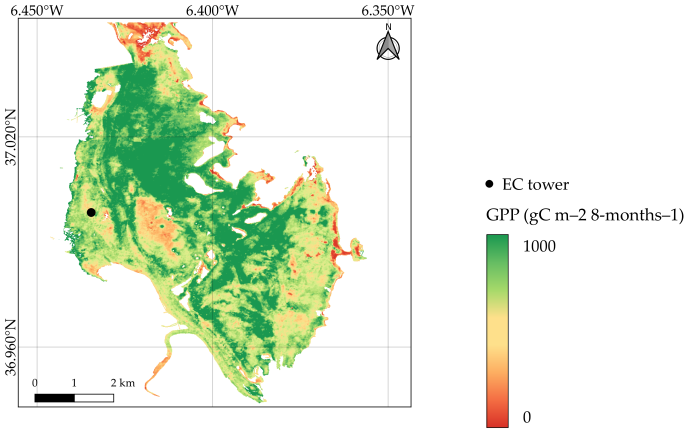

Figure 4.16.: GPP map for the period October 2020 to May 2021 over the study area.

4.4. Discussion

The development and application of a workflow to derive an empirical model of gross primary productivity from remote sensing imagery has been demonstrated at Doñana National Park wetlands. The model has been upscaled for the estimation of GPP in the marsh area surrounding the EC tower. The generated monthly maps of GPP have the potential to provide detailed information on the patterns and dynamics of primary production.

The model selection led to a linear regression model driven by the remote sensing-based red-edge chlorophyll index (CL_r) in combination with the rainfall data. This confirmed previous research outcomes on the sensitivity of the red-edge to canopy biomass, chlorophyll content, and photosynthesis activity [238–240] and thus on the enhanced estimation of the vegetation biophysical characteristics [197, 241, 242]. In general, analyzing each VI proposed in the methodology, we observed that the greenness-sensitive VIs performed the best. Narrowband greenness VIs also showed good performances. The EVI and EVI-2 resulted in being more sensitive than NDVI, confirming that EVI can improve the estimation of productivity in areas with dense vegetation, being less prone than NDVI to noise caused by soil and atmospheric effects [243, 244]. Water-sensitive VIs, such as the LSWI and the MNDWI, did not show a high correlation with in situ GPP. Previous researchers have shown that these indices are more sensitive to drought [198, 245] than greenness-sensitive VIs and, therefore, we suggest further investigation of their performances during dry phases and in ecosystems undergoing seasonal droughts.

The integration of satellite-derived VIs with environmental variables in the model formulation increased the correlation with in situ GPP. Particularly, rainfall data increased the model performances confirming that the biomass production of the Doñana marsh ecosystem is strongly dependent on precipitation [221]. As a result of the high exploitation of water resources in the proximity of the Doñana National Park, the current flooding regime of the natural marsh is mainly determined by local precipitation [182]. The wetlands size and depth change remarkably between years, driven mainly by the variability in the precipitation [211], indicating that the flood levels and associated primary productivity in the ecosystems also correlate with the precipitation regime. The association has also been supported by other authors studying species distribution stating that precipitation is the main driver of primary productivity and associated support of habitats for waterbirds in the ecosystem [246].

The phenological cycle of the vegetation of the study area is also well reproduced, confirming the choice of our model predictors. Green et al. and Lumbierres et al. [211, 221] report that the biomass and associated photosynthesis activity observed through the total intake of carbon dioxide or GPP is low during the start of the rain season (October – December) and the initial stage of the more intense precipitation and flood season (January – February). Then, the GPP content increases in the middle of the wet season when the water availability in the ecosystem reaches a maximum (February – March) [221] and continues to increase till the dry season, when GPP starts to decrease. During the months with higher productivity, the vegetation contributed to 81% of the total GPP produced during the entire period.

This pattern can also be observed in the generated monthly GPP maps. Given the lack of validation data outside the EC tower, we attempt to validate the derived products at

the location of the EC tower. Although the empirical regression model was generally accurate, an overestimation of the monthly GPP was observed when upscaling the method. Smaller time windows were also considered to check the influence of the window size on the model results. The model performances did not improve significantly; however, the smaller time window allowed for a better discretization in time and the identification of GPP variation within the months. Ideally, a smaller time window during the period with high productivity, when the VI selected for the model formulation is rapidly changing, should yield higher model accuracy and abide by the prerequisite of stable VI. At the same time, enlarging the time window could contribute to a reduction in the contamination and noise in the images, and therefore, lead to a smoother GPP estimation [247]. We, therefore, suggest further investigation of the model development when upscaling it.

Including more specific land cover classes to account for different vegetation types or ecosystems [248–250] or applying daily instead of annual climatological footprint [189, 251] can also allow better estimations of GPP and should be pursued in further research. To perform the classification, we used the k-means clustering algorithm [81]. The algorithm was quick and easy to run, a main advantage in comparison with supervised classification, which would have required extensive prior knowledge of the area to be able to identify and label the classes for the training data set [252]. Supervised classification algorithms, however, may also be explored to further improve the land classification of the study area. Supervised classification methods are in general more expensive since they require more time and prior knowledge of the area, but can perform better if a good quality training data set is available [253].

The heterogeneity of the area surrounding the EC tower and the climatological footprint represents a critical factor for carbon flux estimation from satellite imagery [205]. High resolution products that accurately describe the observed patterns and processes occurring at different temporal and spatial scales are needed [199]. We demonstrated that the high spatial resolution of the Sentinel-2 products allowed a detailed description at the time of the distribution of GPP over the ecosystem, enhancing the MOD17 coarse 500-m resolution GPP products. We conclude, therefore, that Sentinel-2 multispectral and high-resolution products can enhance the evaluation of ecosystem responses at a fine scale.

The model versatility is ensured by the integration and assessment of multiple remotely sensed indices with different environmental variables. This can facilitate the uptake of the workflow in different ecosystems. The advantage of assessing multiple indices is justified by the fact that the sensitivity to specific bands combination depends on the characteristics of the vegetation or climatic conditions [196, 197]. A clear example of this is the saturation of NDVI in high biomass vegetation areas and the use of EVI instead [254]. Regardless of the development of multiple vegetation indices formulated to characterize specific vegetation features and processes in different regions, many studies on primary productivity still rely on the use of NDVI or EVI [189, 205, 209, 210, 254]. It can be assumed that those VIs will have sensitivity to any ecosystem component or process. Nevertheless, ecosystem functioning processes such as primary productivity could be explained by multiple remotely sensed information and not exclusively by the fraction of absorbed photosynthetically active radiation (fAPAR), commonly approximated

with the NDVI and EVI. An additional concern about the use of those indices is that multiple studies have derived models for Nordic ecosystems [189, 209]. Regardless of the accuracy derived for those ecosystems, upscaling the approach to other regions would require further analysis. For instance, the assessment of drier ecosystems for which the water or temperature availability can play an essential role, rather than the light availability or fAPAR would require the use of VIs that reflect these limiting factors. Examples of these indices are the water-sensitive VIs such as the Land Surface Water Index (LSWI) and the Modified Normalized Difference Water Index (MNDWI), more sensitive to droughts [198], or the Green Normalized Difference Vegetation Index (GNDVI), more sensitive to chlorophyll and so to photosynthesis activity [196]. Additionally, narrowband VIs should be preferred to broadband VIs since they are more sensitive to water availability than other vegetation indices [198, 245]. Further improvement of the workflow would, therefore, require the inclusion of other VIs that may be more sensitive to the study area. The same would apply to the environmental variables used for the model formulation which also help to better represent the condition of the ecosystem.

Challenges and Outlook

In the present study, the model could not be calibrated and validated for multiple years, or a full year. This was due to the lack of in situ measurements during the dry season that hampered the calculation of the annual GPP and the modeling of the interseason variation of GPP. Moreover, about half of the total available Sentienl-2 data images had to be removed from the original dataset because the cloud coverage was higher than 30% of the total area of the tile. With the increased availability of both in situ measurements and satellite data in the future, it will be possible to fine-tune the model and study not only interseason but also interannual variation in GPP. This was, however, not the main objective of this study which aimed at assessing the capability of Sentinel-2 data for spatiotemporal upscaling of flux tower GPP measurements. Furthermore, the application of the workflow in different regions and different ecosystems may require further development of the tool and will make the upscaling methodology robust.

Further analysis to estimate the effect of the flux partitioning method in the calculation of the ground-based GPP may need to be carried out. Although the night-time method of flux partitioning proposed by Reichstein et al. [255] was generally accurate, further research could investigate the day-time method of flux partitioning suggested by Lasslop et al. [256] or the night-time data-based method proposed by Falge et al. [257]. Using multiple flux partitioning approaches would allow the evaluation of the robustness of the GPP prediction method [258]. Moreover, an uncertainty analysis could also be implemented to better understand the accuracy of the in-situ GPP estimation and its impact on the workflow [259].

Additionally, further analysis to investigate residual noise in the VI time series may be required. In the current study, the noise in the time series was reduced by removing cloudy pixels, water pixels and pixels not belonging to vegetation (e.g., water bodies, snow, temporal floods, or other temporal phenomena). However, other noises arising from surface-viewing geometries or sun sensors can still be hindered [260]. Noise-reduction algorithms such as the SavitzkyGolay filtering [261], the asymmetric Gaussian function fitting [262], the double logistic function fitting [263], or the best index slope extraction (BISE) method [264], might also be implemented in the methodology to in-

crease the accuracy of the derived VIs.

4.5. Conclusions

The adoption of the 2030 Agenda for SDGs reflects the ambitions of the countries to direct their policy and strategy toward ensuring a sustainable future. In this context, monitoring activities, along with the use of satellite-derived information, play a key role in defining implementation strategies to meet the SDGs goals. In this work we assessed the use of Sentinel-2 data-derived indices for the estimation of the GPP in the wetlands of Doñana National Park. The GPP model predictions showed better performance than standard global MOD17 GPP products over the same area. The potential of Sentinel-2 data to enable the estimation of GPP at a finer scale has been demonstrated. Further improvements are foreseen with the increased amount of data and the use of longer time series of Sentinel-2 data, which will result in the modeling of interannual variation of the GPP and a more robust model. High spatial resolution products are key for allowing a detailed description of the distribution of GPP over the ecosystem, especially for heterogeneous ecosystems, thus improving the understanding of ecosystem functions, which are highly correlated to the health condition of ecosystems and the delivery of ecosystem services. Currently, there is a vast amount of unprocessed eddy covariance data in the European Fluxes Database Cluster and other repositories from multiple regions worldwide (https://fluxnet.org/about/regional-networks/, http://www.europe-fluxdata.eu/, etc., both links accessed in May 2026). The present research workflow has been implemented into GitHub (available at the following https://github.com/e-shapePP/vlabs) and into the Virtual Earth Laboratory (VLab), a cloud-based platform openly and easily accessible to users. We encourage relevant stakeholders and protected area managers to make use of the workflow and integrate it into projects and monitoring programs for policy development, implementation, and the ecosystems status evaluation.

5

Modeling gross primary productivity across different European ecosystem types

Predicting Gross Primary Productivity (GPP) is key for understanding ecosystem health and quantifying the global carbon cycle. While data-driven models have shown strong performance in capturing GPP dynamics at specific sites, their ability to generalize across ecosystems without site-specific recalibration remains largely untested. This study addresses this gap by evaluating the applicability of XGBoost and LSTM models in estimating GPP across different European ecosystems. We developed a unified (cross-site) modeling framework that integrates in situ eddy covariance observations and Sentinel-2derived vegetation indices using incremental learning. Models performance was assessed via: (i) site-specific models, developed to capture individual site characteristics, and (ii) cross-site generalization, including evaluation on an independent dataset of unseen ecosystems. SARIMAX is included as a site-specific statistical benchmark for comparison. Our findings indicate that XGBoost consistently outperformed the other models, achieving site-specific R^2 values above 0.90 in forest and grassland ecosystems and an average R^2 of 0.72 across unseen sites (range 0.660.78). LSTM exhibited better accuracy in predicting GPP peaks at site-specific level, particularly in cropland and forest ecosystems. At site-level, SARIMAX showed comparable performance to XGBoost but struggled in capturing the rapid temporal variation of GPP. These findings demonstrate the feasibility of a data-driven framework for cross-site GPP monitoring within European flux-tower networks, making a first step toward transferable GPP prediction without site-specific recalibration.

This chapter has been published in Ecological Informatics Volume 96, Pages 103820, May 2026, https://doi.org/10.1016/j.ecoinf.2026.103820.

5.1. Introduction

Gross Primary Productivity (GPP) indicates the amount of carbon dioxide (CO_2) fixed in an ecosystem through photosynthesis [265]. It represents the largest atmosphere-to-land CO_2 flux and serves as a critical measure in understanding the global carbon cycle [266]. To date, the ocean and terrestrial ecosystems, despite differences among biomes, have absorbed about half of the fossil fuel emissions [267], and are thus vital in mitigating and regulating global warming. Climate change and environmental stressors are, however, altering ecosystem functioning. Hence, accurate estimation of GPP is essential for monitoring terrestrial carbon dynamics and ecosystem health.

Traditionally, GPP estimates have relied on in situ measurements of the total exchange of CO_2 using chamber-based methods or Eddy Covariance (EC) techniques, which provide high-frequency data [223]. Despite the growing development and increasing number of EC towers within global networks (e.g., FLUXNET, ICOS, eLTER, TERN, etc.), these remain spatially limited and unevenly distributed across the globe. Remotely-sensed vegetation indices (VIs) complement EC point-measurement products by enabling broader spatial monitoring of plant productivity [199, 268, 269], vegetation health, growth levels, stress, and other conditions [270]. Together, in situ and remotely sensed data can be used to create long-term and consistent time series data. To quantify GPP consistently across different sites and ecosystem types without site-specific recalibration, a standardized protocol is needed.

Data-driven models, including machine learning (ML) and deep learning (DL), have been increasingly adopted to capture GPP temporal variations and magnitudes, replacing physics-based models, inherently complex and requiring a large number of parameters that are globally available but only at coarse resolution [265]. Yet, most high spatiotemporal data-driven GPP models are trained and validated at individual sites, and their cross-sites transferability remains largely unexplored. As a result, it remains unclear whether data-driven models can provide GPP estimates across biomes without site-specific recalibration.

Among data-driven algorithms for GPP estimation Artificial Neural Networks (ANNs), Support Vector Machines (SVMs), and trees-based models are the most widely used approaches [271–273]. ANNs offer flexible architecture but require careful hyperparameter tuning [274]. SVMs have shown good performance in GPP estimations [275]; yet their training is computationally expensive and requires a large amount of memory. Tree-based models are generally computationally less intense and have the advantage of reducing overfitting while effectively handling heterogeneous predictors. Among ML algorithms, tree-based methods, particularly the Extreme Gradient Boosting (XGBoost), have achieved higher accuracy and computational efficiency than ANN, SVM and Random Forest (RF) in modeling GPP and carbon flux [276–278]. In parallel, DL has also been increasingly adopted in ecological and GPP time-series modeling, outperforming SVM, RF and ANN [275]. Photosynthetic activity exhibits memory effects from prior environmental states, motivating the use of Recurrent Neural Networks (RNNs, a class of DL), designed to be effective in retaining temporal dependencies. Within this class, Long Short-Term Memory (LSTM) networks have shown good performance in modeling GPP, including improved representation of climate-induced productivity extremes [279].

Building on these insights, we selected XGBoost and LSTM for our modeling approach.

XGBoost was chosen also for its balance of interpretability, accuracy, and computational efficiency, as well as its ability to effectively handle heterogeneous predictors, such as vegetation indices and meteorological variables [78]. LSTM was selected because it is particularly suited to capturing complex ecosystem dynamics, reflecting both immediate meteorological conditions and delayed vegetation responses. Additionally, we implemented the Seasonal AutoRegressive Integrated Moving Average with eXogenous variables (SARIMAX), a statistical model successfully applied in ecological applications where seasonality and external environmental drivers play a major role [280]. Its interpretability makes it a useful comparative model for assessing the added predictive value of ML and DL methods.

In this study, we evaluate the feasibility of a cross-site incremental learning framework for transferable GPP prediction without site-specific recalibration. To this end, the research was conducted in two phases. In the first phase, we developed site-specific (individual) models for each training site. The three complementary modeling approaches were compared at site-specif level to highlight the added value and limitations of each method. In the second phase, we used the XGBoost and LSTM models to develop cross-site (unified) models. The models were implemented in an incremental learning framework. Rather than retraining the models from scratch, incremental learning allows the models to assimilate data from additional sites (ecosystems) while retaining information learnt from previous sites (ecosystems). This approach is particularly suited given that the ICOS sites are commissioned at different times, and data are accumulated sequentially, reflecting the realistic conditions of an expanding monitoring network. The cross-site models were further evaluated on an independent testing dataset to assess their ability to predict GPP in ecosystems not included in training. This final step was specifically designed to evaluate the spatial transferability of data-driven approaches in the absence of GPP measurements, that is, whether a pre-trained model can be directly applied to a new site using only predictor variables, without the need for site-specific retraining. This work should be considered a proof of concept, aiming to evaluate the feasibility of a unified modeling framework for transferable data-driven ecosystem monitoring.

5.2. Materials and Methods

5.2.1. Study Area

Four different ecosystem types were selected for the analysis since we aimed at developing a unified model capable of estimating GPP in various European sites and across ecosystem types. The main criterion for site selection was the availability of a complete time series for at least three years to ensure sufficient data for the model training process. Moreover, sites were chosen at different locations spanning a wide latitude and longitude range to achieve the coverage of a large geographical area.

In total, eight sites were selected (Figure 5.1) belonging to four ecosystem types: evergreen needleleaf forest (ENF), deciduous broadleaf forest (DBF), cropland, and grassland. Two sites for each ecosystem type were selected. The eight sites were split into two sets, with one set serving as training sites for building both individual (site-specific) and unified (cross-site) models, and the other set serving as test sites to evaluate the performance of the unified model in predicting GPP on unseen sites. Both sets had the same

combination of ecosystem types (Table 5.1).

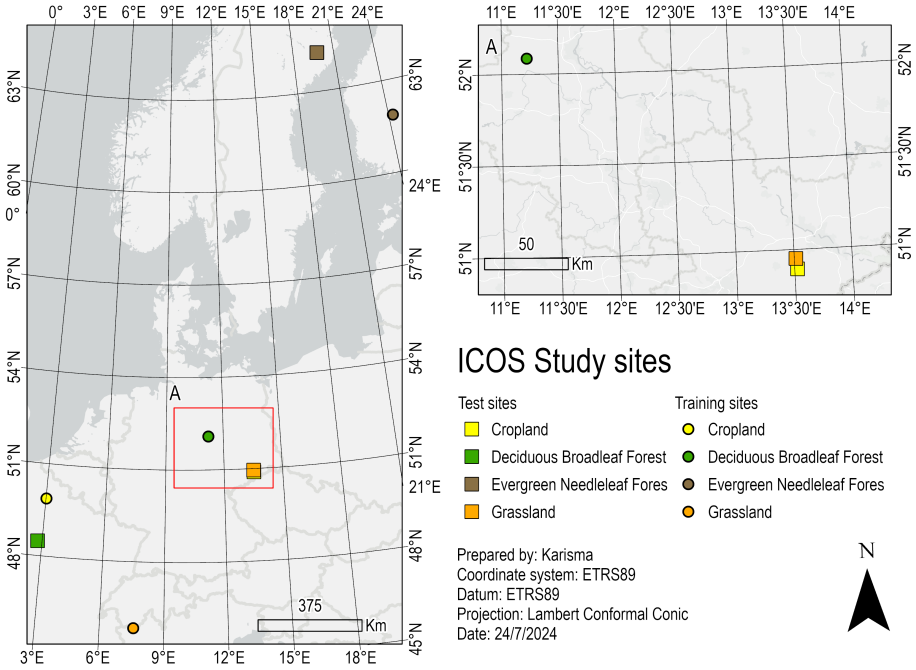

Figure 5.1.: Map of ICOS stations used in this study. Training sites are marked by squares and test sites by circles. Different ecosystems are indicated by color: cropland (yellow), DBF (green), ENF (brown), and grassland (orange).

Table 5.1.: Training and testing sites

Group	Country	Name	Ecosystem type	Start date	End date	Records	ICOS data citation
Train	FR	Estrees-Mons	Croplands	26-05-17	15-10-23	2334	[281]
	DE	Hohes Holz	DBF	01-01-19	26-09-23	1730	[282]
	FI	Hyytiala	ENF	01-01-18	22-09-23	2370	[283]
	IT	Torgnon	Grasslands	01-01-18	22-09-23	2091	[284]
Test	DE	Klingenberg	Croplands	01-01-18	25-09-23	2093	[285]
	FR	Font.Barbeau	DBF	01-01-19	07-09-23	1770	[286]
	SE	Svartberget	ENF	01-01-19	21-10-23	1754	[287]
	DE	Grillenburg	Grasslands	24-04-17	28-09-23	2348	[288]

5.2.2. In situ measurements

The in situ data were collected from the ICOS portal [289]. The ARCHIVE data product for ecosystem measurements at daily resolution was collected, for the period 2017–2023. The ARCHIVE data product contains a set of meteorological variables gap-filled and/or downscaled from the ERA5 dataset [290]. While tower-level observations may be considered more accurate, the ARCHIVE dataset provides consistent and harmonized records across all sites, supporting model reproducibility and transferability. Furthermore, these data have undergone a uniform and standardized quality control process that ensures their reliability [290]. Only the variables that were available for all chosen study sites were used to ensure model reproducibility (Table 5.2). Those variables include independent meteorological observations (short- and longwave radiation, air temperature, atmospheric pressure, precipitation, wind speed, and vapor pressure deficit), which are broadly available across climate networks, and turbulent flux products derived from direct eddy covariance measurements (sensible heat flux and latent heat flux). The latter typically rely on flux observations and are therefore limited to instrumented sites. These variables were used as predictors to train the models since they represent direct environmental drivers of photosynthesis or its proxies. The target variable for model training was GPP derived from the daytime partitioning method, 50th percentile estimates (GPP_DT_VUT_USTAR50) [256]. This product was selected because the daytime (DT) partitioning method accounts for the effect of vapor pressure deficit (VPD) on the light-response function, thereby reducing biases commonly observed in the nighttime (NT) method, where the VPD effects are typically neglected [256]. Additionally, the USTAR50 product, representing the median value (50th percentile) of the variable friction velocity (USTAR) threshold (VUT) distribution, was chosen among recommended reference products due to its robustness and stability across different temporal aggregation resolutions [290].

Table 5.2.: List of the in situ variables collected from ICOS.

Variables	Explanation	Unit
H_F_MDS	Sensible heat turbulent flux	$\mathrm{W\,m^{-2}}$
LE_F_MDS	Latent heat turbulent flux	$\mathrm{W\,m^{-2}}$
LW_IN_F	Incoming (down-welling) longwave radiation	$\mathrm{W\,m^{-2}}$
PA_F	Atmospheric pressure	kPa
P_F	Precipitation	$\mathrm{mm\,d^{-1}}$
SW_IN_F	Shortwave radiation	$\mathrm{W\,m^{-2}}$
TA_F	Air temperature	°C
VPD_F	Vapor pressure saturation deficit	hPa
WS_F	Wind speed	$\mathrm{m\,s^{-1}}$
GPP	Gross primary productivity	$\mathrm{gC\,m^{-2}\,d^{-1}}$

Global variables, time-invariant descriptors, which serve as proxies for the distinct ecosystems of each site, were collected. These variables included elevation, latitude, and longitude. Ecosystem type and season, derived from the months of data collection, were also utilized as categorical explanatory variables. Seasons were categorized as fol-

lows: winter (December to February), spring (March to May), summer (June to August), and autumn (September to November) [291]. Both the type of ecosystem and the season were treated as categorical data, subsequently converted into a binary format using one-hot encoding, a common technique used to represent each category as a separate binary column (1 or 0). This approach facilitates the integration of categorical variables into the analysis and allows their use in machine learning models.

5.2.3. Remote sensing data

Sentinel-2 Level-2A data products, resampled at 10 m resolution, were used to derive the VIs, used as a proxy for GPP. Information on the spectral response functions of Sentinel-2 data can be found in Table 5.3 and on the Sentinel-2 handbook [292].

The vegetation indices derived from Sentinel-2 provide information about leaf pigments, leaf and canopy structure [293]. The Normalized Difference Vegetation Index (NDVI) was originally developed to detect vegetation health over a range of latitudes by comparing reflectance in the red and near-infrared bands. Refinements, such as the Modified Normalized Difference Vegetation Index (MNDVI), the Enhanced Vegetation Index (EVI), and the Two-Band Enhanced Vegetation Index (EVI2) (Table 5.3) were primarily developed for estimating the leaf area index (LAI), defined as the one-sided green leaf area per unit ground surface area, as well as for the retrieval of canopy chlorophyll content. These VIs are derived using bands in the red vegetation maximum chlorophyll absorption (Band 4), the red-edge position (Band 5), and the high reflectance in the near-infrared (NIR) region (Band 8), and enhance estimates of leaf chlorophyll concentration and canopy chlorophyll content. Water-sensitive indices – namely, the Land Surface Water Index (LSWI), Normalized Difference Infrared Index (NDII), and Modified Normalized Difference Water Index (MNDWI) – indicate vegetation water content (plant water status), drought and water stress, and open water detection, respectively.

Different VIs may correlate slightly better for GPP for specific ecosystems and regions [294], and the need for greenness and water-related indices to effectively capture the spatial and temporal pattern of the GPP has been demonstrated [295]. Greenness-related VIs are indeed more effective during the wet phase of the growing season, while water-content-related indices perform better in the dry season due to the sensitivity of GPP to water availability. Therefore, both types of indices were used in this study. The equations used to derive the different VIs from Sentinel-2 data are presented in Table 5.4.

Sentinel-2 Level-2A images were retrieved at the defined locations and time periods. The period corresponded to the time of available in situ measurements, since those are used as ground truth, while the location corresponded to the coordinates of a reference area assigned around each flux tower of each site. The reference area was used as an approximation of the non-static climatological footprint, the surface area contributing to the measured flux [296]. The buffer area around the flux tower was manually determined through satellite image inspection and defined as a circle area with a certain radius. The coordinates of the flux tower were used as the centre of the area. The radius of the buffer area varied for each site to ensure that the retrieved data covered only the desired ecosystem type (Figures B.1–B.2, Table B.1). At first, images within the defined coordinates and period were retrieved. Thereafter, images were filtered by cloud coverage; those with more than 30% cloud coverage were excluded from the analysis. Finally,

Table 5.3.: Spectral responses for each band of Sentinel-2 multispectral instrument. Source: https://sentinels.copernicus.eu/-/copernicus-sentinel-2c-spectral-response-functions (accessed in May 2026).

Band #	Centre λ (nm)	Spectral width $\Delta\lambda$ (nm)	Spatial resolution (m)	Purpose
B1	443	20	60	Atmospheric correction (aerosol scattering).
B2	490	65	10	Sensitive to vegetation senescing, carotenoid, browning and soil background; atmospheric correction (aerosol scattering).
B3	560	35	10	Green peak, sensitive to total chlorophyll in vegetation.
B4	665	30	10	Maximum chlorophyll absorption.
B5	705	15	20	Position of red edge; consolidation of atmospheric corrections/fluorescence baseline.
B6	740	15	20	Position of red edge, atmospheric correction, retrieval of aerosol load.
B7	783	20	20	Leaf Area Index (LAI), edge of the Near-Infrared (NIR) plateau.
B8	842	105	10	LAI.
B8a	865	20	20	NIR plateau, sensitive to total chlorophyll, biomass, LAI and protein; water vapour absorption reference; retrieval of aerosol load and type.
B9	945	20	60	Water vapour absorption, atmospheric correction.
B10	1375	30	60	Detection of thin cirrus for atmospheric correction.
B11	1610	90	20	Sensitive to lignin, starch and forest above ground biomass. Snow/ice/cloud separation.
B12	2190	180	20	Assessment of Mediterranean vegetation conditions. Distinction of clay soils for the monitoring of soil erosion. Distinction between live biomass, dead biomass and soil, e.g. for burn scars mapping.

non-vegetated pixels were removed from the image using the Sentinel-2 Scene Classification Layers (SCL) provided by ESA, which distinguish pixels among twelve classes (e.g., vegetation, snow or ice, defective pixels, etc.) [297].

After cloud filtering, the VIs values calculated per pixel within the buffer area were averaged to obtain a single daily value. To mitigate the impact of outliers on subsequent analysis, a z-score technique was applied. Data points with z-score equal to or higher than 3 were removed. Linear interpolation was used to estimate missing data points, followed by the application of a Savitzky-Golay filter [298] to smooth the time series and

Table 5.4.: List of vegetation and water indices derived from Sentinel-2 Level-2A products.

Abbreviation	Name	Equation
NDVI	Normalized Difference Vegetation Index	$\frac{NIR-Red_{665}}{NIR+Red_{665}}$
MNDVI	Modified Normalized Difference Vegetation Index	$\frac{NIR_{783}-Red_{705}}{NIR_{783}+Red_{705}}$
EVI	Enhanced Vegetation Index	$\frac{NIR-Red_{665}}{NIR+6Red_{665}-7.5Blue+1}$
EVI2	Two-Band Enhanced Vegetation Index	$\frac{NIR-Red_{665}}{NIR+2.4Red_{665}+1}$
CIr	Red-edge Chlorophyll Index	$\frac{NIR_{783}}{Red_{705}}-1$
LSWI	Land Surface Water Index	$\frac{NIR-SWIR1}{NIR+SWIR1}$
NDII	Normalized Difference Infrared Index	$\frac{NIR-SWIR2}{NIR+SWIR2}$
MNDWI	Modified Normalized Difference Water Index	$\frac{Green-SWIR1}{Green+SWIR1}$

5

enhance data quality.

5.2.4. Models

Three different models and their performances were analysed in this study: SARIMAX, XGBoost, and LSTM.

The AutoRegressive Integrated Moving Average (ARIMA) model, popularized by Box and Jenkins [84], has been extensively used to predict trends based on historical data [299, 300]. The SARIMAX model extends the ARIMA framework by incorporating both exogenous variables (external predictors, e.g., meteorological drivers) and seasonal components, allowing for a more accurate representation of periodic environmental influences and climate drivers. SARIMAX has been shown to improve forecasts in the fields of hydrology [301], ecology [302], and healthcare [303, 304]. SARIMAX models are usually denoted $SARIMAX(p,d,q)(P,D,Q,s)$ (nomenclature in Table B.2). The lowercase p,q,d correspond to the number of past observations (lags) used to predict the current value, the number of times the time series is differenced to remove trends and make it stationary (i.e., constant mean and variance over time), and the number of past errors included in the model to predict the current value. The uppercase P,D,Q are the autoregressive, differencing, and moving average terms of the seasonal component s representing the seasonal period (for example, the seasonal period $s=7$ corresponds to a weekly seasonality in the daily data).

The XGBoost model is an ensemble model that builds decision trees sequentially, with each new tree correcting the residuals of the previous ones through gradient boosting. This approach allows the model to learn complex nonlinear relationships while mitigating overfitting through internal regularization [78]. To control the tree's growth and prevent overfitting, which occurs when a model learns patterns specific to the training data, resulting in high accuracy on the training set but poor performance on unseen

test data, hyperparameters like the minimum child weight and the maximum tree depth can be tuned, ensuring the tree's splits are meaningful and limiting the model complexity. Additional hyperparameters, including the learning rate eta, the regularization term $alpha$, and $gamma$, which sets the minimum loss reduction required to make a split, are tuned to allow for stable and conservative learning. The definition of the XGBoost hyperparameters optimized in this study is provided in Table B.2.

LSTM networks, a deep learning variant of recurrent neural networks, are designed to capture long-term temporal dependencies through gated memory cells that regulate information flow over time [305]. During training, the loss function is minimized over multiple epochs, the number of times the model iterates over the entire training dataset. Monitoring the training loss across epochs ensures that the model is learning and not overfitting. Adjusting hyperparameters such as the number of LSTM units per layer, which controls the network learning rate, and the number of epochs, can help improve training performance. The definition of the LSTM hyperparameters optimized in this study is provided in Table B.2.

To capture temporal dependencies in the data, lagged values of the predictor variables are included as input features for XGBoost and LSTM. Lag values at the train/test boundary are derived from training observations only, ensuring no future information is used.

Using the SARIMAX, XGBoost and LSTM models, we performed two experiments (Figure 5.2). In the first experiment, we evaluated the performances of site-specific (or individual) models. For each site, we applied the three different algorithms and assessed their performances to identify the most effective model. In the second experiment, we constructed a cross-site (unified) model using incremental learning. This approach involved sequentially training the model on data from each site, allowing it to retain knowledge from previous training steps and adapt to new sites. Incremental learning was employed for the XGBoost and LSTM algorithms; SARIMAX was used as a site-specific statistical baseline and was not extended to the unified cross-site framework. The performance of the unified model was then compared with that of the site-specific models. Additionally, the unified model was evaluated on the second set of unseen sites (Table 5.1) to assess the models' versatility and performance on data they had not encountered during training, thereby allowing us to assess their ability to generalize to new locations without site-specific calibration.

Experimental design 1: individual (site-specific) models.

In the first stage of model development, individual sites were analysed. The performances of the SARIMAX, XGBoost and LSTM models were assessed and compared using predefined evaluation metrics to determine the most effective approach for each site. The employed evaluation metrics were: Mean Squared Error (MSE), Root Mean Squared Error (RMSE), Mean Absolute Error (MAE), and coefficient of determination (R^2). Additionally, the Akaike Information Criterion (AIC) was computed for the SARIMAX model. AIC was only computed for SARIMAX, as this is a likelihood-based parametric model for which the likelihood and number of estimated parameters are explicitly defined. By contrast, AIC does not apply to XGBoost and LSTM, whose training is based on minimizing regularized loss functions rather than maximizing a statistical likelihood.

Before training, the datasets from each site were partitioned chronologically into train-

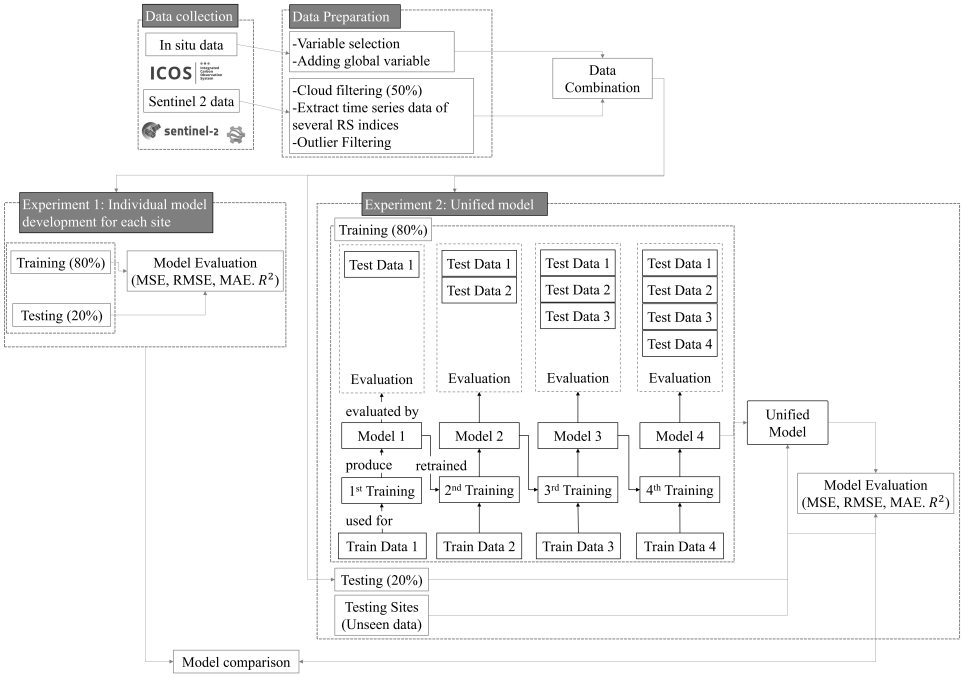

Figure 5.2.: Flowchart of the methodology, including the training process of the unified model used for XGBoost and LSTM.

ing and testing subsets with a split ratio of 80:20. The earliest observations were assigned to training and the most recent 20% reserved for testing. This approach ensures consistency in model training and enhances the reliability of the model evaluation process across different ecological contexts. The models were implemented using: (i) the StatsModels library in Python for SARIMAX [306, 307], (ii) the XGBoost package in Python for XGBoost [308], and (iii) Keras library in Python for LSTM [309].

Parameter optimization was conducted via a systematic grid-based search to optimize the performance of the individual site models. The parameter values used in the optimization phase, together with a detailed description of the optimized parameters, can be found in Tables B.2 and B.3. For SARIMAX, the parameters were the order (p, q, d), and seasonal order (P, Q, D, s). For XGBoost, the tuned hyperparameters included minimum child weight (mcw), eta, $alpha$, $gamma$, maximum depth of a tree (md), and time lags [310]. For the LSTM, the adjusted hyperparameters were the LSTM units of each layer, the number of epochs, and the dropout ratio. A shallow network consisting of two LSTM layers, followed by a dropout layer and an output layer, was used. Dropout is a common method to enhance generalization in neural networks by randomly deactivating neurons during training. This prevents dependency on any single neuron and promotes learning of diverse features [311]. The training of the LSTM was conducted using the Adam optimizer and mean squared error as the loss function. The batch size

for the training process was set at 64.

For the training of site-specific models, all vegetation indices (Table 5.4) were used along with the in situ measurement data (Table 5.2) as explanatory variables. The response variable was GPP. Global variables (location of the site, season, etc.) were excluded from the training dataset for the individual model. The rationale for this exclusion was that the values for global data remained constant within the same site, not providing any additional insight to enhance model performance. Additionally, the study explored the feature importance of the XGBoost model to identify which indicators most significantly influenced the GPP prediction.

Experimental design 2: unified (cross-site) models.

After constructing individual models, the next phase involved building a unified model to explore the capabilities and adaptability of the unified model to generalize GPP prediction across different ecosystem types. The unified model was developed using an incremental learning framework, which entailed continuously training the model with new data. With this approach, adding new sites to the model did not require starting training from scratch; instead, the model utilized the knowledge previously acquired from earlier training sessions. This strategy also addressed the challenge posed by the varying time periods of data availability from different sites.

Data for each site were split chronologically into 80:20 ratios for training and testing, respectively. The model was initially trained using data from the first site. Subsequently, the pre-trained model underwent further training with data from the second site, and so on. The training process of the unified model is illustrated in Figure 5.2.

Initially, training data from the first site (Train Data 1) were used to produce the first model (Model 1). This model was then evaluated using test data from the same site (Test Data 1). Following the evaluation, Model 1 was retrained using training data from the second site (Train Data 2), resulting in Model 2. Model 2 was evaluated using both the test data from the second site (Test Data 2) and the test data from the first site (Test Data 1) to check for consistency and improvement. This process continued through the 4^{th} training session, culminating in the development of Model 4. Model 4, serving as the unified model, was then assessed to determine the performance achieved through this retraining approach.

The hyperparameters for each algorithm were initialized during the first training, and these settings remained constant throughout the training process. The selection of the hyperparameters was based on the optimal parameters identified through the tuning process of the individual models. The selection was primarily guided by a majority vote from the best parameters across all sites; although this was not the exclusive method used, there was also an exploration of parameters to enhance performance. During the exploratory phase, global variables were utilized as features to determine whether their inclusion could enhance the model's performance. The unified model results presented are those trained without global variables for XGBoost and LSTM, since their inclusion did not enhance performance (Tables B.6 and B.8).

Incremental learning was employed for constructing unified models using XGBoost and LSTM. The SARIMAX model was not extended to a unified cross-site configuration because it is designed to be fitted to a single continuous time series. As a result, it does

not support incremental learning, since incorporating new data typically requires retraining the model from scratch due to the tight coupling of the model's state with the entire time series [84]. SARIMAX was therefore used only as a site-specific statistical baseline.

5.3. Results

5.3.1. Individual models

Table 5.5 presents the accuracy of the estimated GPP. XGBoost exhibits the best performance in terms of evaluation metrics compared to the SARIMAX and LSTM models, showing the highest R^2 and lowest MSE, RMSE, and MAE. For the sites of Hohes Holz (DBF), Hyytiala (ENF) and Torgnon (grassland) an R^2 of 0.91 was achieved. The lowest GPP prediction accuracy (R^2 =0.73) was observed at Estrees-Mons (cropland), due to the sudden interannual variability (e.g., GPP values dropped drastically from around 21.5 $gCm^{-2}d^{-1}$ on 6 July 2023 to around 1.1 $gCm^{-2}d^{-1}$ on 14 July, before increasing again on 14 August to 15.9 $gCm^{-2}d^{-1}$ (Figure 5.3)). Among all sites, lowest MSE, RMSE, and MAE values were observed at Torgnon. Model-specific parameter settings are reported in Table B.4 for each model and site.

5

Table 5.5.: Performance metrics by site and method. RMSE and MAE are expressed in $gC\,m^{-2}\,d^{-1}$; MSE in $(gC\,m^{-2}\,d^{-1})^2$. AIC is reported only for SARIMAX models.

Site	MSE	RMSE	MAE	R^2	AIC	Method
	6.59	2.57	1.91	0.65	6527.67	SARIMAX
Estrees-Mons	5.11	2.26	1.84	0.73	–	XGBoost
	6.07	2.46	1.66	0.68	–	LSTM
	3.65	1.91	1.40	0.88	4708.79	SARIMAX
Hohes Holz	2.73	1.65	1.10	0.91	–	XGBoost
	4.03	2.01	1.30	0.86	–	LSTM
	1.09	1.04	0.79	0.90	3304.35	SARIMAX
Hyytiala	1.00	1.00	0.63	0.91	–	XGBoost
	1.69	1.30	0.89	0.85	–	LSTM
	0.95	0.98	0.71	0.89	4083.63	SARIMAX
Torgnon	0.79	0.89	0.52	0.91	–	XGBoost
	0.97	0.99	0.59	0.89	–	LSTM

5.3.2. Unified models on training sites

XGBoost performances

Table 5.6 reports the performance metrics of XGBoost during the training phase of the unified model, using the hyperparameters detailed in Table B.5. A pattern emerged in the evaluation of models across multiple training sessions. After each model was retrained with data from a subsequent site, performance on previously trained sites decreased. For example, at Estrees-Mons, the MSE increased from 5.73 $(gC\,m^{-2}\,d^{-1})^2$ after the first training session to 9.83 $(gC\,m^{-2}\,d^{-1})^2$ after the second training session, before

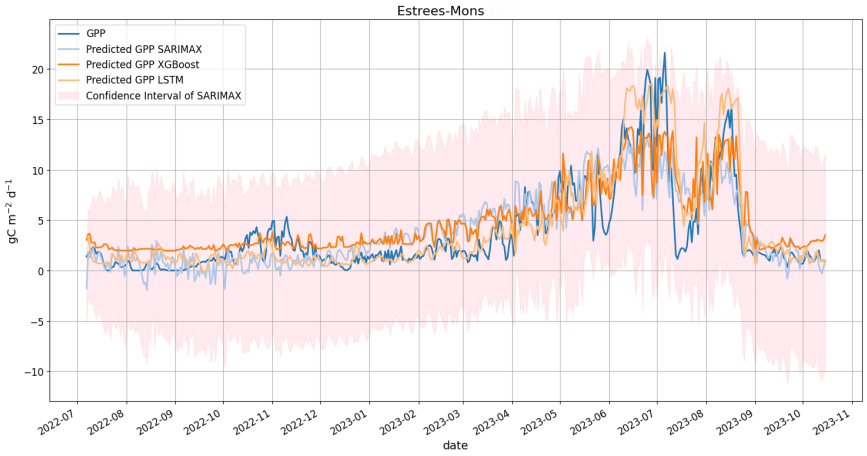

Figure 5.3.: Predicted vs. Observed Value of GPP at Estrees-Mons. Observed GPP is shown in dark blue. Predicted values from SARIMAX, XGBoost, and LSTM, light blue, orange and yellow, respectively. The pink shaded region denotes the confidence interval of the SARIMAX model.

settling down to 6.35 $(gC\,m^{-2}\,d^{-1})^2$ in the final session. The R^2 followed a similar trend, indicating a loss of predictive accuracy, though slightly improved in subsequent sessions. By the final training session, despite some recovery in metric scores at specific sites like Estrees-Mons and Hyytiala, where the MSE improved to 6.35 $(gC\,m^{-2}\,d^{-1})^2$ and 2.31 $(gC\,m^{-2}\,d^{-1})^2$, respectively, the overall model performance declined in comparison to individual models. The average MSE across sites by the last training was 3.95 $(gC\,m^{-2}\,d^{-1})^2$, the average RMSE was 1.95 $gCm^{-2}d^{-1}$, the average MAE was 1.29 $gCm^{-2}d^{-1}$, and the average R^2 was 0.74.

Figure 5.4 displays the feature importance of each individual model, showing the five most important features based on the relative value of the gain metrics. The latent heat turbulent flux contributes to the highest gain value at Hohes Holz and Estrees-Mons, air temperature (TA) emerged as the most significant feature at Hyytiala, whereas at Torgnon, CIr demonstrated the highest gain value.

LSTM performances

Table 5.7 summarizes the LSTM's performance metrics during the training phase of the unified model, obtained using the hyperparameters detailed in Table B.5. The site training sequence differed from XGBoost (alphabetical order), since modifying the training sequence improved the LSTM's performance (for a direct comparison using the alphabetical order, see Table B.7).

The site order influence was further evidenced by the performance degradation observed when testing data from previously trained sites. Specifically, the model showed worsening metrics in subsequent training phases at Hohes Holz and Estrees-Mons. For example, at Hohes Holz the model experienced an increase in MSE, RMSE, and MAE,

Table 5.6.: XGBoost incremental training performance metrics by site and training round. RMSE and MAE in $gC\,m^{-2}\,d^{-1}$; MSE in $(gC\,m^{-2}\,d^{-1})^2$.

Site	Metrics	1^{st} Train	2^{nd} Train	3^{rd} Train	4^{th} Train
Estrees Mons	MSE	5.73	9.83	7.28	6.35
	RMSE	2.39	3.14	2.70	2.52
	MAE	1.91	2.31	1.95	1.73
	R^2	0.69	0.47	0.61	0.66
Hohes Holz	MSE	-	4.29	3.77	4.07
	RMSE	-	2.07	1.94	2.02
	MAE	-	1.57	1.29	1.33
	R^2	-	0.86	0.87	0.86
Hyytiala	MSE	-	-	2.76	2.31
	RMSE	-	-	1.66	1.52
	MAE	-	-	1.20	1.03
	R^2	-	-	0.75	0.79
Torgnon	MSE	-	-	-	3.05
	RMSE	-	-	-	1.75
	MAE	-	-	-	1.06
	R^2	-	-	-	0.65
Average MSE					3.95
Average RMSE					1.95
Average MAE					1.29
Average R^2					0.74

with the third training yielding an MSE of 21.22 $(gC\,m^{-2}\,d^{-1})^2$ and a low R^2 of 0.28. Similarly, at Hyytiala it exhibited poor metrics during the third training phase. During the fourth training phase, Torgnon's metrics contrasted sharply to the other sites, with MSE escalating from 1.10 $(gC\,m^{-2}\,d^{-1})^2$ to 14.89 $(gC\,m^{-2}\,d^{-1})^2$ and the R^2 turning negative, indicating poor performance, as discussed in Chicco et al. [312].

5.3.3. Unified models on testing sites

Table 5.8 compares the performance of the unified models on the unseen testing sites. The XGBoost model achieved higher performance than the LSTM model. The XGBoost average performance metrics across these unseen sites reinforce the models moderate adaptability, with an MSE of 4.55 $(gC\,m^{-2}\,d^{-1})^2$, RMSE of 2.11 $gC\,m^{-2}\,d^{-1}$, MAE of 1.42 $gC\,m^{-2}\,d^{-1}$, and an R^2 value of 0.72.

XGBoost performances

XGBoost model achieved an R^2 value of 0.78 and 0.77 at the sites of Fontainebleau-Barbeau (DBF) and Svartberget (ENF), respectively, indicating good performance and better generalization (Table 5.8). This aligns with the earlier trend depicted in Table 5.6, where the model improved after adapting to similar ecosystems during training, achieving an R^2 value of 0.86 and 0.79 in the fourth training phase for the sites of Hohes Holz

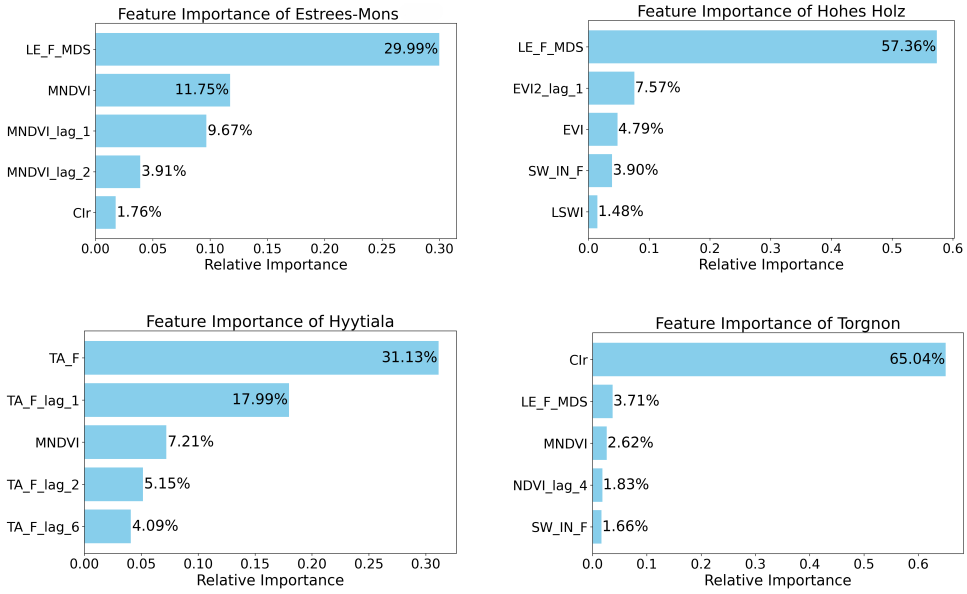

Figure 5.4.: Feature Importance Scores for XGBoost Models Across Different Sites. For details on specific variables refer to Tables 5.2 and 5.4 and Table B.2.

and Hyytiala, respectively. The model, however, showed lower performance at the Grillenburg (grassland) site (R^2 = 0.66) and at the Klingenberg (cropland) site (R^2 = 0.68). Still, the model showed its moderate adaptability at the Klingenberg site (cropland), showing an improvement of performance when compared with Estrees-Mons (cropland), at which the model initially struggled during the training phase.

LSTM performances

Despite poor average evaluation metrics during the training phase (Table 5.7), the LSTM model showed improved performance during the testing phase (Table 5.8), achieving an average R^2 of 0.66 across unseen sites. Similar to XGBoost, the LSTM performed better for deciduous broadleaf and evergreen needleleaf forest ecosystem types with an R^2 of 0.76 at Fontainebleau-Barbeau and 0.73 at Svartberget.

Figures 5.5-5.6 show observed and predicted GPP at Klingenberg and Svarberget. The corresponding plots for the remaining sites are provided in the supplementary (Figures B.3 and B.4). At Klingenberg, XGBoost performed best with an R^2 value of 0.68 and lowest errors. However, it struggled to predict the highest GPP peaks. LSTM overestimated GPP in September. Both XGBoost and LSTM produced occasional negative predicted values, highlighting the need for non-negativity constraints in future model configurations.

At Svartberget, XGBoost and LSTM showed strong performances, with R^2 values of 0.77 and 0.73, respectively. XGBoost overestimated low GPP values from October 2021 until April 2024.

Table 5.7.: STM incremental training performance metrics by site and training round. RMSE and MAE in $gC\,m^{-2}\,d^{-1}$; MSE in $(gC\,m^{-2}\,d^{-1})^2$.

Site	Metrics	1^{st} Train	2^{nd} Train	3^{rd} Train	4^{th} Train
Hohes Holz	MSE	7.57	9.18	21.22	6.90
	RMSE	2.75	3.03	4.61	2.63
	MAE	1.87	2.02	3.01	1.69
	R^2	0.74	0.69	0.28	0.77
Estrees Mons	MSE	-	9.77	15.86	7.41
	RMSE	-	3.13	3.98	2.72
	MAE	-	2.01	2.70	2.02
	R^2	-	0.48	0.15	0.60
Torgnon	MSE	-	-	1.10	14.89
	RMSE	-	-	1.05	3.86
	MAE	-	-	0.61	3.34
	R^2	-	-	0.87	-0.70
Hyytiala	MSE	-	-	-	2.35
	RMSE	-	-	-	1.53
	MAE	-	-	-	0.99
	R^2	-	-	-	0.79
Average MSE					7.89
Average RMSE					2.69
Average MAE					2.01
Average R^2					0.36

Table 5.8.: Unified model performance metrics for the unseen test sites. RMSE and MAE in $gC\,m^{-2}\,d^{-1}$; MSE in $(gC\,m^{-2}\,d^{-1})^2$.

Site	MSE	RMSE	MAE	R^2	Methods
Klingenberg	5.67	2.38	1.43	0.68	XGBoost
	7.34	2.71	1.80	0.59	LSTM
Fontainebleau-Barbeau	4.63	2.15	1.51	0.78	XGBoost
	4.99	2.23	1.60	0.76	LSTM
Svartberget	2.74	1.66	1.15	0.77	XGBoost
	3.16	1.78	1.10	0.73	LSTM
Grillenburg	5.15	2.27	1.60	0.66	XGBoost
	6.59	2.57	1.78	0.56	LSTM
Average XGBoost	4.55	2.11	1.42	0.72	XGBoost
Average LSTM	5.52	2.32	1.57	0.66	LSTM

5.4. Discussion

In this study, we assessed and compared the performances of three models for time series analysis: the SARIMAX model, a statistical method, the XGBoost model, a machine learning approach, and the LSTM, a deep learning model, for predicting GPP at different sites belonging to different ecosystem types.

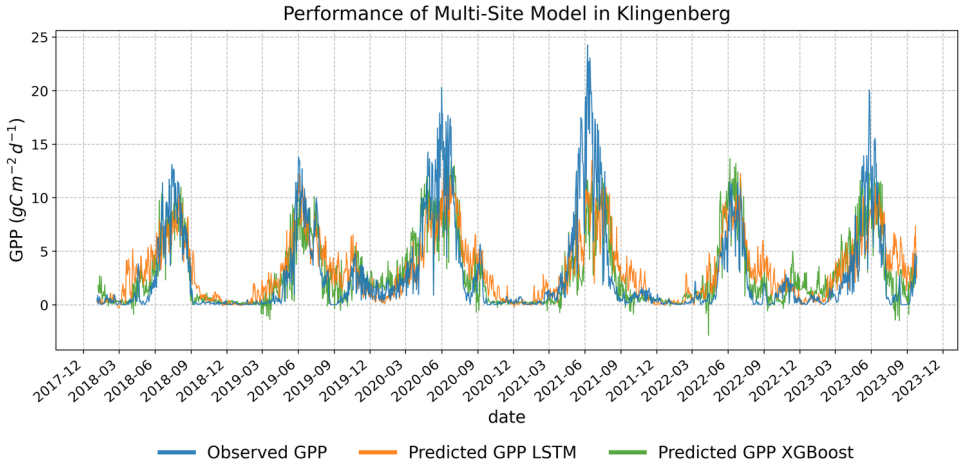

Figure 5.5.: Predicted vs. observed values of GPP from Klingenberg. Observed GPP in blue, XGBoost predictions in green, and LSTM predictions in orange.

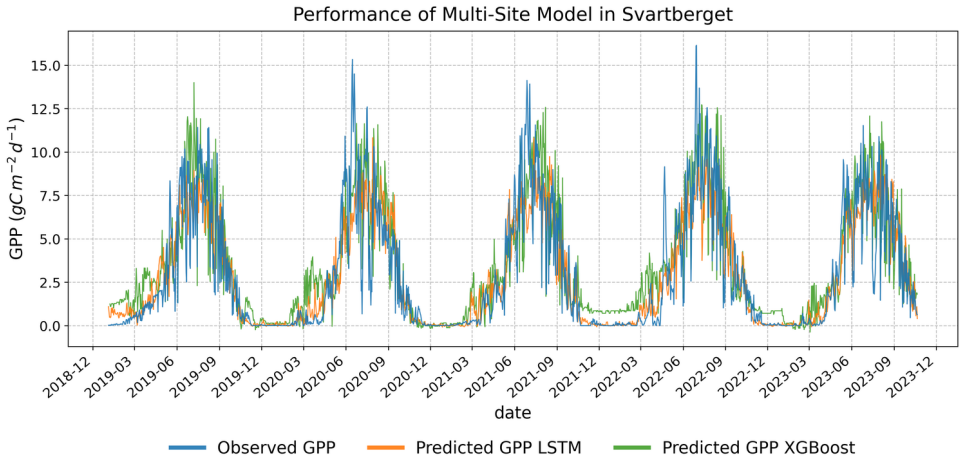

Figure 5.6.: Predicted vs. observed values of GPP from Svartberget. Observed GPP in blue, XGBoost predictions in green, and LSTM predictions in orange.

5.4.1. Individual models

Among the three methods, XGBoost consistently delivered the best performance metrics across all sites. SARIMAX outperformed LSTM in predicting GPP at Hohes Holz, Hyytiala, and Torgnon (Table 5.5), demonstrating that DL methods are not always superior to classical statistical approaches. Although at those sites, the performance of SARIMAX was closely matched with that of XGBoost, the model struggled with rapid temporal changes and tended to underestimate GPP. Consistency between the AIC and

the distribution-free error metrics (RMSE, MAE, and R^2) was observed across sites. A significant drawback of SARIMAX was its longer computational time. For instance, the SARIMAX estimation process for the Hyytiala site took about 31 minutes, whereas XGBoost completed the same task in approximately 4 seconds (evaluated on an Intel UHD Graphics 620 with 3.9 GB shared GPU memory). This advantage of XGBoost results from its gradient-boosting strategy, which enables faster convergence by incrementally correcting errors with each tree addition, rather than optimizing all parameters simultaneously [78]. XGBoost showed better overall performance; however, at some sites, it tended to overestimate GPP during the low-productivity period and underestimate GPP during the high-productivity period. LSTM performed competitively. Its GPP-predicted values tended to be smoother than those from XGBoost and SARIMAX, suggesting LSTMs better generalization capability, particularly in capturing seasonality. While smoothness might be advantageous for constructing a global model that generalizes well across different sites, it is crucial to balance it with the need for accurate GPP predictions. Additionally, LSTM was the only model able to capture strong productivity peaks.

Models tended to underestimate GPP during low-productivity periods, occasionally producing negative values of GPP. This is a clear model limitation. To ensure that the outputs remain ecologically realistic, future implementation should incorporate a non-negativity constraint, for example through output transformations or a positive-only objective function. The latter was not implemented here to preserve full model comparability and evaluate the intrinsic behaviour of the unconstrained modeling framework.

Across sites, the predictive performance of the individual models at the Hyytiala evergreen needleleaf forest site showed comparable results to those achieved by Cai et al., [189] (R^2 of 0.89) and by Wang et al. [313] (R^2 of 0.76), which utilized a Light Use Efficiency (LUE) modeling approach. Models showed similar results in deciduous broadleaf forest. Lower error metrics were observed at Torgnon, however, these results may not fully reflect the relative effectiveness of the models due to the larger range of GPP values of other training sites. High values of GPP, especially in croplands, were expected and align with observed carbon fixation rates in productive agricultural settings, as documented by Hu et al. [314]. The larger the value to predict, the greater the potential squared error [315]. This phenomenon accounts for the higher MSE observed at Estrees-Mons compared to other sites.

Estrees-Mons, an arable crops site characterized by rotational management practices, posed the greatest challenge for all three models. Rotational management practice introduces interannual variability in vegetation growth patterns and, consequently, in GPP dynamics. Each crop type has distinct growing and harvesting periods, resulting in variable timing and magnitude of productivity peaks across years. For instance, the unusual GPP pattern observed in 2023 likely reflects the harvesting time of the crop, followed by the subsequent planting of fast-growing crops, explaining the quick recovery in GPP in August. A similar pattern has been observed in previous years but remains unexplained by the in situ explanatory variables (e.g., air temperature). SARIMAX model failed in properly capturing this drop, and while XGBoost showed better overall performance, it tended to overestimate GPP during the low-productivity period and underestimate GPP during the high-productivity period. Among the tested methods, LSTM captured the GPP pattern more accurately, predicting both the significant lows and the subsequent

high peaks. This was expected, since the ARIMA model requires stationarity, achieved by removing the trends using (seasonal) differencing. This makes the model more prone to miss peaks (or highly non-linear patterns). In contrast, NN models are capable of learning non-linear relationships and have a longer memory than SARIMAX, which enables them to better identify the peaks. Slightly better performance of the LSTM in predicting GPP extremes was also shown by Montero et al. [279]. Researchers [316–318] have demonstrated that accurate cropland-GPP estimation requires accounting for crop type-specific characteristics, such as photosynthetic capacity, growth patterns, and harvesting time. Incorporating such crop-type information could explain croplands high GPP range and reduced natural variability, and is therefore suggested to enhance the model performance.

5.4.2. Unified models

After constructing and evaluating individual models, we built unified (cross-site) models to test their adaptability to generalize across ecosystems by sequentially adding data from multiple sites via incremental learning. Both the XGBoost and LSTM unified models showed lower performance than those on individual sites, indicating the challenge of capturing ecosystem-specific GPP dynamics within a single cross-site model.

Under the unified incremental framework, XGBoost outperformed LSTM on both the training and unseen test sites. Yet, the performances of the unified model were lower than those of the individual one. During incremental learning training, the performance on the earliest-trained site (i.e., Estrees Mons) declined as new sites were added (Table 5.6), suggesting that the model adapted to new site data while losing some of its predictive capabilities. This phenomenon could be indicative of overfitting to the new site data or of an inability of the model to generalize effectively across different environmental conditions [277]. Successive training sessions, though aimed at enhancing the models robustness, might have inadvertently introduced complexities that reduced the models performance on previously well-modelled sites. In future studies, different methods like the Light Gradient-Boosting Machine (LightGBM) with stronger regularization can be used to improve the model results [319, 320]. Additionally, the model produced negative GPP predictions under near-zero GPP conditions, such as during winter. This behavior likely results from statistical noise, since the model generates unconstrained continuous outputs that may overshoot below zero. In future developments, predictions should be constrained through transformations or positive-only objective functions to better reflect the biophysical nature of GPP. When tested on unseen sites, the XGBoost unified model demonstrated moderate generalization, with an average R^2 of 0.72. Variability in performance metrics, however, highlights the need to further investigate and fine-tune the model to enhance its robustness and consistency across different ecological settings.

LSTM showed sensitivity to the order in which sites were introduced during incremental learning. Performance fluctuated across training phases, with models trained on early sites (i.e., Hohes Holz) experiencing decline in performances when new sites were added. Model instability indicated its susceptibility to catastrophic forgetting, where it fails to retain previously learned information when exposed to new data [321]. Despite recovery in performance during the fourth training phase, the need for strategies such as parameter freezing [322], which has been shown to preserve learned information and

prevent overfitting to new data, or regularization, which might mitigate catastrophic forgetting in neural networks [323], was highlighted and therefore further investigation is suggested. When tested on unseen sites, the model reached an average R^2 of 0.66.

Across ecosystems, the unified models showed consistent patterns. XGBoost and LSTM models performed best at deciduous broadleaf forest and evergreen needleleaf forest sites ($R^2 > 0.76$), where the seasonal cycle of GPP could be more effectively captured [324]. Both LSTM and XGBoost require improvements for better predictions in grassland sites. Although the unified models well captured seasonal GPP trends, they also showed limitations. Those are not solely model-driven but also reflect the ecosystem-specific processes not fully represented by the current predictors, which do not include direct drivers of GPP as snow cover duration, soil properties, or species-specific physiological responses. For instance, while the sites of Torgnon and Grillenburg (grasslands) are characterized by similar climate conditions, their different elevation (2160 m Torgnon, 385m Grillenburg) leads to different snow cover periods, which affects the length of the carbon uptake period [325, 326]. Likewise, carbon uptake in cropland and grassland is highly dependent on the nutrient availability and growing season length [325, 327], while species-specific responses to late spring frost affect forests like Fontainebleau-Barbeau (oak forest) and Hohes Holz (beech forest), differently, with oak being more resilient than beech forest [328]. Owen et al. [327] further demonstrated that annual GPP in deciduous forest sites generally decreases from south to north, primarily due to shorter growing seasons, a pattern evident in the Fontainebleau-Barbeau and Hohes Holz sites. The fact that the addition of geographic coordinates did not improve model results suggests that air temperature and precipitation already covered the relevant gradient in the growing environment.

To expand model applicability and robustness, the inclusion of soil information, such as soil moisture and evapotranspiration, CO_2 trends, fertilization rates, and drought indicators, among others, should be incorporated as they may provide additional information on the water status and plant physiology that can affect photosynthetic activities. Satellite-based products such as the solar-induced fluorescence (SIF) from Tropospheric Monitoring Instrument (TROPOMI) [329] or soil moisture from the Soil Moisture Active Passive Mission (SMAP) [330] and ERA5 dataset can provide more direct and physiologically relevant information on vegetation functioning and plant water stress, not fully captured by precipitation or water and greenness indices alone. Further work may explore the integration of such additional and complementary satellite-based products, whilst accounting for the different temporal and spatial resolutions among the datasets and ensuring the reliability of upscaled estimates and the development of harmonized products. Downscaled products, such as TroDSIF, achieve a resolution of 500 m for 16-day composites [329]. Higher-resolution SIF observations from NASAs Orbiting Carbon Observatory (OCO)-2 and OCO-3 missions (~ 12 km) are available globally but with spatial discontinuities due to narrow swaths. The upcoming ESA FLEX mission (launch planned for 2026) will further enhance SIF monitoring by providing spatially continuous observations at 300 m resolution. Similarly, soil moisture products from the Copernicus Land Monitoring Service (1 km) and the SMAP/Sentinel-1 synergy (13 km) [331] offer detailed spatial information relevant for ecosystem-scale GPP estimation. Yet, the integration of these heterogeneous datasets with in situ or Sentinel-2 measurements will

require careful temporal and spatial harmonization to ensure the consistency and reliability of upscaled GPP estimates.

Despite currently relying only on environmental variables and proxies of leaf water content and greenness, the models still demonstrated promising potential in predicting GPP values across different ecosystem types, using a limited and relatively simple predictor set. To further strengthen model transferability, future research should focus on improving the representativeness of the data. The current study is based on a limited number of European sites. As a result, the dataset does not fully capture variability within ecosystem types, since a single site cannot capture or represent the full range of conditions within a biome, where factors such as community structure or stand age may vary widely. Incorporating additional sites and longer time series will be essential to characterise variability better and increase model robustness. As longer continuous datasets of both in situ and satellite data become available, future works should also explore temporal validation using independent years or datasets to better assess predictive models. Expanding the framework to a broader range of sites, ecosystem types, and geographical regions beyond Europe will be necessary not only to increase the robustness of the models but also to strengthen their generalization and assess transferability. Yet, expanding the dataset requires careful consideration, as in global repositories, some ecosystems are better represented than others. Future research should therefore aim to strike a balance between the number of sites, the representativeness of different ecosystem types, and the availability of comparable data lengths across sites, ensuring both diversity and consistency in the training dataset.

The current framework was designed using eddy covariance observations, as EC-derived measurements are essential for training and validating the model. When trained on a more representative dataset spanning a broader range of ecosystems, the framework may support application at new sites without site-specific recalibration. This requires that the same predictor variables are available, whether derived from in situ observations, satellite or model products. In this context, integrating sensible and latent heat fluxes from model results based on satellite observations [332, 333] may support broader spatial applicability of the framework. This may also be relevant for future studies aiming to upscale site-level GPP estimates from flux towers [334–336]. Yet, differences in uncertainty, spatial representativeness, and temporal resolution across predictor sources would require careful validation before upscaling.

5.4.3. Variable contribution

Feature importance provides insights into which indicators were most relevant for predicting GPP in each ecosystem. Across sites, the contribution of remote sensing VIs and in situ variables varied, reflecting how productivity is regulated differently across ecosystems and how the joint use of in situ variables (including meteorological drivers and derived flux products) and remote sensingderived products can provide complementary information on ecosystem functioning.

For the cropland (Estrees Mons) and deciduous broadleaf forest (Hohes Holz), the latent heat turbulent flux was the most influential predictor in the XGBoost model. The latent heat turbulent flux results from the correlation between the measured turbulent flux of water vapour and the measured vertical wind speed, as measured by the eddy-

covariance technique. While negative values reflect condensation (or dew) on the leaves, positive values indicate evaporation from water, soil or leaf surfaces, or transpiration from leaves. These processes are driven by the water vapour pressure of the surrounding air and the movement of water through the plant, from the roots, through the leaves and their stomata, to the atmosphere, and are tightly coupled to the photosynthesis rate [337].

For the evergreen needleleaf forest (Hyytiala), air temperature was identified as the most important feature. This finding aligns with previous research. Wu et al. [338], found that air temperature was the major limiting factor for photosynthesis in early spring, autumn, and winter. This indicates the significant impact of temperature on photosynthetic rates during seasons characterized by lower temperatures, common in the Nordic climate of Hyytiala, and in evergreen needleleaf forests [274].

For the grassland (Torgnon), the Red-edge Chlorophyll Index scored as the most important variable. This is consistent with the results of Lin et al. [339], who found that Clr-based GPP estimates exhibited the highest correlation and low uncertainties with GPP from EC across grassland sites. The occurrence of MDVI, EVI and NDVI as feature importance aligns with the study of Wang et al. [277], who identified these indices as key predictors of grassland productivity.

The unified models built with XGBoost and LSTM did not benefit from the inclusion of global variables (e.g., elevation, latitude, and longitude) (Tables B.6 and B.8). This result indicates that these factors were either adequately captured by other variables (e.g., air temperature, radiation) or less critical than expected in influencing GPP prediction in different sites.

5.5. Conclusions

In this study, we evaluated the feasibility of a unified (cross-sites) modeling approach for estimating GPP across multiple ecosystem types without site-specific recalibration. By combining ICOS in situ measurements with Sentinel-2 derived vegetation indices, we compared a statistical (SARIMAX), a machine learning (XGBoost), and a deep learning (LSTM) approach. In the site-specific setting, the three methods performed similarly, achieving R^2 up to 0.91. SARIMAX served as a site-specific statistical baseline. It struggled with rapid non-linear GPP changes, including peak predictions. XGBoost tended to underestimate high peaks and overestimate low GPP values, particularly during the off-peak season. LSTM showed stronger performance in capturing non-linear GPP dynamics and productivity peaks. All models produced occasional negative GPP predictions under near-zero conditions, highlighting the need for non-negativity constraints in future research. In the cross-site setting, XGBoost and LSTM were employed under the incremental cross-site framework, with XGBoost reaching higher performance than LSTM both on seen (average R^2 = 0.74, range 0.65–0.86) and unseen sites (average R^2 = 0.72, range 0.66–0.78). Though both models exhibited training instability, XGBoost and LSTM proved to be suitable tools for cross-site GPP prediction.

Overall, this work provides a proof of concept that data-driven frameworks can support spatially transferable GPP monitoring. While the present analysis is based on a limited number of European sites and ecosystem conditions, the results highlight the po-

tential of this approach for cross-site application. Future work should expand the model framework by including additional sites, ecosystem types, ecosystem-specific information, and validating them across a broader geographical range to enhance their robustness, generalization and reliability, especially in global contexts beyond Europe. Further scaling up the modeling framework to generate products at a broader spatial scale and high frequency represents an important next step of this research. Taking this step in this direction, we move closer to improving environmental monitoring and supporting informed ecosystem management using cutting-edge technologies and their developments.

6

Conclusions and Recommendations

6.1. Conclusions

This thesis presents a multi-disciplinary research where the use of remote sensing imagery and data-driven methods is explored for the development of spatially scalable tools for environmental monitoring. It contributes to two main topics introduced at the beginning of this work (Figure 1.1): spatial scalability, by developing methods that can be applied across regions and ecosystems, and data integration, by comparing and combining satellite with in situ data to enhance the accuracy and transferability of the developed methodologies. The central contribution of this thesis lies in demonstrating the potential of Earth Intelligence – the use of Earth observation data to produce actionable, understandable, and accessible insights for decision-making and sustainable development. While the work presented here represents only a small step forward in this direction, it demonstrates the benefits of Earth observation with data-driven methods. A lot can be said about the limitations of those data and methods from the ecological and statistical scientific point of view. Yet, making compromises on the trade-offs between spatio-temporal details of the provided information across different scales (local, regional, global) is the key to advancing our knowledge on ecosystem health.

This chapter draws the main conclusions from each presented study, and then it revisits the main limitations encountered and provides recommendations for future work. The main overarching conclusions can be summarized as follows:

- **Spatial scalability of methods**: the developed approaches demonstrated strong potential for upscaling, from local applications such as shoreline detection (Chapter 3) and gross primary productivity estimation (Chapter 4) to regional and cross-ecosystem monitoring (Chapter 5).

- **Data integration**: the combination of satellite, in situ, and environmental data enhanced model accuracy and robustness at a local scale (Chapter 4) and model transferability across ecosystems on a broader scale (Chapter 5). These findings highlight the importance of diverse and complementary data sources for developing scalable data-driven tools for environmental assessment.

In Chapter 3, we investigated the potential of Synthetic Aperture Radar (SAR) imagery from ESAs Sentinel-1 satellites for fully automated detection of the shoreline position. The methodology was applied to the Apulia region in Italy, and the retrieved shorelines were validated against video monitoring systems measurements. The method achieved a mean positional accuracy of about 12 m, indicating a sub-pixel accuracy. The methods adaptability to different geographic areas was also investigated. The approach was evaluated on a narrow beach near a basin and applied to optical aerial images to assess its versatility on different image types. Preliminary results were promising, although challenges were observed. The approach was designed to be scalable and suitable for large-scale coastal monitoring, as it relies on freely available satellite data and does not require manual intervention.

In Chapter 4, we explored the potential of Multi-Spectral Instrument (MSI) imagery from ESAs Sentinel-2 satellites for estimating gross primary productivity (GPP). The approach was developed and assessed on a wetland ecosystem, using Doñana National Park in Spain as a case study. An empirical model was built. The model correlates in situ measurements of GPP with vegetation indices derived from Sentinel-2 imagery and environmental variables, automatically selecting the most statistically robust configuration. The model demonstrated high accuracy ($R^2 = 0.93$), outperforming the state-of-art MODIS GPP product. It was successfully upscaled beyond the climatological footprint, and the phenological cycle of the vegetation was well reproduced. The integration of various remote sensing indices and different environmental variables enhanced the models flexibility by enabling the automatic selection of predictors that reflect the specific properties and climate-driven responses of wetland ecosystems. Finally, the advantage of high resolution products in better capturing the spatial pattern of GPP was demonstrated by comparing the generated maps with state-of-art global products.

In Chapter 5, we extended Chapter 4 work by generalizing GPP modelling across ecosystem types. Cross-site models, combining in situ and satellite data collected across different sites, were developed. Three modelling approaches – SARIMAX, XGBoost, and LSTM were assessed and compared. Additionally, for a robust comparison of the models, site-specific models were developed and used as a baseline. XGBoost consistently delivered the highest accuracy for individual models ($R^2 > 0.9$) and for generalizing purposes across unseen sites (avarage $R^2 > 0.7$). LSTM showed promise in capturing extreme values of GPP, whereas SARIMAX struggled with nonlinear patterns and peak predictions. Unified models showed lower performance than those of the individual sites. Performance and generalization capacity varied across ecosystem types, with forests being better represented. Results confirmed the importance of integrating multiple environmental and spectral variables (approach developed in Chapter 4), with the relevant predictors being site-specific. The integration of high-resolution satellite data with ground-based observations supported spatial upscaling across ecosystems and thus broader environmental monitoring.

This thesis work demonstrated the critical role of integrating data from multiple sources to enhance environmental monitoring. In Chapter 3, remote sensing proved to be a complementary tool to video monitoring systems for the retrieval of shoreline position. Although data integration was not performed in this Chapter, the comparison highlighted that satellite data may represent a cost-effective and low maintenance

complementary alternative to in situ measurements. For gross primary productivity estimates, the combination of in situ and satellite-based data improved the models' predictions, both in Chapters 4 and 5. The use of multiple vegetation indices, including both water- and greenness-sensitive vegetation indices, enhanced models transferability across ecosystem types. Similarly, the inclusion of different environmental drivers was important, as their influence on predictions varied between sites.

Collectively, these findings demonstrate the potential of Earth observation data to complement traditional monitoring systems and envision and support their integration into national and international environmental reporting frameworks, including those aligned with the Sustainable Development Goals, Water Framework Directive, and European Union Biodiversity Strategy for 2030.

6.2. Limitations and recommendations

While the work presented in this thesis revealed a significant potential of using data-driven tools based on remote sensing data, limitations still arose. The most critical are discussed below, along with recommendations for future work.

For shoreline detection, the need for highly accurate georeferenced and orthorectified products was highlighted, as well as the impact of coastal morphology on model performance. The detection of narrow beaches, with widths comparable to the pixel size, may be hampered by the coarse spatial resolution of current satellite images, whereas, in intertidal zone, the high degree of saturation and beach moisture content can hinder shoreline positioning. Moreover, shallow beaches and the presence of wave foam can affect shoreline detection, particularly using optical images. Improvements could be achieved through different polarization choices, inclusion of additional filters, adaptive thresholding methods, image fusion, and the use of higher resolution data from emerging satellite constellations. Extending the approach could further enhance shoreline monitoring, identifying areas in accretion or erosion and thus assist in restoration efforts.

In Chapter 4, GPP estimates were succesfully upscaled beyond the climatological footprint; however, the lack of validation data outside the eddy covariance tower limited the validation of the upscaled maps, which could only be compared with state-of-art products. Limitations also arose from the spatial heterogeneity of the area and the models reliance on data within the towers climatological footprint, which constrained spatial upscaling. Trade-offs between the classes had to be made when using k-means clustering for classification, and validation relied on visual inspection. Supervised classification could improve the reliability of the derived classification map; however, it requires additional effort and prior knowledge of the area. Consequently, a balance between computational efficiency and classification accuracy must be considered, particularly when upscaling to larger areas.

While showing promising results, cross-site models (Chapter 5) still performed below site-specific models. LSTM models susceptibility to catastrophic forgetting, XGBoost and SARIMAX negative value predictions, and limited geographic and temporal coverage highlighted the need for further model refinement. Future research should integrate additional sites and ecosystem types, ecosystem-specific drivers of primary pro-

ductivity, and longer time series to better capture variability within and across ecosystems. Expanding the dataset would increase the model's robustness and generalization across ecosystems. Yet, careful consideration is needed to balance site representativeness, ecosystem diversity, and the availability of comparable time series. Additionally, extending validation across larger geographic areas, including regions beyond Europe, will further strengthen model transferability and reliability.

Although the value of data integration across sensors, resolutions, and sources has been demonstrated, further efforts should focus on data fusion. Data fusion is key to overcoming the inherent limitations of satellite data, such as the inability to retrieve information from depth, gaps caused by cloud coverage, and lower temporal resolution compared to automatic in situ measurements. However, when working with multisourced and multidimensional data, careful attention should also be given to assessing variation and noise within each dataset. While evaluating and reducing uncertainty from each data source was beyond the scope of this thesis, incorporating uncertainty assessments in future work is strongly recommended to increase confidence in model outputs.

Current limitations due to resolution disparity, sensor representativeness, spatial variability, and scale mismatch between satellite and in situ measurements remain a well-recognized barrier for the uptake of satellite remote sensing in environmental management. Yet, given the uneven spatial distribution of in situ measurements across the globe, there is a clear necessity to place greater trust in remote sensing products. Remote sensing provides broad spatial coverage, which can not only fill monitoring gaps but also serve as a valuable tool to guide and optimize the design of in situ campaigns by identifying priority areas and times for data collection. This does not imply that remote sensing should replace in situ observations. On the contrary, the two are complementary. Remote sensing requires calibration and validation to ensure reliability, and in situ measurements typically offer higher frequency and finer vertical resolution. By enhancing confidence in remote sensing products and integrating them strategically with in situ and modelled data, monitoring efforts may become more efficient, robust, and scalable to the global level. Future progress in environmental monitoring requires not only technical improvements, but also data standardization and stronger global collaboration. Data standardization is important to ensure data consistency and facilitate data sharing, integration, and long-term management. Collaboration is key to sharing best practices, involving stakeholders at different levels, and promoting the uptake of the developed and innovative technologies into policies. At the same time, particular attention should be directed toward areas that remain underrepresented in current monitoring frameworks. Expanding coverage in these regions is imperative not only to improve the equity and inclusiveness of global observation systems but also to increase their overall robustness. The way forward requires a strong commitment to coordination and cooperation across the in situ and remote sensing communities. Networks such as Global Earth Observation, FluxNET, ICOS, demonstrate the value of collective effort. Their roles should be expanded and supported to promote and accelerate data standardization, improve interoperability, and raise global awareness of the importance of Earth observations. Only through such collaboration can we ensure that the produced information is not fragmented but instead forms part of a coherent, shared system that serves both science and society. Lastly, it is essential to include, in an active participatory way,

the long-silenced and ignored Indigenous knowledge, as advocated, for example, by the GEO Indigenous Alliance. This will ensure cultural balance, equity, and the integration of traditional expertise into global observation efforts. The challenge is clear: to build an inclusive and coordinated observation framework where knowledge is openly shared, standards are harmonized, and no region is left behind.

A

Sentinel-2 GPP: vegetation indices and additional results

A

Table A.1.: Remote sensing based vegetation indexes used in the current study.

Index	Description	Equation
Normalized Difference Vegetation Index (NDVI)	NDVI [340] is the most common VI in studies of vegetation covers. It combines the near-infrared band (NIR) with the red band (R).	$NDVI = \frac{NIR-R}{NIR+R}$
Enhanced Vegetation Index (EVI)	EVI is an improved version of the NDVI that handles the saturation of this index in high biomass ecosystems [243]. It combines the near-infrared (NIR), red (R) and blue (B) bands.	$EVI = \frac{NIR-R}{NIR+6R-7.5B+1}$
Two-bands Enhanced Vegetation Index (EVI-2)	EVI-2 is an alternative to the EVI using only the near-infrared (NIR) and red (R) band [341].	$EVI = \frac{NIR-R}{NIR+2.4R+1}$
Red-edge Index (CLr)	CLr is a vegetation index built with the narrow red-edge bands of Satellite products with high spectral resolution [197]. It combines the red-edge bands with a central wavelength of 705 nm (Re1) and 783 nm (Re3).	$\frac{Re3}{Re1} + 1$
Modified Normalized Difference Vegetation Index (MNDVI)	MNDVI is a normalized difference between the narrow red-edge bands with a central wavelength of 705 nm (Re1) and 783 nm (Re3) [222].	$MNDVI = \frac{Re3-Re1}{I} Re3 + Re1$
Modified Normalized Difference Water Index (MNDWI)	MNDWI is a normalized difference between the green (G) and the short-wave infrared band (SWIR1) proposed by Xu [342] and applied in studies of carbon fluxes by Noumonvi et al. [198].	$MNDWI = \frac{G-SWIR1}{G+SWIR1}$
Land Surface Water Index (LSWI)	LSWI is a normalized difference between the near-infrared (NIR) and the short-wave infrared band (SWIR1). This index has been applied in studies of carbon fluxes by Noumonvi et al. [198]. Other authors have studied the same combination of bands under the name of Normalized Difference Water Index (NDWI) or Normalized Difference Moisture Index (NDMI) [196, 342, 343].	$LSWI = \frac{NIR-SWIR1}{NIR+SWIR1}$
Normalized Difference Infrared Index (NDII)	NDII is a normalized difference between the near-infrared (NIR) and the short-wave infrared band (SWIR2) proposed by [344] and applied in studies of primary productivity by Adan [342].	$NDII = \frac{NIR-SWIR2}{NIR+SWIR2}$

Table A.2.: Coefficient of determination of the first fifty VIs and environmental variables combinations showing higher correlation with groud measurements of GPP.

VI × EV	R^2	VI × EV	R^2
CLr × RAIN_90_150	0.9327	NDVI × RAIN_C_90_180	0.8750
MNDVI × RAIN_90_150	0.9316	NDVI × RAIN_90_150	0.8714
CLr × RAIN_C_90_150	0.9270	MNDVI × AT_OSC	0.8701
MNDVI × RAIN_C_90_150	0.9228	MNDVI × RAIN_90_120	0.8663
CLr × AT_MAX	0.9178	CLr × RAIN_60_120	0.8651
CLr × RAIN_C_60_150	0.9160	EVI × AT_MEAN_f	0.8628
MNDVI × AT_MAX	0.9128	EVI2 × AT_MEAN_f	0.8594
CLr × VPD	0.9114	MNDVI × RAIN_C_90_180	0.8573
MNDVI × RAIN_60_150	0.9109	CLr × RAIN_C_90_120	0.8545
CLr × RAIN_60_150	0.9108	CLr × RAIN_C_60_120	0.8522
CLr × AT_MEAN_f	0.9082	NDVI × AT_MAX	0.8479
MNDVI × VPD_f	0.9047	NDVI × RAIN_60_150	0.8453
MNDVI × AT_MEAN_f	0.9041	CLr × RAIN_90_180	0.8436
CLr × AT_MED	0.9039	EVI × RAIN_C_60_150	0.8435
MNDVI × RAIN_C_60_150	0.9022	EVI × RAIN_90_120	0.8434
CLr × RAIN_90_120	0.8910	EVI2 × RAIN_90_120	0.8431
MNDVI × AT_MED	0.8908	CLr × RAIN_C_60_180	0.8419
EVI2 × RAIN_90_150	0.8895	EVI2 × RAIN_C_60_150	0.8419
EVI × RAIN_90_150	0.8862	NDVI × RAIN_C_90_150	0.8256
CLr × AT_OSC	0.8852	NDVI × RAIN_C_60_180	0.8244
EVI × RAIN_60_150	0.8840	MNDVI × RAIN_C_90_120	0.8212
EVI2 × RAIN_60_150	0.8823	NDVI × RAIN_90_180	0.8209
CLr × RAIN_C_90_180	0.8821	MNDVI × RAIN_C_60_180	0.8198
EVI2 × RAIN_C_90_150	0.8816	NDII × RAIN_90_180	0.8161
EVI × RAIN_C_90_150	0.8771	MNDVI × RAIN_60_120	0.8156

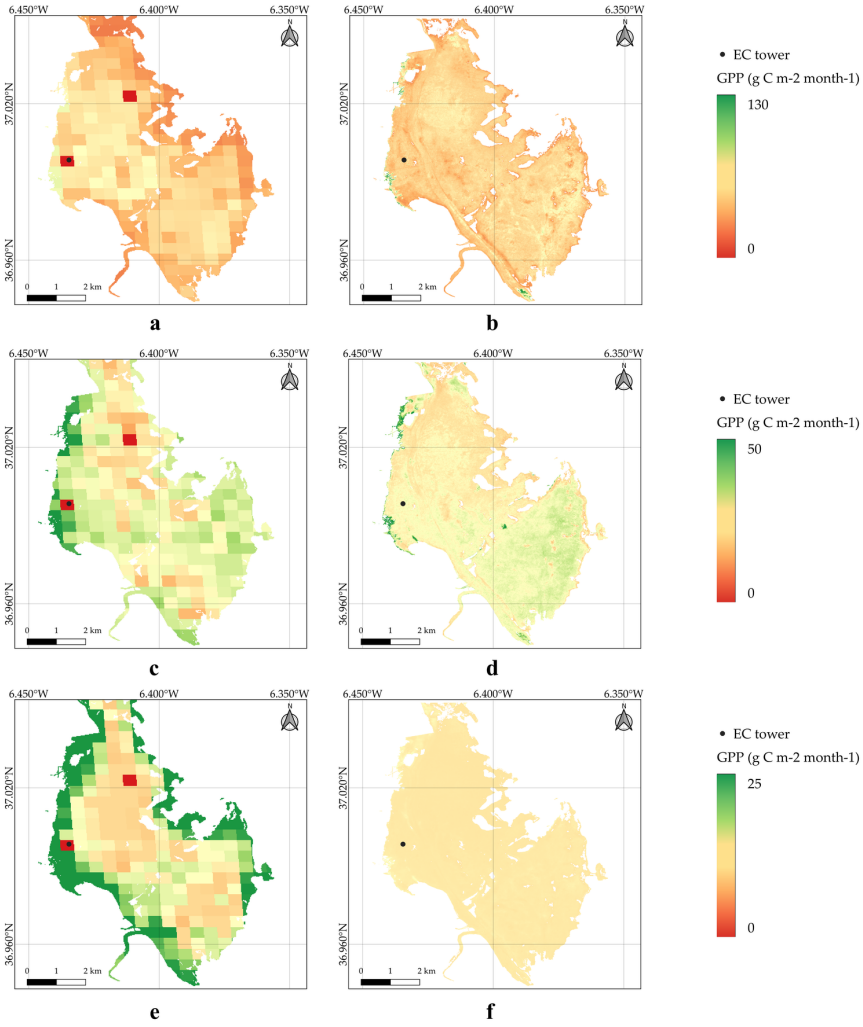

Figure A.1 *Cont.*

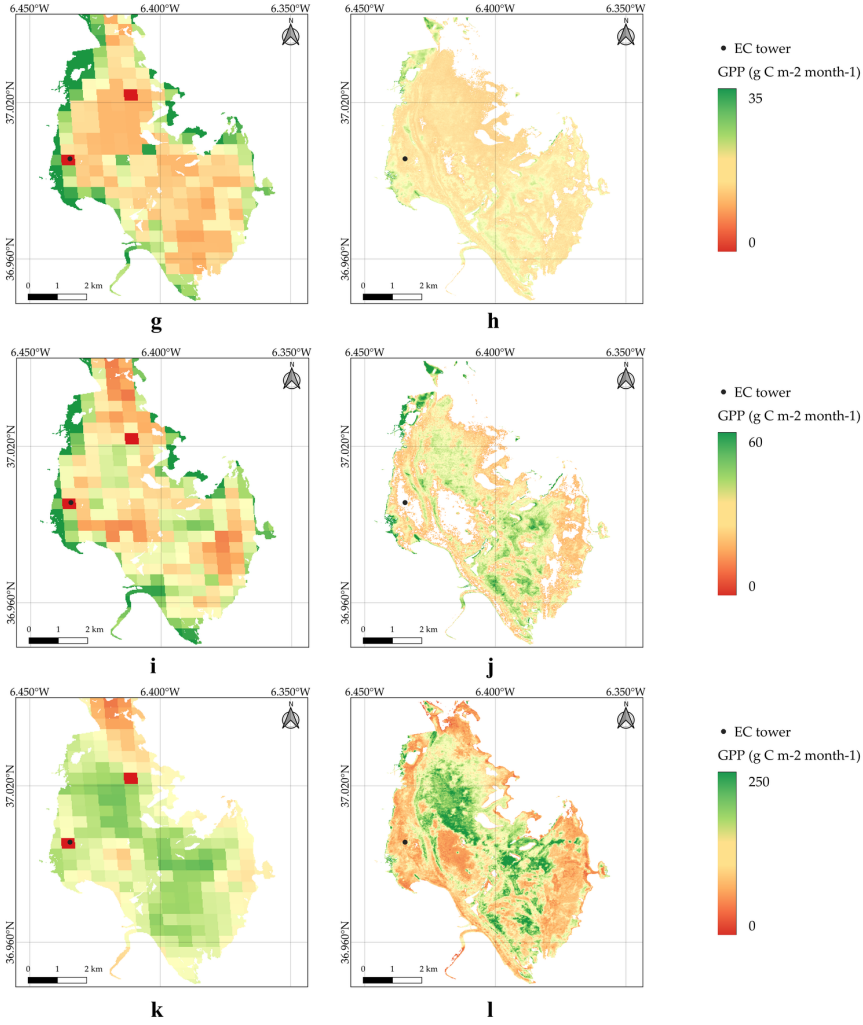

Figure A.1 *Cont.*

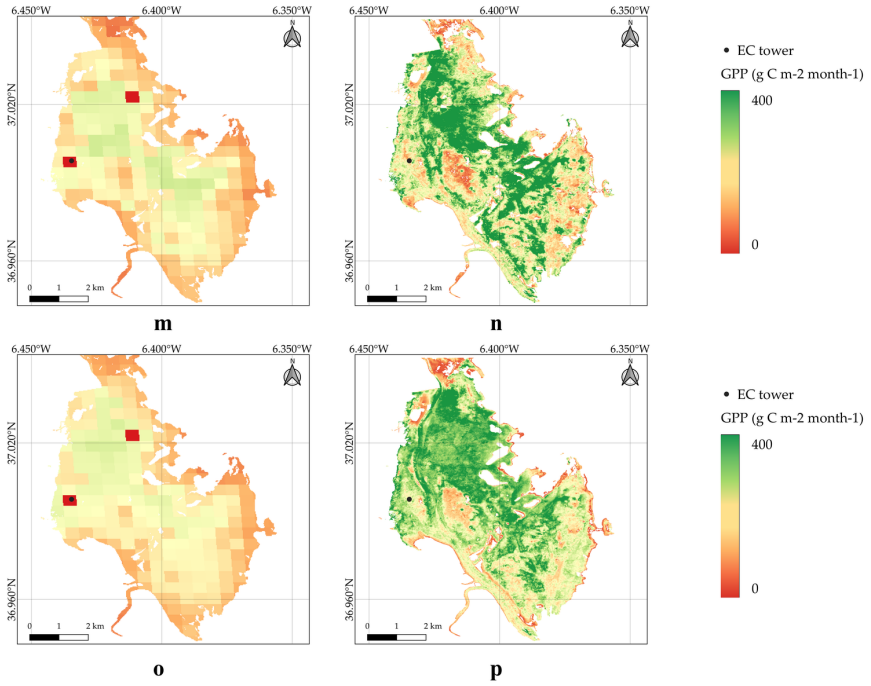

Figure A.1.: Comparison of Sentinel-2 (S2) and MOD17 GPP maps obtained using a monthly composite image. The maps show the spatial and temporal pattern of GPP ($gCm^{-2}month^{-1}$) and the difference captured by the two satellites given their different spatial resolution. (a) MOD17 October 2020, (b) S2 October 2020, (c) MOD17 November 2020, (d) S2 November 2020, (e) MOD17 December 2020, (f) S2 December 2020, (g) MOD17 January 2021, (h) S2 January 2021, (i) MOD17 February 2021, (j) S2 February 2021, (k) MOD17 March 2021, (l) S2 March 2021, (m) MOD17 April 2021, (n) S2 April 2021, (o) MOD17 May 2021, (p) S2 May 2021.

B

Data-driven GPP across ecosystems: definitions and additional results

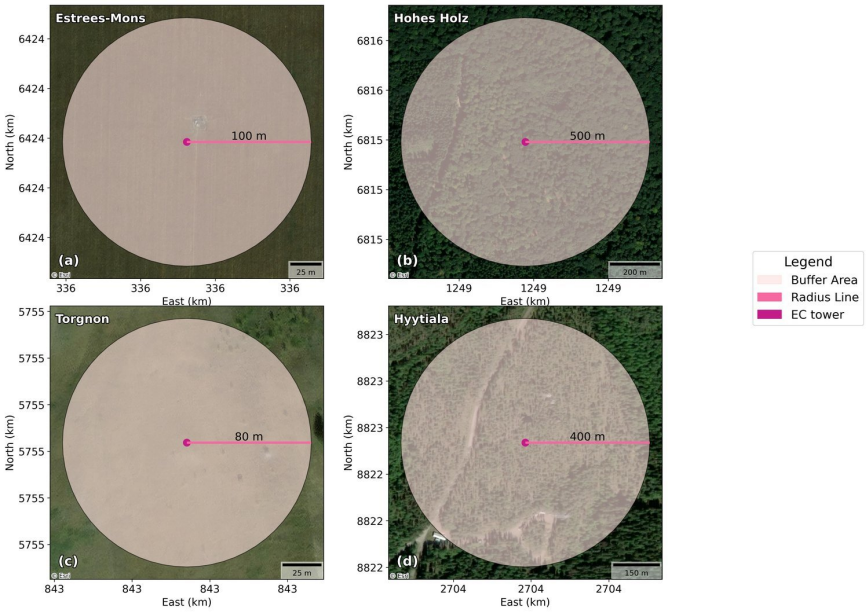

Figure B.1.: Buffer area used as proxy for the climatological footprint for the training sites.

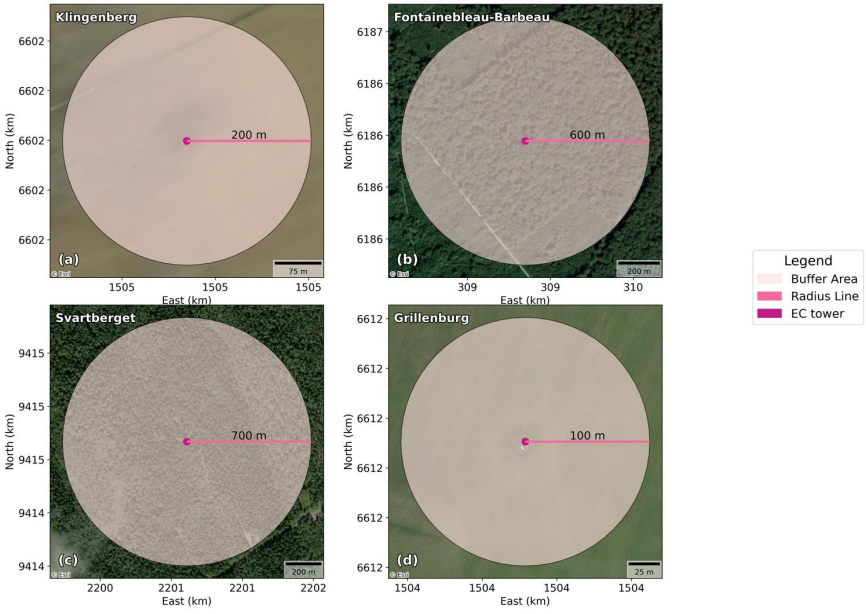

Figure B.2.: Buffer area used as proxy for the climatological footprint for the testing sites.

Table B.1.: Eddy covariance tower coordinates and buffer area radius.

Site	Latitude (N)	Longitude (E)	Radius (m)
Estrees-Mons	49.87211	3.02065	100
Hohes Holz	52.08656	11.22235	500
Torgnon	45.84444	7.578055	80
Hyytiala	61.84741	24.29477	400
Klingenberg	50.8931	13.5224	200
Fontainebleau-Barbeau	48.4764	2.7801	600
Svartberget	64.2561	19.7745	700
Grillenburg	50.95	13.5126	100

Table B.2.: Definition of data science terms.

Term	Definition
Training	Training refers to the process of fitting the model to data during which the model learns by adjusting internal parameters (e.g., weights) to reduce the loss function governing the learning process.
Parameter optimization	Selection of hyperparameters (e.g., maximum tree depth) that guide learning but are not learned during training.
Stationarity	A time series whose statistical properties (mean, variance) remain constant over time.
Exogenous variable	In SARIMAX, external independent variables that influence the modeled series and are measured outside the model.
SARIMAX	Seasonal (S) Autoregressive (AR) Integrated (I) Moving Average (MA) + exogenous variables. A SARIMAX model is usually denoted as SARIMAX$(p,d,q)(P,D,Q,s)$.
SARIMAX order (p,d,q)	Order of the model for the AR (p: the number of lagged observations used to predict the current value), I (d: the number of times the time series is differenced to make it stationary), and MA components (q: the number of past errors included in the model to predict the current value), respectively.
SARIMAX seasonal order (P,D,Q,s)	Order of the seasonal component of the model for the AR, I, MA, and S (s: the periodicity) components, respectively.
Gradient boosting	Ensemble learning method that combines multiple decision trees trained sequentially, where each model improves upon the errors of its predecessor to produce more accurate predictions.
XGBoost hyperparameters optimized in this study	
η	Learning rate: step size shrinkage used in the update to prevent overfitting.
α	L1 regularization term on weights.

Continued on next page

Term	Definition
γ	Minimum split loss: minimum loss reduction required to make a further partition on a leaf node of the tree.
maximum tree depth (md)	Maximum depth of a tree.
minimum child weight (mcw)	Minimum sum of instance weight (hessian) needed in a child.
L	Time lags.
LSTM hyperparameters optimized in this study	
epoch	The number of times the entire training dataset is processed during training.
Unit1	LSTM unit of the first layer.
Unit2	LSTM unit of the second layer.
L	Time lags.
dropout	Dropout rate, regularization term.

Table B.3.: SARIMAX, XGBoost and LSTM parameter values used in the optimization phase.

Algorithm	Parameters	Details	Parameter Values
SARIMAX	(p,d,q)	(1, 0, 0)	(1,0,1), (1,1,1), (3,0,1), (3,0,3), (3,1,1), (3,1,3), (7,0,3), (7,0,7), (7,1,3), (7,1,7), (14,0,7), (14,1,7), (30,0,3), (30,1,3)
	(P,D,Q,s)	(0,0,0,0)	(3,1,3,7), (3,1,3,14), (3,1,3,30)
XGBoost	η	0.3	0.01, 0.1, 0.2, 0.3
	α	0	0, 0.1, 1, 5
	γ	–	0, 0.1, 0.2, 0.5, 1
	md	6	3, 4, 6, 8, 10
	mcw	1	1, 2, 5, 10
	L	–	3, 5, 7
LSTM	epoch	–	50, 100, 150
	Unit1	–	32, 64, 128
	Unit2	–	32, 64, 128
	L	–	3, 5, 7, 14
	dropout	–	0.1, 0.2, 0.3

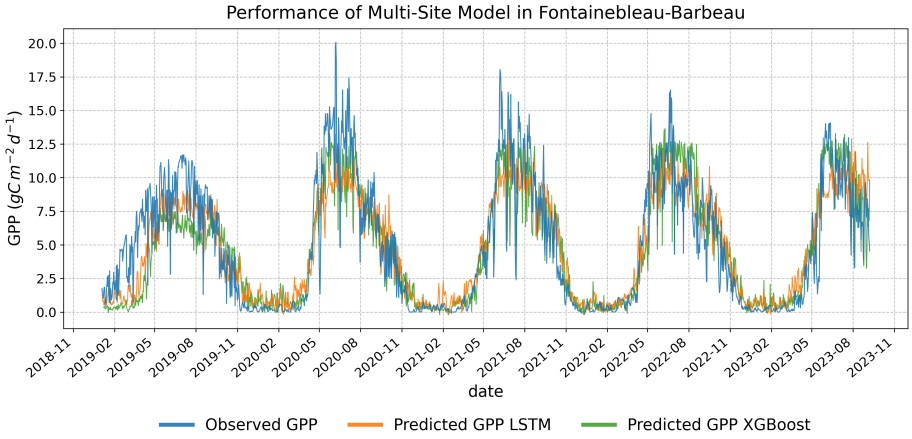

Figure B.3.: Predicted vs. observed values of GPP from Fontainebleau-Barbeau. Observed GPP in blue, SARIMAX predictions in red, XGBoost predictions in green, and LSTM predictions in orange.

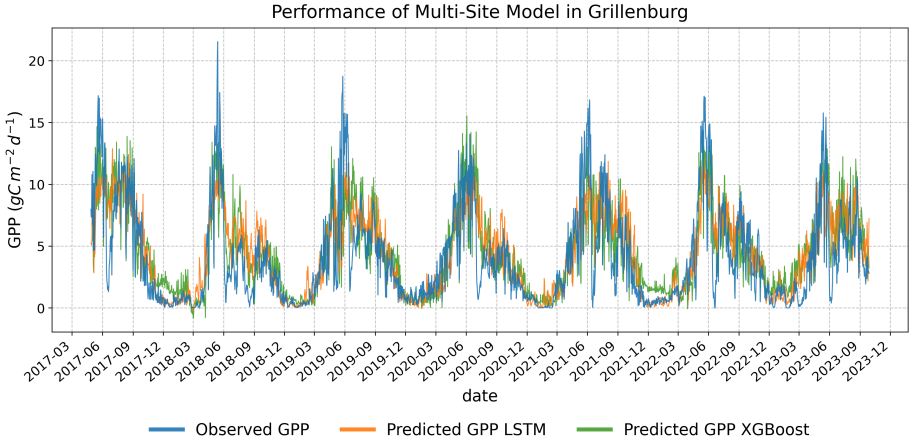

Figure B.4.: Predicted vs. observed values of GPP from Grillenburg. Observed GPP in blue, SARIMAX predictions in red, XGBoost predictions in green, and LSTM predictions in orange.

Table B.4.: Parameters used for the individual models.

Site	Order	Seasonal	(md, mcw)	$(L, \eta, \gamma, \alpha)$	$(L$, epochs)	(Unit1, Unit2, dropout)
Estrees Mons	(3,0,3)	(3,1,3,7)	(6,10)	(5, 0.01, 1, 1)	(3,50)	(128,32,0.2)
Hohes Holz	(3,0,3)	(3,1,3,7)	(6,5)	(5, 0.1, 0, 1)	(14,50)	(32,128,0.1)
Hyytiala	(1,0,1)	(3,1,3,30)	(4,1)	(7, 0.1, 0.1, 0.1)	(5,50)	(64,32,0.3)
Torgnon	(14,0,7)	(3,1,3,30)	(6,2)	(7, 0.2, 0, 5)	(5,50)	(32,128,0.3)

Table B.5.: Parameters used for the unified models.

SARIMAX		XGBoost		LSTM	
Order	Seasonal	(mc, mcw)	$(L, \eta, \gamma, \alpha)$	L, epochs	Unit1, Unit2, dropout
(3, 0, 1)	(3, 1, 3, 7)	(6, 5)	(7, 0.1, 0, 1)	(3, 50)	(128, 128, 0.2)

Table B.6.: XGBoost performance with global variables (unified model).

Site	Metrics	1st Train	2nd Train	3rd Train	4st Train
Estrees Mons	MSE	5.66	9.40	7.65	7.66
	RMSE	2.38	3.07	2.77	2.77
	MAE	1.88	2.22	1.96	1.96
	R2	0.70	0.50	0.59	0.59
Hohes Holz	MSE		4.20	4.12	4.12
	RMSE		2.05	2.03	2.03
	MAE		1 .55	1.37	1.37
	R2		0.86	0.86	0.86
Hyytiala	MSE			2.61	2.61
	RMSE			1.61	1.61
	MAE			1.11	1.11
	R2			0.76	0.76
Torgnon	MSE				3.01
	RMSE				1.77
	MAE				1.07
	R2				0.66
	Average MSE				4.34
	Average RMSE				2.04
	Average MAE				1.38
	Average R2				0.72

Table B.7.: LSTM performance metrics by site when sites are trained in alphabetic order (unified model).

Site	Metrics	1st Train	2nd Train	3rd Train	4st Train
Estrees Mons	MSE	9.66	10.15	7.47	21.58
	RMSE	3.11	3.19	2.73	4.65
	MAE	2.01	2.26	2.12	2.99
	R2	0.48	0.46	0.60	-0.15
Hohes Holz	MSE		6.73	5.53	0.18
	RMSE		2.59	2.3	4.94
	MAE		1.56	1.53	3.20
	R2		0.77	0.81	0.18
Hyytiala	MSE			2.87	11.45
	RMSE			1.70	3.38
	MAE			1.08	3.36
	R2			0.74	-0.04
Torgnon	MSE				1.27
	RMSE				1.13
	MAE				0.65
	R2				0.86
	Average MSE				14.68
	Average RMSE				3.52
	Average MAE				2.30
	Average R2				0.21

B

Table B.8.: LSTM performance with global variables (unified model).

Site	Metric	1^{st} Train	2^{nd} Train	3^{rd} Train	4^{th} Train
Hohes Holz	MSE	7.02	31.70	13.69	6.29
	RMSE	2.65	5.63	3.70	2.51
	MAE	1.78	3.78	2.44	1.58
	R^2	0.76	-0.07	0.54	0.79
Estrees Mons	MSE	7.38	15.76	28.82	
	RMSE	2.72	3.97	5.37	
	MAE	1.74	3.13	4.68	
	R^2	0.61	0.16	-0.54	
Torgnon	MSE		1.38	6.92	
	RMSE		1.17	2.63	
	MAE		0.72	1.56	
	R^2		0.84	0.21	
Hyytiala	MSE			2.16	
	RMSE			1.47	
	MAE			0.94	
	R^2			0.80	
Average	MSE			11.05	
	RMSE			2.99	
	MAE			2.19	
	R^2			0.30	

Curriculum Vitæ

Anna SPINOSA

Born in Noci and grew up in Castellana Grotte, I started my academic journey in classical studies. Back then, my days were filled with Greek and Latin verbs, philosophical debates, and literature. The fascination for nature and mathematics eventually surpassed my interest in the past, and guided my decision to enroll at university.

During my bachelors studies in Civil and Environmental Engineering at the Technical University of Bari, I worked on a theoretical thesis in which I combined literature review and simulations to understand the impact of wastewater discharge on the life of Posidonia oceanica in the Mediterranean Sea. That experience made me realize how much I enjoyed research, and it encouraged me to pursue a masters degree in Environmental Engineering at the same university, with a focus on coastal protection. During the master, I was introduced to satellite imagery for the first time. The idea that a single image could contain thousands of data points about vegetation health, water quality, or land use patterns fascinated me, and I decided to specialize in that field.

When I started looking for a PhD, I eventually landed at Deltares in Delft. There, I began working on a European project that required me to process and understand large volumes of satellite data. The first project I worked on grew into the third chapter of this thesis: the development of an algorithm for coastal retrieval using Sentinel-1 imagery. From there, my path continued quite naturally. I specialized further in the use and analysis of remote sensing data and in integrated monitoring approaches, combining data-driven remote sensing with monitoring and numerical model data. I am committed to addressing societal and environmental challenges within my research, and I strive to translate modeling outputs into accessible insights through visualization tools, digital platforms, workshops, and conferences.

Today, I work as an environmental researcher specialized in remote sensing data analysis for coastal water quality and ecosystem health monitoring. Alongside my PhD work, presented in this thesis, I have successfully led and contributed to several research and consultancy projects, including international projects for the European Commission and the European Space Agency. To promote multidisciplinary collaboration and address major challenges such as ecosystem recovery and climate change, I actively engage with international communities, including the Group on Earth Observations Biodiversity Observation Network (GEO BON), and the Water Youth Network (WYN). I also coordinated the GEO AquaWatch group at Deltares.

List of Publications

Journal papers related to this thesis work

- **Spinosa, A.**, Karisma, K., Eleveld, M., Fuentes-Monjaraz, M. A., Mobilia, V., Mallast, U., Peterseil, J., & El Serafy, G., Modelling gross primary productivity across different European ecosystem types: evaluating the versatility of SARIMAX, XGBoost, and LSTM using ICOS FLUXNET and Sentinel-2 data. Ecological Informatics, 96, 103820. **2026**. https://doi.org/10.1016/j.ecoinf.2026.103820.

- **Spinosa, A.**, Fuentes-Monjaraz, M. A., & El Serafy, G., Assessing the use of Sentinel-2 data for spatio-temporal upscaling of flux tower gross primary productivity measurements. Remote Sensing, 15(3), 562. **2023**. **2023**. https://doi.org/10.3390/rs15030562.

- **Spinosa, A.**, Ziemba, A., Saponieri, A., Damiani, L., & El Serafy, G., Remote sensing-based automatic detection of shoreline position: A case study in Apulia region. Journal of Marine Science and Engineering, 9(6), 575. **2021**. https://doi.org/10.3390/jmse9060575.

Conference paper

- **Spinosa, A.**, Eleveld, M., Mallast, U., Peterseil, J., Mobilia, V., Karisma, K., Fuentes-Monjaraz, M.A., & El Serafy, G., Automated Gross Primary Production Application for Monitoring Ecosystem Health Within GEOSS. *IGARSS 2024-2024 IEEE International Geoscience and Remote Sensing Symposium, pp. 4544-4547*. **2024**. doi:10.1109/IGARSS53475.2024.10642481. https://ieeexplore.ieee.org/document/10642481.

Additional journal papers

- Fernandes, J., Borja, A., Anabitarte, A., Granado, I., Lekunberri, X., Sagarminaga, Y., Canals, O., Lanzen, A., Azhar, M., Kotta, J., Ojaveer, H., **Spinosa, A.**, Ari-Pekka, J., Lumi, H., Stæhr, S. , Pérez, A., Inza, I., Villasante, S., Oanta, G. ,Silva, C., Tiller, R. ,Lilkendey, J., et al.. Towards trustworthy Artificial Intelligence in marine research, fisheries and environmental management. Fish and Fisheries, 27: 248-263. **2026**. https://doi.org/10.1111/faf.70052.

- Louise, F., Ari-Pekka, J., Vanderzande, D., Azhar, M., Berov, D., Carstensen, J., Drakopoulou, V., Gerakaris, V., Gundersen, H., Kotta, J.,; Mobilia, V., Prodanov, B., Papadopoulou, N., Reizopoulou, S., Smith, C., **Spinosa, A.**, Staehr, P. A. U., Upadhyay Stæhr, S., Todorova, V., Virtanen, E., & Vanhatalo, J., Comparative analysis of

species distribution modelling and remote sensing techniques in predicting spatial distribution of coastal habitats. Submitted to Remote Sensing of Environment. **Nov 2025**.

- El Serafy, G. Y., Schaeffer, B. A., Neely, M. B., **Spinosa, A.**, Odermatt, D., Weathers, K. C., ... & Tzortziou, M., Integrating inland and coastal water quality data for actionable knowledge. Remote Sensing, 13(15), 2899. **2021**. https://doi.org/10.3390/rs13152899.

- Shettigar, N. A., Bhattacharya, B., Mészáros, L., **Spinosa, A.**, & El Serafy, G., 3d ensemble simulation of seawater temperaturean application for aquaculture operations. Frontiers in Marine Science, 7, 592147. **2020**. https://doi.org/10.3389/fmars.2020.592147.

References

[1] United Nations. *Convention on Biological Diversity*. 1992. URL: https://www.cbd.int/doc/legal/cbd-en.pdf.

[2] WWF. *Living Planet Report 2024A System in Peril*. 2024.

[3] IPBES. *Global assessment report on biodiversity and ecosystem services of the Intergovernmental Science-Policy Platform on Biodiversity and Ecosystem Services*. Journal Article. 2019. URL: https://doi.org/10.5281/zenodo.3831673.

[4] V. H. Dale and S. C. Beyeler. "Challenges in the development and use of ecological indicators". In: *Ecological indicators* 1.1 (2001), pp. 3–10. URL: https://doi.org/10.1016/S1470-160X(01)00003-6.

[5] F. S. Chapin, P. A. Matson, H. A. Mooney, and P. M. Vitousek. *Principles of terrestrial ecosystem ecology*. 2002. DOI: 10.1007/978-1-4419-9504-9_1.

[6] R. Costanza, R. d'Arge, R. de Groot, S. Farber, M. Grasso, B. Hannon, K. Limburg, S. Naeem, R. V. O'Neill, and J. Paruelo. "The value of the world's ecosystem services and natural capital". In: *Nature* 387.6630 (1997), pp. 253–260. ISSN: 0028-0836. URL: https://doi.org/10.1038/387253a0.

[7] FAO. *Forests: nature-based solutions for water*. 2019. URL: https://openknowledge.fao.org/server/api/core/bitstreams/54d08ac1-c0d8-4953-b0d8-04bf32b7bbcf/content.

[8] Ramsar Convention Secretariat. *The Ramsar Convention Manual: A Guide to the Convention on Wetlands (Ramsar, Iran, 1971)*. Gland, Switzerland, 2013. URL: https://www.ramsar.org/sites/default/files/documents/library/manual6-2013-e.pdf.

[9] European Environment Agency. *State of nature in the EU. Results from reporting under the nature directives 2013-2018*. Journal Article. 2020. DOI: 10.2800/705440.

[10] H. M. Pereira, L. M. Navarro, and I. S. Martins. "Global biodiversity change: the bad, the good, and the unknown". In: *Annual Review of Environment and Resources* 37 (2012), pp. 25–50. ISSN: 1543-5938. URL: https://doi.org/10.1146/annurev-environ-042911-093511.

[11] S. Díaz, J. Settele, E. S. Brondízio, H. T. Ngo, J. Agard, A. Arneth, P. Balvanera, K. A. Brauman, S. H. Butchart, K. M. Chan, *et al.* "Pervasive human-driven decline of life on Earth points to the need for transformative change". In: *Science* 366.6471 (2019), eaax3100. DOI: 10.1126/science.aax3100.

[12] G. Ceballos, P. R. Ehrlich, A. D. Barnosky, A. García, R. M. Pringle, and T. M. Palmer. "Accelerated modern human–induced species losses: Entering the sixth mass extinction". In: *Science advances* 1.5 (2015), e1400253. DOI: 10.1126/sciadv.1400253.

[13] H. Mooney, A. Larigauderie, M. Cesario, T. Elmquist, O. Hoegh-Guldberg, S. Lavorel, G. M. Mace, M. Palmer, R. Scholes, and T. Yahara. "Biodiversity, climate change, and ecosystem services". In: *Current Opinion in Environmental Sustainability* 1.1 (2009), pp. 46–54. ISSN: 1877-3435. URL: https://doi.org/10.1016/j.cosust.2009.07.006.

[14] A. Marques, I. S. Martins, T. Kastner, C. Plutzar, M. C. Theurl, N. Eisenmenger, M. A. Huijbregts, R. Wood, K. Stadler, M. Bruckner, *et al.* "Increasing impacts of land use on biodiversity and carbon sequestration driven by population and economic growth". In: *Nature Ecology & Evolution* 3.4 (2019), pp. 628–637. URL: https://doi.org/10.1038/s41559-019-0824-3.

[15] F. E. MullerKarger, E. Hestir, C. Ade, K. Turpie, D. A. Roberts, D. Siegel, R. J. Miller, D. Humm, N. Izenberg, and M. Keller. "Satellite sensor requirements for monitoring essential biodiversity variables of coastal ecosystems". In: *Ecological applications* 28.3 (2018), pp. 749–760. ISSN: 1051-0761. URL: https://doi.org/10.1002/eap.1682.

[16] S. E. Rees, N. L. Foster, O. Langmead, S. Pittman, and D. E. Johnson. "Defining the qualitative elements of Aichi Biodiversity Target 11 with regard to the marine and coastal environment in order to strengthen global efforts for marine biodiversity conservation outlined in the United Nations Sustainable Development Goal 14". In: *Marine Policy* 93 (2018), pp. 241–250. ISSN: 0308-597X. URL: https://doi.org/10.1016/j.marpol.2017.05.016.

[17] L. M. Navarro, N. Fernández, C. Guerra, R. Guralnick, W. D. Kissling, M. C. Londoño, F. Muller-Karger, E. Turak, P. Balvanera, M. J. Costello, *et al.* "Monitoring biodiversity change through effective global coordination". In: *Current Opinion in Environmental Sustainability* 29 (2017), pp. 158–169. DOI: 10.1016/j.cosust.2018.02.005.

[18] G. Stark, J. Dertien, N. R. Poulsen, E. Berti, A. C. M. Guijarro, M. Weissgerber, N. Fernandez, and H. M. Pereira. "The Hidden Costs of Climate Change Tracking: Climate Velocity, Movement Energetics, and Connectivity in European Protected Areas". In: *bioRxiv* (2026). DOI: 10.64898/2026.04.20.719608.

[19] CBD. *The Strategic Plan for Biodiversity 2011-2020 and the Aichi Biodiversity Targets*. 2010. URL: https://www.cbd.int/doc/decisions/cop-10/cop-10-dec-02-en.pdf.

[20] UNEP. *Indicators for the Strategic Plan for Biodiversity 2011-2020 and the Aichi Biodiversity Targets*. 2016. URL: https://www.cbd.int/doc/decisions/cop-13/cop-13-dec-28-en.pdf.

[21] United Nations. *Transforming our world: the 2030 Agenda for Sustainable Development*. 2015. URL: https://docs.un.org/en/A/RES/70/1.

[22] European Commission. *Our Life Insurance, Our Natural Capital: An EU Biodiversity Strategy to 2020*. COM/2011/0244 final. 2011.

[23] European Parliament and Council of the European Union. *Directive 2008/56/EC of the European Parliament and of the Council of 17 June 2008 establishing a framework for community action in the field of marine environmental policy (Marine Strategy Framework Directive)*. 2008. URL: https://eur-lex.europa.eu/eli/dir/2008/56/oj/eng.

[24] European Commission. *EU Biodiversity Strategy for 2030: Bringing nature back into our lives*. 2020. URL: https://environment.ec.europa.eu/strategy/biodiversity-strategy-2030_en.

[25] European Parliament and Council of the European Union. *Directive 2009/147/EC on the conservation of wild birds*. Official Journal of the European Union L 20. Originally adopted 1979, amended version 2009. 2009.

[26] Council of the European Communities. *Directive 92/43/EEC on the conservation of natural habitats and of wild fauna and flora*. Official Journal of the European Communities L 206. 1992.

[27] European Commission. *Communication from the Commission to the European Parliament, the Council, the European Economic and Social Committee and the Committee of the Regions: EU Pollinators Initiative*. COM(2018) 395 final. 2018. URL: https://eur-lex.europa.eu/legal-content/EN/TXT/?uri=CELEX:52018DC0395.

[28] European Commission. *Communication from the Commission to the European Parliament, the European Council, the Council, the European Economic and Social Committee and the Committee of the Regions: The European Green Deal*. COM(2019) 640 final. 2019. URL: https://eur-lex.europa.eu/legal-content/EN/TXT/?uri=CELEX:52019DC0640.

[29] European Commission. *Regulation (EU) 2024/1991 of the European Parliament and of the Council of 24 June 2024 on nature restoration and amending Regulation (EU) 2022/869*. 2024. URL: http://data.europa.eu/eli/reg/2024/1991/oj.

[30] S. Broszeit, N. J. Beaumont, M. C. Uyarra, A.-S. Heiskanen, M. Frost, P. J. Somerfield, A. G. Rossberg, H. Teixeira, and M. C. Austen. "What can indicators of good environmental status tell us about ecosystem services?: Reducing efforts and increasing cost-effectiveness by reapplying biodiversity indicator data". In: *Ecological indicators* 81 (2017), pp. 409–442. URL: https://doi.org/10.1016/j.ecolind.2017.05.057.

[31] European Commission. *Communication from the Commission to the European Parliament, the Council, the European Economic and Social Committee and the Committee of the Regions: New EU Forest Strategy for 2030*. SWD(2021) 651 final - SWD(2021) 652 final. 2021. URL: https://eur-lex.europa.eu/legal-content/EN/TXT/?uri=CELEX%3A52021DC0082.

[32] R. Danovaro, L. Carugati, M. Berzano, A. E. Cahill, S. Carvalho, A. Chenuil, C. Corinaldesi, S. Cristina, R. David, A. Dell'Anno, *et al.* "Implementing and innovating marine monitoring approaches for assessing marine environmental status". In: *Frontiers in Marine Science* 3 (2016), p. 213. URL: https://doi.org/10.3389/fmars.2016.00213.

[33] G. Y. El Serafy, B. A. Schaeffer, M.-B. Neely, A. Spinosa, D. Odermatt, K. C. Weathers, T. Baracchini, D. Bouffard, L. Carvalho, R. N. Conmy, *et al.* "Integrating inland and coastal water quality data for actionable knowledge". In: *Remote Sensing* 13.15 (2021), p. 2899. URL: https://doi.org/10.3390/rs13152899.

[34] Y. Zeng, D. Hao, A. Huete, B. Dechant, J. Berry, J. M. Chen, J. Joiner, C. Frankenberg, B. Bond-Lamberty, and Y. Ryu. "Optical vegetation indices for monitoring terrestrial ecosystems globally". In: *Nature Reviews Earth & Environment* (2022), pp. 1–17. ISSN: 2662-138X. DOI: 10.1038/s43017-022-00298-5.

[35] N. Pettorelli, H. Schulte to Bühne, A. Tulloch, G. Dubois, C. MacinnisNg, A. M. Queirós, D. A. Keith, M. Wegmann, F. Schrodt, and M. Stellmes. "Satellite remote sensing of ecosystem functions: opportunities, challenges and way forward". In: *Remote Sensing in Ecology and Conservation* 4.2 (2018), pp. 71–93. ISSN: 2056-3485. DOI: 10.1002/rse2.59.

[36] A. K. Skidmore, N. Pettorelli, N. C. Coops, G. N. Geller, M. Hansen, R. Lucas, C. A. Mücher, B. O'Connor, M. Paganini, H. M. Pereira, *et al.* "Environmental science: Agree on biodiversity metrics to track from space". In: *Nature* 523.7561 (2015), pp. 403–405. URL: https://doi.org/10.1038/523403a.

[37] N. Pettorelli, M. Wegmann, A. Skidmore, S. Mücher, T. P. Dawson, M. Fernandez, R. Lucas, M. E. Schaepman, T. Wang, B. O'Connor, *et al.* "Framing the concept of satellite remote sensing essential biodiversity variables: challenges and future directions". In: *Remote Sensing in Ecology and Conservation* 2.3 (2016), pp. 122–131. URL: https://doi.org/10.1002/rse2.15.

[38] H. M. Pereira, S. Ferrier, M. Walters, G. N. Geller, R. H. Jongman, R. J. Scholes, M. W. Bruford, N. Brummitt, S. H. Butchart, and A. Cardoso. "Essential biodiversity variables". In: *Science* 339.6117 (2013), pp. 277–278. ISSN: 0036-8075. DOI: 10.1126/science.1229931.

[39] J. Cabello, N. Fernández, D. Alcaraz-Segura, C. Oyonarte, G. Pineiro, A. Altesor, M. Delibes, and J. M. Paruelo. "The ecosystem functioning dimension in conservation: insights from remote sensing". In: *Biodiversity and Conservation* 21 (2012), pp. 3287–3305. DOI: 10.1007/s10531-012-0370-7.

[40] J. Cabello, P. Mairota, D. Alcaraz-Segura, S. Arenas-Castro, P. Escribano, P. J. Leitão, J. Martínez-López, A. Regos, and J. M. Requena-Mullor. "Satellite Remote Sensing of Ecosystem Functions: Opportunities and Challenges for Reporting Obligations of the EU Habitat Directive". In: *IGARSS 2018 - 2018 IEEE International Geoscience and Remote Sensing Symposium*, pp. 6604–6607. ISBN: 2153-7003. DOI: 10.1109/IGARSS.2018.8517296.

[41] A. Ishtiaque, A. Masrur, Y. W. Rabby, T. Jerin, and A. Dewan. "Remote sensing-based research for monitoring progress towards SDG 15 in Bangladesh: A review". In: *Remote sensing* 12.4 (2020), p. 691. ISSN: 2072-4292. DOI: 10.3390/rs12040691.

[42] J. Maso, A. Zabala, and I. Serral. "Earth observations for sustainable development goals". In: *Remote Sensing* 15.10 (2023), p. 2570. URL: https://doi.org/10.3390/rs15102570.

[43] IOCCG. *Synergy between Ocean Colour and Biogeochemical/Ecosystem Models*. Ed. by S. Dutkiewicz. IOCCG Report Series 19. Dartmouth, Canada: International Ocean Colour Coordinating Group, 2020. DOI: 10.25607/OBP-711.

[44] E. M. Jones, M. E. Baird, M. Mongin, J. Parslow, J. Skerratt, J. Lovell, N. Margvelashvili, R. J. Matear, K. Wild-Allen, B. Robson, *et al.* "Use of remote-sensing reflectance to constrain a data assimilating marine biogeochemical model of the Great Barrier Reef". In: *Biogeosciences* 13.23 (2016), pp. 6441–6469. URL: https://doi.org/10.5194/bg-13-6441-2016.

[45] D. Pasetto, S. Arenas-Castro, J. Bustamante, R. Casagrandi, N. Chrysoulakis, A. F. Cord, A. Dittrich, C. Domingo-Marimon, G. El Serafy, A. Karnieli, *et al.* "Integration of satellite remote sensing data in ecosystem modelling at local scales: Practices and trends". In: *Methods in Ecology and Evolution* 9.8 (2018), pp. 1810–1821. URL: https://doi.org/10.1111/2041-210X.13018.

[46] M. Reichstein, G. Camps-Valls, B. Stevens, M. Jung, J. Denzler, N. Carvalhais, and F. Prabhat. "Deep learning and process understanding for data-driven Earth system science". In: *Nature* 566.7743 (2019), pp. 195–204. URL: https://doi.org/10.1038/s41586-019-0912-1.

[47] European Commission. *Regulation (EU) 2024/1689 of the European Parliament and of the Council of 13 June 2024 laying down harmonised rules on artificial intelligence and amending Regulations (EC): Artificial Intelligence Act*. Text with EEA relevance. No 300/2008, (EU) No 167/2013, (EU) No 168/2013, (EU) 2018/858, (EU) 2018/1139 and (EU) 2019/2144 and Directives 2014/90/EU, (EU) 2016/797 and (EU) 2020/1828. 2024. URL: https://eur-lex.europa.eu/eli/reg/2024/1689/oj/eng.

[48] M. Lenzerini. "Data integration: A theoretical perspective". In: *Proceedings of the twenty-first ACM SIGMOD-SIGACT-SIGART symposium on Principles of database systems*. 2002, pp. 233–246. DOI: 10.1145/543613.543644.

[49] R. Hull. "Managing semantic heterogeneity in databases: a theoretical prospective". In: *Proceedings of the sixteenth ACM SIGACT-SIGMOD-SIGART symposium on Principles of database systems*. 1997, pp. 51–61. URL: https://doi.org/10.1145/263661.263668.

[50] J. A. Fernandes-Salvador, A. Borja, A. Anabitarte, I. Granado, X. Lekunberri, Y. Sagarminaga, O. Canals, A. Lanzen, M. Azhar, J. Kotta, *et al.* "Towards Trustworthy Artificial Intelligence for Marine Research, Fisheries and Environmental Management". In: *Fish and Fisheries* (2026). URL: https://doi.org/10.1111/faf.70052.

[51] J. Lintz and D. S. Simonett. *Remote Sensing of Environment*. Reading, MA: Addison-Wesley, 1976, p. 694.

[52] J. C. Ho, A. M. Michalak, and N. Pahlevan. "Widespread global increase in intense lake phytoplankton blooms since the 1980s". In: *Nature* 574.7780 (2019), pp. 667–670. URL: https://doi.org/10.1038/s41586-019-1648-7.

[53] N. Pahlevan, S. Sarkar, B. A. Franz, S. V. Balasubramanian, and J. He. "Sentinel-2 MultiSpectral Instrument (MSI) data processing for aquatic science applications: Demonstrations and validations". In: *Remote Sensing of Environment* 201 (2017), pp. 47–56. URL: https://doi.org/10.1016/j.rse.2017.08.033.

[54] Y. Yu, C. Wang, Q. Fu, R. Kou, F. Huang, B. Yang, T. Yang, and M. Gao. "Techniques and challenges of image segmentation: A review". In: *Electronics* 12.5 (2023), p. 1199. URL: https://doi.org/10.3390/electronics12051199.

[55] V. Dey, Y. Zhang, and M. Zhong. *A review on image segmentation techniques with remote sensing perspective*. Vol. 38. na Vienna, Austria, 2010. URL: https://www.isprs.org/proceedings/xxxviii/part7/a/pdf/31_xxxviii-part7a.pdf.

[56] D. Kaur and Y. Kaur. "Various image segmentation techniques: a review". In: *International Journal of Computer Science and Mobile Computing* 3.5 (2014), pp. 809–814. URL: https://ijcsmc.com/docs/papers/May2014/V3I5201499a84.pdf.

[57] M. Ciecholewski. "Review of segmentation methods for coastline detection in SAR images". In: *Archives of Computational Methods in Engineering* 31.2 (2024), pp. 839–869. URL: https://doi.org/10.1007/s11831-023-10000-7.

[58] C. Xu and J. L. Prince. "Snakes, shapes, and gradient vector flow". In: *IEEE Transactions on image processing* 7.3 (1998), pp. 359–369. DOI: 10.1109/83.661186.

[59] Y. Chen, P. Ge, G. Wang, G. Weng, and H. Chen. "An overview of intelligent image segmentation using active contour models". In: *Intell. Robot* 3.1 (2023), pp. 23–55. URL: http://dx.doi.org/10.20517/ir.2023.02.

[60] O. Ronneberger, P. Fischer, and T. Brox. "U-net: Convolutional networks for biomedical image segmentation". In: *Medical image computing and computer-assisted intervention–MICCAI 2015: 18th international conference, Munich, Germany, October 5-9, 2015, proceedings, part III 18*. Springer. 2015, pp. 234–241. DOI: 10.1007/978-3-319-24574-4_28.

[61] N. Siddique, S. Paheding, C. P. Elkin, and V. Devabhaktuni. "U-net and its variants for medical image segmentation: A review of theory and applications". In: *IEEE access* 9 (2021), pp. 82031–82057. DOI: 10.1109/ACCESS.2021.3086020.

[62] N. Otsu. "A threshold selection method from gray-level histograms." In: *IEEE transactions on Systems, Man, and Cybernetics* (1979), pp. 62–66. DOI: 10.1109/TSMC.1979.4310076.

[63] J.-S. Lee, L. Jurkevich, P. Dewaele, P. Wambacq, and A. Oosterlinck. "Speckle filtering of synthetic aperture radar images: A review". In: *Remote Sensing Reviews* 8.4 (1994), pp. 313–340. URL: https://doi.org/10.1080/02757259409532206.

[64] H.-J. He, C. Zheng, and D.-W. Sun. “Image segmentation techniques”. In: *Computer Vision Technology for Food Quality Evaluation*. Elsevier, 2016, pp. 45–63. URL: https://doi.org/10.1016/B978-0-12-802232-0.00002-5.

[65] T. Huang, G. J. T. G. Y. Yang, and G. Tang. “A fast two-dimensional median filtering algorithm”. In: *IEEE Transactions on Acoustics, Speech, and Signal Processing* 27.1 (1979), pp. 13–18. DOI: 10.1109/TASSP.1979.1163188.

[66] D. T. Kuan, A. A. Sawchuk, T. C. Strand, and P. Chavel. “Adaptive noise smoothing filter for images with signal-dependent noise”. In: *IEEE Transactions on Pattern Analysis and Machine Intelligence* 2 (1985), pp. 165–177. DOI: 10.1109/TPAMI.1985.4767641.

[67] V. S. Frost, J. A. Stiles, K. S. Shanmugan, and J. C. Holtzman. “A model for radar images and its application to adaptive digital filtering of multiplicative noise”. In: *IEEE Transactions on Pattern Analysis & Machine Intelligence* 2 (1982), pp. 157–166. DOI: 10.1109/tpami.1982.4767223.

[68] A. Lopes, E. Nezry, R. Touzi, and H. Laur. “Structure detection and statistical adaptive speckle filtering in SAR images”. In: *International Journal of Remote Sensing* 14.9 (1993), pp. 1735–1758. URL: https://doi.org/10.1080/01431169308953999.

[69] M. I. Jordan and T. M. Mitchell. “Machine learning: Trends, perspectives, and prospects”. In: *Science* 349.6245 (2015), pp. 255–260. DOI: 10.1126/science.aaa841.

[70] A. Moreno-Rodenas, K. Verbist, A. Mertens, I. Gerritsma, J. Deng, A. Haag, Ü. Taner, J. D. Nuttall, R. Dahm, A. Meshgi, *et al. AI Applications for Water Management: A Comprehensive Review*. UNESCO, 2025. DOI: 10.54677/VGVL7976.

[71] T. Mitchell. *Machine Learning*. McGraw-Hill International Editions. McGraw-Hill, 1997. ISBN: 9780071154673. URL: https://books.google.nl/books?id=EoYBngEACAAJ.

[72] Y. LeCun, Y. Bengio, and G. Hinton. “Deep learning”. In: *nature* 521.7553 (2015), pp. 436–444. URL: https://doi.org/10.1038/nature14539.

[73] F. Chollet. *Deep learning with Python*. ISBN: 9781617296864. Simon and Schuster, 2021.

[74] M. Belkin, D. Hsu, S. Ma, and S. Mandal. “Reconciling modern machine-learning practice and the classical bias–variance trade-off”. In: *Proceedings of the National Academy of Sciences* 116.32 (2019), pp. 15849–15854. URL: https://doi.org/10.48550/arXiv.1812.11118.

[75] B. Ding, H. Qian, and J. Zhou. “Activation functions and their characteristics in deep neural networks”. In: *2018 Chinese control and decision conference (CCDC)*. IEEE. 2018, pp. 1836–1841. DOI: 10.1109/CCDC.2018.8407425.

[76] S. Hochreiter and J. Schmidhuber. “Long short-term memory”. In: *Neural computation* 9.8 (1997), pp. 1735–1780. DOI: 10.1162/neco.1997.9.8.1735.

[77] T. K. Ho. “Random decision forests”. In: *Proceedings of 3rd international conference on document analysis and recognition*. Vol. 1. IEEE. 1995, pp. 278–282. DOI: 10.1109/ICDAR.1995.598994.

[78] T. Chen and C. Guestrin. “XGBoost: A Scalable Tree Boosting System”. In: *Proceedings of the 22nd ACM SIGKDD International Conference on Knowledge Discovery and Data Mining*. 2016, pp. 785–794. DOI: 10.1145/2939672.2939785.

[79] M. E. Celebi. “Improving the performance of k-means for color quantization”. In: *Image and Vision Computing* 29.4 (2011), pp. 260–271. URL: https://doi.org/10.1016/j.imavis.2010.10.002.

[80] M. E. Celebi, H. A. Kingravi, and P. A. Vela. “A comparative study of efficient initialization methods for the k-means clustering algorithm”. In: *Expert systems with applications* 40.1 (2013), pp. 200–210. URL: https://doi.org/10.1016/j.eswa.2012.07.021.

[81] D. Arthur and S. Vassilvitskii. “k-means++: The Advantages of Careful Seeding”. In: *Proceedings of the Eighteenth Annual ACM-SIAM Symposium on Discrete Algorithms (SODA)*. Society for Industrial and Applied Mathematics, 2007, pp. 1027–1035.

[82] R. S. Sutton, A. G. Barto, *et al. Reinforcement learning: An introduction*. Vol. 1. 1. MIT press Cambridge, 1998. URL: https://doi.org/10.1017/S0263574799271172.

[83] L. P. Kaelbling, M. L. Littman, and A. W. Moore. “Reinforcement learning: A survey”. In: *Journal of artificial intelligence research* 4 (1996), pp. 237–285. URL: https://doi.org/10.1613/jair.301.

[84] G. E. P. Box and G. M. Jenkins. *Time Series Analysis: Forecasting and Control*. San Francisco: Holden-Day, 1970.

[85] V. Gornitz. “Global coastal hazards from future sea level rise”. In: *Palaeogeography, Palaeoclimatology, Palaeoecology* 89.4 (1991), pp. 379–398. URL: https://doi.org/10.1016/0031-0182(91)90173-O.

[86] C. D. Harley, A. Randall Hughes, K. M. Hultgren, B. G. Miner, C. J. Sorte, C. S. Thornber, L. F. Rodriguez, L. Tomanek, and S. L. Williams. “The impacts of climate change in coastal marine systems”. In: *Ecology letters* 9.2 (2006), pp. 228–241. DOI: 10.1111/j.1461-0248.2005.00871.x.

[87] Y. S. Androulidakis, K. D. Kombiadou, C. V. Makris, V. N. Baltikas, and Y. N. Krestenitis. “Storm surges in the Mediterranean Sea: Variability and trends under future climatic conditions”. In: *Dynamics of Atmospheres and Oceans* 71 (2015), pp. 56–82. URL: https://doi.org/10.1016/j.dynatmoce.2015.06.001.

[88] S. E. Saye, D. Van der Wal, K. Pye, and S. J. Blott. “Beach–dune morphological relationships and erosion/accretion: an investigation at five sites in England and Wales using LIDAR data”. In: *Geomorphology* 72.1-4 (2005), pp. 128–155. URL: https://doi.org/10.1016/j.geomorph.2005.05.007.

[89] C. M. Duarte, I. J. Losada, I. E. Hendriks, I. Mazarrasa, and N. Marbà. "The role of coastal plant communities for climate change mitigation and adaptation". In: *Nature Climate Change* 3.11 (2013), p. 961. URL: https://doi.org/10.1038/nclimate1970.

[90] D. M. Alongi. "Mangrove forests: resilience, protection from tsunamis, and responses to global climate change". In: *Estuarine, Coastal and Shelf Science* 76.1 (2008), pp. 1–13. URL: https://doi.org/10.1016/j.ecss.2007.08.024.

[91] F. Antonioli, M. Anzidei, A. Amorosi, V. L. Presti, G. Mastronuzzi, G. Deiana, G. De Falco, A. Fontana, G. Fontolan, S. Lisco, *et al.* "Sea-level rise and potential drowning of the Italian coastal plains: Flooding risk scenarios for 2100". In: *Quaternary Science Reviews* 158 (2017), pp. 29–43. URL: https://doi.org/10.1016/j.quascirev.2016.12.021.

[92] M. F. Bruno, A. Saponieri, M. G. Molfetta, and L. Damiani. "The DPSIR Approach for Coastal Risk Assessment under Climate Change at Regional Scale: The Case of Apulian Coast (Italy)". In: *Journal of Marine Science and Engineering* 8.7 (2020), p. 531. URL: https://doi.org/10.3390/jmse8070531.

[93] M. Maiolo, R. A. Mel, and S. Sinopoli. "A Stepwise Approach to Beach Restoration at Calabaia Beach". In: *Water* 12.10 (2020), p. 2677. URL: https://doi.org/10.3390/w12102677.

[94] L. Sinay and R. Carter. "Climate change adaptation options for coastal communities and local governments". In: *Climate* 8.1 (2020), p. 7. URL: https://doi.org/10.3390/cli8010007.

[95] S. Temmerman, P. Meire, T. J. Bouma, P. M. Herman, T. Ysebaert, and H. J. De Vriend. "Ecosystem-based coastal defence in the face of global change". In: *Nature* 504.7478 (2013), pp. 79–83. URL: https://doi.org/10.1038/nature12859.

[96] A. P. Young and S. A. Ashford. "Application of airborne LIDAR for seacliff volumetric change and beach-sediment budget contributions". In: *Journal of Coastal Research* (2006), pp. 307–318. URL: https://doi.org/10.2112/05-0548.1.

[97] M. J. Stive, S. G. Aarninkhof, L. Hamm, H. Hanson, M. Larson, K. M. Wijnberg, R. J. Nicholls, and M. Capobianco. "Variability of shore and shoreline evolution". In: *Coastal engineering* 47.2 (2002), pp. 211–235. URL: https://doi.org/10.1016/S0378-3839(02)00126-6.

[98] G. Anfuso, E. Pranzini, and G. Vitale. "An integrated approach to coastal erosion problems in northern Tuscany (Italy): littoral morphological evolution and cell distribution". In: *Geomorphology* 129.3-4 (2011), pp. 204–214. URL: https://doi.org/10.1016/j.geomorph.2011.01.023.

[99] R. Dolan, B. P. Hayden, P. May, and S. May. "The reliability of shoreline change measurements from aerial photographs". In: *Shore and beach* 48.4 (1980), pp. 22–29.

[100] E. H. Boak and I. L. Turner. “Shoreline definition and detection: a review”. In: *Journal of coastal research* (2005), pp. 688–703. URL: https://doi.org/10.2112/03-0071.1.

[101] R. Dolan, B. Hayden, and J. Heywood. “Analysis of coastal erosion and storm surge hazards”. In: *Coastal Engineering* 2 (1978), pp. 41–53. URL: https://doi.org/10.1016/0378-3839(78)90004-2.

[102] J. A. G. Cooper and F. Navas. “Natural bathymetric change as a control on century-scale shoreline behavior”. In: *Geology* 32.6 (2004), pp. 513–516. URL: https://doi.org/10.1130/G20377.1.

[103] S. A. White and Y. Wang. “Utilizing DEMs derived from LIDAR data to analyze morphologic change in the North Carolina coastline”. In: *Remote Sensing of Environment* 85.1 (2003), pp. 39–47. URL: https://doi.org/10.1016/S0034-4257(02)00185-2.

[104] D. O. Nitti, R. Nutricato, R. Lorusso, N. Lombardi, F. Bovenga, M. F. Bruno, M. T. Chiaradia, and G. Milillo. “On the geolocation accuracy of COSMO-SkyMed products”. In: *SAR Image Analysis, Modeling, and Techniques XV*. Vol. 9642. International Society for Optics and Photonics. 2015, p. 96420D. URL: https://doi.org/10.1117/12.2196870.

[105] A. Luijendijk, G. Hagenaars, R. Ranasinghe, F. Baart, G. Donchyts, and S. Aarninkhof. “The state of the worlds beaches”. In: *Scientific Reports* 8.1 (2018), pp. 1–11. URL: https://doi.org/10.1038/s41598-018-24630-6.

[106] K. Vos, K. D. Splinter, M. D. Harley, J. A. Simmons, and I. L. Turner. “CoastSat: A Google Earth Engine-enabled Python toolkit to extract shorelines from publicly available satellite imagery”. In: *Environmental Modelling & Software* 122 (2019), p. 104528. URL: https://doi.org/10.1016/j.envsoft.2019.104528.

[107] K. Vos, M. D. Harley, K. D. Splinter, J. A. Simmons, and I. L. Turner. “Sub-annual to multi-decadal shoreline variability from publicly available satellite imagery”. In: *Coastal Engineering* 150 (2019), pp. 160–174. URL: https://doi.org/10.1016/j.coastaleng.2019.04.004.

[108] G. García-Rubio, D. Huntley, and P. Russell. “Evaluating shoreline identification using optical satellite images”. In: *Marine Geology* 359 (2015), pp. 96–105. URL: https://doi.org/10.1016/j.margeo.2014.11.002.

[109] X. Wei, W. Zheng, C. Xi, and S. Shang. “Shoreline Extraction in SAR Image Based on Advanced Geometric Active Contour Model”. In: *Remote Sensing* 13.4 (2021), p. 642. URL: https://doi.org/10.3390/rs13040642.

[110] S. Zollini, M. Alicandro, M. Cuevas-González, V. Baiocchi, D. Dominici, and P. M. Buscema. “Shoreline extraction based on an active connection matrix (ACM) image enhancement strategy”. In: *Journal of Marine Science and Engineering* 8.1 (2020), p. 9. URL: https://doi.org/10.3390/jmse8010009.

[111] J. E. Pardo-Pascual, J. Almonacid-Caballer, L. A. Ruiz, and J. Palomar-Vázquez. "Automatic extraction of shorelines from Landsat TM and ETM+ multi-temporal images with subpixel precision". In: *Remote Sensing of Environment* 123 (2012), pp. 1–11. URL: https://doi.org/10.1016/j.rse.2012.02.024.

[112] N. Valentini, A. Saponieri, and L. Damiani. "A new video monitoring system in support of Coastal Zone Management at Apulia Region, Italy". In: *Ocean & Coastal Management* 142 (2017), pp. 122–135. URL: https://doi.org/10.1016/j.ocecoaman.2017.03.032.

[113] L. Damiani and M. G. Molfetta. "A video based technique for shoreline monitoring in Alimini (LE)". In: *Coastlab0* 8 (2008), pp. 153–156.

[114] K. D. Splinter, M. D. Harley, and I. L. Turner. "Remote sensing is changing our view of the coast: Insights from 40 years of monitoring at Narrabeen-Collaroy, Australia". In: *Remote Sensing* 10.11 (2018), p. 1744. URL: https://doi.org/10.3390/rs10111744.

[115] R. A. Holman and J. Stanley. "The history and technical capabilities of Argus". In: *Coastal engineering* 54.6-7 (2007), pp. 477–491. URL: https://doi.org/10.1016/j.coastaleng.2007.01.003.

[116] R. A. Morton, M. P. Leach, J. G. Paine, and M. A. Cardoza. "Monitoring beach changes using GPS surveying techniques". In: *Journal of Coastal Research* (1993), pp. 702–720.

[117] G. Medellín, A. Torres-Freyermuth, G. R. Tomasicchio, A. Francone, P. A. Tereszkiewicz, L. Lusito, L. Palemón-Arcos, and J. López. "Field and Numerical Study of Resistance and Resilience on a Sea Breeze Dominated Beach in Yucatan (Mexico)". In: *Water* 10.12 (2018). URL: https://www.mdpi.com/2073-4441/10/12/1806.

[118] G. R. Tomasicchio, A. Francone, D. J. Simmonds, F. DAlessandro, and F. Frega. "Prediction of Shoreline Evolution. Reliability of a General Model for the Mixed Beach Case". In: *Journal of Marine Science and Engineering* 8.5 (2020). DOI: 10.3390/jmse8050361.

[119] S. Dellepiane, R. De Laurentiis, and F. Giordano. "Coastline extraction from SAR images and a method for the evaluation of the coastline precision". In: *Pattern Recognition Letters* 25.13 (2004), pp. 1461–1470. URL: https://doi.org/10.1016/j.patrec.2004.05.022.

[120] N. Valentini, A. Saponieri, M. G. Molfetta, and L. Damiani. "New algorithms for shoreline monitoring from coastal video systems." In: *Earth Science Informatics* 10.4 (2017), pp. 495–506. URL: https://doi.org/10.1007/s12145-017-0302-x.

[121] S. G. Aarninkhof, I. L. Turner, T. D. Dronkers, M. Caljouw, and L. Nipius. "A video-based technique for mapping intertidal beach bathymetry". In: *Coastal Engineering* 49.4 (2003), pp. 275–289. URL: https://doi.org/10.1016/S0378-3839(03)00064-4.

[122] T. Aagaard and J. Holm. “Digitization of wave run-up using video records”. In: *Journal of Coastal Research* (1989), pp. 547–551.

[123] M. I. Vousdoukas, D. Wziatek, and L. P. Almeida. “Coastal vulnerability assessment based on video wave run-up observations at a mesotidal, steep-sloped beach”. In: *Ocean Dynamics* 62.1 (2012), pp. 123–137. URL: https://doi.org/10.1007/s10236-011-0480-x.

[124] A. Hoitink, Z. Wang, B. Vermeulen, Y. Huismans, and K. Kästner. “Tidal controls on river delta morphology”. In: *Nature geoscience* 10.9 (2017), pp. 637–645. URL: https://doi.org/10.1038/ngeo3000.

[125] M. Moulton, S. Elgar, B. Raubenheimer, J. C. Warner, and N. Kumar. “Rip currents and alongshore flows in single channels dredged in the surf zone”. In: *Journal of Geophysical Research: Oceans* 122.5 (2017), pp. 3799–3816. URL: https://doi.org/10.1002/2016JC012222.

[126] R. Medina, I. Marino-Tapia, A. Osorio, M. Davidson, and F. Martin. “Management of dynamic navigational channels using video techniques”. In: *Coastal Engineering* 54.6-7 (2007), pp. 523–537. URL: https://doi.org/10.1016/j.coastaleng.2007.01.008.

[127] A. Martínez, E. M. Eckert, T. Artois, G. Careddu, M. Casu, M. Curini-Galletti, V. Gazale, S. Gobert, V. N. Ivanenko, U. Jondelius, *et al.* “Human access impacts biodiversity of microscopic animals in sandy beaches”. In: *Communications biology* 3.1 (2020), pp. 1–9. URL: https://doi.org/10.1038/s42003-020-0912-6.

[128] P. M. Machado, M. C. Suciu, L. L. Costa, D. C. Tavares, and I. R. Zalmon. “Tourism impacts on benthic communities of sandy beaches”. In: *Marine Ecology* 38.4 (2017), e12440. URL: https://doi.org/10.1111/maec.12440.

[129] H. J. Gons, M. Rijkeboer, and K. G. Ruddick. “A chlorophyll-retrieval algorithm for satellite imagery (Medium Resolution Imaging Spectrometer) of inland and coastal waters”. In: *Journal of Plankton Research* 24.9 (2002), pp. 947–951. URL: https://doi.org/10.1093/plankt/24.9.947.

[130] E. Chassot, S. Bonhommeau, G. Reygondeau, K. Nieto, J. J. Polovina, M. Huret, N. K. Dulvy, and H. Demarcq. “Satellite remote sensing for an ecosystem approach to fisheries management”. In: *ICES Journal of Marine Science* 68.4 (2011), pp. 651–666. URL: https://doi.org/10.1093/icesjms/fsq195.

[131] W. Emery, D. Matthews, and D. Baldwin. “Mapping surface coastal currents with satellite imagery and altimetry”. In: *2004 USA-Baltic International Symposium*. IEEE. 2004, pp. 1–5. DOI: 10.1109/BALTIC.2004.7296821.

[132] H. Liu and K. Jezek. “Automated extraction of coastline from satellite imagery by integrating Canny edge detection and locally adaptive thresholding methods”. In: *International journal of remote sensing* 25.5 (2004), pp. 937–958. URL: https://doi.org/10.1080/0143116031000139890.

[133] J. S. Lee and I. Jurkevich. “Coastline detection and tracing in SAR images”. In: *IEEE Transactions on Geoscience and Remote Sensing* 28.4 (1990), pp. 662–668. DOI: 10.1109/TGRS.1990.572976.

[134] D. C. Mason and I. J. Davenport. “Accurate and efficient determination of the shoreline in ERS-1 SAR images”. In: *IEEE Transactions on Geoscience and Remote Sensing* 34.5 (1996), pp. 1243–1253. DOI: 10.1109/36.536540.

[135] A. Niedermeier, E. Romaneessen, and S. Lehner. “Detection of coastlines in SAR images using wavelet methods”. In: *IEEE Transactions on Geoscience and Remote Sensing* 38.5 (2000), pp. 2270–2281. DOI: 10.1109/36.868884.

[136] S. Mallat, S. Zhong, *et al.* “Characterization of signals from multiscale edges”. In: *IEEE Transactions on pattern analysis and machine intelligence* 14.7 (1992), pp. 710–732. DOI: 10.1109/34.142909.

[137] S. Mallat and W. L. Hwang. “Singularity detection and processing with wavelets”. In: *IEEE Transactions on Information Theory* 38.2 (1992), pp. 617–643. DOI: 10.1109/18.119727.

[138] N. Padmasini, R. Umamaheswari, and M. Y. Sikkandar. “State-of-the-Art of Level-Set Methods in Segmentation and Registration of Spectral Domain Optical Coherence Tomographic Retinal Images”. In: *Soft Computing Based Medical Image Analysis* (2018), pp. 163–181. DOI: 10.1016/B978-0-12-813087-2.00009-9.

[139] A. Meta, P. Prats, U. Steinbrecher, J. Mittermayer, and R. Scheiber. “TerraSAR-X TOPSAR and ScanSAR comparison”. In: *In. Synthetic Aperture Radar (EUSAR)* 2008.7 (2008), pp. 1–4.

[140] A. Gulácsi and F. Kovács. “Sentinel-1-imagery-based high-resolution water cover detection on wetlands, Aided by Google Earth Engine”. In: *Remote Sensing* 12.10 (2020), p. 1614. URL: https://doi.org/10.3390/rs12101614.

[141] L. Xing, X. Tang, H. Wang, W. Fan, and G. Wang. “Monitoring monthly surface water dynamics of Dongting Lake using Sentinel-1 data at 10 m”. In: *PeerJ* 6 (2018), e4992. URL: https://doi.org/10.7717/peerj.4992.

[142] B. Brisco. “Mapping and monitoring surface water and wetlands with synthetic aperture radar”. In: *Remote Sensing of Wetlands: Applications and Advances* (2015), pp. 119–136.

[143] N. Valentini, L. Damiani, M. G. Molfetta, and A. Saponieri. “New coastal video-monitoring system achievement and development”. In: *Coastal Engineering Proceedings* 1.35 (2017), p. 11.

[144] G. Bradski and A. Kaehler. *OpenCV*. Accessed on May 22, 2026. Dr. Dobb’s journal of software tools, 2000. URL: https://www.scirp.org/reference/ReferencesPapers?ReferenceID=1692176.

[145] S. Van der Walt, J. L. Schönberger, J. Nunez-Iglesias, F. Boulogne, J. D. Warner, N. Yager, E. Gouillart, and T. Yu. “scikit-image: image processing in Python”. In: *PeerJ* 2 (2014), e453. URL: https://doi.org/10.7717/peerj.453.

[146] L. Gagnon and A. Jouan. “Speckle filtering of SAR images: a comparative study between complex-wavelet-based and standard filters”. In: *In I. S. Photonics, Wavelet Applications in Signal and Image Processing V* 3169 (1997), pp. 80–92. URL: https://doi.org/10.1117/12.279681.

[147] A. Rajamani and V. Krishnaveni. “Performance analysis survey of various SAR image despeckling techniques”. In: *International Journal of Computer Applications* 90.7 (2014).

[148] F. De Vries. *Speckle reduction in SAR Imagery by various multi-look techniques*. Tech. rep. Fysich en Elektronisch lab TNO, The Hague (Netherlands), 1998.

[149] N. Saxena and N. Rathore. “A review on speckle noise filtering techniques for SAR images”. In: *International Journal of Advanced Research in Computer Science and Electronics Engineering (IJARCSEE)* 2.2 (2013), p. 243.

[150] M. Modava and G. Akbarizadeh. “Coastline extraction from SAR images using spatial fuzzy clustering and the active contour method”. In: *International journal of remote sensing* 38.2 (2017), pp. 355–370. URL: https://doi.org/10.1080/01431161.2016.1266104.

[151] G. Donchyts, J. Schellekens, H. Winsemius, E. Eisemann, and N. Van de Giesen. “A 30 m Resolution Surface Water Mask Including Estimation of Positional and Thematic Differences Using Landsat 8, SRTM and OpenStreetMap: A Case Study in the Murray-Darling Basin, Australia”. In: *Remote Sensing* 8.5 (2016), p. 386. ISSN: 2072-4292. DOI: 10.3390/rs8050386.

[152] W. Li, Z. Du, F. Ling, D. Zhou, H. Wang, Y. Gui, B. Sun, and X. Zhang. “A comparison of land surface water mapping using the normalized difference water index from TM, ETM+ and ALI”. In: *Remote Sensing* 5.11 (2013), pp. 5530–5549. URL: https://doi.org/10.3390/rs5115530.

[153] J. Kittler and J. Illingworth. “On threshold selection using clustering criteria”. In: *IEEE transactions on Systems, Man, and Cybernetics* 5 (1985), pp. 652–655. URL: https://doi.org/10.1109/TSMC.1985.6313443.

[154] J. Serra and P. Soille. *Mathematical morphology and its applications to image processing*. Vol. 2. Springer Science & Business Media, 2012.

[155] R. M. Haralick, S. R. Sternberg, and X. Zhuang. “Image analysis using mathematical morphology”. In: *IEEE Transactions on Pattern Analysis and Machine Intelligence* 4 (1987), pp. 532–550. DOI: 10.1109/TPAMI.1987.4767941.

[156] R. Kasturi. *Image analysis applications*. CRC Press, 1990.

[157] B. D. Baets, E. Kerre, and M. Gupta. “The fundamentals of fuzzy mathematical morphology part 1: basic concepts”. In: *International Journal of General Systems* 23.2 (1995), pp. 155–171. DOI: 10.1080/03081079508908037.

[158] R. Maini and H. Aggarwal. “Study and comparison of various image edge detection techniques”. In: *International journal of image processing (IJIP)* 3.1 (2009), pp. 1–11.

[159] D. Marr and E. Hildreth. “Theory of edge detection”. In: *Proc. R.* 207: Soc. Lond. B, 1980, pp. 187–217. URL: https://doi.org/10.1098/rspb.1980.0020.

[160] J. Canny. “A computational approach to edge detection”. In: *IEEE Transactions on Pattern Analysis and Machine Intelligence* 6 (1986), pp. 679–698. URL: 10.1109/TPAMI.1986.4767851.

[161] G. T. Shrivakshan and C. Chandrasekar. “A comparison of various edge detection techniques used in image processing”. In: *International Journal of Computer Science Issues (IJCSI)* 9.5 (2012), p. 269. ISSN: 1694-0814.

[162] R. Pelich, M. Chini, R. Hostache, P. Matgen, and C. López-Martínez. “Coastline Detection Based on Sentinel-1 Time Series for Ship-and Flood-Monitoring Applications”. In: *IEEE Geoscience and Remote Sensing Letters* (2020). DOI: 10.1109/LGRS.2020.3008011.

[163] C. Nolet, A. Poortinga, P. Roosjen, H. Bartholomeus, and G. Ruessink. “Measuring and modeling the effect of surface moisture on the spectral reflectance of coastal beach sand”. In: *PLoS One* 9.11 (2014), e112151. URL: https://doi.org/10.1371/journal.pone.0112151.

[164] L. P. Almeida, I. E. de Oliveira, R. Lyra, R. L. S. Dazzi, V. G. Martins, and A. H. da Fontoura Klein. “Coastal Analyst System from Space Imagery Engine (CASSIE): shoreline management module”. In: *Environmental Modelling & Software* (2021), p. 105033. URL: https://doi.org/10.1016/j.envsoft.2021.105033.

[165] J. Montgomery, B. Brisco, L. Chasmer, K. Devito, D. Cobbaert, and C. Hopkinson. “SAR and LiDAR temporal data fusion approaches to boreal wetland ecosystem monitoring”. In: *Remote Sensing* 11.2 (2019), p. 161. URL: https://doi.org/10.3390/rs11020161.

[166] C. Lin, C.-C. Wu, K. Tsogt, Y.-C. Ouyang, and C.-I. Chang. “Effects of atmospheric correction and pansharpening on LULC classification accuracy using WorldView-2 imagery”. In: *Information Processing in Agriculture* 2.1 (2015), pp. 25–36. URL: https://doi.org/10.1016/j.inpa.2015.01.003.

[167] P. Du, S. Liu, J. Xia, and Y. Zhao. “Information fusion techniques for change detection from multi-temporal remote sensing images”. In: *Information Fusion* 14.1 (2013), pp. 19–27. URL: https://doi.org/10.1016/j.inffus.2012.05.003.

[168] L. Cenci, M. G. Persichillo, L. Disperati, E. R. Oliveira, F. L. Alves, L. Pulvirenti, N. Rebora, G. Boni, and M. Phillips. “Remote sensing for coastal risk reduction purposes: Optical and microwave data fusion for shoreline evolution monitoring and modelling”. In: *2015 IEEE international geoscience and remote sensing symposium (IGARSS)*. IEEE. 2015, pp. 1417–1420. DOI: 10.1109/IGARSS.2015.7326043.

[169] A. P. Ruiz-Beltran, A. Astorga-Moar, P. Salles, and C. M. Appendini. “Short-term shoreline trend detection patterns using SPOT-5 image fusion in the northwest of Yucatan, Mexico”. In: *Estuaries and Coasts* 42.7 (2019), pp. 1761–1773. URL: https://doi.org/10.1007/s12237-019-00573-7.

[170] A. Al Fugura, L. Billa, B. Pradhan, *et al.* “Semi-automated procedures for shoreline extraction using single RADARSAT-1 SAR image”. In: *Estuarine, Coastal and Shelf Science* 95.4 (2011), pp. 395–400. DOI: 10.1016/j.ecss.2011.10.009.

[171] M. Alicandro, V. Baiocchi, R. Brigante, and F. Radicioni. “Automatic shoreline detection from eight-band VHR satellite imagery”. In: *Journal of Marine Science and Engineering* 7.12 (2019), p. 459. DOI: 10.3390/jmse7120459.

[172] F. Palazzo, D. Latini, V. Baiocchi, F. Del Frate, F. Giannone, D. Dominici, and S. Remondiere. “An application of COSMO-Sky Med to coastal erosion studies”. In: *European Journal of Remote Sensing* 45.1 (2012), pp. 361–370. URL: https://doi.org/10.5721/EuJRS20124531.

[173] B. Orradóttir and H. H. Aegisdóttir. “Healthy Ecosystems, Healthy Earth, Healthy People”. In: *United Nations University* (2015).

[174] UNFCCC. *Paris Agreement*. 2015. URL: https://unfccc.int/sites/default/files/english_paris_agreement.pdf.

[175] Z. Zhang, W. Ju, and Y. Zhou. “The effect of water stress on net primary productivity in northwest China”. In: *Environmental Science and Pollution Research* 28.46 (2021), pp. 65885–65898. ISSN: 1614-7499. URL: https://doi.org/10.1007/s11356-021-15314-2.

[176] N. T. Boelman, M. Stieglitz, H. M. Rueth, M. Sommerkorn, K. L. Griffin, G. R. Shaver, and J. A. Gamon. “Response of NDVI, biomass, and ecosystem gas exchange to long-term warming and fertilization in wet sedge tundra”. In: *Oecologia* 135.3 (2003), pp. 414–421. ISSN: 1432-1939. URL: https://doi.org/10.1007/s00442-003-1198-3.

[177] I. Soubry, T. Doan, T. Chu, and X. Guo. “A systematic review on the integration of remote sensing and gis to forest and grassland ecosystem health attributes, indicators, and measures”. In: *Remote Sensing* 13.16 (2021), p. 3262. ISSN: 2072-4292. URL: https://doi.org/10.3390/rs13163262.

[178] M. Paganini, A. K. Leidner, G. Geller, W. Turner, and M. Wegmann. “The role of space agencies in remotely sensed essential biodiversity variables”. In: *Remote Sensing in Ecology and Conservation* 2.3 (2016), pp. 132–140. ISSN: 2056-3485. URL: https://doi.org/10.1002/rse2.29.

[179] J. B. Callicott, L. B. Crowder, and K. Mumford. “Current normative concepts in conservation”. In: *Conservation biology* 13.1 (1999), pp. 22–35. ISSN: 0888-8892. URL: https://doi.org/10.1046/j.1523-1739.1999.97333.x.

[180] A. E. Magurran. “Biological diversity”. In: *Current Biology* 15.4 (2005), R116–R118. ISSN: 0960-9822. URL: https://doi.org/10.1016/j.cub.2005.02.006.

[181] M. Schröter, C. Albert, A. Marques, W. Tobon, S. Lavorel, J. Maes, C. Brown, S. Klotz, and A. Bonn. “National ecosystem assessments in Europe: a review”. In: *BioScience* 66.10 (2016), pp. 813–828. ISSN: 1525-3244. URL: https://doi.org/10.1093/biosci/biw101.

[182] P. Escribano and N. Fernández. “6 Ecosystem Functioning Observations for Assessing Conservation in the Doñana National Park, Spain”. In: *Satellite Remote Sensing for Conservation Action: Case Studies from Aquatic and Terrestrial Ecosystems* (2018), p. 164. ISSN: 1108596940. DOI: 10.1017/9781108631129.007.

[183] Z. Li, D. Xu, and X. Guo. “Remote sensing of ecosystem health: opportunities, challenges, and future perspectives”. In: *Sensors* 14.11 (2014), pp. 21117–21139. ISSN: 1424-8220. URL: https://doi.org/10.3390/s141121117.

[184] A. Norkko, A. Villnäs, J. Norkko, S. Valanko, and C. Pilditch. “Size matters: implications of the loss of large individuals for ecosystem function”. In: *Scientific Reports* 3.1 (2013), pp. 1–7. ISSN: 2045-2322. DOI: 10.1038/srep02646.

[185] G. M. Lovett, C. G. Jones, M. G. Turner, and K. C. Weathers. “Ecosystem function in heterogeneous landscapes”. In: *Ecosystem function in heterogeneous landscapes*. Springer, 2005, pp. 1–4. URL: https://doi.org/10.1007/b104357.

[186] B. K. Wylie, D. A. Johnson, E. Laca, N. Z. Saliendra, T. G. Gilmanov, B. C. Reed, L. L. Tieszen, and B. B. Worstell. “Calibration of remotely sensed, coarse resolution NDVI to CO2 fluxes in a sagebrushsteppe ecosystem”. In: *Remote Sensing of Environment* 85.2 (2003), pp. 243–255. ISSN: 0034-4257. URL: https://doi.org/10.1016/S0034-4257(03)00004-X.

[187] P. Olofsson, F. Lagergren, A. Lindroth, J. Lindström, L. Klemedtsson, W. Kutsch, and L. Eklundh. “Towards operational remote sensing of forest carbon balance across Northern Europe”. In: *Biogeosciences* 5.3 (2008), pp. 817–832. ISSN: 1726-4170. URL: https://doi.org/10.5194/bg-5-817-2008.

[188] C. Xu, Y. Li, J. Hu, X. Yang, S. Sheng, and M. Liu. “Evaluating the difference between the normalized difference vegetation index and net primary productivity as the indicators of vegetation vigor assessment at landscape scale”. In: *Environmental Monitoring and Assessment* 184.3 (2012), pp. 1275–1286. ISSN: 1573-2959. URL: https://doi.org/10.1007/s10661-011-2039-1.

[189] Z. Cai, S. Junttila, J. Holst, H. Jin, J. Ardö, A. Ibrom, M. Peichl, M. Mölder, P. Jönsson, and J. Rinne. “Modelling daily gross primary productivity with sentinel-2 data in the nordic regioncomparison with data from modis”. In: *Remote Sensing* 13.3 (2021), p. 469. ISSN: 2072-4292. DOI: 10.3390/rs13030469.

[190] G. Badgley, C. B. Field, and J. A. Berry. “Canopy near-infrared reflectance and terrestrial photosynthesis”. In: *Science advances* 3.3 (2017), e1602244. ISSN: 2375-2548. DOI: 10.1126/sciadv.1602244.

[191] G. Badgley, L. D. Anderegg, J. A. Berry, and C. B. Field. “Terrestrial gross primary production: Using NIRV to scale from site to globe”. In: *Global change biology* 25.11 (2019), pp. 3731–3740. ISSN: 1354-1013. URL: https://doi.org/10.1111/gcb.14729.

[192] D. D. Baldocchi, Y. Ryu, B. Dechant, E. Eichelmann, K. Hemes, S. Ma, C. R. Sanchez, R. Shortt, D. Szutu, and A. Valach. “Outgoing nearinfrared radiation from vegetation scales with canopy photosynthesis across a spectrum of function, structure, physiological capacity, and weather”. In: *Journal of Geophysical Research: Biogeosciences* 125.7 (2020). ISSN: 2169-8953. URL: https://doi.org/10.1029/2019JG005534.

[193] S. Wang, Y. Zhang, W. Ju, B. Qiu, and Z. Zhang. “Tracking the seasonal and interannual variations of global gross primary production during last four decades using satellite near-infrared reflectance data”. In: *Science of the Total Environment* 755 (2021), p. 142569. ISSN: 0048-9697. URL: https://doi.org/10.1016/j.scitotenv.2020.142569.

[194] G. Wu, K. Guan, C. Jiang, B. Peng, H. Kimm, M. Chen, X. Yang, S. Wang, A. E. Suyker, and C. J. Bernacchi. "Radiance-based NIRv as a proxy for GPP of corn and soybean". In: *Environmental Research Letters* 15.3 (2020), p. 034009. ISSN: 1748-9326. DOI: 10.1088/1748-9326/ab65cc.

[195] G. Yin, A. Verger, A. Descals, I. Filella, and J. Peñuelas. "A broadband green-red vegetation index for monitoring gross primary production phenology". In: *Journal of Remote Sensing* 2022 (2022). ISSN: 2694-1589. URL: https://doi.org/10.34133/2022/9764982.

[196] S. Cerasoli, M. Campagnolo, J. Faria, C. Nogueira, and M. d. C. Caldeira. "On estimating the gross primary productivity of Mediterranean grasslands under different fertilization regimes using vegetation indices and hyperspectral reflectance". In: *Biogeosciences* 15.17 (2018), pp. 5455–5471. ISSN: 1726-4170. URL: https://doi.org/10.5194/bg-15-5455-2018.

[197] S. Lin, J. Li, Q. Liu, L. Li, J. Zhao, and W. Yu. "Evaluating the effectiveness of using vegetation indices based on red-edge reflectance from Sentinel-2 to estimate gross primary productivity". In: *Remote Sensing* 11.11 (2019), p. 1303. ISSN: 2072-4292. URL: https://doi.org/10.3390/rs11111303.

[198] K. D. Noumonvi, M. Ferlan, K. Eler, G. Alberti, A. Peressotti, and S. Cerasoli. "Estimation of carbon fluxes from eddy covariance data and satellite-derived vegetation indices in a karst grassland (Podgorski Kras, Slovenia)". In: *Remote Sensing* 11.6 (2019), p. 649. URL: https://doi.org/10.3390/rs11060649.

[199] N. P. Robinson, B. W. Allred, W. K. Smith, M. O. Jones, A. Moreno, T. A. Erickson, D. E. Naugle, and S. W. Running. "Terrestrial primary production for the conterminous United States derived from Landsat 30 m and MODIS 250 m". In: *Remote Sensing in Ecology and Conservation* 4.3 (2018), pp. 264–280. ISSN: 2056-3485. URL: https://doi.org/10.1002/rse2.74.

[200] S. W. Running, R. R. Nemani, F. A. Heinsch, M. Zhao, M. C. Reeves, and H. Hashimoto. "A Continuous Satellite-Derived Measure of Global Terrestrial Primary Production". In: URL: https://doi.org/10.1641/0006-3568(2004)054[0547:ACSMOG]2.0.CO;2.

[201] M. Zhao, F. A. Heinsch, R. R. Nemani, and S. W. Running. "Improvements of the MODIS terrestrial gross and net primary production global data set". In: *Remote sensing of Environment* 95.2 (2005), pp. 164–176. ISSN: 0034-4257. URL: https://doi.org/10.1016/j.rse.2004.12.011.

[202] H. Zhu, A. Lin, L. Wang, Y. Xia, and L. Zou. "Evaluation of MODIS gross primary production across multiple biomes in China using eddy covariance flux data". In: *Remote Sensing* 8.5 (2016), p. 395. ISSN: 2072-4292. URL: https://doi.org/10.3390/rs8050395.

[203] F. A. Heinsch, Z. Maosheng, S. W. Running, J. S. Kimball, R. R. Nemani, K. J. Davis, P. V. Bolstad, B. D. Cook, A. R. Desai, D. M. Ricciuto, B. E. Law, W. C. Oechel, K. Hyojung, L. Hongyan, S. C. Wofsy, A. L. Dunn, J. W. Munger, D. D. Baldocchi, X. Liukang, D. Y. Hollinger, A. D. Richardson, P. C. Stoy, M. B. S. Siqueira, R. K. Monson, S. P. Burns, and L. B. Flanagan. "Evaluation of remote sensing based

terrestrial productivity from MODIS using regional tower eddy flux network observations". In: *IEEE Transactions on Geoscience and Remote Sensing* 44.7 (2006), pp. 1908–1925. ISSN: 1558-0644. DOI: 10.1109/TGRS.2005.853936.

[204] D. P. Turner, W. D. Ritts, W. B. Cohen, S. T. Gower, M. Zhao, S. W. Running, S. C. Wofsy, S. Urbanski, A. L. Dunn, and J. Munger. "Scaling gross primary production (GPP) over boreal and deciduous forest landscapes in support of MODIS GPP product validation". In: *Remote Sensing of Environment* 88.3 (2003), pp. 256–270. ISSN: 0034-4257. URL: https://doi.org/10.1016/j.rse.2003.06.005.

[205] M. Balzarolo, J. Peñuelas, and F. Veroustraete. "Influence of landscape heterogeneity and spatial resolution in multi-temporal in situ and MODIS NDVI data proxies for seasonal GPP dynamics". In: *Remote Sensing* 11.14 (2019), p. 1656. ISSN: 2072-4292. URL: https://doi.org/10.3390/rs11141656.

[206] S. Wang, M. Garcia, P. Bauer-Gottwein, J. Jakobsen, P. J. Zarco-Tejada, F. Bandini, V. S. Paz, and A. Ibrom. "High spatial resolution monitoring land surface energy, water and CO2 fluxes from an Unmanned Aerial System". In: *Remote Sensing of Environment* 229 (2019), pp. 14–31. ISSN: 0034-4257. URL: https://doi.org/10.1016/j.rse.2019.03.040.

[207] M. Neumann, A. Moreno, C. Thurnher, V. Mues, S. Härkönen, M. Mura, O. Bouriaud, M. Lang, G. Cardellini, and A. Thivolle-Cazat. "Creating a regional MODIS satellite-driven net primary production dataset for European forests". In: *Remote Sensing* 8.7 (2016), p. 554. ISSN: 2072-4292. URL: https://doi.org/10.3390/rs8070554.

[208] S. W. Running, P. E. Thornton, R. Nemani, and J. M. Glassy. "Global terrestrial gross and net primary productivity from the earth observing system". In: *Methods in ecosystem science*. Springer, 2000, pp. 44–57. URL: https://doi.org/10.1007/978-1-4612-1224-9_4.

[209] P. Schubert, F. Lagergren, M. Aurela, T. Christensen, A. Grelle, M. Heliasz, L. Klemedtsson, A. Lindroth, K. Pilegaard, and T. Vesala. "Modeling GPP in the Nordic forest landscape with MODIS time series dataComparison with the MODIS GPP product". In: *Remote Sensing of Environment* 126 (2012), pp. 136–147. ISSN: 0034-4257. URL: https://doi.org/10.1016/j.rse.2012.08.005.

[210] D. A. Sims, A. F. Rahman, V. D. Cordova, B. Z. ElMasri, D. D. Baldocchi, L. B. Flanagan, A. H. Goldstein, D. Y. Hollinger, L. Misson, and R. K. Monson. "On the use of MODIS EVI to assess gross primary productivity of North American ecosystems". In: *Journal of Geophysical Research: Biogeosciences* 111.G4 (2006). ISSN: 0148-0227. URL: https://doi.org/10.1029/2006JG000162.

[211] A. J. Green, J. Bustamante, G. F. E. Janss, R. Fernández-Zamudio, and C. Díaz-Paniagua. "Doñana Wetlands (Spain)". In: *The Wetland Book: II: Distribution, Description and Conservation*. Ed. by C. M. Finlayson, G. R. Milton, R. C. Prentice, and N. C. Davidson. Dordrecht: Springer Netherlands, 2016, pp. 1–14. ISBN: 978-94-007-6173-5. URL: https://doi.org/10.1007/978-94-007-6173-5_139-1
.

[212] F. García Novo and C. Marín Cabrera. “Doñana: water and biosphere, Doñana 2005 Project”. In: *Guadalquivir Hydrologic Basin Authority, Spanish Ministry of the Environment, Madrid* (2006). URL: https://www.researchgate.net/profile/Francisco-Barrera-6/publication/260990490_Donana_Water_and_Biosphere/links/0a85e532f31a8515d9000000/Donana-Water-and-Biosphere.pdf.

[213] A. J. Green and J. Elmberg. “Ecosystem services provided by waterbirds”. In: *Biological reviews* 89.1 (2014), pp. 105–122. ISSN: 1464-7931. URL: https://doi.org/10.1111/brv.12045.

[214] L. M. Hernández, B. Gómara, M. Fernández, B. Jiménez, M. González, R. Baos, F. Hiraldo, M. Ferrer, V. Benito, and M. Suner. “Accumulation of heavy metals and As in wetland birds in the area around Donana National Park affected by the Aznalcollar toxic spill”. In: *Science of the Total Environment* 242.1-3 (1999), pp. 293–308. ISSN: 0048-9697. URL: https://doi.org/10.1016/S0048-9697(99)00397-6.

[215] D. Pain, A. Sánchez, and A. Meharg. “The Donana ecological disaster: contamination of a world heritage estuarine marsh ecosystem with acidified pyrite mine waste”. In: *Science of the Total Environment* 222.1-2 (1998), pp. 45–54. ISSN: 0048-9697. URL: https://doi.org/10.1016/S0048-9697(98)00290-3.

[216] J. A. Adame, L. Lope, P. J. Hidalgo, M. Sorribas, I. Gutiérrez-Álvarez, A. del Águila, A. Saiz-Lopez, and M. Yela. “Study of the exceptional meteorological conditions, trace gases and particulate matter measured during the 2017 forest fire in Doñana Natural Park, Spain”. In: *Science of The Total Environment* 645 (2018), pp. 710–720. ISSN: 0048-9697. URL: https://doi.org/10.1016/j.scitotenv.2018.07.181.

[217] W. Informe. “Contaminación del agua en Doñana”. In: *Evaluación de los vertidos sin depurar de los municipios de Almonte, Rociana del Condado y Bollullos Par del Contado (Comarca de Doñana, Huelva)* (2012). URL: https://www.wwf.es/?28640/Impactantes-imgenes-de-WWF-demuestran-cmo-las-cloacas-vierten-directamente-a-Doana.

[218] M. A. Taggart, J. Figuerola, A. J. Green, R. Mateo, C. Deacon, D. Osborn, and A. A. Meharg. “After the Aznalcóllar mine spill: Arsenic, zinc, selenium, lead and copper levels in the livers and bones of five waterfowl species”. In: *Environmental Research* 100.3 (2006), pp. 349–361. ISSN: 0013-9351. URL: https://doi.org/10.1016/j.envres.2005.07.009.

[219] C. Guardiola-Albert and C. R. Jackson. “Potential impacts of climate change on groundwater supplies to the Doñana wetland, Spain”. In: *Wetlands* 31.5 (2011), pp. 907–920. ISSN: 1943-6246. URL: https://doi.org/10.1007/s13157-011-0205-4.

[220] M. Manzano, E. Custodio, E. Lozano, and H. Higueras. “Relationships between wetlands and the Doñana coastal aquifer (SW Spain)”. In: *Groundw. Ecosyst* 169 (2013), pp. 169–182. URL: https://doi.org/10.1201/b15003.

[221] M. Lumbierres, P. F. Méndez, J. Bustamante, R. Soriguer, and L. Santamaría. "Modeling biomass production in seasonal wetlands using MODIS NDVI land surface phenology". In: *Remote Sensing* 9.4 (2017), p. 392. ISSN: 2072-4292. URL: https://doi.org/10.3390/rs9040392.

[222] G. A. Kordelas, I. Manakos, D. Aragonés, R. Díaz-Delgado, and J. Bustamante. "Fast and Automatic Data-Driven Thresholding for Inundation Mapping with Sentinel-2 Data". In: *Remote Sensing* 10.6 (2018), p. 910. ISSN: 2072-4292. URL: https://www.mdpi.com/2072-4292/10/6/910.

[223] D. Papale, M. Reichstein, M. Aubinet, E. Canfora, C. Bernhofer, W. Kutsch, B. Longdoz, S. Rambal, R. Valentini, and T. Vesala. "Towards a standardized processing of Net Ecosystem Exchange measured with eddy covariance technique: algorithms and uncertainty estimation". In: *Biogeosciences* 3.4 (2006), pp. 571–583. ISSN: 1726-4170. URL: https://doi.org/10.5194/bg-3-571-2006.

[224] M. Cuntz. *hesseflux: a Python library to process and post-process Eddy covariance data*. 2020. DOI: 10.5281/zenodo.6954772.

[225] I. Forbrich and A. E. Giblin. "Marsh-atmosphere CO2 exchange in a New England salt marsh". In: *Journal of Geophysical Research: Biogeosciences* 120.9 (2015), pp. 1825–1838. ISSN: 2169-8953. URL: https://doi.org/10.1002/2015JG003044.

[226] N. Kljun, P. Calanca, M. Rotach, and H. Schmid. "A simple two-dimensional parameterisation for Flux Footprint Predictions FFP". In: *Geoscientific Model Development Discussions* 8.8 (2015). ISSN: 1991-9611. DOI: 10.5194/gmdd-8-6757-2015.

[227] A. Sathe, J. Mann, J. Gottschall, and M. Courtney. "Estimating the systematic errors in turbulence sensed by wind lidars". In: *Risø National Laboratory, Roskilde, Denmark. Risø* (2010), p. 24.

[228] R. G. Allen, L. S. Pereira, T. A. Howell, and M. E. Jensen. "Evapotranspiration information reporting: I. Factors governing measurement accuracy". In: *Agricultural Water Management* 98.6 (2011), pp. 899–920. ISSN: 0378-3774. URL: https://doi.org/10.1016/j.agwat.2010.12.015.

[229] H. Akima. "A new method of interpolation and smooth curve fitting based on local procedures". In: *Journal of the ACM (JACM)* 17.4 (1970), pp. 589–602. ISSN: 0004-5411. DOI: 10.1145/321607.321609.

[230] G. Churkina, S. W. Running, A. L. Schloss, and T. P. O. T. P. N. M. Intercomparison. "Comparing global models of terrestrial net primary productivity (NPP): the importance of water availability". In: *Global Change Biology* 5.S1 (1999), pp. 46–55. ISSN: 1354-1013. URL: https://doi.org/10.1046/j.1365-2486.1999.00006.x.

[231] R. Díaz-Delgado, F. Carro, F. Quirós Herruzo, A. Osuna, and M. Baena. "Contribución del seguimiento ecológico a largo plazo a la investigación y la gestión en la plataforma LTSER-Doñana". In: *Ecosistemas* 25.1 (2016), pp. 9–18. DOI: 10.7818/ECOS.2016.25-1.03.

[232] I. E. Huertas, S. Flecha, J. Figuerola, E. Costas, and E. P. Morris. “Effect of hydroperiod on CO2 fluxes at the airwater interface in the Mediterranean coastal wetlands of Doñana”. In: *Journal of Geophysical Research: Biogeosciences* 122.7 (2017), pp. 1615–1631. ISSN: 2169-8953. URL: https://doi.org/10.1002/2017JG003793.

[233] D. M. G. dela Torre, J. Gao, C. Macinnis-Ng, and Y. Shi. “Phenology-based delineation of irrigated and rain-fed paddy fields with Sentinel-2 imagery in Google Earth Engine”. In: *Geo-spatial Information Science* 24.4 (2021), pp. 695–710. ISSN: 1009-5020. DOI: 10.1080/10095020.2021.1984183.

[234] R. Sharma, A. Ghosh, and P. K. Joshi. “Decision tree approach for classification of remotely sensed satellite data using open source support”. In: *Journal of Earth System Science* 122.5 (2013), pp. 1237–1247. ISSN: 0973-774X. DOI: 10.1007/s12040-013-0339-2.

[235] L. Yang, J. Driscol, S. Sarigai, Q. Wu, H. Chen, and C. D. Lippitt. “Google Earth Engine and Artificial Intelligence (AI): A Comprehensive Review”. In: *Remote Sensing* 14.14 (2022), p. 3253. ISSN: 2072-4292. URL: https://www.mdpi.com/2072-4292/14/14/3253.

[236] M. S. Domingo, D. M. Martín-Perea, C. Badgley, E. Cantero, P. López-Guerrero, A. Oliver, and J. J. Negro. “Taphonomic information from the modern vertebrate death assemblage of Doñana National Park, Spain”. In: *PLOS ONE* 15.11 (2020), e0242082. DOI: 10.1371/journal.pone.0242082.

[237] L. Serrano. “Balancing water uses at the Donana national park, Spain”. In: *The Wetland Book: I: Structure and Function, Management and Methods*. Ed. by C. M. Finlayson, M. Everard, K. Irvine, R. J. McInnes, B. A. Middleton, A. A. van Dam, and N. C. Davidson. Dordrecht: Springer Netherlands, 2016, pp. 1–8. ISBN: 978-94-007-6172-8. DOI: 10.1007/978-94-007-6172-8_232-4.

[238] G. A. Blackburn and J. Pitman. “Biophysical controls on the directional spectral reflectance properties of bracken (Pteridium aquilinum) canopies: results of a field experiment”. In: *International Journal of Remote Sensing* 20.11 (1999), pp. 2265–2282. ISSN: 0143-1161. DOI: 10.1080/014311699212245.

[239] O. Mutanga, A. K. Skidmore, and S. Van Wieren. “Discriminating tropical grass (Cenchrus ciliaris) canopies grown under different nitrogen treatments using spectroradiometry”. In: *ISPRS Journal of Photogrammetry and Remote Sensing* 57.4 (2003), pp. 263–272. ISSN: 0924-2716. URL: https://doi.org/10.1016/S0924-2716(02)00158-2.

[240] P. S. Thenkabail, R. B. Smith, and E. De Pauw. “Hyperspectral vegetation indices and their relationships with agricultural crop characteristics”. In: *Remote sensing of Environment* 71.2 (2000), pp. 158–182. ISSN: 0034-4257. URL: https://doi.org/10.1016/S0034-4257(99)00067-X.

[241] D. Gianelle and L. Vescovo. “Determination of green herbage ratio in grasslands using spectral reflectance. Methods and ground measurements”. In: *International Journal of Remote Sensing* 28.5 (2007), pp. 931–942. ISSN: 0143-1161. DOI: 10.1080/01431160500196398.

[242] O. Mutanga and A. K. Skidmore. “Narrow band vegetation indices overcome the saturation problem in biomass estimation”. In: *International journal of remote sensing* 25.19 (2004), pp. 3999–4014. ISSN: 0143-1161. DOI: 10.1080/01431160310001654923.

[243] A. Huete, K. Didan, T. Miura, E. P. Rodriguez, X. Gao, and L. G. Ferreira. “Overview of the radiometric and biophysical performance of the MODIS vegetation indices”. In: *Remote Sensing of Environment* 83.1 (2002), pp. 195–213. ISSN: 0034-4257. URL: https://doi.org/10.1016/S0034-4257(02)00096-2.

[244] B. C. Reed, M. D. Schwartz, and X. Xiao. “Remote Sensing Phenology”. In: *Phenology of Ecosystem Processes: Applications in Global Change Research*. Ed. by A. Noormets. New York, NY: Springer New York, 2009, pp. 231–246. ISBN: 978-1-4419-0026-5. URL: https://doi.org/10.1007/978-1-4419-0026-5_10.

[245] R. Bajgain, X. Xiao, P. Wagle, J. Basara, and Y. Zhou. “Sensitivity analysis of vegetation indices to drought over two tallgrass prairie sites”. In: *ISPRS Journal of Photogrammetry and Remote Sensing* 108 (2015), pp. 151–160. ISSN: 0924-2716. URL: https://doi.org/10.1016/j.isprsjprs.2015.07.004.

[246] M. Máñez, L. García, F. Ibáñez, H. Garrido, J. M. Espinar, J. L. Arroyo, J. L. D. Valle, A. Chico, A. Martínez, and R. Rodríguez. “Endangered waterbirds at Doñana natural space”. In: *Conservation Monitoring in Freshwater Habitats* (2010), pp. 357–373. URL: https://doi.org/10.1007/978-1-4020-9278-7_30.

[247] N. Flood. “Seasonal composite Landsat TM/ETM+ images using the medoid (a multi-dimensional median)”. In: *Remote Sensing* 5.12 (2013), pp. 6481–6500. ISSN: 2072-4292. URL: https://doi.org/10.3390/rs5126481.

[248] G. Duveiller and A. Cescatti. “Spatially downscaling sun-induced chlorophyll fluorescence leads to an improved temporal correlation with gross primary productivity”. In: *Remote Sensing of Environment* 182 (2016), pp. 72–89. ISSN: 0034-4257. URL: https://doi.org/10.1016/j.rse.2016.04.027.

[249] E. P. Glenn, A. R. Huete, P. L. Nagler, and S. G. Nelson. “Relationship Between Remotely-sensed Vegetation Indices, Canopy Attributes and Plant Physiological Processes: What Vegetation Indices Can and Cannot Tell Us About the Landscape”. In: *Sensors* 8.4 (2008), pp. 2136–2160. ISSN: 1424-8220. URL: https://doi.org/10.3390/s8042136.

[250] Y. Wang, C. E. Woodcock, W. Buermann, P. Stenberg, P. Voipio, H. Smolander, T. Häme, Y. Tian, J. Hu, Y. Knyazikhin, and R. B. Myneni. “Evaluation of the MODIS LAI algorithm at a coniferous forest site in Finland”. In: *Remote Sensing of Environment* 91.1 (2004), pp. 114–127. ISSN: 0034-4257. DOI: 10.1016/j.rse.2004.02.007.

[251] G. Gelybó, Z. Barcza, A. Kern, and N. Kljun. “Effect of spatial heterogeneity on the validation of remote sensing based GPP estimations”. In: *Agricultural and Forest Meteorology* 174-175 (2013), pp. 43–53. ISSN: 0168-1923. URL: https://doi.org/10.1016/j.agrformet.2013.02.003.

[252] T. Duda and M. Canty. “Unsupervised classification of satellite imagery: choosing a good algorithm”. In: *International Journal of Remote Sensing* 23.11 (2002), pp. 2193–2212. ISSN: 0143-1161. URL: https://doi.org/10.1080/01431160110078467.

[253] M. Hasmadi, H. Pakhriazad, and M. Shahrin. “Evaluating supervised and unsupervised techniques for land cover mapping using remote sensing data”. In: *Geografia: Malaysian Journal of Society and Space* 5.1 (2009), pp. 1–10. ISSN: 2180-2491.

[254] M. Meroni, D. Fasbender, R. Lopez-Lozano, and M. Migliavacca. “Assimilation of Earth observation data over cropland and grassland sites into a simple GPP model”. In: *Remote Sensing* 11.7 (2019), p. 749. URL: https://doi.org/10.3390/rs11070749.

[255] M. Reichstein, E. Falge, D. Baldocchi, D. Papale, M. Aubinet, P. Berbigier, C. Bernhofer, N. Buchmann, T. Gilmanov, A. Granier, *et al.* “On the separation of net ecosystem exchange into assimilation and ecosystem respiration: review and improved algorithm”. In: *Global change biology* 11.9 (2005), pp. 1424–1439. URL: https://doi.org/10.1111/j.1365-2486.2005.001002.x.

[256] G. Lasslop, M. Reichstein, D. Papale, A. D. Richardson, A. Arneth, A. Barr, P. Stoy, and G. Wohlfahrt. “Separation of net ecosystem exchange into assimilation and respiration using a light response curve approach: critical issues and global evaluation”. In: *Global change biology* 16.1 (2010), pp. 187–208. ISSN: 1354-1013. URL: https://doi.org/10.1111/j.1365-2486.2009.02041.x.

[257] E. Falge, D. Baldocchi, R. Olson, P. Anthoni, M. Aubinet, C. Bernhofer, G. Burba, R. Ceulemans, R. Clement, and H. Dolman. “Gap filling strategies for defensible annual sums of net ecosystem exchange”. In: *Agricultural and forest meteorology* 107.1 (2001), pp. 43–69. ISSN: 0168-1923. URL: https://doi.org/10.1016/S0168-1923(00)00225-2.

[258] A. V. Rocha and M. L. Goulden. “Why is marsh productivity so high? New insights from eddy covariance and biomass measurements in a Typha marsh”. In: *Agricultural and Forest Meteorology* 149.1 (2009), pp. 159–168. ISSN: 0168-1923. URL: https://doi.org/10.1016/j.agrformet.2008.07.010.

[259] G. Lasslop, M. Reichstein, J. Kattge, and D. Papale. “Influences of observation errors in eddy flux data on inverse model parameter estimation”. In: *Biogeosciences* 5.5 (2008), pp. 1311–1324. ISSN: 1726-4189. DOI: 10.5194/bg-5-1311-2008.

[260] W. Zhu, Y. Pan, H. He, L. Wang, M. Mou, and J. Liu. “A changing-weight filter method for reconstructing a high-quality NDVI time series to preserve the integrity of vegetation phenology”. In: *IEEE Transactions on Geoscience and Remote Sensing* 50.4 (2011), pp. 1085–1094. URL: https://doi.org/10.1109/TGRS.2011.2166965.

[261] J. Chen, P. Jönsson, M. Tamura, Z. Gu, B. Matsushita, and L. Eklundh. “A simple method for reconstructing a high-quality NDVI time-series data set based on the SavitzkyGolay filter”. In: *Remote sensing of Environment* 91.3-4 (2004), pp. 332–344. ISSN: 0034-4257. URL: https://doi.org/10.1016/j.rse.2004.03.014.

[262] P. Jonsson and L. Eklundh. “Seasonality extraction by function fitting to time-series of satellite sensor data”. In: *IEEE transactions on Geoscience and Remote Sensing* 40.8 (2002), pp. 1824–1832. ISSN: 0196-2892. DOI: 10.1109/TGRS.2002.802519.

[263] P. S. Beck, C. Atzberger, K. A. Høgda, B. Johansen, and A. K. Skidmore. “Improved monitoring of vegetation dynamics at very high latitudes: A new method using MODIS NDVI”. In: *Remote sensing of Environment* 100.3 (2006), pp. 321–334. ISSN: 0034-4257. URL: https://doi.org/10.1016/j.rse.2005.10.021.

[264] N. Viovy, O. Arino, and A. Belward. “The Best Index Slope Extraction (BISE): A method for reducing noise in NDVI time-series”. In: *International Journal of remote sensing* 13.8 (1992), pp. 1585–1590. ISSN: 0143-1161. DOI: 10.1080/01431169208904212.

[265] Q. Lu, H. Liu, L. Wei, Y. Zhong, and Z. Zhou. “Global prediction of gross primary productivity under future climate change”. In: *Science of The Total Environment* 912 (2024), p. 169239. URL: https://doi.org/10.1016/j.scitotenv.2023.169239.

[266] J. Grace. “Understanding and managing the global carbon cycle”. In: *Journal of Ecology* 92.2 (2004), pp. 189–202. URL: https://doi.org/10.1111/j.0022-0477.2004.00874.x.

[267] Integrated Carbon Observation System. *FLUXES - The European Greenhouse Gas Bulletin*. Accessed May 22, 2026. 2022. URL: https://www.icos-cp.eu/fluxes/1.

[268] T. Zhang, J. Zhou, P. Yu, *et al.* “Response of Ecosystem Gross Primary Productivity to Drought in Northern China Based on Multi-Source Remote Sensing Data”. In: *Journal of Hydrology* 616 (2023), p. 128808. ISSN: 0022-1694. DOI: 10.1016/j.jhydrol.2022.128808.

[269] H. Astola, T. Häme, L. Sirro, *et al.* “Comparison of Sentinel-2 and Landsat 8 imagery for forest variable prediction in boreal region”. In: *Remote Sensing of Environment* 223 (Mar. 2019), pp. 257–273. ISSN: 00344257. DOI: 10.1016/j.rse.2019.01.019.

[270] W. Zhu, Z. Xie, C. Zhao, Z. Zheng, K. Qiao, D. Peng, and Y. H. Fu. “Remote sensing of terrestrial gross primary productivity: a review of advances in theoretical foundation, key parameters and methods”. In: *GIScience & Remote Sensing* 61.1 (2024), p. 2318846. URL: https://doi.org/10.1080/15481603.2024.2318846.

[271] Z. Liao, B. Zhou, J. Zhu, H. Jia, and X. Fei. “A critical review of methods, principles and progress for estimating the gross primary productivity of terrestrial ecosystems”. In: *Frontiers in Environmental Science* 11 (2023), p. 1093095. URL: https://doi.org/10.3389/fenvs.2023.1093095.

[272] G. Tramontana, K. Ichii, G. Camps-Valls, E. Tomelleri, and D. Papale. “Uncertainty analysis of gross primary production upscaling using Random Forests, remote sensing and eddy covariance data”. In: *Remote Sensing of Environment* 168 (2015), pp. 360–373. URL: https://doi.org/10.1016/j.rse.2015.07.015.

[273] S. Liu, Q. Zhuang, Y. He, A. Noormets, J. Chen, and L. Gu. “Evaluating atmospheric CO2 effects on gross primary productivity and net ecosystem exchanges of terrestrial ecosystems in the conterminous United States using the AmeriFlux data and an artificial neural network approach”. In: *Agricultural and forest meteorology* 220 (2016), pp. 38–49. URL: https://doi.org/10.1016/j.agrformet.2016.01.007.

[274] Y. Chen, X. Xu, C. Huang, *et al.* “Selection of Prediction Factors of Gross Primary Productivity Based on Artificial Neural Network”. In: *2022 International Conference on Artificial Intelligence, Information Processing and Cloud Computing (AIIPCC)*. 2022, pp. 426–429. DOI: 10.1109/AIIPCC57291.2022.00096.

[275] B. Lee, N. Kim, E.-S. Kim, K. Jang, M. Kang, J.-H. Lim, J. Cho, and Y. Lee. “An artificial intelligence approach to predict gross primary productivity in the forests of South Korea using satellite remote sensing data”. In: *Forests* 11.9 (2020), p. 1000. URL: https://doi.org/10.3390/f11091000.

[276] Q. Na, Q. Lai, G. Bao, J. Xue, X. Liu, and R. Gao. “Estimation of Gross Primary Productivity Using Performance-Optimized Machine Learning Methods for the Forest Ecosystems in China”. In: *Forests* 16.3 (2025), p. 518. URL: https://doi.org/10.3390/f16030518.

[277] H. Wang, W. Shao, Y. Hu, *et al.* “Assessment of Six Machine Learning Methods for Predicting Gross Primary Productivity in Grassland”. In: *Remote Sensing* 15.14 (2023). Publisher: Multidisciplinary Digital Publishing Institute (MDPI). ISSN: 20724292. DOI: 10.3390/rs15143475.

[278] J. Liu, Y. Zuo, N. Wang, F. Yuan, X. Zhu, L. Zhang, J. Zhang, Y. Sun, Z. Guo, Y. Guo, *et al.* “Comparative analysis of two machine learning algorithms in predicting site-level net ecosystem exchange in major biomes”. In: *Remote Sensing* 13.12 (2021), p. 2242. URL: https://doi.org/10.3390/rs13122242.

[279] D. Montero, M. D. Mahecha, F. Martinuzzi, C. Aybar, A. Klosterhalfen, A. Knohl, F. Koebsch, J. Anaya, and S. Wieneke. “Recurrent Neural Networks for Modelling Gross Primary Production”. In: *IGARSS 2024-2024 IEEE International Geoscience and Remote Sensing Symposium*. IEEE. 2024, pp. 4214–4217. DOI: 10.1109/IGARSS53475.2024.10640715.

[280] X. Zhao, P. Zhao, L. Zhu, and G. Zhang. “A comparison of multivariate and univariate time series models applied in tree sap flux analyses”. In: *Forest science* 68.5-6 (2022), pp. 473–486. URL: https://doi.org/10.1093/forsci/fxac027.

[281] J. Leonard, F. Bornet, B. François, and E. Grehan. *ETC L2 Fluxes from Estrees-Mons A28, 2016-12-31–2024-12-31*. 2025. URL: https://hdl.handle.net/11676/4lrU6O5qv9KCuvuhMM6veY8D.

[282] C. Rebmann, L. Dienstbach, P. Schmidt, R. Wiesen, J. Meis, I. Feldmann, F. B. Campos, S. Dejosez, I. G. Quiros, S. Gimper, D. Hautmann, A. Hildebrandt, P. Kempka, and S. Paasch. *ETC L2 Fluxes from Hohes Holz, 2018-12-31–2025-09-30*. 2025. URL: https://hdl.handle.net/11676/2L1kNpUSC5efdHkzpoNCpyDT.

[283] I. Mammarella, J. Aalto, J. Back, P. Kolari, H. Laakso, J. Levula, T. Matilainen, M. Pihlatie, J. Pumpanen, R. Taipale, and T. Vesala. *ETC L2 Fluxes from Hyytiala, 2017-12-31–2023-10-31*. 2023. URL: https://hdl.handle.net/11676/Ke4Y-W71Kj_Tc8l2Q-ZZpMZ.

[284] E. Cremonese, M. Galvagno, and U. M. di Cella. *ETC L2 Fluxes from Torgnon, 2015-12-31–2024-12-31*. 2025. URL: https://hdl.handle.net/11676/oWX79D_bh4t41D7IWxkmEmsF.

[285] C. Bernhofer, U. Eichelmann, T. Grünwald, M. Hehn, M. Mauder, U. Moderow, and H. Prasse. *ETC L2 ARCHIVE from Klingenberg, 2018–2024*. 2025. URL: https://hdl.handle.net/11676/c8lbCxWNrXNAFQcdJ7aYeHkv.

[286] D. Berveiller, E. Dufrêne, N. Delpierre, A. Morfin, C. Francois, G. Vincent, S. Bazot, K. Soudani, C. Girardin, T. Guillot, and C. Perot-Guillaume. *ETC L2 Fluxes from Fontainebleau-Barbeau, 2018-12-31–2025-09-30*. 2025. URL: https://hdl.handle.net/11676/WgPSFQlVYui2ANucafunTOY9.

[287] M. Peichl, M. Nilsson, E. Larmanou, P. Smith, P. Marklund, G. D. Simon, P. Lofvenius, R. Dignam, J. Holst, M. Molder, T. Andersson, F. Boschetti, N. Kozii, M.-L. Linderson, and M. Ottosson-Löfvenius. *ETC L2 Fluxnet (half-hourly) from Svartberget, 2018-12-31–2025-09-30*. 2025. URL: https://hdl.handle.net/11676/qR-2VNMiMXAsYwMLzwucjOsR.

[288] C. Bernhofer, U. Eichelmann, T. Grünwald, M. Hehn, M. Mauder, U. Moderow, and H. Prasse. *ETC L2 Fluxes from Grillenburg, 2016-12-31–2024-12-31*. 2025. URL: https://hdl.handle.net/11676/vdrkLkMNY5MXqW5htw5adeyw.

[289] Integrated Carbon Observation System. *ICOS Community Portal*. Accessed May 22, 2026. 2025. URL: https://www.icos-cp.eu/.

[290] G. Pastorello, C. Trotta, E. Canfora, *et al.* "The FLUXNET2015 Dataset and the ONEFlux Processing Pipeline for Eddy Covariance Data". In: *Scientific Data 2020 7:1* 7.1 (2020), pp. 1–27. ISSN: 2052-4463. DOI: 10.1038/s41597-020-0534-3.

[291] X. Chang, Y. Xing, W. Gong, *et al.* "Evaluating Gross Primary Productivity over 9 ChinaFlux Sites Based on Random Forest Regression Models, Remote Sensing, and Eddy Covariance Data". In: *Science of the Total Environment* 875 (2023), p. 162601. ISSN: 0048-9697. URL: https://doi.org/10.1016/j.scitotenv.2023.162601.

[292] ESA. *Sentinel-2 User Handbook*. Accessed May 22, 2026. 2025. URL: https://sentinels.copernicus.eu/documents/247904/685211/Sentinel-2_User_Handbook.

[293] W. J. Frampton, J. Dash, G. Watmough, and E. J. Milton. "Evaluating the capabilities of Sentinel-2 for quantitative estimation of biophysical variables in vegetation". In: *ISPRS journal of photogrammetry and remote sensing* 82 (2013), pp. 83–92. URL: https://doi.org/10.1016/j.isprsjprs.2013.04.007.

[294] A. Spinosa, M. A. Fuentes-Monjaraz, and G. El Serafy. "Assessing the use of Sentinel-2 data for spatio-temporal upscaling of flux tower gross primary productivity measurements". In: *Remote Sensing* 15.3 (2023), p. 562. URL: https://doi.org/10.3390/rs15030562.

[295] K. Noumonvi, M. Ferlan, K. Eler, *et al.* "Estimation of Carbon Fluxes from Eddy Covariance Data and Satellite-Derived Vegetation Indices in a Karst Grassland (Podgorski Kras, Slovenia)". In: *Remote Sensing* 11 (2019), p. 649. DOI: 10.3390/rs11060649.

[296] T. Pluntke, C. Bernhofer, T. Grünwald, M. Renner, and H. Prasse. "Long-term climatological and ecohydrological analysis of a paired catchment flux tower observatory near Dresden (Germany). Is there evidence of climate change in local evapotranspiration?" In: *Journal of Hydrology* 617 (2023). ISSN: 0022-1694. URL: https://doi.org/10.1016/j.jhydrol.2022.128873.

[297] C. S. Hub. *Sentinel-2 Level-2A Data Documentation*. Accessed May 22, 2026. 2025. URL: https://documentation.dataspace.copernicus.eu/APIs/SentinelHub/Data/S2L2A.html.

[298] A. Savitzky and M. J. E. Golay. "Smoothing and Differentiation of Data by Simplified Least Squares Procedures." In: *Analytical Chemistry* 36.8 (July 1964). Publisher: American Chemical Society, pp. 1627–1639. ISSN: 0003-2700. DOI: 10.1021/ac60214a047.

[299] J. Fattah, L. Ezzine, Z. Aman, *et al.* "Forecasting of Demand Using ARIMA Model". In: *International Journal of Engineering Business Management* 10 (2018). DOI: 10.1177/1847979018808673.

[300] A. A. Ariyo, A. O. Adewumi, and C. K. Ayo. "Stock price prediction using the ARIMA model". In: *2014 UKSim-AMSS 16th international conference on computer modelling and simulation*. IEEE. 2014, pp. 106–112. DOI: 10.1109/UKSim.2014.67.

[301] M. M. Fathi, A. G. Awadallah, A. M. Abdelbaki, *et al.* "A New Budyko Framework Extension Using Time Series SARIMAX Model". In: *Journal of Hydrology* 570 (2019), pp. 827–838. ISSN: 0022-1694. URL: https://doi.org/10.1016/j.jhydrol.2019.01.037.

[302] Y. Guo, X. Lai, and M. Gan. "Cyanobacterial Biomass Prediction in a Shallow Lake Using the Time Series SARIMAX Models". In: *Ecological Informatics* 78 (2023), p. 102292. ISSN: 1574-9541. URL: https://doi.org/10.1016/j.ecoinf.2023.102292.

[303] T. D. Tolcha. "The State of Africa's Air Transport Market Amid COVID-19, and Forecasts for Recovery". In: *Journal of Air Transport Management* 108 (2023), p. 102380. ISSN: 0969-6997. URL: https://doi.org/10.1016/j.jairtraman.2023.102380.

[304] N. Kumar, V. Jain, K. Joshi, *et al.* "Prediction of Epidemic Disease Cases Using ARIMA and SARIMAX Models". In: *2023 Sixth International Conference of Women in Data Science at Prince Sultan University (WiDS PSU)*. 2023, pp. 201–205. DOI: 10.1109/WiDS-PSU57071.2023.00049.

[305] S. Hochreiter and J. Schmidhuber. “Long Short-Term Memory”. In: *Neural computation* 9.8 (1997), pp. 1735–1780. DOI: 10.1162/neco.1997.9.8.1735.

[306] *SARIMAX statsmodels 0.13.2 documentation*. Accessed May 22, 2026. 2025. URL: https://www.statsmodels.org/dev/generated/statsmodels.tsa.statespace.sarimax.SARIMAX.html.

[307] S. Seabold and J. Perktold. “Statsmodels: Econometric and Statistical Modeling with Python”. In: *9th Python in Science Conference*. 2010.

[308] *XGBoost Python Package*. Accessed May 22, 2026. 2025. URL: https://xgboost.readthedocs.io/en/stable/python/index.html.

[309] *LSTM layer - Keras Documentation*. Accessed May 22, 2026. 2025. URL: https://keras.io/api/layers/recurrent_layers/lstm/.

[310] *XGBoost Parameters*. Accessed May 22, 2026. 2025. URL: https://xgboost.readthedocs.io/en/stable/parameter.html.

[311] L. Alzubaidi, J. Zhang, A. Humaidi, *et al.* “Review of Deep Learning: Concepts, CNN Architectures, Challenges, Applications, Future Directions”. In: *Journal of Big Data* 8 (2021), p. 53. DOI: 10.1186/s40537-021-00444-8.

[312] D. Chicco, M. Warrens, and G. Jurman. “The Coefficient of Determination R-Squared Is More Informative Than SMAPE, MAE, MAPE, MSE, and RMSE in Regression Analysis Evaluation”. In: *PeerJ Comput. Sci.* 7 (July 5, 2021), e623. DOI: 10.7717/peerj-cs.623.

[313] Y. Wang, R. Li, J. Hu, *et al.* “Daily estimation of gross primary production under all sky using a light use efficiency model coupled with satellite passive microwave measurements”. In: *Remote Sensing of Environment* 267 (2021), p. 112721. ISSN: 0034-4257. URL: https://doi.org/10.1016/j.rse.2021.112721.

[314] C. Hu, S. Hu, L. Zeng, *et al.* “Estimation of Daily Maize Gross Primary Productivity by Considering Specific Leaf Nitrogen and Phenology via Machine Learning Methods”. In: *Remote Sensing* 16.2 (2024). ISSN: 2072-4292. DOI: 10.3390/rs16020341.

[315] A. Tiwari. “Chapter 2 - Supervised Learning: From Theory to Applications”. In: *Artificial Intelligence and Machine Learning for EDGE Computing*. Ed. by R. Pandey, S. K. Khatri, N. kumar Singh, and P. Verma. Academic Press, 2022, pp. 23–32. ISBN: 978-0-12-824054-0. URL: https://doi.org/10.1016/B978-0-12-824054-0.00026-5.

[316] X. Xing, M. Wu, H. Zhu, W. Duan, W. Ju, X. Wang, Y. Ran, Y. Zhang, and F. Jiang. “Optimized gross primary productivity over the croplands within the BEPS particle filtering data assimilation system (BEPS_PF v1. 0)”. In: *Journal of Advances in Modeling Earth Systems* 17.1 (2025), e2024MS004412. DOI: http://dx.doi.org/10.1029/2024MS004412.

[317] D. Du, C. Zheng, L. Jia, Q. Chen, M. Jiang, G. Hu, and J. Lu. “Estimation of global cropland gross primary production from satellite observations by integrating water availability variable in light-use-efficiency model”. In: *Remote Sensing* 14.7 (2022), p. 1722. URL: https://doi.org/10.3390/rs14071722.

[318] W. Yuan, W. Cai, A. L. Nguy-Robertson, H. Fang, A. E. Suyker, Y. Chen, W. Dong, S. Liu, and H. Zhang. "Uncertainty in simulating gross primary production of cropland ecosystem from satellite-based models". In: *Agricultural and Forest Meteorology* 207 (2015), pp. 48–57. URL: https://doi.org/10.1016/j.agrformet.2015.03.016.

[319] Z. Cui, X. Qing, H. Chai, S. Yang, Y. Zhu, and F. Wang. "Real-time rainfall-runoff prediction using light gradient boosting machine coupled with singular spectrum analysis". In: *Journal of Hydrology* 603 (2021), p. 127124. URL: https://doi.org/10.1016/j.jhydrol.2021.127124.

[320] G. Ke, Q. Meng, T. Finley, T. Wang, W. Chen, W. Ma, Q. Ye, and T.-Y. Liu. "Lightgbm: A highly efficient gradient boosting decision tree". In: *Advances in neural information processing systems* 30 (2017). URL: https://proceedings.neurips.cc/paper_files/paper/2017/file/6449f44a102fde848669bdd9eb6b76fa-Paper.pdf.

[321] H. Jung, J. Ju, M. Jung, *et al.* "Less-forgetting Learning in Deep Neural Networks". In: *ArXiv* abs/1607.00122 (2016). URL: https://api.semanticscholar.org/CorpusID:18398195.

[322] S. Ede, S. Baghdadlian, L. Weber, *et al. Explain to Not Forget: Defending Against Catastrophic Forgetting with XAI*. 2022. URL: https://arxiv.org/abs/2205.01929.

[323] A. E. Khatib and F. Karray. "Preempting Catastrophic Forgetting in Continual Learning Models by Anticipatory Regularization". In: *2019 International Joint Conference on Neural Networks (IJCNN)*. 2019, pp. 1–7. DOI: 10.1109/IJCNN.2019.8852426.

[324] J. Lai, Y. Zhang, A. Wang, W. Fei, Y. Diao, R. Li, and J. Wu. "FLAML version 2.3.3: Model-based assessment of gross primary productivity at forest, grassland, and cropland ecosystem sites". In: *Geoscientific Model Development Discussions* 2025 (2025), pp. 1–54. DOI: 10.5194/gmd-18-5115-2025.

[325] M. Galvagno, G. Wohlfahrt, E. Cremonese, M. Rossini, R. Colombo, G. Filippa, T. Julitta, G. Manca, C. Siniscalco, U. M. Di Cella, *et al.* "Phenology and carbon dioxide source/sink strength of a subalpine grassland in response to an exceptionally short snow season". In: *Environmental Research Letters* 8.2 (2013), p. 025008. DOI: 10.1088/1748-9326/8/2/025008.

[326] M. Rossini, M. Migliavacca, M. Galvagno, M. Meroni, S. Cogliati, E. Cremonese, F. Fava, A. Gitelson, T. Julitta, U. M. di Cella, *et al.* "Remote estimation of grassland gross primary production during extreme meteorological seasons". In: *International journal of applied earth observation and geoinformation* 29 (2014), pp. 1–10. URL: https://doi.org/10.1016/j.jag.2013.12.008.

[327] K. E. Owen, J. Tenhunen, M. Reichstein, Q. Wang, E. Falge, R. Geyer, X. Xiao, P. Stoy, C. Ammann, A. Arain, *et al.* "Linking flux network measurements to continental scale simulations: Ecosystem carbon dioxide exchange capacity under non-water-stressed conditions". In: *Global Change Biology* 13.4 (2007), pp. 734–760. URL: https://doi.org/10.1111/j.1365-2486.2007.01326.x.

[328] Á. Rubio-Cuadrado, C. Gómez, J. Rodríguez-Calcerrada, R. Perea, G. G. Gordaliza, J. J. Camarero, F. Montes, and L. Gil. "Differential response of oak and beech to late frost damage: an integrated analysis from organ to forest". In: *Agricultural and Forest Meteorology* 297 (2021), p. 108243. URL: https://doi.org/10.1016/j.agrformet.2020.108243.

[329] S. Chen, L. Liu, L. Sui, X. Liu, and Y. Ma. "An improved spatially downscaled solar-induced chlorophyll fluorescence dataset from the TROPOMI product". In: *Scientific Data* 12.1 (2025), p. 135. URL: https://doi.org/10.1038/s41597-024-04325-6.

[330] A. J. Purdy, J. B. Fisher, M. L. Goulden, A. Colliander, G. Halverson, K. Tu, and J. S. Famiglietti. "SMAP soil moisture improves global evapotranspiration". In: *Remote Sensing of Environment* 219 (2018), pp. 1–14. URL: https://doi.org/10.1016/j.rse.2018.09.023.

[331] N. Das, D. Entekhabi, R. Dunbar, S. Kim, S. Yueh, A. Colliander, P. ONeill, T. Jackson, T. Jagdhuber, F. Chen, *et al.* "SMAP_Sentinel-1 L2 radiometer/radar 30-second scene 3 km EASE-grid soil moisture, version 2". In: *NASA National Snow and Ice Data Center Distributed Active Archive Center (DAAC) data set* (2018), KE1CSVXMI95Y. URL: https://doi.org/10.5067/KE1CSVXMI95Y.

[332] B. Martens, D. L. Schumacher, H. Wouters, J. Muñoz-Sabater, N. E. C. Verhoest, and D. G. Miralles. "Evaluating the Land-Surface Energy Partitioning in ERA5". In: *Geoscientific Model Development* 13 (2020), pp. 4159–4181. DOI: 10.5194/gmd-13-4159-2020.

[333] D. G. Miralles, O. Bonte, A. Koppa, O. M. Baez-Villanueva, E. Tronquo, F. Zhong, H. E. Beck, P. Hulsman, W. Dorigo, N. E. C. Verhoest, *et al.* "GLEAM4: Global Land Evaporation and Soil Moisture Dataset at 0.1° Resolution from 1980 to Near Present". In: *Scientific Data* 12 (2025), p. 416. URL: https://doi.org/10.1038/s41597-025-04610-y.

[334] S. W. Running, R. R. Nemani, F. A. Heinsch, M. Zhao, M. Reeves, and H. Hashimoto. "A Continuous Satellite-Derived Measure of Global Terrestrial Primary Production". In: *BioScience* 54 (2004), pp. 547–560. DOI: 10.1641/0006-3568(2004)054[0547:ACSMOG]2.0.CO;2.

[335] D. P. Turner, W. D. Ritts, W. B. Cohen, S. T. Gower, S. W. Running, M. Zhao, M. H. Costa, A. A. Kirschbaum, J. M. Ham, S. R. Saleska, *et al.* "Evaluation of MODIS NPP and GPP Products Across Multiple Biomes". In: *Remote Sensing of Environment* 102 (2006), pp. 282–292. DOI: 10.1016/j.rse.2006.02.017.

[336] M. Jung, S. Koirala, U. Weber, K. Ichii, F. Gans, G. Camps-Valls, D. Papale, C. Schwalm, G. Tramontana, and M. Reichstein. "The FLUXCOM Ensemble of Global Land–Atmosphere Energy Fluxes". In: *Scientific Data* 6 (2019), p. 74. DOI: 10.1038/s41597-019-0076-8.

[337] S. He, Y. Zhang, N. Ma, J. Tian, D. Kong, and C. Liu. "A daily and 500 m coupled evapotranspiration and gross primary production product across China during 2000–2020". In: *Earth System Science Data Discussions* 2022 (2022), pp. 1–42. URL: https://doi.org/10.5194/essd-14-5463-2022.

[338] S. H. Wu, P.-E. Jansson, and P. Kolari. “The role of air and soil temperature in the seasonality of photosynthesis and transpiration in a boreal Scots pine ecosystem”. In: *Agricultural and Forest Meteorology* 156 (2012), pp. 85–103. ISSN: 0168-1923. URL: https://doi.org/10.1016/j.agrformet.2012.01.006.

[339] S. Lin, J. Li, Q. Liu, *et al.* “Evaluating the Effectiveness of Using Vegetation Indices Based on Red-Edge Reflectance from Sentinel-2 to Estimate Gross Primary Productivity”. In: *Remote Sensing* 11.11 (2019). ISSN: 2072-4292. DOI: 10.3390/rs11111303.

[340] J. Rouse, R. Haas, J. Schell, and D. Deering. “Monitoring Vegetation Systems in the Great Plains with Erts”. In: *Nasa Special Publication* 351 (1974), p. 309. URL: https://ntrs.nasa.gov/citations/19740022614.

[341] Z. Jiang, A. R. Huete, K. Didan, and T. Miura. “Development of a two-band enhanced vegetation index without a blue band”. In: *Remote sensing of Environment* 112.10 (2008), pp. 3833–3845. ISSN: 0034-4257. DOI: 10.1016/j.rse.2008.06.006.

[342] M. S. Adan. “Integrating Sentinel-2 derived vegetation indices and terrestrial laser scanner to estimate above-ground biomass/Carbon in Ayer Hitam tropical forest Malaysia”. Thesis. 2017. URL: http://essay.utwente.nl/83579/1/adan.pdf.

[343] B.-c. Gao. “NDWIA normalized difference water index for remote sensing of vegetation liquid water from space”. In: *Remote Sensing of Environment* 58.3 (1996), pp. 257–266. ISSN: 0034-4257. URL: https://doi.org/10.1016/S0034-4257(96)00067-3.

[344] M. A. Hardisky, V. Klemas, and R. Smart. “The influence of soil salinity, growth form, and leaf moisture on the spectral radiance of Spartina alterniflora Canopies”. In: *Photogrammetric Engineering and Remote Sensing* 49 (1983), pp. 77–83.

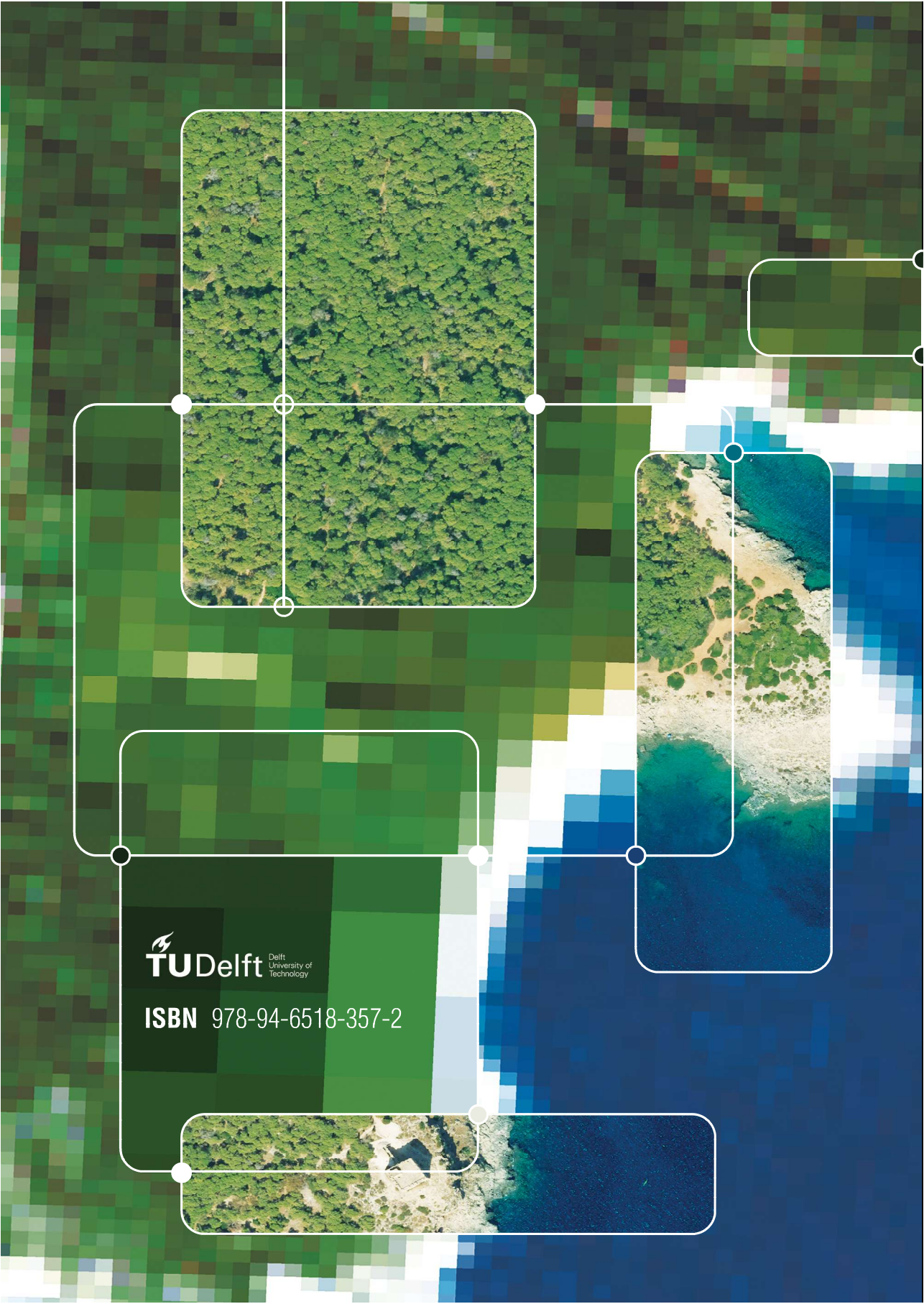

TU Delft Delft University of Technology

ISBN 978-94-6518-357-2